



Universität Hamburg  
DER FORSCHUNG | DER LEHRE | DER BILDUNG

# Identifying electron-phonon interactions in 3D topological insulator nanoflakes by inelastic light scattering

## Dissertation

zur Erlangung des Doktorgrades  
an der Fakultät für Mathematik, Informatik und Naturwissenschaften  
Fachbereich Physik  
der Universität Hamburg

vorgelegt von

Sarah Scheitz

Hamburg 2022

Gutachter der Dissertation:

Prof. Dr. Michael A. Rübhausen  
Prof. Dr. Nils Huse

Zusammensetzung der Prüfungskommission:

Prof. Dr. Daniela Pfannkuche  
Prof. Dr. Michael A. Rübhausen  
Prof. Dr. Nils Huse  
Prof. Dr. Dorota Koziej  
Prof. Dr. Kai Rossnagel

Vorsitzende der Prüfungskommission:

Prof. Dr. Daniela Pfannkuche

Vorsitzender des Fach-Promotionsausschusses Physik:

Prof. Dr. Wolfgang J. Parak

Leiter des Fachbereichs Physik:

Prof. Dr. Günter H. W. Sigl

Dekan der Fakultät MIN:

Prof. Dr. Heinrich Graener

Datum der Disputation :

27.10.2022

# Eidesstattliche Erklärung

Ich versichere, dass ich die beigefügte schriftliche Dissertationsschrift selbstständig angefertigt und keine anderen als die angegebenen Hilfsmittel benutzt habe. Alle Stellen, die dem Wortlaut oder dem Sinn nach anderen Werken entnommen sind, habe ich in jedem einzelnen Fall unter genauer Angabe der Quelle deutlich als Entlehnung kenntlich gemacht. Dies gilt auch für alle Informationen, die dem Internet oder anderer elektronischer Datensammlungen entnommen wurden.

Ich erkläre ferner, dass die von mir angefertigte Dissertation in der vorgelegten oder einer ähnlichen Form nicht schon einmal in einem früheren Promotionsverfahren angenommen oder als ungenügend beurteilt wurde.

Die von mir eingereichte schriftliche Fassung entspricht jener auf dem elektronischen Speichermedium.

Hamburg, 22.07.2022

---

Ort, den | City, date



---

Unterschrift | Signature

*Sometimes my courage fails me and I think I ought to stop working, live in the country and devote myself to gardening. But I am held by a thousand bonds, and I don't know when I shall be able to arrange things otherwise. Nor do I know whether, even by writing scientific books, I could live without the laboratory.*

**Marie Curie**

- letter to her sister Bronya, september 1927



# Abstract

The 3D topological insulator (TI) materials  $\text{Bi}_2\text{Se}_3$  and  $\text{Bi}_2\text{Te}_3$  belong to a new class of materials that are characterized by insulating bulk properties but host quasi-relativistic states at their surface. These topological surface states form as a consequence of the differing topology of the underlying Hamiltonian of the material and air and have been shown to be very robust at ambient conditions as long as the topological character of the bulk is unchanged. In addition, the strong spin-momentum locking that is present in  $\text{Bi}_2\text{Se}_3$  and  $\text{Bi}_2\text{Te}_3$  leads to helical spin-polarization and protects the surface states against backscattering and enables dissipationless transport. Since their discovery these novel quantum states have led to a vast interest in the condensed matter community for the realization of applications in spintronics, quantum computing and low-resistance materials at room temperature.

This work presents studies on  $\text{Bi}_2\text{Se}_3$  and  $\text{Bi}_2\text{Te}_3$  in the form of 2D nanoflakes, which greatly reduces bulk contribution and enhances the topological surface properties. By the use of Raman spectroscopy this work investigates the interaction of the crystal lattice with the electronic degrees of freedom in the ultrathin limit. Hereby, the investigation of the phonon's frequency and line shape is used to identify significant electron-phonon interactions. By investigating the 2D nanoflakes' Raman response under the influence of different external parameters like low temperatures, strong magnetic fields, and the interface to a gold substrate, the changes in electron-phonon coupling are identified. These are used to deduct information on the nature and manipulation of the topological band structure in the ultrathin flakes.

In detail, high resolution temperature dependent Raman measurements in the range between 300 K to 3 K reveal for  $\text{Bi}_2\text{Se}_3$  additional phonon self-energy corrections at low temperatures caused by interactions with an electronic susceptibility in the energy range of the phonons. This electronic susceptibility can be related to the quasi-relativistic electrons and shows the high contribution of topological surface states in the studied nanoflakes. The topological nature of the coupling electrons is confirmed in magnetic field dependent Raman measurements. The application of magnetic fields above 3 T reveals further changes in the  $\text{Bi}_2\text{Se}_3$  phonon's self-energy that are shown to origin from the manipulation of the electronic susceptibility due to a gap opening in the topological surface states.

For potential applications of  $\text{Bi}_2\text{Se}_3$  and  $\text{Bi}_2\text{Te}_3$  in devices, the influence of a gold-interface on the electronic surface band structure is studied. By investigating the Raman response of single nanoflakes on gold as a function of flake thickness carrier injection from the gold into the contacted surface is identified. Our study confirms the Au-interface induced downward band bending in  $\text{Bi}_2\text{Se}_3$  and  $\text{Bi}_2\text{Te}_3$  and demonstrates high contributions of

trivial bulk electrons for nanoflakes below 10 nm and 12 nm, respectively. The obtained results are finally discussed with respect to possible thickness limitations in accessing the topological transport regime.

# Zusammenfassung

$\text{Bi}_2\text{Se}_3$  und  $\text{Bi}_2\text{Te}_3$  gehören zur Gruppe der sogenannten 3D topologischen Isolatoren (TI), welche sich durch isolierenden Eigenschaften im Inneren und leitenden Kanälen mit quasi-relativistischen Elektronen an der Oberfläche auszeichnen. Diese sind das Ergebnis der topologischen Eigenschaften des zugehörigen Hamiltonians, welcher das Schließen der elektronischen Bandlücke im Übergang zu einem angrenzenden Material mit abweichender Topologie, sowie z.B. Luft, erfordert. Die Oberflächenzustände zeichnen sich durch spin-polarisierte Bänder aus, welche quasi verlustfreien Transport ermöglichen und durch ihren topologischen Ursprung robust gegenüber Deformationen des Materials sind. Diese Eigenschaften führten zu einer intensiven Erforschung der topologischen Isolatoren für potentielle Anwendungen im Bereich der Spintronik, Quantencomputern, und als widerstandsfreie Leiter bei Raumtemperatur.

Im Rahmen dieser Arbeit wurden als Vertreter der 3D TI  $\text{Bi}_2\text{Se}_3$  und  $\text{Bi}_2\text{Te}_3$  in Form von zweidimensionalen Nanoflakes hergestellt, um den Beitrag der topologischen Oberflächeneigenschaften zu erhöhen. Die Untersuchung der Nanoflakes mittels Raman Spektroskopie ermöglicht es Informationen über die Wechselwirkung der topologisch geschützten OberflächenElektronen mit den Gitterschwingungen des Kristalls abzuleiten. Dabei konnten über eine Analyse der Phononen Selbst-Energie zusätzliche Beiträge durch die Ankopplung an elektronischen Freiheitsgrade des Materials identifiziert werden. Die Elektron-Phonon Wechselwirkungen wurden unter verschiedenen externen Rahmenbedingungen untersucht. Dabei wurden Raman Messungen als Funktion der Temperatur, unter dem Einfluss starker magnetischer Felder, und an Nanoflake Proben im Kontakt zu einem Gold Substrat durchgeführt. Über die Analyse der Phononen Linienformen und daraus abgeleiteter Wechselwirkungen mit den Elektronen des Systems wurden Schlussfolgerungen auf die topologische Bandstruktur der ultradünnen Flakes gezogen.

Im Detail, in temperaturabhängigen Raman Messungen im Bereich von 300 K bis 3 K wurden die Lebensdauern und Zerfallskanäle der Phononen untersucht. Dabei weist  $\text{Bi}_2\text{Se}_3$  bei niedrigen Temperaturen starke Phononen Selbst-Energie Korrekturen auf, welche durch die Wechselwirkung mit einer niederenergetischen elektrischen Anregung erklärt werden können. Dies lässt sich auf eine Ankopplung an die quasi-relativistischen OberflächenElektronen zurückführen und demonstriert den erhöhten Beitrag der topologischen Oberflächeneigenschaften in den Nanoflakes. Der topologische Charakter der wechselwirkenden Elektronen wurde über Raman Messungen in starken Magnetfeldern verifiziert. Es ist bekannt, dass in 3D TI der Einfluss eines Magnetfeldes die Zeit-Umkehr Symmetrie im Material bricht, welche zu einer Änderung des topologischen Charakters führt. Tatsächlich werden ab Feldstärken von über 3 T weitere Selbst-Energie Korrekturen in  $\text{Bi}_2\text{Se}_3$  festgestellt, welche auf die Öffnung einer Bandlücke und damit einhergehende Modifizierung

der Oberflächenzustände schließen lassen.

Des Weiteren wurde der Kontakt zwischen Gold und einzelnen  $\text{Bi}_2\text{Se}_3$ , sowie  $\text{Bi}_2\text{Te}_3$  Nanoflakes untersucht um den Einfluss des Goldkontaktes auf die elektronische Bandstruktur der TI Materialien zu charakterisieren. Für potentielle Anwendungen ultradünner TI Schichten ist das Interface zu Goldkontakten von besonderem Interesse, da durch die unterschiedliche Elektronenaffinitäten der Materialien ein Ladungstransfer und Beeinflussung der topologischen Bandstruktur zu erwarten sind. In dieser Arbeit wurde dieser Ladungstransfer durch Raman Spektroskopie an einzelnen Nanoflakes mit variierenden Dicken im Bereich von wenigen Nanometern nachgewiesen. Die beobachteten starken Selbst-Energie Effekte in den Phononen von  $\text{Bi}_2\text{Se}_3$  und  $\text{Bi}_2\text{Te}_3$  Nanoflakes mit Dicken unter jeweils 10 nm und 12 nm sind das Ergebnis der vom Gold injizierten Ladungsträger. Diese führen zu einer Besetzung der trivialen Leitungsbänder in den TI Nanoflakes, welche einen reinen Transport über die topologischen Oberflächenkanäle verhindern. Damit liefert diese Studie wichtige Ergebnisse über die Bandverbiegung in  $\text{Bi}_2\text{Se}_3/\text{Bi}_2\text{Te}_3$ -Gold Kontakten, welche im Hinblick auf mögliche Dicken-Begrenzungen der zu verwendeten TI Schichten in zukünftigen Anwendungen diskutiert werden.

# Contents

<b>Eidesstattliche Erklärung</b>	<b>i</b>
<b>Abstract</b>	<b>iii</b>
<b>Zusammenfassung</b>	<b>v</b>
<b>1 Motivation</b>	<b>1</b>
1.1 Topological order in condensed matter physics . . . . .	1
1.2 Three-dimensional topological insulators - $\text{Bi}_2\text{Se}_3$ & $\text{Bi}_2\text{Te}_3$ . . . . .	4
1.3 Enhanced surface state contribution in 2D Nanoflakes . . . . .	6
1.4 Raman measurements on TIs as chance of probing TSS . . . . .	7
1.5 Outline of thesis . . . . .	9
<b>2 Synthesis and Characterization of 2D Nanoflakes</b>	<b>11</b>
<b>3 Raman Response of Topological Insulator 2D Nanoflakes</b>	<b>15</b>
3.1 Theory of Raman scattering . . . . .	15
3.1.1 Introduction - General scattering process . . . . .	15
3.1.2 Quantum mechanical approach . . . . .	17
3.1.3 Raman line shapes obtained from electron-phonon interactions . . . . .	21
3.1.4 Selection rules . . . . .	25
3.1.5 Temperature dependence of first-order Raman scattering . . . . .	26
3.1.6 Raman Response of $\text{Bi}_2\text{Se}_3$ and $\text{Bi}_2\text{Te}_3$ . . . . .	29
3.2 Experimental setups . . . . .	33
3.2.1 Raman setup for temperature and magnetic field dependence . . . . .	33
3.2.2 Micro-Raman setup for single nanoflake investigations . . . . .	36
3.2.3 Ultimate Triple-Grating spectrometer . . . . .	40
<b>4 Macro-Raman investigations of thin film samples</b>	<b>43</b>
4.1 Motivation . . . . .	43
4.2 Sample Preparation of NF thin films . . . . .	44
4.3 Measurement configuration and data analysis . . . . .	46
4.4 Results - Temperature dependence . . . . .	48
4.4.1 Mode symmetry analysis . . . . .	48
4.4.2 Inversion symmetry breaking in 2D NFs observable at low temperatures . . . . .	49
4.4.3 Temperature dependent self-energy effects . . . . .	51
4.4.4 Self-energy corrections by electron-phonon interactions . . . . .	54
4.5 Results - Magnetic field dependence . . . . .	58

## Contents

4.6	Summary . . . . .	61
4.7	Paper I . . . . .	63
<b>5</b>	<b>Micro-Raman investigations of the TI-gold interface</b>	<b>73</b>
5.1	Motivation . . . . .	73
5.2	Sample Preparation of single NFs . . . . .	74
5.3	Measurement configuration and data analysis . . . . .	76
5.4	Results - Resonance Raman study of Bi <sub>2</sub> Se <sub>3</sub> on Si and Au substrates . . .	80
5.5	Results - Carrier injection by Au substrate . . . . .	82
5.6	Summary . . . . .	91
5.7	Paper II . . . . .	93
<b>6</b>	<b>Conclusion and Outlook</b>	<b>103</b>
	<b>Bibliography</b>	<b>107</b>
	<b>Abbreviations</b>	<b>122</b>
	<b>List of Figures</b>	<b>123</b>
	<b>List of Tables</b>	<b>125</b>
	<b>APPENDIX</b>	<b>127</b>
	<b>List of publications</b>	<b>143</b>
	<b>Further publications</b>	<b>145</b>
	<b>Acknowledgments</b>	<b>169</b>

# 1

## Motivation

In the following, section 1.1 contains a brief introduction on the topological nature of matter, and their importance for potential applications in spintronics or quantum computing is given. For further information on the historical development of the field as well as mathematical derivations of topological invariants the reader is referred to the following reviews<sup>[1–4]</sup>. As model 3D topological insulator materials  $\text{Bi}_2\text{Se}_3$  and  $\text{Bi}_2\text{Te}_3$  are introduced in section 1.2 with a focus on their topological band structure. Since the topological properties result in the formation of surface states at the interface between matter of different topological phases, section 1.3 motivates the use of  $\text{Bi}_2\text{Se}_3$  and  $\text{Bi}_2\text{Te}_3$  in the form of ultrathin nanoflakes with a high surface-to-bulk ratio. Finally, section 1.4 explains the advantages and possibilities of studying the TI nanoflakes by means of Raman spectroscopy revealing the interaction of the topological electrons with the crystal lattice. Section 1.5 gives the outline of this thesis.

### 1.1 Topological order in condensed matter physics

Topological insulators (TIs) represent a new quantum state of matter exhibiting peculiar quasi-relativistic surface states that form at the interface to conventional insulators. In condensed matter physics the classification of orders in solid systems was historically determined by types of spontaneous broken symmetry. For instance, crystalline phases break translational and rotational symmetry of free space, and magnetic phases break time-reversal symmetry and the rotational symmetry of spin space. The need for an additional concept in describing types of order became apparent in 1980 with the discovery of the quantum Hall effect (QHE) by van Klitzing *et al.*<sup>[5]</sup> In the QHE the application of a magnetic field perpendicular to a 2D electron gas (2DEG) leads to the condensation of electronic states into discrete Landau levels. As a result the transversal conductivity  $\sigma_{xy}$  is quantized due to the shifting of Landau levels through the chemical potential as a function of  $\vec{B}$ . However, even in the insulating state with the chemical potential residing between two Landau levels, the cyclotron motion of electrons leads to a continuous propagation along the edge of the sample as schematically depicted in Figure 1.1(a).

These conducting edge states proved to be very robust against disorder and independent of the exact form of the sample. This robustness to smooth deformations is the result of the underlying topology of the system. The concept of topology originates from a branch of mathematics that classifies phases into topologically equivalent and non-equivalent classes, where a fundamental property of one topological class is invariant under continuous transformation.<sup>[6]</sup> This concept makes topological phases very robust as the topological properties are conserved under continuous deformations. As a result, objects belonging

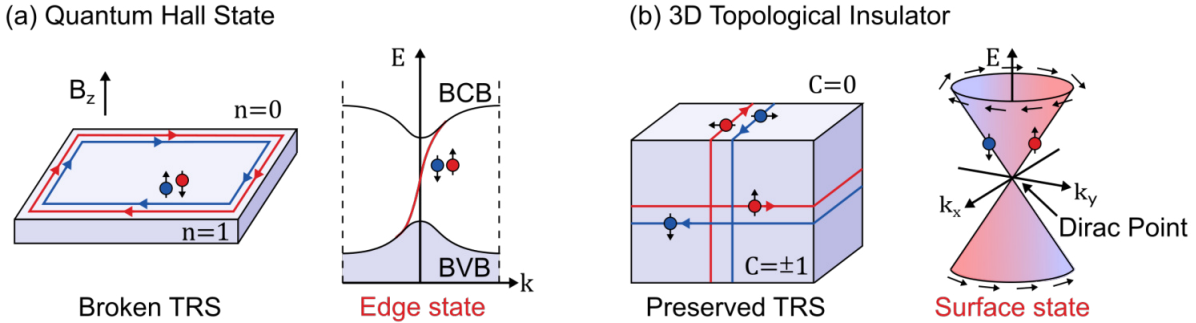


**Figure 1.1:** Topological phases in condensed matter systems and bulk boundary correspondence. (a) Schematic geometry of a Quantum Hall bar with external magnetic field  $B_z$  that breaks time-reversal symmetry and creates a non-trivial topology ( $n = 1$ ). The interface to vacuum with trivial topology ( $n = 0$ ) leads to the formation of a topologically protected, chiral edge state. The edge state connects the bulk valence band (BVB) with the conduction band (BCB) as shown in the 1D band structure and is spin degenerate. (b) Topological non-trivial phase in a time-reversal invariant system. The interface to vacuum creates conducting surface states that form a 2D Dirac cone in the surface band structure. The presence of strong spin-orbit coupling leads to helical spin-polarization. Adapted from<sup>[1,8]</sup>

to an equivalent topological class can be transformed into one another, whereas objects with different topological invariants cannot. This leads to novel phenomena appearing at the interface between two systems of different topology. These topological edge or surface states are the key reason for the excitement within the scientific community as they hold great promise in realizing new quantum states of matter.<sup>[7]</sup>

Historically the first topological edge state was discovered in the case of the QHE, where a topological invariant assigned to the 2D electron gas under the influence of an external magnetic field turns out to be distinct from the topological invariant of the vacuum. Connecting the QH state to a topological invariant was first introduced in 1982 by Thouless, Kohmoto, Nightingale, and den Nijs (TKNN).<sup>[9]</sup> The defined TKNN invariant  $n$ , also called the first Chern number, can be directly related to the quantized Hall conductivity  $\sigma_{xy} = ne^2/h$ , where  $n = 0$  classifies a topologically trivial insulator and non-trivial topology is given by  $n = 1$ . Hence, even though the QH state and the vacuum are both insulating they are characterized by different Chern numbers ( $n = 1$ , and  $n = 0$ , respectively), making them topologically non-equivalent. At the interface of these topologically distinct systems the topology cannot be continuously transformed and the associated electronic band structure has to close the band gap across the interface, which forms the conducting edge states as shown in Figure 1.1(a). The occurrence of gapless states at the interface between a system with non-trivial and trivial topology is a fundamental property of topological phases and defined as the so-called *bulk boundary correspondence*.<sup>[1]</sup>

In condensed matter physics, topological phases can be classified according to the symmetry properties of the electronic band structure in reciprocal space.<sup>[4]</sup> Hereby, the identification of topological invariants is related to the continuous transformation of the systems Hamiltonian in parameter space. Therefore, two insulators can be assigned to different topological



classes if their underlying Hamiltonians cannot be adiabatically transformed into each other. This led to the identification of a number of different electronic band insulators.<sup>[1]</sup> The topological equivalence of Hamiltonians is determined by the so-called Berry phase.<sup>[10]</sup> M. Berry showed that after an adiabatic transformation of an eigenstate of the system's Hamiltonian on a closed path in Hilbert space, the system remains in its eigenstate and acquires a dynamic phase that accounts for the time evolution. Surprisingly, the electronic state, represented by a Bloch wave function, acquires an additional phase factor that is time-independent and only depends on the closed path in phase space. It can be shown that this Berry phase  $\gamma_m$  is in direct analogy to the Chern number  $C_m = \gamma_m/2\pi$ ,<sup>[8]</sup> and can be used to define a topological invariant of the electronic band structure by summing over all  $n$  valence bands of the system  $C = \sum_{m=1}^n C_m$ . Insulators with  $C = 0$  are the topological trivial band insulators, whereas  $C \neq 0$  characterizes insulators with non-trivial topology and a finite Berry phase.

The concept of topological classification via suitable topological invariants was readily extended to other condensed matter systems in 2D<sup>[11,12]</sup> and 3D<sup>[13,14]</sup> without the need for an external magnetic field. Nowadays, there exists a general classification scheme for topological insulators that depends on the dimension of the system as well as the presence or absence of symmetries, like e.g. time-reversal symmetry (TRS).<sup>[8,15]</sup> In contrast to the quantum Hall state (QHS), where the non-trivial topology of the 2DEG is induced by the broken TRS due to the applied magnetic field, there exists a different topological class where TRS is unbroken and the non-trivial topology is induced by strong spin-orbit interactions.<sup>[16]</sup> This is the class of time-reversal invariant 3D topological insulators, that are in focus in this work. In 3D TIs a strong spin-orbit coupling (SOC) leads to an inverted band structure and provides a non-trivial topology.<sup>[1]</sup> The topology has in principle no effect on the bulk structure where the insulating properties remain. However, in contact to a trivial insulator, e.g. air or vacuum, the topological invariant cannot smoothly transform across the interface. As a result, the gapped electronic band structures cannot be adiabatically transformed and the only solution is obtained by the formation of electronic bands crossing the gap, as shown in Figure 1.1(b). These metallic states are confined to the surface of the TI.

In 3D TIs the topological surface states (TSS) form a cone-shaped dispersion in the  $k_{xy}$ -plane. The almost linear dispersion can be described by the Dirac-equation for quasi-relativistic electrons, where the energy eigenvalues become gapless assuming a vanishing rest mass.<sup>[17]</sup> The gapless dispersion is therefore referred to as a Dirac cone and said to host 'massless' Dirac fermions.<sup>[4]</sup> Due to the strong SOC the TSS have helical spin polarization with the spin of the Dirac fermions always locked to their momentum, as shown in Figure 1.1(b). Furthermore, an important property of the TSS is their topological protection where three aspects contribute. First, the non-trivial topology is preserved as long as the TRS is unperturbed, which guarantees the presence of the gapless surface states. Secondly, the spin-helical TSS show reduced backscattering as Dirac fermions with opposite momenta  $\vec{k}$  and  $-\vec{k}$  cannot scatter into each other due to the spin mismatch.<sup>[4]</sup> Finally,

the non-trivial Berry phase  $\pi$  associated to the Dirac fermions protects them from weak localization as the time-reversed path around an impurity interfere destructively.<sup>[1]</sup> The stability of the TSS against any perturbations that do not break TRS, in conjunction with the spin-helicity, has led to a great interest in the 3D TIs for implications in spintronics, zero-resistance applications,<sup>[18]</sup> and realization of novel quantum states.<sup>[2]</sup>

## 1.2 Three-dimensional topological insulators - $\text{Bi}_2\text{Se}_3$ & $\text{Bi}_2\text{Te}_3$

Within the class of 3D topological insulators the two bismuth chalcogenides  $\text{Bi}_2\text{Se}_3$  and  $\text{Bi}_2\text{Te}_3$  have gained extensive interest since the discovery of their non-trivial topological band structure.<sup>[19,20]</sup> These two candidates provide great potential of accessing the quasi-relativistic surface states due to their comparatively large bulk band gaps and simple band structure with a single surface Dirac cone centered at the  $\Gamma$  point.<sup>[21]</sup>

Both  $\text{Bi}_2\text{Se}_3$  and  $\text{Bi}_2\text{Te}_3$  share the same rhombohedral crystal structure with five atoms in one unit cell.<sup>[22]</sup> The crystal structure is arranged out of repetitive stacks of the so-called quintuple layers (QL), where each QL consists of five alternating layers of Bi or Se/Te atoms. The crystal structure is discussed in more detail in section 3.1.6. The Brillouin zone of the material is shown in Figure 1.2(a) that exhibits four non-equivalent time-reversal-invariant points  $\Gamma(0,0,0)$ ,  $L(\pi,0,0)$ ,  $F(\pi,\pi,0)$  and  $Z(\pi,\pi,\pi)$ .<sup>[23]</sup> This results in three high-symmetry points for the surface 2D Brillouin zone, namely  $\bar{\Gamma}$ ,  $\bar{K}$ , and  $\bar{M}$ . Zhang *et al.* have shown that the topological character of  $\text{Bi}_2\text{Se}_3$  and  $\text{Bi}_2\text{Te}_3$  is determined at the  $\Gamma$  point, where strong SOC leads to a band inversion between two p-orbitals and the creation of topological surface states.<sup>[21]</sup> The dimension of the bulk band gaps have been determined via angle-resolved photoelectron spectroscopy (ARPES) or infrared (IR) transmission to be around 300–350 meV for  $\text{Bi}_2\text{Se}_3$ <sup>[19,24,25]</sup> and 160–170 meV for  $\text{Bi}_2\text{Te}_3$ <sup>[20,26]</sup>. Discrepancies in the gap energy are usually due to the difficulty in determining the bulk valence band (BVB) maximum.<sup>[27]</sup> Exemplary ARPES measurements of the surface band structures in the  $\bar{\Gamma}\bar{K}$ -direction are given in Figure 1.2(b,c) and show the TSS crossing the bulk band gaps. Due to the large separation between the BCB and BVB the Fermi level can in principle be tuned into the gap to access only the topological Dirac fermions. The nearly linear band dispersion of the surface states is almost isotropic in the momentum  $k_x$ - $k_y$  plane and forms the Dirac cone composed of spin-momentum-locked helical states as schematically depicted in Figure 1.2(d). Hence, both bismuth chalcogenides were identified to be primary candidates for studies of the exotic quantum phenomena related to the TSS. Especially the large bulk band gaps would allow the utilization of the TSS even at room temperature, which corresponds to a typical energy scale of 25 meV. The difference between both materials in terms of their topological band structure is that in  $\text{Bi}_2\text{Se}_3$  the Dirac point (DP) is typically located within the bulk band gap about 190 meV below the

BVB minimum<sup>[28]</sup> and exhibits an idealized Dirac cone with almost linear dispersion. In contrast, in  $\text{Bi}_2\text{Te}_3$  the Dirac node is typically harder to resolve in ARPES measurements as it is buried about 130 meV below the BVB maximum<sup>[20]</sup> as indicated in Figure 1.2(e,f). Thus, only the upper Dirac cone is accessible in  $\text{Bi}_2\text{Te}_3$  for probing of the topological transport regime, whereas in  $\text{Bi}_2\text{Se}_3$  the physics around the Dirac node can also be studied for e.g. the observation of the quantum anomalous Hall effect (QAHE) or realization of topological magnets.<sup>[29,30]</sup>

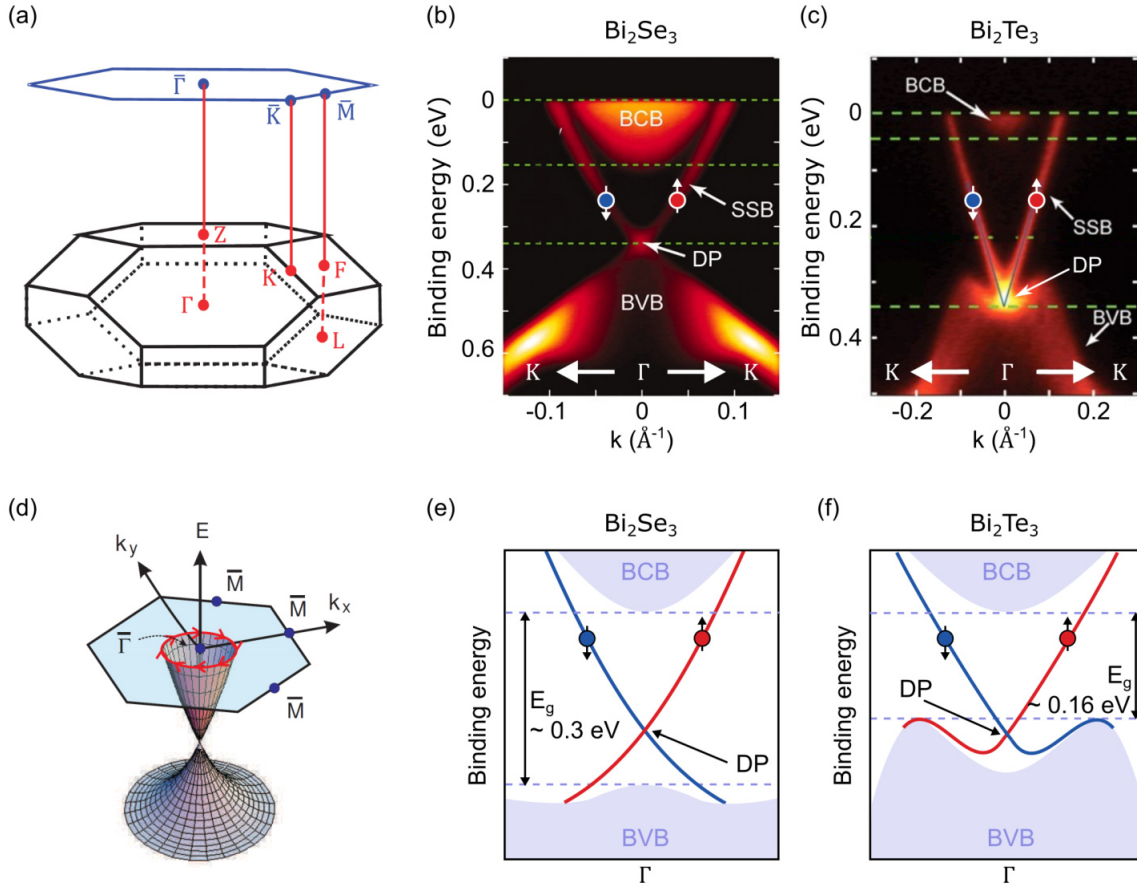


**Figure 1.2:** Surface electronic band structure of the 3D TIs  $\text{Bi}_2\text{Se}_3$  and  $\text{Bi}_2\text{Te}_3$ . (a) 3D bulk (black) and projected 2D surface (blue) Brillouin zone with the labeled high-symmetry points. Reprinted with permission from<sup>[21]</sup>. Copyright 2009 Macmillan Publishers Limited. (b,c) ARPES measurements along the  $\bar{\Gamma}\bar{K}$ -direction of  $\text{Bi}_2\text{Se}_3$  and  $\text{Bi}_2\text{Te}_3$ , respectively. The topological surface state band (SSB), bulk valence band (BVB), and bulk conduction band (BCB) are indicated. (b) Adapted from<sup>[28]</sup>. Reprinted with permission from AAAS. (c) Adapted from<sup>[20]</sup>. Reprinted with permission from AAAS. (d) Schematic representation of the Dirac cone dispersion in momentum plane of the (111) surface Brillouin zone with the TSS Fermi surface encircling the time-reversal invariant  $\bar{\Gamma}$  point. Reprinted with permission from<sup>[31]</sup>. Copyright 2009 by the American Physical Society. (e,f) Schematic surface band structures of  $\text{Bi}_2\text{Se}_3$  and  $\text{Bi}_2\text{Te}_3$ , respectively, with indicated spin polarizations, values for the bulk band gap  $E_g$ , and Dirac point (DP).

## 1.3 Enhanced surface state contribution in 2D Nanoflakes

One of the main challenges in accessing the TSS reported in literature is the significant contribution of bulk conduction.<sup>[32]</sup> Although stoichiometric  $\text{Bi}_2\text{X}_3$  ( $\text{X}=\text{Se},\text{Te}$ ) are narrow-gap semiconductors with the Fermi level positioned inside the bulk band gap, investigated samples are known to show intrinsic  $n$ - or  $p$ -type doping as a result of excess carriers introduced via Se or Te site defects, respectively.<sup>[33,34]</sup> The native defects form at the surface under ambient conditions and introduce additional charges leading to the population of the bulk conduction bands and significant band bending at the surface. The accumulated carriers form non-topological 2DEG quantum well states that coexist next to the topological surface states.<sup>[35–38]</sup> Hence, the electronic properties of the TSS are often masked by the trivial bulk surface states and dominate in transport measurements of  $\text{Bi}_2\text{Se}_3$ <sup>[39–41]</sup> and  $\text{Bi}_2\text{Te}_3$ .<sup>[42]</sup> It is noteworthy, that even though the trivial surface states complicate the identification of effects related to the TSS, they do not destroy the topological phase. The TSS have been shown to be very robust in ambient conditions<sup>[35,43,44]</sup> and are merely located deeper into the surface of the material when trivial 2DEGs form.<sup>[45]</sup> Reducing the formation of trivial surface states has been tackled in a variety of ways; like counter doping<sup>[20,33,36,46–48]</sup> or electrostatic gating<sup>[32,48–53]</sup>, which enables a positioning of the Fermi level inside the bulk band gap. As a result, the Fermi level only crosses the topological Dirac states providing access to the purely topological transport regime. With these techniques a reduction of trivial bulk carrier concentration and realization of the QHE on the surface Dirac states is possible.<sup>[33,54]</sup>

The most promising approach in reducing bulk contribution is by increasing the surface-to-bulk ratio by manufacturing ultrathin samples. This is commonly achieved by using nanostructuring methods like exfoliation or growth of thin films via molecular beam epitaxy (MBE).<sup>[55]</sup> However, especially MBE is very demanding as it requires sophisticated setups, ultra-high vacuums and long preparation times. Additionally, created samples still provide only one accessible surface hosting the TSS. An alternative approach taken in this thesis is the manufacturing of a sample with a manifold of superimposed TI surfaces by synthesizing two-dimensional nanoflakes (NFs) using a wet-chemical approach. By synthesizing a large amount of ultrathin NFs larger clusters are created that allow to simultaneously probe multiple surfaces. Additionally, the surface of the NFs is protected by an attached polymer ligand. This leads to a more inert surface and protection from ambient environment. The wet-chemical synthesis is presented in further detail in chapter 2. As a result, the study of clusters of ultrathin NFs has the potential to enhance the TSS contribution by averaging over many surfaces.

On the other hand, the investigation of single NFs, while tuning their thickness down to a few nm, enables the investigation of the topological character in the ultrathin limit. It is well-known that the surface state wave functions of opposing surfaces can overlap below a

certain thickness. This leads to a hybridization of the TSS and creates a gap opening in the Dirac cone ultimately destroying the spin helicity around the  $\Gamma$  point. The thickness limit of an intact Dirac cone in  $\text{Bi}_2\text{Se}_3$  was determined to be above 5 QL<sup>[56–58]</sup>, whereas in  $\text{Bi}_2\text{Te}_3$  the full Dirac cone is already recovered in 2 QL films.<sup>[26]</sup> This can be related to the different TSS decay lengths into the material, which is shorter for  $\text{Bi}_2\text{Te}_3$  with about 1 nm<sup>[26,59]</sup> in comparison with  $\text{Bi}_2\text{Se}_3$  of about 2–3 nm.<sup>[59]</sup> The investigation of  $\text{Bi}_2\text{Se}_3$  and  $\text{Bi}_2\text{Te}_3$  NFs as a function of thickness consequently helps to connect observed results with the topological character of the samples.

## 1.4 Raman measurements on TIs as chance of probing TSS

The desired topological properties of protected spin-polarized conduction channels can be directly identified in magneto-transport measurements by means of Shubnikov-de Haas oscillations and weak anti-localization (WAL).<sup>[60]</sup> These direct measurements of the topological electrons can reveal many important properties like carrier densities and Fermi velocities.

As a complementary tool, the signatures of the TSS can be measured by means of inelastic light scattering: revealing the TSS directly in the form of an electronic background or indirectly via the interaction with other quasi particles, like phonons. In this thesis, Raman spectroscopy is employed that provides a non-destructive technique to explicitly study the interactions between the electrons in  $\text{Bi}_2\text{X}_3$  and the lattice. Indeed, Raman scattering is known to serve as a powerful technique to study the electronic properties in quasi 2D electron systems like graphene<sup>[61]</sup> and has revealed the scattering of Dirac states in topological insulator materials.<sup>[62–65]</sup> Even though the TSS are protected by TRS against moderate disorder<sup>[66]</sup> the investigation of their interaction with the crystal lattice provides crucial information on their electrical properties for future applications. Since the topological insulators are promising candidate materials for devices at room temperature, their coupling to the lattice vibrations becomes even more significant due to the high occupation of phonon states. Therefore, Raman spectroscopy provides a valuable technique to study the electron-phonon interactions and possible limitations of the TSS especially in the limit of ultrathin samples. Furthermore, Raman scattering enables a contact free measurement of the TI material without the impact from interfaces to e.g. electrical contacts, which are inevitable for transport experiments.

Generally, since inelastic light scattering is characterized by a weak intensity, as discussed in further detail in section 3.1.1, this technique requires a strongly enlarged interaction volume. This is provided by our NF cluster samples that yield an increased scattering volume of surface states to account for the lower interaction strength. The cluster of NFs enabled us to study the TSS under the influence of high magnetic fields and as a function of temperature as further discussed in chapter 4. Nevertheless, even single NFs

## *1 Motivation*

with very small scattering volumes are successfully studied by employing a high-resolution microscope setup as presented in chapter 5.

In addition, Raman scattering is a volume scattering technique, which allows to probe the TSS even in obscured interfaces. As pointed out in the previous section, ambient conditions or interfaces to different substrates can lead to a modification of the surface band structure and a relocation of the TSS into deeper layers of the surface. By the use of Raman scattering, the band bending effects at interfaces can be probed locally, which provides a unique way to reveal the exclusive influence of different substrates on the TSS. Moreover, the local manipulation of the electronic band structure can be revealed by probing resonant electronic transitions in resonant Raman spectroscopy experiments.

## 1.5 Outline of thesis

The main objective of this work is the investigation of topological insulator  $\text{Bi}_2\text{Se}_3$  and  $\text{Bi}_2\text{Te}_3$  in the form of two-dimensional nanoflakes by means of Raman spectroscopy. Due to the high surface-to-bulk ratio of the flakes the Raman response of the materials encodes the interaction of the topological surface states with the crystal lattice. By studying the changes of the spectroscopic response under different external perturbations like systematic temperature variations, high magnetic field strengths, or the interface to different substrates, the changes in electron-phonon interactions are identified. For the temperature and magnetic field dependent studies samples of NF clusters were investigated in a macro-Raman setup. On the other hand, high-resolution measurements on single NFs on different substrates were conducted using a microscope setup. Thus, this thesis studies in a comprehensive fashion the topological surface states in  $\text{Bi}_2\text{Se}_3$  and  $\text{Bi}_2\text{Te}_3$  in the limit of low thicknesses between 7 nm to 15 nm and at the obscured interfaces to a gold substrate, which become accessible due to the use of Raman spectroscopy.

The thesis is structured as follows: In chapter 1 the introduction of the concept of topological phases and  $\text{Bi}_2\text{Se}_3$  and  $\text{Bi}_2\text{Te}_3$  as candidate 3D topological insulators is given. Furthermore, the investigation of the materials in the form of two-dimensional nanoflakes by means of Raman spectroscopy is motivated. Chapter 2 summarizes the synthesis of the investigated nanoflakes and gives relevant references for further details on the characterization of the flakes. In chapter 3 the main experimental technique of Raman spectroscopy is introduced. Firstly, the theoretical concepts of inelastic light scattering necessary to understand the analysis of Raman spectra and the deduction of electron-phonon interactions are given. Secondly, the two employed experimental setups for the magnetic field (macro) and micro-Raman measurements are presented, which allow for the acquisition of Raman spectra with focus on different sample properties. In chapter 4 the first study is presented investigating the topological insulator nanoflakes in a thin film geometry in a temperature range of 3–300 K. Furthermore, the influence of high magnetic fields up to 7 T is studied. Chapter 5 presents the second Raman study that focuses on the Raman response of single  $\text{Bi}_2\text{Se}_3$  and  $\text{Bi}_2\text{Te}_3$  NFs in contact to a gold interface using the micro-Raman setup. Finally, the results of the macroscopic and microscopic Raman responses are summarized in chapter 6 and discussed with respect to the limitations of the topological properties in ultrathin flakes.

## *1 Motivation*



## Chapter 2

# 2 Synthesis and Characterization of 2D Nanoflakes

The  $\text{Bi}_2\text{X}_3$  ( $\text{X} = \text{Se}/\text{Te}$ ) nanoflakes were synthesized following a wet-chemical polyol approach that was first introduced by Fievet *et al.*<sup>[67]</sup> for the synthesis of metallic nanoparticles and adapted by Zhang *et al.*<sup>[56]</sup> for  $\text{Bi}_2\text{Se}_3$ . The polyol synthesis is one of the most simple methods to produce high quality, ultrathin TI nanoflakes since it requires only very few ingredients: (i) Stoichiometric quantities of two precursor salts providing the Bi and Se/Te ions, (ii) the polyol solvent that simultaneously functions as a reducing agent for the salts, and (iii) a ligand polymer that selectively binds to the (001) facet of the growing crystals and facilitates the two-dimensional growth. The exact quantities for the synthesis of the investigated NFs in this thesis are summarized in the appendix (Table B.1). In total, three different synthesis batches were investigated by Raman spectroscopy for this thesis. One  $\text{Bi}_2\text{Te}_3$  batch that was used for both the preparation of thin film and single NF samples, and two  $\text{Bi}_2\text{Se}_3$  batches for each Raman study (labeled Macro and Micro). All ingredients are mixed in a three-necked flask and heated up to  $180^\circ\text{C}$  under continuous magnetic stirring and refluxing conditions. During the heating the polyol, ethylene glycole, is gradually oxidized to the reactive glycol aldehyde, which further reduces the precursor salts.<sup>[67–69]</sup> The  $\text{Bi}_2\text{X}_3$  nuclei form via an ionic reaction mechanism and continue to grow in the  $a, b$ -plane due to the restricted growth in  $c$ -direction by the attached ligand.<sup>[70,71]</sup> It is important to note, that for the synthesis of  $\text{Bi}_2\text{Te}_3$  NFs it is not solely sufficient to only replace the Se-salt with a Te-salt.<sup>[72]</sup> Due to the higher reduction potential of the Te precursor an alkaline environment is necessary for the acetaldehyde to reduce the Te atoms to Te ions.<sup>[72,73]</sup> For this reason, NaOH has to be added to synthesize  $\text{Bi}_2\text{Te}_3$  nanoflakes otherwise the Te atoms will preferably form into rodlike structures.<sup>[73,74]</sup> During the course of this thesis the optimization of the  $\text{Bi}_2\text{Te}_3$  synthesis by systematic parameter variation and the role of the alkaline additive were thoroughly investigated within the work of two bachelor's theses.<sup>[75,76]</sup>

Details on the synthesis procedure of the  $\text{Bi}_2\text{X}_3$  NFs can be found in the previous master's thesis.<sup>[77]</sup>

The morphology and lateral dimensions of the synthesized NFs were characterized with scanning electron microscopy (SEM) (Hitachi Regulus 8820 and Zeiss Sigma) and atomic force microscopy (AFM) (Dimension 3100, Bruker, USA). The  $\text{Bi}_2\text{Se}_3$  NFs obtained larger lateral dimensions between  $1\text{--}7\ \mu\text{m}$  in comparison with the smaller  $\text{Bi}_2\text{Te}_3$  NFs ranging between  $50\ \text{nm}$  to  $3\ \mu\text{m}$ . Exemplary NFs are shown in Figure 2.1(a,e). The  $\text{Bi}_2\text{Te}_3$  product contained a large number of smaller bulk-like nanoparticles as apparent from Figure 2.1(e). The thickness of the  $\text{Bi}_2\text{X}_3$  NFs of only a few nm was readily determined via AFM

## 2 Synthesis and Characterization of 2D Nanoflakes

measurements, where exemplary measurements and extracted height profiles are shown in Figure 2.1(b,c,f,g). The  $\text{Bi}_2\text{X}_3$  NFs used to produce the thin film samples obtained average thicknesses of 8.9 nm for  $\text{Bi}_2\text{Se}_3$  and slightly thicker  $\text{Bi}_2\text{Te}_3$  NFs with average thicknesses of 14.7 nm as apparent from height histograms shown in Figure 2.1(d,h). Further information on the characterization of the NFs used for the thin film samples are given in ref. [78].

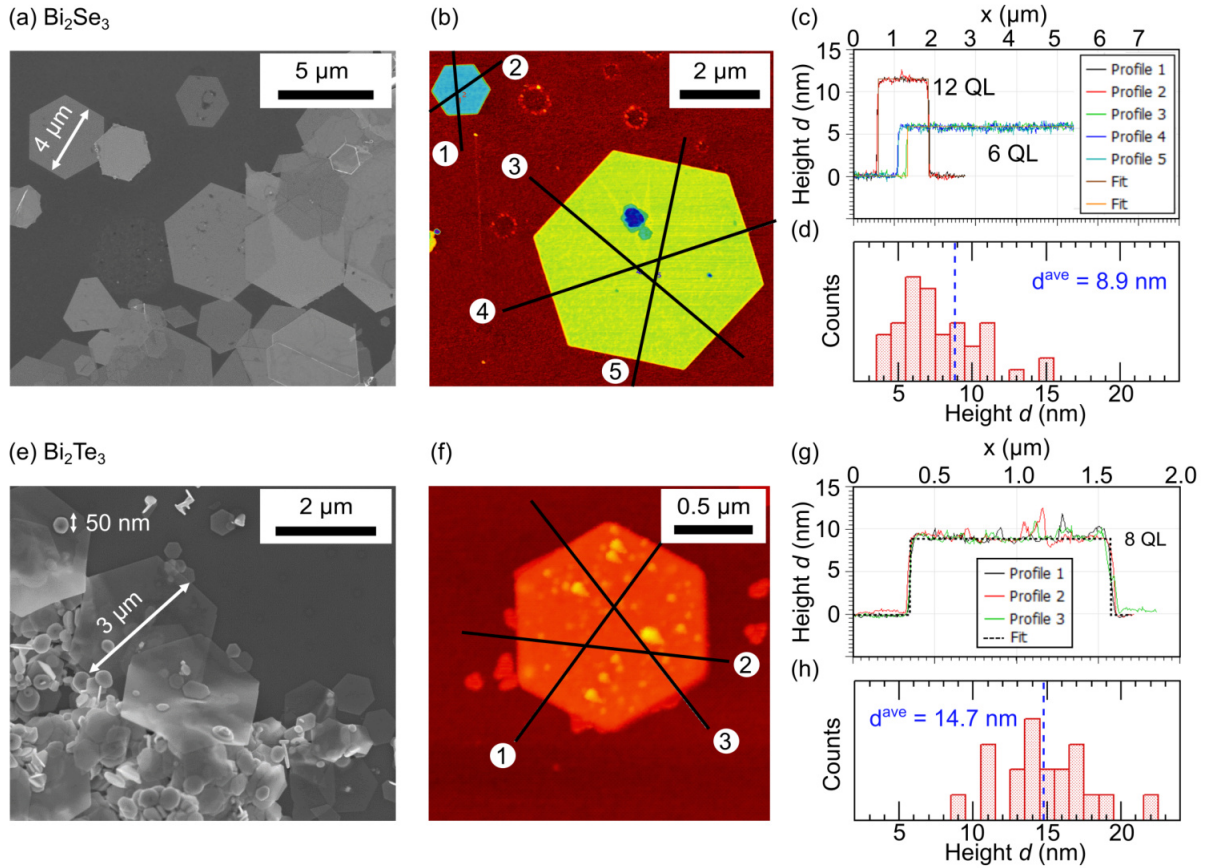


**Figure 2.1:** Morphology and thickness of  $\text{Bi}_2\text{Se}_3$  (upper row) and  $\text{Bi}_2\text{Te}_3$  (lower row) NFs employed for the thin film samples. (a,e) Representative SEM micrographs, (b,f) AFM topography images with extracted height profiles shown in (c,g). (d,h) Height histograms for  $\text{Bi}_2\text{Se}_3$  and  $\text{Bi}_2\text{Te}_3$ , respectively. All panels were adapted with permission from [78]. Copyright 2020 by the American Physical Society.

The stoichiometry of the NFs was examined via energy dispersive X-ray spectroscopy (EDX) on the SEM setup and revealed average elemental ratios of Bi to Se/Te atoms of 0.68 for  $\text{Bi}_2\text{Se}_3$  and 0.64 for  $\text{Bi}_2\text{Te}_3$ . [78] Both ratios are very close to the perfect stoichiometry of 0.66. In Figure 2.2 transmission electron microscopy (TEM) and selected area electron diffraction (SAED) measurements of the three NF batches investigated in this thesis are presented. The rhombohedral crystal structure is verified by the TEM measurements (FEI Tecnai F30 G<sup>2</sup> STwin for Macro batches, and JEOL JEM-2200FS for  $\text{Bi}_2\text{Se}_3$ -Micro batch) and SAED measurements that show the strong reflexes for the corresponding  $R\bar{3}m$  space group. Weaker superlattice reflections marked by blue circles are evident in all NF samples that fit well to a  $P\bar{3}m1$  phase. This additional phase can be attributed to minor stoichiometry changes such as Se or Te vacancies, or to surface reconstruction. [79]

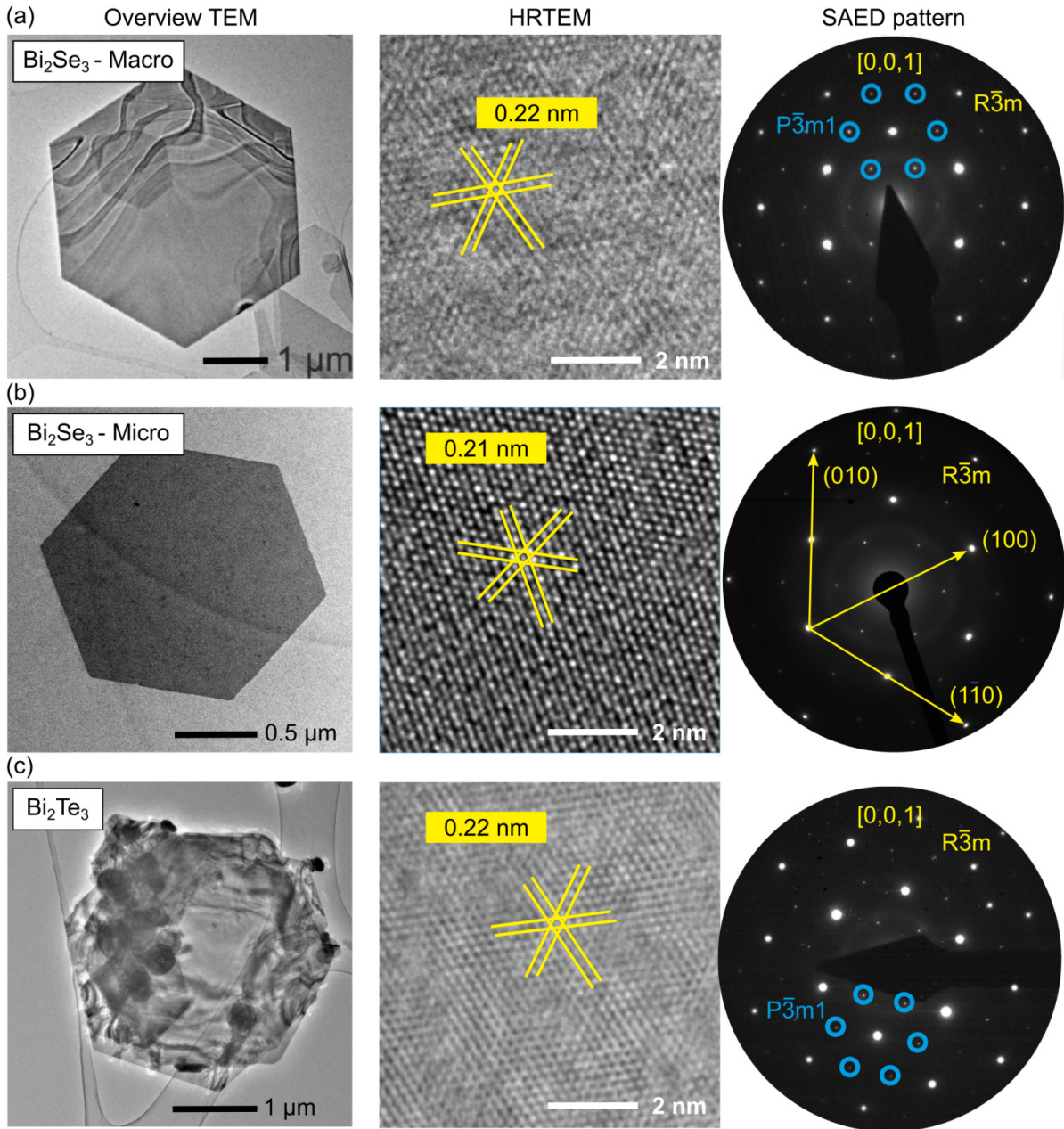


**Figure 2.2:** TEM investigations of three NF batches with data obtained from row (a)  $\text{Bi}_2\text{Se}_3$  used for macro-Raman investigations, row (b)  $\text{Bi}_2\text{Se}_3$  used for micro-Raman measurements, and (c)  $\text{Bi}_2\text{Te}_3$  NFs used for macro- as well as micro-Raman measurements. For each sample overview TEM micrographs, high-resolution TEM micrographs, and SAED patterns are presented in the first, second, and third column, respectively. SAED patterns obtained in the  $[001]$  zone axis of all NFs reveal the hexagonal lattice spacings of 0.21–0.22 nm that are indicated by yellow lines in the HRTEM images and confirm the growth of the NFs in the  $a, b$ -plane. Weaker superlattice reflections due to surface reconstruction are marked by blue circles. All panels from row (a) are adapted with permission from<sup>[78]</sup>. Copyright 2020 by the American Physical Society. The overview TEM image of row (c) was adapted with permission from<sup>[80]</sup>. Copyright 2019 Springer Nature.

The high single crystalline quality of the NFs is evident from the high-resolution TEM (HRTEM) micrographs shown in Figure 2.2. In combination with the SAED patterns the

## 2 Synthesis and Characterization of 2D Nanoflakes

determined lattice spacings of 0.21–0.22 nm for all investigated NF batches correspond perfectly with the  $11\bar{2}0$  spacing in the  $a,b$ -plane (JCPDS Card No. 33-0214) and are in agreement with literature values.<sup>[81,82]</sup>

# 3 Raman Response of Topological Insulator 2D Nanoflakes

## 3.1 Theory of Raman scattering

In this chapter the Raman scattering process is reviewed. Following a short introductory description of the general Raman scattering process in section 3.1.1, the inelastic light scattering is described using a quantum mechanical approach in section 3.1.2 where the Raman scattering cross section is depending on the system's transition probability according to Fermi's 'Golden rule' and contributing matrix elements. In section 3.1.3 typical line shapes obtained in phononic Raman scattering are discussed that help to identify corrections to the phonon's self-energy and reveal electron-phonon interactions. Section 3.1.4 gives an overview on the selection rules determining the Raman activity of phonons. In section 3.1.5 the general temperature dependence of the phonon Raman response is discussed. Finally, section 3.1.6 presents the Raman-active phonons of  $\text{Bi}_2\text{Se}_3$  and  $\text{Bi}_2\text{Te}_3$  that are mainly analyzed in the results section of this thesis.

### 3.1.1 Introduction - General scattering process

In Raman spectroscopy the inelastically scattered light of polarizable matter is detected. Hereby, the sample is illuminated with a monochromatic excitation source whereby the incident photons couple to the system by the creation or absorption of elementary excitations and experience an energy correction. In that way, Raman spectroscopy provides a versatile tool to study a wide range of quasi particles such as phonons, magnons, plasmons, etc. The Raman scattering of phonons mainly occurs indirectly through the intermediary of the electronic system in the material.<sup>[83]</sup> During each scattering event three main processes occur: 1) the incident photon with frequency  $\omega_i$  is absorbed by coupling to the electronic system, 2) the electrons interact with quasi particles and transfer energy (and momentum), and 3) a scattered photon with frequency  $\omega_s$  is created and emitted. Since the incident photon is destroyed and recreated, Raman scattering, or in that sense every form of inelastic light scattering, is a two-photon process.

In the following, the theory is focused on phononic Raman scattering in first-order, where the scattered photon experiences an energy shift due to the creation or absorption of a phonon with the frequency  $\omega_0$ . Here, first order relates to one phonon being created or absorbed, with the neglect of possible higher order phonon-phonon interactions.<sup>[84]</sup> The frequency shifted photon is defined as Stokes frequency for phonon creation and

### 3 Raman Response of Topological Insulator 2D Nanoflakes

Anti-Stokes frequency for phonon absorption as shown in Figure 3.1. The optical phonons give rise to first-order Raman scattering under the conservation of energy,  $\omega_i = \omega_s + \omega_0$ , and momentum,  $\vec{q}_i = \vec{q}_s + \vec{q}_0$ . The momentum of typical lasers, e.g. He-Ne laser with 633 nm and  $q = 2\pi n/\lambda = 1 \cdot 10^5 \text{ cm}^{-1}$ , is three orders of magnitude smaller than the available momenta for the phonons, which are determined by the size of the Brillouin zone  $q = \pi/a$ , e.g. for  $\text{Bi}_2\text{Se}_3$  with  $a = 0.22 \text{ nm}$  the maximum phonon momentum is  $q = 1.4 \cdot 10^8 \text{ cm}^{-1}$ . It follows that the created phonon momenta is magnitudes smaller than the dimensions of the Brillouin zone and hence only phonons around  $q = 0$  participate in Raman scattering. In Figure 3.1 a schematic general Raman spectrum is presented, where the elastically scattered light or Rayleigh signal, is defined to have zero Raman shift and Stokes and Anti-Stokes signals correspond to the created and annihilated phonons, respectively.

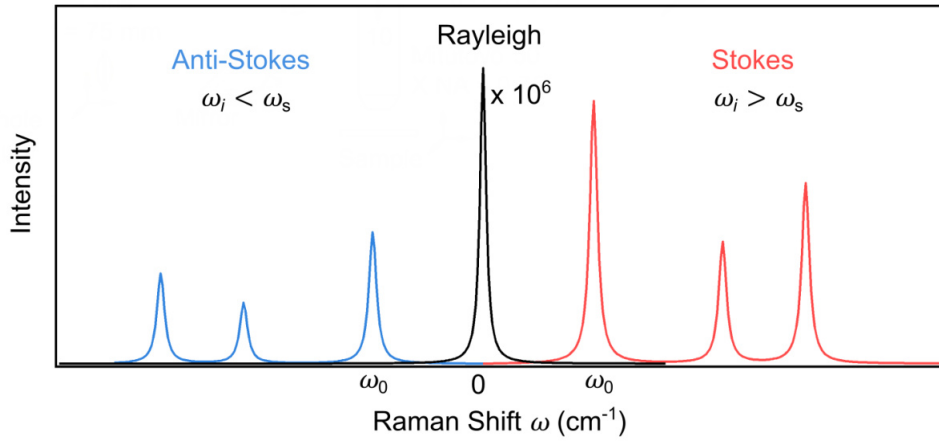


**Figure 3.1:** General Raman spectra for phononic scattering with indicated orders of magnitude of scattering intensities for the different contributions.

To calculate the Raman scattering intensity the efficiency between the coupling of the photons to the material's electronic system and subsequent interaction with elementary excitations has to be determined, which can be done using a semi-classical or a quantum mechanical approach. In the classical theory, the inelastic scattering process is described by fluctuations of the electric susceptibility  $\tilde{\chi}$  that can be induced from the lattice vibrations or other quasi particles. Detailed mathematical derivations of Raman scattering cross sections from the modulations of the susceptibility and the related polarizability can be found in literature on Raman scattering<sup>[84,85]</sup> and are only briefly mentioned here. The quantity of interest for both theoretical approaches is the *differential Raman scattering cross section*, which quantifies for Stokes scattering the rate of energy removal from the incident beam due to scattering in a scattering volume  $V$  and solid angle element  $d\Omega$  in a scattering frequency increment  $d\omega$ . Employing the classical approach the scattering cross section for phononic Raman scattering is given as:<sup>[84]</sup>

$$\frac{d^2\sigma}{d\Omega d\omega} = \frac{\omega_i^4 V}{(4\pi)^2 c^4} |\vec{e}_s \cdot \frac{d\tilde{\chi}}{dQ} \cdot \vec{e}_i|^2 \langle QQ^* \rangle \delta(\omega_0 - \omega), \quad (3.1)$$



with the incident light frequency  $\omega_i$ , the phonon modes frequency  $\omega_0$  and its statistical factor given by the thermally averaged displacement function  $\langle QQ^* \rangle = \frac{\hbar}{2\omega_0}(n+1)$  for the Stokes contribution, where  $n$  is the Bose-Einstein occupation factor  $n(\omega, T) = 1/(e^{\hbar\omega/k_B T} - 1)$ . Most importantly, the factor  $|\vec{e}_s \cdot \frac{d\tilde{\chi}}{dQ} \cdot \vec{e}_i|^2$  reveals that the observation of a Raman mode critically depends on the polarization of the incident  $\vec{e}_i$  and scattered light  $\vec{e}_s$ , as well as the modulation of the susceptibility  $\tilde{\chi}$  by the normal mode coordinates  $Q$  of the elementary excitation. The derivative of the susceptibility tensor,  $\frac{d\tilde{\chi}}{dQ}$ , also defined as the *Raman tensor*, is specific for any given phonon mode and determines its Raman activity in the material. It further plays an important role in the identification of the modes symmetry, which is discussed further in section 3.1.4. Depending on the Raman shift  $\omega$  the Raman mode theoretically corresponds to a  $\delta$ -function. However, for finite lifetimes and interactions to other quasi particles  $\delta(\omega_0 - \omega)$  can be replaced by a suitable line shape function. The time and space dependent fluctuations in the electric susceptibility induced by the phonon atomic displacements can also be derived using a quantum mechanical approach that describes the changes in  $\tilde{\chi}$  by the transition electric susceptibility operator. The transition matrix elements, in turn, characterize the transition probability that accompany the annihilation and creation of the incident and scattered photon and, for Stokes, the creation of phonons. Their quantum mechanical derivation using perturbation theory is described in detail in the next section.

### 3.1.2 Quantum mechanical approach

From the introduction of the Raman scattering process it is apparent that both the electronic and phononic systems in the material have to undergo transitions between states to yield a scattered photon. From a quantum mechanical approach the interaction between the incident photon and the material can be described as a time-dependent perturbation insetting at an initial time  $t = t_0$ , leading to an interaction Hamiltonian  $\hat{H}_{int}(t)$  that gives corrections to the unperturbed Hamiltonian  $\hat{H}_0$ . The probability for such a perturbation to induce transitions in the material can be deduced using perturbation theory to first-order in time, which results in Fermi's '*Golden Rule*'<sup>[86,87]</sup>

$$P_{i \rightarrow f} = \frac{2\pi}{\hbar} \sum_f |T|^2 \delta(E_f - E_i). \quad (3.2)$$

Here the transition matrix elements  $T = \langle f | \hat{H}_{int} | i \rangle$  determine the scattering probability and the  $\delta$ -function expresses energy conservation in the process. Summed over all possible initial and final states the probability for these transitions can be shown to be directly proportional to the Raman scattering cross section.<sup>[83]</sup> Therefore, the intensity of a Raman mode can be related to the contributing transition matrix elements involved in the scattering process. In the following, I will disentangle the different interactions between

elementary excitations that occur during a Raman scattering event and contribute to the interaction Hamiltonian  $\hat{H}_{int}$ .

As mentioned in the introduction in section 3.1.1, each Raman scattering event involves both the electronic and phononic systems of a material. The total Hamiltonian of the system prior to any perturbation is<sup>[88]</sup>

$$\hat{H}^0 = \hat{H}_{el}^0 + \hat{H}_{ph}^0 + \hat{H}_{el-ph}^0, \quad (3.3)$$

which describes the unperturbed system with elementary excitations, like electrons and phonons, as well as interactions between these. Here we restrict the description to the theory of vibrational scattering and neglect other possible elementary excitations like plasmons, spin waves, etc. During a Raman scattering event the incident light leads to a perturbation of the system resulting in a total Hamiltonian of

$$\begin{aligned} \hat{H}^{tot} &= \hat{H}^0 + \hat{H}^{int} \\ &= \hat{H}_{el}^0 + \hat{H}_{ph}^0 + \hat{H}_{el-ph}^0 + \hat{H}_{rad}^0 + \hat{H}_{el-rad}^{int}. \end{aligned} \quad (3.4)$$

This includes the radiation field Hamiltonian  $\hat{H}_{rad}^0$ , taking into account both incident and scattered light, the total Hamiltonian of the scattering medium  $\hat{H}^0$ , as well as an interaction Hamiltonian  $\hat{H}_{el-rad}^{int}$  arising from the coupling of the incident radiation field to the electrons. For Raman scattering with incident photon frequencies in the visible range this coupling to the electronic system is the most relevant contribution to the transition electric susceptibility and we will hence focus here on electronic Raman scattering.<sup>[84]</sup>

Independent from the quasi particle studied with Raman spectroscopy, the preliminary step is always the interaction of the incident radiation with the electrons of the material. Therefore, we will first consider the coupling of photons to the electronic system and discuss the corresponding transition matrix elements associated to  $\hat{H}_{el-rad}^{int}$ .

### Electronic Raman scattering

The matrix element entering in the expression for the scattering cross-section can be rewritten in terms of a transition electric susceptibility.<sup>[83]</sup> We consider a material under illumination, where the electrons are influenced by the vector potential of the incoming electromagnetic field  $\vec{A}$ . This leads to a substitution of the electrons canonical momentum  $\hat{p}_i \rightarrow \hat{p}_i - \frac{e}{c}\hat{A}(\vec{r}_i)$  and yields for the electrons under an electromagnetic field a correction to their kinetic energy of<sup>[84]</sup>

$$\hat{H}_{el}^{kin} = \frac{1}{2m} \sum_i \left[ \vec{p}_i - \frac{e}{c}\vec{A}(\vec{r}_i) \right]^2, \quad (3.5)$$

where the summation index  $i$  runs over all electrons. In the Coulomb gauge ( $\nabla \cdot \hat{A} = 0$ ),  $\hat{p}$  and  $\hat{A}$  commute and the Hamiltonian can be further grouped into contributions from the unperturbed, free electron and contributions arising from the electron-radiation



interactions:

$$\begin{aligned}\hat{H}_{el}^{kin} &= \hat{H}_{el}^0 + \hat{H}_{rad-el}^{int} \\ &= \frac{1}{2m} \sum_i \vec{p}_i^2 - \underbrace{\frac{e}{mc} \sum_i \vec{p}_i \cdot \vec{A}(\vec{r}_i)}_{\hat{H}_{pA}} + \underbrace{\frac{e^2}{2mc^2} \sum_i \vec{A}(\vec{r}_i)^2}_{\hat{H}_{A^2}}\end{aligned}\quad (3.6)$$

It is apparent from Equation (3.6) that there are two different coupling processes between the electrons and the radiation field, where the first interaction term  $\hat{H}_{pA}$  is linear in  $\vec{A}$  and the second term  $\hat{H}_{A^2}$  is quadratic with  $\vec{A}^2$ . For the inelastic light scattering cross section the transition matrix elements corresponding to  $\hat{H}_{rad-el}^{int}$  are obtained using perturbation theory. In general, during a scattering event the incoming photon field is absorbed by the medium and a new photon field is re-emitted isotropically. This means that any scattering event is a two-photon process and has to involve two radiation fields. It follows from Equation (3.6) that the interaction Hamiltonian  $H_{A^2}$  contributes to first-order in perturbation theory, whereas  $\hat{H}_{pA}$  produces scattering of light only in second-order.<sup>[84]</sup> Hence, the resulting total transition matrix element contributing to the transition electric susceptibility is given as<sup>[83]</sup>

$$\begin{aligned}T_{el-rad} &= T_{A^2} + T_{pA} \\ &= \langle f | \hat{H}_{A^2} | i \rangle + \sum_m \frac{\langle f | \hat{H}_{pA} | m \rangle \langle m | \hat{H}_{pA} | i \rangle}{(E_m - E_i) - \hbar\omega_i} + \frac{\langle f | \hat{H}_{pA} | m \rangle \langle m | \hat{H}_{pA} | i \rangle}{(E_m - E_i) + \hbar\omega_s}.\end{aligned}\quad (3.7)$$

Here,  $|i\rangle$ ,  $|f\rangle$ , and  $|m\rangle$  are the initial, final and intermediate states of the crystal with their corresponding eigenenergies. Due to the coupling of the radiation to the electrons, both the photon and electron states undergo a transition, where the incoming photon is destroyed and a scattered photon is created accompanied by electronic transitions. Therefore, it is convenient to evaluate the matrix elements using the second quantization formalism, that quantizes the electron and photon states.<sup>[84]</sup> The resulting matrix elements reveal that  $T_{A^2}$  is dependent on the electronic carrier density and obtains dominant contributions for electronic *intraband* transitions. Hence, the  $T_{A^2}$  term describes the coupling of photons to an available low-energy electric susceptibility, which is typically represented by conduction electrons in metals or doped semiconductors. On the other hand, the contribution of  $T_{pA}$  includes the electron momenta  $\vec{p}$  and allows scattering for electronic interband transitions. The  $T_{pA}$  becomes dominant for allowed *interband* transitions since it includes a resonant denominator when the incident excitation frequency of the laser corresponds to a transition between electronic bands.

### Relating the Raman scattering cross section to the response function

Having identified the two coupling mechanisms of the incoming light to the electronic system, it becomes apparent that the Raman scattering intensity is dependent on the

fluctuations in the electric susceptibility  $\tilde{\chi}$ . This is the identical conclusion already apparent in the classical expression of the scattering cross section in Equation (3.1). The modulation of the electric susceptibility by phonons or other elementary excitations is a complex process involving the collective motion of particles in the whole system. It is therefore convenient to describe the coupling between the electronic and phononic systems within the formalism of many-body theory.<sup>[89]</sup> In the many-body approach the collective excitations like the electric susceptibility or phonons are represented by propagators and the modulation of the electric susceptibility by the phonons can be described by corrections to its self-energy. For the electric susceptibility a two-particle propagator describing the polarizability bubble or electron-hole bubble is commonly used.<sup>[89]</sup> The propagators represent the response functions  $R(\omega)$  of the system, which in turn can directly be related to the scattering intensity via the *fluctuation dissipation theorem*.<sup>[88]</sup> This theorem connects the fluctuation spectrum of a system with the imaginary part of its response function. The Raman scattering intensity can thus be directly expressed in terms of the negative imaginary part of the phonon's response function<sup>[83]</sup>

$$\frac{d^2\sigma}{d\Omega d\omega} \propto -\frac{\hbar}{\pi} [n(\omega) + 1] \text{Im}[R(\vec{q}, \omega)]. \quad (3.8)$$

Hence, in order to determine the Raman scattering intensity the response function  $R(\omega)$  of the system has to be defined for the possible scattering mechanisms. To derive the response function it is convenient to describe the propagators with the help of Feynman diagrams.<sup>[89]</sup> This diagrammatic approach enables an illustrative way to describe the complex many-particle interactions contributing to a scattering event. Connecting the Raman scattering intensity to the contributing Feynman diagrams will help to:

- identify elementary excitations that accompany a Raman scattering event
- interpret the line shape functions of Raman phonons with respect to the phonon's self-energy corrections
- discuss observed Raman scattering intensities by entangling contributions from different Feynman diagrams

For a Raman scattering event the propagators defining the Raman response function have been described by Kawabata *et al.* by using a four-photons Green's-function.<sup>[90]</sup> From this the phononic Raman response function can be deduced taking into account appropriate vertex corrections for the electron-phonon interactions.<sup>[89,91]</sup> According to Equation (3.7) the incoming radiation can couple to the electronic system via the resonant  $T_{pA}$  or non-resonant  $T_{A2}$  matrix elements. Therefore, there exist two possible Feynman diagrams corresponding to phononic Raman scattering under non-resonant and resonant conditions, which are displayed in Figure 3.2. In the following the possible phonon line shapes obtained from the two different coupling processes are discussed in detail. The deductions of the Raman response functions from the two displayed Feynman diagrams are also summarized in<sup>[92]</sup>.

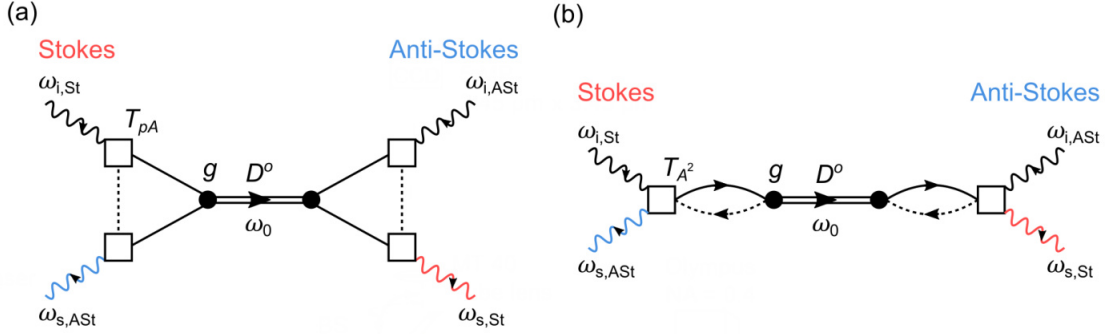


**Figure 3.2:** Feynman diagrams of the four-photon Green's function for phononic Raman scattering via coupling to two different electronic matrix elements. Photons are represented by wiggly lines that couple to electronic transitions (solid and dashed lines) via the transition matrix elements  $T$  depicted as squares. The electron-phonon coupling constant  $g$  is given as black circles and the phonon is represented by a double line. The Stokes process, creation of a phonon, is read from the top left to the bottom right. The Anti-Stokes process, annihilation of a phonon, is read from the top right to the bottom left in both diagrams. (a) Feynman diagram for a resonant Raman scattering process by coupling to electronic interband transitions via  $T_{pA}$  matrix elements. (b) Feynman diagram for non-resonant coupling to electronic intraband excitations via  $T_A^2$  matrix elements. The low-energy electric susceptibility corresponds to the polarization bubble with an electron (solid) and hole (dotted) line.

### 3.1.3 Raman line shapes obtained from electron-phonon interactions

#### Phononic Raman scattering via electronic *interband* transitions

We will first consider the coupling of the radiation to the electronic system via the resonant  $T_{pA}$  term corresponding to electronic *interband* transitions. The Feynman diagram depicted in Figure 3.2(a) is the main contribution to Raman scattering intensity in insulators and semiconductors, where the Fermi level is expected to lie within the band gap and no free carriers are available that could contribute via the electronic intraband excitations ( $T_A^2$ ).<sup>[88]</sup> Additionally, typical excitation laser frequencies used in this thesis lie around 2 eV and will therefore always lead to electronic transitions across the semiconductor's band gap that are examined in this work. Examining the Feynman diagram in Figure 3.2(a) the propagator can be readily translated using the typical conventions.<sup>[89]</sup> The response function for phononic Raman scattering in the case of interband transitions is hence given as<sup>[92,93]</sup>

$$R_{res}(\omega) = T_{pA}^4(\omega_i) g^2 \chi_{el}^2(\omega) D^o(0, \omega), \quad (3.9)$$

### 3 Raman Response of Topological Insulator 2D Nanoflakes

where both the propagator for the electron-hole pair  $\chi_{el}$  and the phonon  $D^o$  are dependent on the Raman shift frequency  $\omega$ . The coupling constant  $g$  determines the coupling strength between the electronic transition and the phonons and is assumed to be real, constant and independent of momentum and energy. Furthermore, as discussed in the previous section, the strength of the transition matrix element  $T_{pA}$  depends on the incoming laser frequency  $\omega_i$ . The phonon propagator corresponds to the complex Green's function of a damped harmonic oscillator and is given by<sup>[89]</sup>

$$\begin{aligned} D^o(0, \omega) &= \frac{1}{\omega^2 - \omega_0^2 + i\Gamma\omega} = D_{re}^o + iD_{im}^o \\ &= \frac{(\omega^2 - \omega_0^2)}{(\omega^2 - \omega_0^2)^2 + (\Gamma\omega)^2} - i \frac{\Gamma\omega}{(\omega^2 - \omega_0^2)^2 + (\Gamma\omega)^2}. \end{aligned} \quad (3.10)$$

The Green's function for an electric susceptibility related to an interband transition can also be expressed in terms of a real and imaginary part independent of the exact form

$$\chi_{el}(\omega) = \pi_{re} + i\pi_{im}. \quad (3.11)$$

Inserting both propagators into the resulting response function Equation (3.9), we will see that after multiplication the only surviving imaginary mixing terms contributing to the scattering intensity according to Equation (3.8) are

$$\text{Im}[R_{res}(\omega)] = T_{pA}^4(\omega_i)g^2 \left[ (\pi_{re}^2 D_{im}^o - \pi_{im}^2 D_{im}^o + 2\pi_{re}\pi_{im}D_{re}^o) \right]. \quad (3.12)$$

For semiconductors and insulators the resonance frequency  $\omega_{res}$  of an electronic interband susceptibility  $\chi_{el}$  lies typically in the order of several eV and has, therefore, much higher energies compared to typical phonon frequencies  $\omega_0$  around 20–200 meV. As a result the imaginary part can be assumed to be  $\pi_{im} \approx 0$  in the frequency range of the phonon and we will find that the phonon propagator at low frequencies only couples to the real part of  $\chi_{el}$ . The phononic Raman response via the resonant matrix elements  $T_{pA}$  hence is determined in the non-resonant limit of the electronic interband transition by finite contributions of  $\pi_{re}$  as depicted in Figure 3.3(a). The resulting Raman scattering intensity in the non-resonant limit is finally obtained by inserting Equation (3.12) and  $D_{im}^o$  in Equation (3.8):

$$\begin{aligned} I_{res}(\omega, \omega_i) &\propto -[T_{pA}^4(\omega_i)g^2\pi_{re}^2 D_{im}^o] \\ &\propto T_{pA}^4(\omega_i)g^2\pi_{re}^2 \cdot \underbrace{\frac{\Gamma\omega}{(\omega^2 - \omega_0^2)^2 + (\Gamma\omega)^2}}_{\text{Lorentzian}} \end{aligned} \quad (3.13)$$

In the frequency range of the phonon  $\omega = \omega_0$ , the real part  $\pi_{re}$  can be taken as constant and independent of the Raman shift  $\omega$ . The resulting phonon line shape obtained by the resonant Raman scattering is, therefore, solely dependent on the imaginary part of the phonons propagator  $D_{im}^o$ , which resembles a symmetric *Lorentzian* profile. Equation (3.13) shows that the obtained phonon scattering intensity highly depends on the resonant

transition matrix element  $T_{pA}$ , which can lead to a strong amplification of the phonon signal when the incoming laser frequency is in resonance with an electronic interband transition.

To summarize, the phononic Raman scattering process in semiconductors and insulators always occurs via electronic interband transitions leading to typical Lorentzian phonon line shapes. By tuning the excitation laser frequency the electronic band structure of the material can be probed as the  $T_{pA}$  matrix element is expected to enhance the phononic Raman signal by a factor of  $10^3$  when the photon frequency coincides with an electronic interband transition.

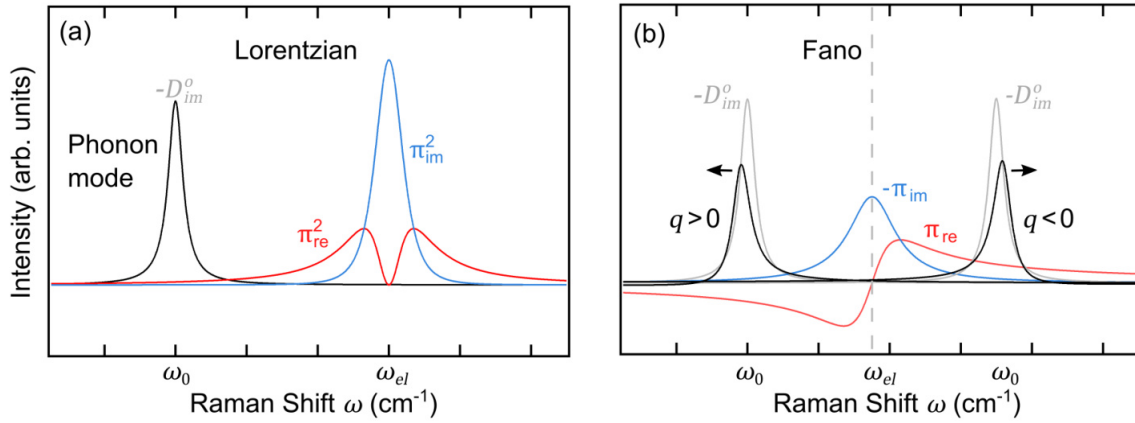


**Figure 3.3:** Phonon line shapes obtained for different electron-phonon coupling mechanisms. (a) Lorentzian line shape (black graph) obtained for the resonant Raman scattering process in the non-resonant limit by coupling to the  $\pi_{re}^2$  of the electric susceptibility via  $T_{pA}$ . (b) Asymmetric Fano line shapes obtained for two phonons coupling to a low-energy electric susceptibility via  $T_{A2}$ . Fano line shapes were calculated using an overdamped  $\chi_{el}$ . The frequency and line width renormalizations in comparison to the bare phonon propagator  $D_{im}^o$  (gray) are displayed with exaggeration for visibility purpose. A phonon with  $\omega_0 < \omega_{el}$  obtains a positive Fano parameter  $q$ , whereas a high frequency phonon with  $\omega_0 > \omega_{el}$  would obtain a negative  $q$ .

### Phononic Raman scattering via electronic *intraband* transitions

The incoming radiation can couple to available free electrons in a system by the creation of dipole moments and leads to a polarization of the medium. This is depicted in the Feynman diagram in Figure 3.2(b) where the incident photon couples to the so-called polarization bubble via the  $T_{A2}$  element. The polarization bubbles can couple between each other through interactions with the phonons in the system leading to a correction of the electronic self-energy. The response function for  $T_{A2}$  contribution after summation over all bubble diagrams yields:<sup>[91,92,94]</sup>

$$R_{non-res}(\omega) = T_{A2}^2 \chi_{el}(\omega) - T_{A2}^2 g^2 \chi_{el}^2(\omega) \tilde{D}(\omega) \quad (3.14)$$

with the full (renormalized) phonon propagator<sup>[94,95]</sup>

$$\begin{aligned}\tilde{D}(\omega) &= \frac{D^o(\omega)}{1 + g^2 \chi_{el}(\omega) D^o(\omega)} \\ &= \frac{1}{\omega^2 - \omega_0^2 - g^2 \pi_{re} + i(\Gamma\omega - g^2 \pi_{im})},\end{aligned}\quad (3.15)$$

where we have used the free phonon propagator  $D^o(0, \omega)$  according to Equation (3.10). In comparison with the free phonon propagator, we can define a renormalized phonon frequency  $\tilde{\omega}_0^2$  and line width  $\tilde{\Gamma}$

$$\tilde{\omega}_0^2 = \omega_0^2 + g^2 \pi_{re} \quad (3.16)$$

and

$$\tilde{\Gamma}\omega = \Gamma\omega - g^2 \pi_{im}. \quad (3.17)$$

This underlines how the phonon frequency is renormalized by coupling to the real part of the electric susceptibility and the line width is altered by coupling to the imaginary part. Separating the full phonon propagator into its real and imaginary part and using the definitions for  $\tilde{\omega}$  and  $\tilde{\Gamma}$  we obtain:

$$\begin{aligned}\tilde{D}(\omega) &= \tilde{D}_{re} + i\tilde{D}_{im} \\ &= \frac{(\omega^2 - \tilde{\omega}_0^2)}{(\omega^2 - \tilde{\omega}_0^2)^2 + (\tilde{\Gamma}\omega)^2} - i \frac{\tilde{\Gamma}\omega}{(\omega^2 - \tilde{\omega}_0^2)^2 + (\tilde{\Gamma}\omega)^2}\end{aligned}\quad (3.18)$$

Inserting the full phonon propagator and an electric susceptibility in the response function, the imaginary terms contribute to the Raman scattering intensity, which is given by

$$I(\omega) \propto -T_{A^2}^2 \pi_{im} + T_{A^2}^2 g^2 \underbrace{\frac{\tilde{\Gamma}\omega}{(\omega^2 - \tilde{\omega}_0^2)^2 + (\tilde{\Gamma}\omega)^2}}_{\text{renormalized Lorentzian}} \left[ -\pi_{re}^2 + \pi_{im}^2 + 2\pi_{re}\pi_{im} \frac{(\omega^2 - \tilde{\omega}_0^2)}{\tilde{\Gamma}\omega} \right]. \quad (3.19)$$

In this picture we assume that the phonon is only renormalized by the low-energy Raman-active electronic response  $\chi_{el}$  and neglect self-energy contributions e.g. those due to anharmonic phonon-phonon interactions.<sup>[94]</sup>

It can be shown that the above equation resembles the well known Fano-profile,<sup>[96]</sup> when defining the Fano-parameter as  $q = \pi_{im}(\omega)/\pi_{re}(\omega)$ <sup>[92]</sup>, where  $q$  is nearly constant for a flat electronic continuum  $\chi_{el}$ :<sup>[91]</sup>

$$I(\omega) \propto -T_{A^2}^2 \pi_{im} + T_{A^2}^2 g^2 \pi_{re}^2 \underbrace{\frac{\tilde{\Gamma}\omega}{(\omega^2 - \tilde{\omega}_0^2)^2 + (\tilde{\Gamma}\omega)^2} \left[ -1 + q^2 + 2q \frac{(\omega^2 - \tilde{\omega}_0^2)}{\tilde{\Gamma}\omega} \right]}_{\text{Fano}} \quad (3.20)$$

The low-frequency electric susceptibility of quasi free electrons can be described by an

effective one-particle propagator that yields for a fermionic particle<sup>[89]</sup>

$$\chi_{el} = \frac{\omega - \omega_{el}}{(\omega - \omega_{el})^2 + \delta^2} - i \frac{\delta}{(\omega - \omega_{el})^2 + \delta^2} \quad (3.21)$$

$$= \pi_{re} + \pi_{im}, \quad (3.22)$$

where  $\omega_{el} = \epsilon_{el}(k)/\hbar$  describes the dispersion relation of the electrons. Such a low-frequency susceptibility is depicted in Figure 3.3(b) that indicates how a phonon with frequencies below  $\omega_{el}$  is described by a Fano profile with positive values of  $q$ , and a high frequency phonon would yield a Fano profile with negative  $q$ .

### 3.1.4 Selection rules

The Raman activity of a phonon mode is determined by its symmetry of vibration of the atoms, which has to modify the polarizability in the system and lead to a finite polarizability derivative  $d\tilde{\chi}/dQ$  according to Equation (3.1).<sup>[84]</sup> The symmetries of phonons in a crystal can be characterized by the irreducible representations of the crystals space group  $\Gamma$ , assuming an infinite expansion of the phonons wavelength. For a phonon to modulate the polarizability it can be shown by group-theoretical methods that it has to have the same symmetry as an irreducible component of the representation of the polarizability tensor.<sup>[85]</sup> The irreducible representations of phonons transforming the polarizability tensor determine the so-called '*Raman selection rules*' and are tabulated for all crystal point groups (see e.g. Hayes & Loudon (1964)<sup>[85]</sup>). The irreducible representations for Raman active phonons of a given symmetry  $\Gamma_{ph}$  correspond to a set of reduced second rank tensors, named the '*Raman tensor*'  $\tilde{R}_{\Gamma_{ph}}$ . These represent the non-vanishing components of the polarizability tensor, which belong to the same irreducible representation as the phonon.<sup>[84]</sup> The nine elements of  $\tilde{R}_{\Gamma_{ph}}$  are obtained by allowing the polarization of the incoming and scattered photons to take on the values of the principal axes  $x, y$  and  $z$ . The Raman tensors presented in this thesis have been given in the convention that  $x, y$  and  $z$  correspond to the principal axes of a crystals point group, which was defined for all crystal classes by Nye (1957)<sup>[97]</sup>. Other choices of axes, e.g. orienting  $x, y$  and  $z$  with respect to rotation axes and reflection planes, leads to different forms of matrices.<sup>[88]</sup> This is stressed here, because especially the twofold degenerate matrices, which occur for example in the  $R\bar{3}m$  group of bismuth chalcogenides for the  $E_g$  modes, are often shown with different forms corresponding to an alternative choice of  $x$  and  $y$  axes according to Koster et al.<sup>[98]</sup> These alternate forms of Raman tensors are tabulated in<sup>[84,88]</sup>.

For phononic Raman scattering the scattering intensity is therefore determined by their Raman tensor and given as:<sup>[84]</sup>

$$I(\omega) \propto [\vec{e}_i \cdot \tilde{R}_{\Gamma_{ph}} \cdot \vec{e}_s]^2. \quad (3.23)$$

The selection rules lead to the complementary nature of phonons that in crystals with

inversion symmetry even-parity vibrations ( $g$ ) are exclusively Raman-active and odd-parity vibrations ( $u$ ) are infrared-active. The Raman scattering intensity is further dependent on the polarization of the incoming  $\vec{e}_i$  and scattered (or detected)  $\vec{e}_s$  light relative to the orientation of the crystal's principal axes. Hence, by aligning the principal crystal axes to the incoming photon polarization, the tabulated Raman tensors can directly be used to analyze phonon symmetries by measuring in different polarization configurations. The Raman selection rules for bismuth chalcogenides are presented in section 3.1.6.

Strictly speaking, the irreducible representation classifies the symmetry of a phonon only when assuming an infinite dimension of the crystal, which is typically valid in bulk materials. For nanoscaled finite materials this assumption no longer holds and lifts the validity of the selection rules derived from the bulks irreducible representations.<sup>[85]</sup> For instance in ultrathin nanoflakes the inversion symmetry of the crystal is broken perpendicular to the flakes surface. The consequences of symmetry breaking for the Raman response is in more detail discussed for  $\text{Bi}_2\text{Se}_3$  and  $\text{Bi}_2\text{Te}_3$  in section 3.1.6.

### 3.1.5 Temperature dependence of first-order Raman scattering

The temperature dependence of the Raman mode's frequency and line width is determined by the anharmonic lattice potential and can be derived from phonon self-energy corrections due to the anharmonic interactions.<sup>[99]</sup> In general, the anharmonic contributions to a crystal's lattice potential energy lead to a shift in the Raman-active optical mode's harmonic frequency  $\omega_0$  and dampen it. The self-energy corrections affect the mode's line shape, in particular the frequency is corrected by the real part  $\Delta$  and the line width is corrected by the imaginary part  $\Gamma$  of the self-energy leading to following expression for the line shape:<sup>[100]</sup>

$$I_S(\omega, j, T) \propto \frac{\Gamma(\omega, j, T)}{(\omega_0(j) + \Delta(\omega, j, T) - \omega)^2 + \Gamma^2(\omega, j, T)} \cdot [n(\omega) + 1] \quad (3.24)$$

The index  $j$  labels the particular examined phonon mode. We first focus on the corrections to the phonon's frequency. The anharmonic terms in a crystal's potential energy lead to two contributions that affect the harmonic frequency of the phonon.

$$\omega(T) = \omega_0 + \underbrace{\Delta\omega_{\text{lattice}}(T) + \Delta\omega_{\text{anharm}}(T)}_{\Delta(\omega, j, T)} \quad (3.25)$$

$\Delta\omega_{\text{lattice}}(T)$  includes the thermal expansion of the crystal volume and  $\Delta\omega_{\text{anharm}}(T)$  describes phonon-phonon interactions through the anharmonic lattice potential. The first term,  $\Delta\omega_{\text{lattice}}(T)$ , is a frequency-independent contribution to a mode's frequency shift caused by the lattice volume expansion with increasing temperature. Due to the deviation from the normal harmonic value  $\omega_0$  of the mode's frequency this term is referred to as the quasi-harmonic frequency. This correction is solely due to the lattice thermal expansion



and gives a linear temperature dependence, where the slope is the so-called first-order thermal expansion coefficient  $\chi^{\text{th}}$ . Specifically, this first term is given for a hexagonal crystal as<sup>[101]</sup>

$$\Delta\omega_{\text{lattice}}(T) = \chi^{\text{th}} \cdot T \quad (3.26)$$

$$= \omega_0 \left( \exp \left[ -\gamma \int_0^T \alpha_c(T') + 2\alpha_a(T') dT' \right] - 1 \right). \quad (3.27)$$

Here,  $\gamma$  is the Grüneisen parameter and  $\alpha_{a,c}(T)$  are the coefficients of linear thermal expansion along the corresponding  $a$ - and  $c$ -crystal axes.

The second term of Equation (3.25),  $\Delta\omega_{\text{anharm}}(T)$ , gives rise to a further temperature-dependent frequency correction induced by the coupling of phonon modes through the anharmonicities. The contribution of the anharmonic correction is thereby dependent on the phonon-phonon coupling coefficient  $A$  and the thermal occupation  $n_{\vec{q},j}(\omega) = (\exp[\frac{\hbar\omega}{k_B T}] - 1)^{-1}$  of the involved modes and can be written as<sup>[100]</sup>

$$\omega_{\text{anharm}}(T) = A \left[ n(\vec{q}, j_1) + n(-\vec{q}, j_2) + 1 \right] \quad (3.28)$$

with  $n_{\vec{q},j}(\omega) = n(\vec{q}, j)$  for better readability. In contrast to  $\Delta\omega_{\text{lattice}}(T)$  that changes linear with temperature,  $\omega_{\text{anharm}}(T)$  shows a temperature dependence according to the changing phonon population factors with temperature. In that way,  $\omega_{\text{anharm}}(T)$  gives rise to a frequency shift even when the crystal would be held at constant volume and is, therefore, often referred to as the pure temperature effect. The detailed expression for the anharmonic contribution is given as<sup>[100]</sup>

$$\omega_{\text{anharm}}(T) = \underbrace{-\frac{18}{\hbar^2} \sum_{\vec{q}, j_1, j_2} \left| V \begin{pmatrix} \vec{0} & \vec{q} & -\vec{q} \\ j & j_1 & j_2 \end{pmatrix} \right|^2}_{=A} \cdot \frac{1}{\omega(\vec{q}, j_1) + \omega(-\vec{q}, j_2) - \omega} \cdot \left[ n(\vec{q}, j_1) + n(-\vec{q}, j_2) + 1 \right], \quad (3.29)$$

where the strength of the phonon-phonon coupling coefficient  $A$  is dependent on the coefficient  $V$ , which is derived from the lattice potential energy of deformation at constant volume,  $j$  is the band index of the Raman zone-center ( $\vec{q}=0$ ) phonon and  $j_{1,2}$  are the band indices of the coupling modes with momentum  $\pm\vec{q}$ . Equation (3.29) is the so-called cubic anharmonicity and higher order anharmonicity terms in  $\omega_{\text{anharm}}(T)$  have been neglected due to their usually much weaker contribution.<sup>[102]</sup>

In conclusion, if only anharmonic contributions are considered for the phonon's self-energy corrections, the frequency shift with temperature is in total arising from the temperature-dependent first-order thermal expansion coefficient  $\chi^{\text{th}}(T)$  and the modes occupation factor  $n(\vec{q}, j, T)$  assuming that the  $A$  is constant. This leads to the final expression for the

### 3 Raman Response of Topological Insulator 2D Nanoflakes

temperature-dependent frequency shift:

$$\omega(T) = \omega_0 + \chi^{\text{th}} \cdot T + A \left[ \frac{1}{\exp\left[\frac{\hbar\omega_{j1}}{k_B T}\right] - 1} + \frac{1}{\exp\left[\frac{\hbar\omega_{j2}}{k_B T}\right] - 1} + 1 \right]. \quad (3.30)$$

Turning now to the temperature dependence of the phonon's line width  $\Gamma(T)$ , we will find that the modes line width is related to its lifetime. The phonon lifetime is inversely proportional to the rate at which the excited phonon relaxes to its equilibrium state. This relaxation rate  $\tau$  is determined by the possible available relaxation mechanisms. In a classical approach each of these scattering mechanisms can be associated to a relaxation rate, or equivalently line width, given by the Matthiessen rule:

$$\Gamma(T) = \Gamma_0 + \Gamma_{\text{ph-ph}}(T) + \Gamma_{\text{el-ph}}(T) \quad (3.31)$$

$\Gamma_0$  describes a temperature-independent background contribution arising from disorder and boundary scattering, whereas  $\Gamma_{\text{ph-ph}}$  and  $\Gamma_{\text{el-ph}}$  describe the interactions to other phonon modes or electronic excitations, respectively. For insulators there are typically no low-energy electronic excitations available for coupling and, therefore, we will neglect  $\Gamma_{\text{el-ph}}$  in this first discussion and focus on the contributions arising from phonon-phonon interactions contributing to  $\Gamma_{\text{ph-ph}}$ .

In a quantum mechanical picture the resulting line shape can again be derived from the phonon's self-energy corrections due to the anharmonic potential mediating the phonon-phonon interactions according to Equation (3.24). The temperature-dependent broadening of the Raman mode due to phonon-phonon interactions is given by<sup>[100]</sup>

$$\Gamma(T) = \Gamma_0 + A^* \left[ n(\vec{q}, j_1) + n(-\vec{q}, j_2) + 1 \right], \quad (3.32)$$

where  $A^*$  represents the phonon-phonon coupling coefficient. The coupling coefficient  $A^*$  is again related to the same cubic anharmonicity contribution, which also influences the mode's frequency (see Equation (3.33)), and is expressed in detail as<sup>[100]</sup>:

$$\Gamma_{\text{ph-ph}} = \underbrace{\frac{18}{\hbar^2} \sum_{\vec{q}, j_1, j_2} \left| V \begin{pmatrix} \vec{0} & \vec{q} & -\vec{q} \\ j & j_1 & j_2 \end{pmatrix} \right|^2 \cdot \delta(\omega(\vec{q}, j_1) + \omega(-\vec{q}, j_2) - \omega)}_{=A^*} \cdot \left[ n(\vec{q}, j_1) + n(-\vec{q}, j_2) + 1 \right] \quad (3.33)$$

This equation describes the decay of the optical phonon into a combination of two phonons  $\omega(\vec{q}, j_1)$  and  $\omega(-\vec{q}, j_2)$  under the conservation of momentum and energy. It is obvious from comparison with Equation (3.29) that the contribution from the cubic anharmonicity is both responsible for the softening and broadening of the Raman mode with increasing temperature and that the coupling parameters  $A$  and  $A^*$  are related via Kramers-Kronig transformation.<sup>[100,103]</sup> The form of Equation (3.33) does not explicitly define into which

final states the phonon will decay. The probability for each possible decay channel is determined by the joined phonon density of states and transition matrix elements for a certain combination of phonon modes  $j$ . If the matrix elements are assumed to be constant, a large  $\Gamma_{\text{ph-ph}}$  is expected whenever the Raman modes frequency  $\omega_0$  coincides with a high value in the two-phonon density of states. Hence, in the most complete model the correct line width correction would be obtained by summing over all possible decay processes.<sup>[99]</sup> However, there are more simple evaluations of Equation (3.33) that focus on one particular phonon decay channel and are presented here due to their wide application within the community.

### Symmetric anharmonic decay model

In the most simple model, the so-called Klemens model, a symmetric decay of the Raman phonon into two acoustical phonons of opposite momenta and equal frequency leading to  $\omega(\vec{q}, j_1) = \omega(-\vec{q}, j_2) = \omega_0/2$  with  $j_1 = j_2$  is assumed. Within this model the temperature dependence of the phonon frequency and line width according to Equation (3.30) and Equation (3.32) simplifies to<sup>[104]</sup>

$$\omega_{\text{anh}}(T) = \omega_0 + \chi^{\text{th}} \cdot T + A \cdot \left[ 1 + \frac{2}{\exp\left[\frac{\hbar\omega_0}{2k_B T}\right] - 1} \right], \quad (3.34)$$

$$\Gamma_{\text{anh}}(T) = \Gamma_0 + A^* \cdot \left[ 1 + \frac{2}{\exp\left[\frac{\hbar\omega_0}{2k_B T}\right] - 1} \right]. \quad (3.35)$$

### 3.1.6 Raman Response of Bi<sub>2</sub>Se<sub>3</sub> and Bi<sub>2</sub>Te<sub>3</sub>

The rhombohedral crystal structure of the V<sub>2</sub>-VI<sub>3</sub> compounds belongs to the crystal space group R $\bar{3}m$  (D<sub>3d</sub><sup>5</sup>) in Hermann-Mauguin (Schönflies) notation.<sup>[22]</sup> The crystal is build up of stacked QLs, consisting of X-Bi-X-Bi-X (X=Se,Te) that are weakly bond to each other by van der Waals forces. The height of one QL is 0.958 nm for Bi<sub>2</sub>Se<sub>3</sub> and 1.02 nm for Bi<sub>2</sub>Te<sub>3</sub>.<sup>[37,105]</sup> The primitive unit cell shown in Figure 3.4(a) consists of five atoms, which allows for 15 degrees of freedom and yields an irreducible representation at  $q = 0$  of:<sup>[22,106]</sup>

$$\Gamma = 2A_{1g} + 3A_{1u} + 2E_g + 3E_u.$$

These can be classified according to group theory into three acoustic ( $A_{1u}$  and one doubly degenerate  $E_u$ ) and twelve optical modes. In Figure 3.4(b,c) the atomic displacements of the optical phonons are shown, with two vibrations each of  $E_g$ ,  $A_{1g}$ ,  $E_u$ , and  $A_{1u}$  symmetry, where the modes with E-symmetry are additionally twofold degenerate. Due to the VI<sup>(2)</sup> atoms acting as inversion centers in a single QL, the even-parity vibrations are

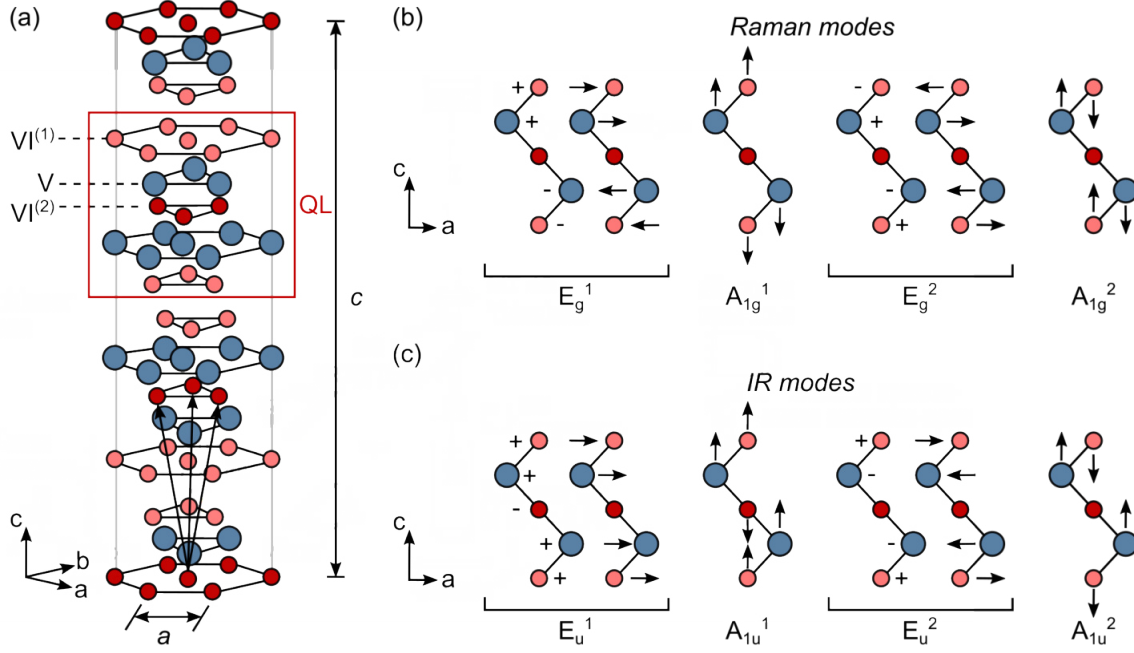


**Figure 3.4:** (a) Crystal structure of the  $V_2$ - $VI_3$  compounds with the black lattice vectors for the rhombohedral unit cell and one quintuple layer (QL) indicated. (b) Atomic displacements of the Raman-active and (c) IR-active lattice vibrations with propagation direction along the  $c$ -axis. The order of the phonons is given according to their increasing frequency from left to right. Plus and minus correspond to the atoms vibrating out of and into the image plane.

exclusively Raman and odd-parity vibrations are exclusively IR-active modes as assigned in Figure 3.4(b,c). The Raman-active vibrations of  $A_{1g}$  and  $E_g$  symmetry can be distinguished from one another according to their Raman tensors given as<sup>[85]</sup>:

$$R_{A_{1g}} = \begin{pmatrix} a & 0 & 0 \\ 0 & a & 0 \\ 0 & 0 & b \end{pmatrix} \quad R'_{E_g} = \begin{pmatrix} c & 0 & 0 \\ 0 & -c & d \\ 0 & d & 0 \end{pmatrix} \quad R''_{E_g} = \begin{pmatrix} 0 & -c & -d \\ -c & 0 & 0 \\ -d & 0 & 0 \end{pmatrix}$$

When conducting polarization dependent Raman measurements the off-diagonal elements in the  $E_g$  tensors lead to a finite Raman intensity in both parallel (xx) and cross (xy) scattering configuration, whereas the  $A_{1g}$  modes only give rise to a Raman signal in parallel scattering configuration. The Raman selection rules according to Equation (3.23) for the parallel and cross polarization geometries are hence given as:

$$\begin{aligned} \text{(xx)} : \vec{e}_i &= \begin{pmatrix} 1 \\ 0 \\ 0 \end{pmatrix} & \vec{e}_s &= \begin{pmatrix} 1 \\ 0 \\ 0 \end{pmatrix} & I_{A_{1g}} &\propto a^2 & I_{E_g} &\propto c^2 \\ \text{(xy)} : \vec{e}_i &= \begin{pmatrix} 1 \\ 0 \\ 0 \end{pmatrix} & \vec{e}_s &= \begin{pmatrix} 0 \\ 1 \\ 0 \end{pmatrix} & I_{A_{1g}} &\propto 0 & I_{E_g} &\propto c^2 \end{aligned}$$

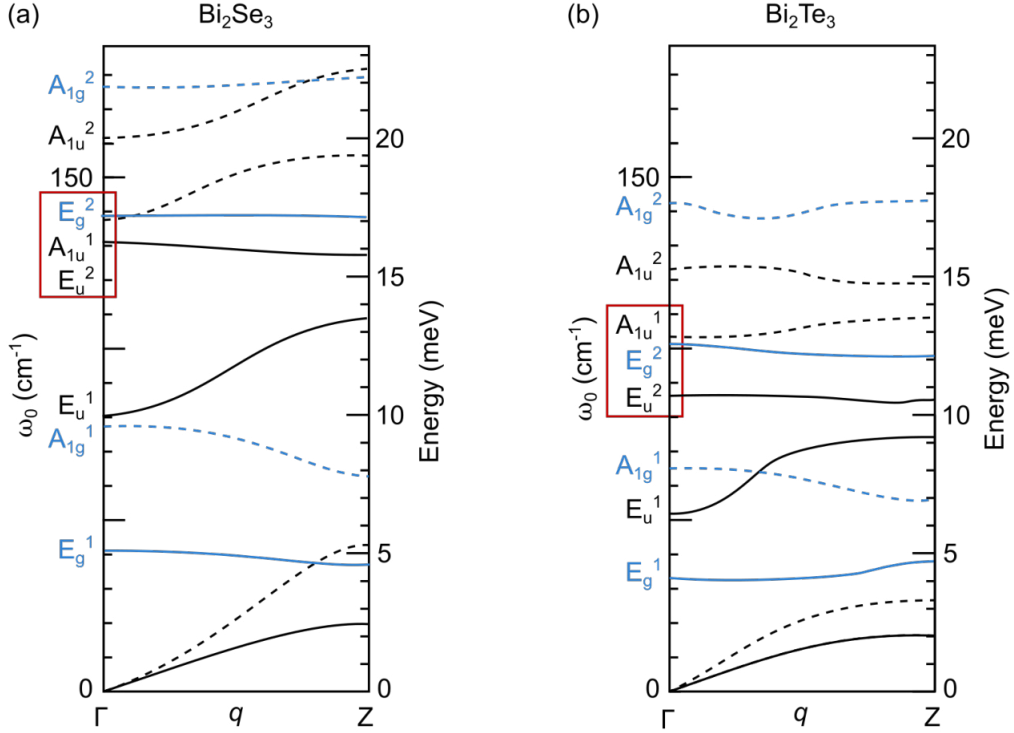


**Figure 3.5:** Dispersion relation for (a)  $\text{Bi}_2\text{Se}_3$  calculated using density functional theory<sup>[108]</sup> and (b)  $\text{Bi}_2\text{Te}_3$  measured via inelastic neutron scattering at 77 K<sup>[107]</sup>. Raman- (blue) and IR-active (black) modes are indicated with longitudinal (dashed) and transversal (solid) vibrations. Graphs are traced from the original data of<sup>[107–109]</sup>. The frequency order of modes corresponds to values measured in literature via Raman and IR spectroscopy (see also appendix A), with the exception of the  $A_{1g}^1$  and  $E_u^1$  modes in (a). The red squares in (a) and (b) highlight the closely adjacent frequencies of the three enclosed modes that gives rise to varying mode assignments in literature.

From Figure 3.4 it is apparent that all phonons involve motions of entire planes of atoms, with the atoms vibrating in the  $a, b$ -plane for modes with E-symmetry and out-of-plane for modes with A-symmetry. Furthermore, all modes propagate along the  $c$ -axis, leading to a classification of longitudinal (A-symmetry) and transversal modes (E-symmetry).<sup>[22,107]</sup>

The dispersion relations of the phonon branches for  $\text{Bi}_2\text{Se}_3$  and  $\text{Bi}_2\text{Te}_3$  are shown in Figure 3.5 with the Raman-active modes given as blue graphs. For both materials the order of the mode frequencies at the  $\Gamma$  point is almost identical. However, there exists a large variety in literature for the ordering of the  $E_u^2$ ,  $E_g^2$ , and  $A_{1u}^1$  modes due to their very closely adjacent frequencies, see the red boxes in Figure 3.5, that can vary depending on the employed simulation model.<sup>[108,110,111]</sup> This becomes further clear in comparison with experimentally determined values. The frequencies of the  $\text{Bi}_2\text{Se}_3$  and  $\text{Bi}_2\text{Te}_3$  Raman-active phonons at the Brillouin zone center have been measured in literature for a variety of sample geometries such as single crystals, films or nanostructures. A comprehensive overview of mode frequencies classified for the different sample geometries is given for  $\text{Bi}_2\text{Se}_3$  in Table A.2 and for  $\text{Bi}_2\text{Te}_3$  in Table A.1 in the appendix. The overview is given to show the frequency range of modes and underline the cautious assignment of mode

### 3 Raman Response of Topological Insulator 2D Nanoflakes

symmetries for phonons with very similar frequencies. In comparison to  $\text{Bi}_2\text{Se}_3$ , all mode frequencies for equivalent vibrations in  $\text{Bi}_2\text{Te}_3$  are shifted towards lower frequencies, which is expected due to the higher atomic mass of the Te atoms compared to the Se atoms.<sup>[22,110]</sup> At room temperature the Raman mode frequencies for bulk samples are listed for a quick reference in Table 3.1.

**Table 3.1:** Average Raman mode frequencies in  $\text{cm}^{-1}$  at room temperature for bulk samples reported in literature.

	$\mathbf{E_g}^1$	$\mathbf{A_{1g}}^1$	$\mathbf{E_g}^2$	$\mathbf{A_{1g}}^2$
$\text{Bi}_2\text{Se}_3$ <sup>[22,81,101,110,112]</sup>	37.0	72.2	131.4	175.1
$\text{Bi}_2\text{Te}_3$ <sup>[22,107,110]</sup>	35.3	61.5	101.7	133.6

#### Detection of IR modes via Raman spectroscopy

Table A.2 and Table A.1 further include frequencies of the IR-active phonons that were determined using IR absorption spectroscopy. Knowledge about the IR mode frequencies becomes increasingly relevant for Raman studies on ultrathin samples. The reduced periodicity in the  $c$ -direction breaks the inversion symmetry for the terminating QLs and hence leads to a reduction of the crystals point group to  $C_{3v}$ . This changes the selection rules for Raman scattering and results in the detection of the previously exclusive IR-active modes in Raman measurements. In the  $C_{3v}$  point group the irreducible representations  $A_{1g}$  and  $A_{2u}$  merge into  $A_1$ ,  $A_{2g}$  and  $A_{1u}$  merge into  $A_2$ , and  $E_g$  and  $E_u$  merge into  $E$ .<sup>[85,113]</sup> The Raman selection rules for the bulk and surface point groups are summarized in Table 3.2 for the different polarization geometries. In literature, the Raman activity of IR-active modes due to the breaking of inversion symmetry along the  $c$ -direction has been observed (a) at the surface of bulk samples at temperatures below 80 K<sup>[62,113–115]</sup> or (b) at room temperature for ultrathin ( $< 40$  nm) exfoliated and epitaxially grown films.<sup>[73,116–121]</sup>

In this work, the detection of bulk IR-active modes was achieved for Raman measurements at low temperatures and for room temperature measurements of single nanoflakes on gold substrate and is discussed in detail in the macro-Raman measurements in section 4.4 and the micro-Raman measurements in section 5.5.

**Table 3.2:** Raman selection rules for the different point groups applicable in the bulk and at the surface for the bismuth chalcogenides.<sup>[85,113]</sup>

Scattering geometry	Bulk ( $\mathbf{D_{3d}}$ )	Surface ( $\mathbf{C_{3v}}$ )
xx (parallel)	$A_{1g} + E_g$	$A_1 + E$
yx (cross)	$A_{2g} + E_g$	$A_2 + E$

## 3.2 Experimental setups

The topological insulator 2D NFs were investigated by means of Raman spectroscopy both in the form of multiple overlapping NFs representing a thin film geometry, as well as single isolated NFs. The investigation of a manifold of drop cast, overlapping NFs provides information on the average properties of the materials, whereas measurements on single NFs allows to distinguish the subtle influences in the materials properties by the NFs thicknesses or compositions. Therefore, both sample geometries were studied using different Raman setups, namely a magnetic field setup for temperature and magnetic field dependent measurements (section 3.2.1) and a microscope setup (section 3.2.1) for high-resolution measurements on single NFs. This section highlights the features of both setups with regard to the different demand on the experimental results, while also presenting the related triple-grating spectrometer employed in each setup in section 3.2.3.

### 3.2.1 Raman setup for temperature and magnetic field dependence

Magnetic field and temperature dependent measurements on NF samples in thin film geometry were conducted on a custom-made ‘ultimate triple’ (UT) system originally designed by Miles Klein and continuously improved in the group of Prof. Dr. Lance Cooper at the University of Illinois Urbana-Champaign (UIUC), Department of Physics and Materials Research Laboratory, in the United States of America.<sup>[122,123]</sup> The setup is equipped with a continuous He-flow cryostat (Oxford Instruments, CF-1201) that is mounted into the center of a superconducting magnet. This enables the unique capability of simultaneous temperature (3–300 K) and magnetic field (0–7 T) dependent measurements on the thin film samples. For macro measurements the 647.1 nm excitation line of a continuous-wave (CW) krypton ion ( $\text{Kr}^+$ ) gas laser (Coherent inc.) was used. To probe a large sample area representing the average properties of the NFs the collimated beam was focused down to a rather wide laser spot size of about 50  $\mu\text{m}$  employing a simple lens. The beam path is schematically illustrated in Figure 3.6. The advantage of the use of gas lasers for Raman scattering experiments is their intense emission lines, very narrow bandwidth and single mode output allowing the detection of Raman bands down to about  $55\text{ cm}^{-1}$ . A disadvantage of gas lasers is the number of competing weaker emission bands that can interfere with the recorded Raman spectra. In the macro-Raman setup these side bands are filtered by first passing the laser beam through a narrow bandpass filter (BF), eliminating lines close to 647.1 nm. This step is most crucial since the neighboring emission lines would overlay with the detected Raman spectrum and appear as additional narrow peaks in the spectra. Secondly, lines further away from 647.1 nm are removed by a prism monochromator (PM). The monochromatic beam is finally, directed onto the focusing lens (L1) that focuses the laser onto the sample.

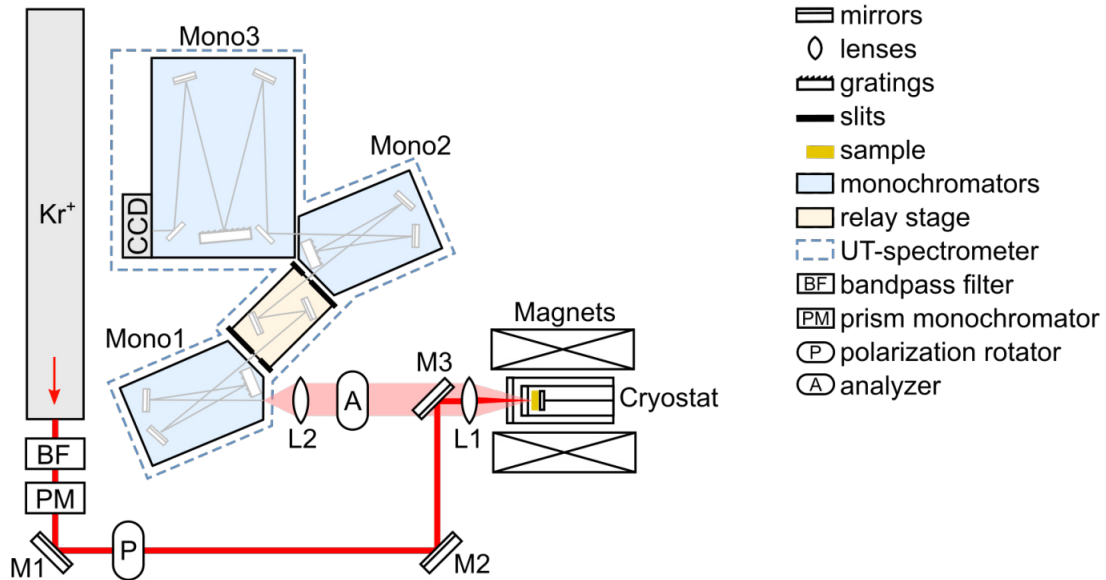


**Figure 3.6:** Schematic top view of the experimental environment for macro-Raman measurements adapted from<sup>[122,123]</sup>. The excitation laser is directed and focused onto the sample, which is glued onto a sample holder within a cryostat. The cryostat is placed in the open bore of a superconducting magnet. The scattered signal is collected in a true backscattering configuration and directed into the UT-spectrometer.

The UT system operates in a ‘true’ backscattering geometry, which only uses one lens (L1) to focus the incident beam onto the sample and simultaneously collects the scattered Raman signal. L1 collimates the Raman signal onto a second lens L2 that in turn focuses it onto the entrance slit of the spectrometer. The f-number of L2 is chosen to sufficiently fill the optics of the first monochromator without overfilling the mirrors and diffraction grating to reduce signal loss. The triple-grating spectrometer is similar in design to the one used for the micro-Raman measurements in the sense that both setups employ a relay stage for effective stray light reflection. The spectrometer is discussed in detail in a separate section 3.2.3. Finally, to study the symmetry properties of recorded Raman signals the polarization of the incident laser and scattered light can be selected by a polarization rotator (P) and an analyzer (A) that transmit only one polarization component. The combination of both P and A enables Raman measurements in different scattering geometries as discussed in section 3.1.6. The analyzer is most efficient when being placed between lens L1 and L2 where the scattered light beam is collimated, because in an emerging beam the polarizer itself would affect the polarization of the signal. To switch between different scattering geometries only the orientation of P is changed. The orientation of A is set to transmit the horizontal polarization of the scattered light since the diffraction gratings of the spectrometer are most efficient for this polarization.<sup>[124]</sup> The spectral resolution of the UT system in the desired spectral range was calibrated by recording sharp emission lines of a Xenon gas discharge lamp. By averaging the Gaussian width of the emission lines a spectral resolution of  $\Gamma_G = 1.44 \pm 0.1 \text{ cm}^{-1}$  is obtained.<sup>[77]</sup>



### Temperature and Magnetic field properties

For temperature dependent measurements in the range between 3 K to 300 K the samples are attached to a sample rod via silver paint as shown in Figure 3.7(a) that is inserted into a continuous He-flow cryostat (Oxford Instruments, CF1201). The temperature is regulated by adjusting the He flow into the sample space via a needle valve. The temperature is stabilized at the desired value by a temperature controller and resistive heater located in the cryostat. The cryostat is mounted horizontally into the open bore of a superconducting magnet as indicated in Figure 3.7(b).

Magnetic field strength dependent Raman measurements were conducted in Faraday geometry ( $\vec{q} \parallel \vec{H}$ ) with the magnetic field vector  $\vec{H}$  aligned parallel to the wave vector  $\vec{q}$  of the incident light. The sample was mounted in a way such that the magnetic field  $\vec{H}$  was oriented normal to the sample plane, and thus also to the topological surface of the nanoflakes as shown in Figure 3.7(c).

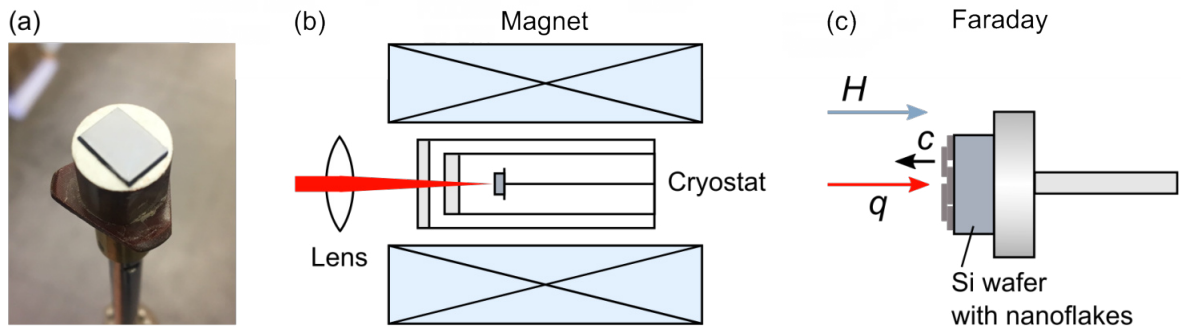


**Figure 3.7:** (a) Image of a sample glued on top of the sample rod. (b) Schematic illustration of the inserted cryostat containing the sample rod with the surrounding superconducting magnet adapted from<sup>[125]</sup>. The laser is focused onto the sample and areas in gray represent the cryostat windows. (c) Schematic illustration of the sample with nanoflakes in thin film geometry. The magnetic field is applied in Faraday geometry ( $\vec{q} \parallel \vec{H}$ ).

#### The Magnetic Field-Setup enables

- Raman studies on averaged NF clusters with a high contribution of topological surface properties
- Temperature adjustments between 3 K to 300 K
- Magnetic field dependence between 0 T to 7 T

### 3.2.2 Micro-Raman setup for single nanoflake investigations

The custom-made micro-Raman setup was developed in the group of Prof. Michael Rübhausen at the University of Hamburg, Germany, and enables in combination with the UT-3 spectrometer<sup>[126]</sup> high-resolution Raman spectroscopy on single nano- and micro-structures. A detailed description of the micro-Raman setup and further characterizations can be found in<sup>[127,128]</sup>. This section provides details on the experimental setup critical for the investigation of ultrathin, single TI NFs.

In order to study single NFs down to lateral dimensions of 500 nm, a low contribution of surrounding substrate and high sufficiency of collecting the very weak Raman signal of an ultrathin NF have to be met. This is achieved in the micro-Raman setup by the use of efficiently matched optical components for focusing the laser, a visual control on the relative laser-to-sample position by an optical microscope, and finally a three-axis sample stage. The beam path of the micro-Raman unit, that can be placed before the collecting entrance optics of the detecting UT-3 spectrometer, is schematically shown in Figure 3.8.

#### Micro-Raman unit

The sub-micron laser spot diameters with homogeneous beam profiles are achieved by first widening the monochromatic laser light using a spatial filter and subsequent direction onto a focusing objective (FO). The high numerical aperture of the FO (Mitutoyo 50 Plan Apo HR, NA = 0.75) leads to the creation of diffraction limited laser spot sizes down to  $\sim 210$  nm depending on the used laser wavelength (see Table 3.3 for exact laser spot sizes). A huge advantage of this setup is the possibility to simultaneously observe the nanostructured sample, as well as the laser spot position, to ensure a precise location on the nanostructure. This is achieved by coupling a white light source into the laser beam path using a first beam splitter (BS1) (Reflection:70/Transmission:30) that is also focused onto the sample along with the laser. The infinity corrected FO in combination with a matched tube lens creates an image of the sample on a charged-coupled device (CCD) camera, which is read out using a framegrabber software (IC Measure 2.0.0.161, The Imaging Source Europe GmbH). The sample holder is attached to a  $xyz$ - $\mu\text{m}$ -stage for coarse alignment, which itself is mounted onto a multi-axis piezo scanner P-517 (PI, Germany). The piezo-stage enables to accurately choose the desired laser spot location on the nanostructure and bring the sample into the laser focus. After sample alignment, a motorized mirror (MM) can be inserted into the beam path to block the camera view and enable Raman measurements. During measurements the created Raman signal, similar to the macro-Raman setup in section 3.2.1, is again collected in a ‘true’ backscattering configuration by the FO. A second beam splitter (BS2) transmits 10% of the incident laser light onto the FO and at the same time allows transmission of the collected Raman signal with a 90% efficiency. The FO collimates the collected Raman signal and the MM directs the beam onto an entrance objective (EO) (Olympus, NA = 0.4) that focuses the beam into the focal point of the entrance optics. Hereby, the numerical aperture of the

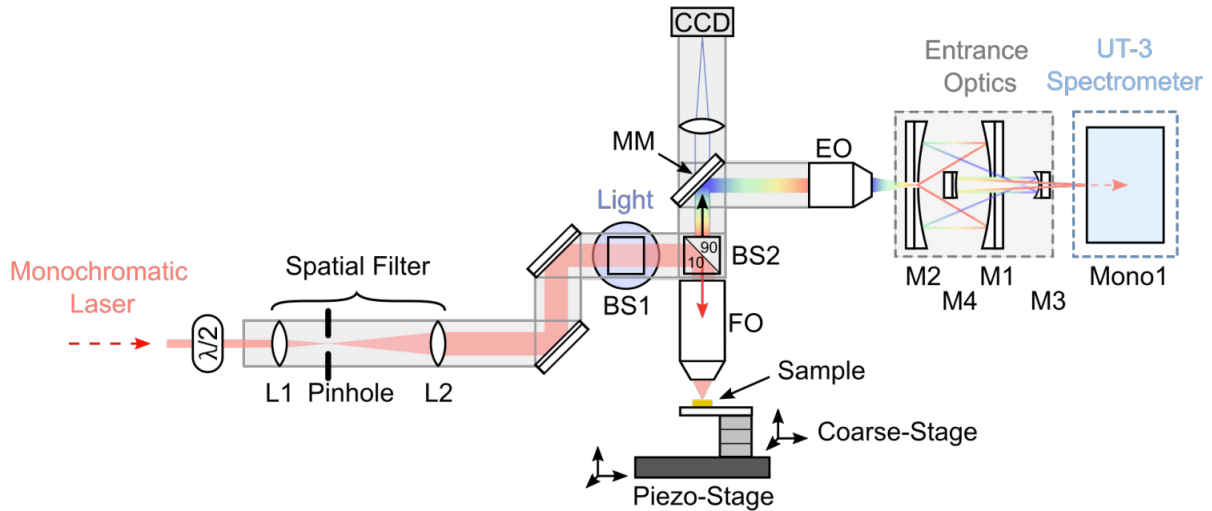


**Figure 3.8:** Schematic side view of the micro-Raman unit placed in front of the entrance optics that focus the collected Raman signal into the UT-3 spectrometer. Adapted with permission from<sup>[128]</sup>

EO roughly matches that of the entrance optics ( $NA = 0.5$ ) to fully fill the entrance optics and consequently ensure high resolution in the following spectrometer.

### Entrance Optics

The entrance optics resemble an all-reflecting, fully achromatic objective that collects the Raman signal from the EO and focuses the light beam further into the entrance slit of the spectrometer.<sup>[126]</sup> In detail, the entrance optics consist of four on-axis parabolic mirrors, as shown in Figure 3.8. The first mirror M1 collects the Raman signal and collimates it onto M2. M2 forms an intermediate image before M3, which in turn collimates the beam again onto M4 that finally focuses the beam into the entrance slit of the spectrometer. Details on the mirror specifications are given in<sup>[126]</sup>. Finally, the Raman signal is spectrally resolved in the UT-spectrometer, which is discussed in detail in section 3.2.3.

### Laser power configuration

To choose suitable laser power densities for intense Raman signals, while simultaneously excluding laser damage or heating of the NFs, a filter-unit with several optical density (OD) filters can be inserted in front of the micro-Raman unit. The incident laser power was determined depending on the obtained Raman signal and absorption properties of the sample. Due to the number of optics and beam splitters build in the micro-Raman unit only 0.24 % of the laser power entering the unit is directed onto the sample.<sup>[128]</sup> The laser power at the sample position was precisely measured by a Si photodiode power meter (Thorlabs, PM160).

### Excitation wavelengths

All optical components integrated in the micro-Raman setup were chosen to optimally function in the visible light range between 705 nm to 400 nm. This allows for resonance Raman studies on single nanostructures, a critical advantage not met in commercially available Micro-Raman spectrometers due to the limited number of provided lasers. For the resonance Raman study on Bi<sub>2</sub>Se<sub>3</sub> NFs presented in section 5.4 five excitation wavelengths with equidistant energies in the visible spectrum were chosen. An overview of employed laser sources is given in Table 3.3.

### Laser spot diameter on sample

The use of the FO with a high numerical aperture ( $NA = 0.75$ ) creates beam spot diameters  $d$  with full width at half maximum (FWHM)  $\Gamma$  in agreement with the classical Abbe diffraction limit

$$a = \frac{\lambda}{2NA}, \quad (3.36)$$

whereby  $a$  is the distance between two distinguishable points. Beam spot diameters were determined by evaluating intensity profiles of recorded spot images on Si(111) substrate as shown in Figure 3.9. To record images without saturation of pixels a suitable OD was chosen for each wavelength and the white light source was turned off. In Figure 3.9 vertical and horizontal intensity line cuts of the recorded gray scale images are shown. All intensity profiles are readily fit by a Gaussian profile and the low deviation in FWHM between vertical and horizontal cuts of less than 3% validates the homogeneous beam profiles. With a camera resolution of 69 nm per pixel the determined FWHM lead to the

**Table 3.3:** Laser sources employed for resonance micro-Raman measurements.

Wavelength	Laser type	Model	Manufacturer	Beam FWHM
704.96 nm	Mode locked Ti:sapphire laser pumped by a Millenia eV	Tsunami 3950- X1BB	Spectra-Physics Lasers, Inc.	$283 \pm 3$ nm
632.82 nm	Gas	05-LHP- 123-496 HeNe	Melles Griot	$211 \pm 2$ nm
593.72 nm	Diode	OBIS 594LS 1233468	Coherent, Inc.	$269 \pm 2$ nm
560.35 nm	Diode	OBIS 561LS 1223779	Coherent, Inc.	$389 \pm 2$ nm
532.04 nm	Diode	Millenia Pro 10sJS	Spectra-Physics Lasers, Inc.	$255 \pm 4$ nm

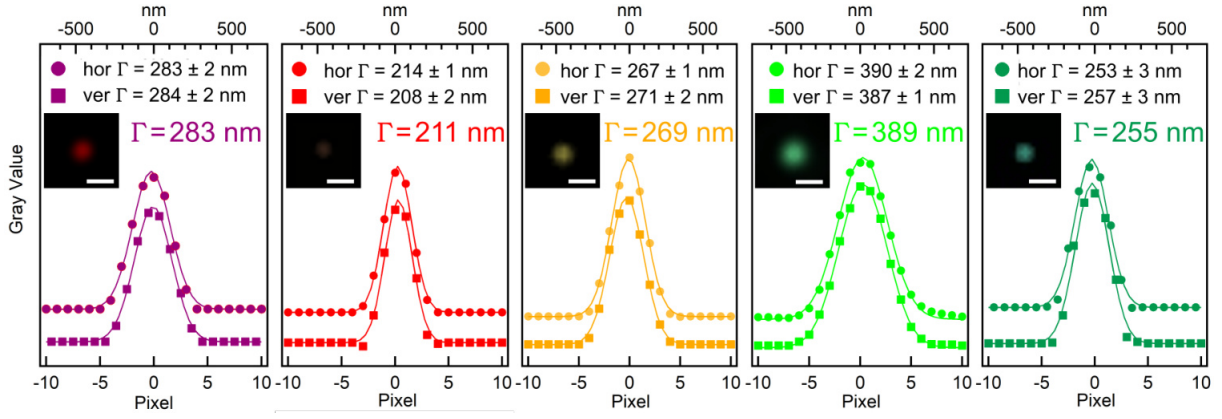


**Figure 3.9:** Laser spot characterization. Intensity line profiles of the shown laser spot microscope images without white light illumination. The panels from left to right show the recorded laser spot images of the used excitation sources with wavelength of 705 nm, 633 nm, 594 nm, 560 nm, and 532 nm, respectively. The scale bar in the laser spot images ( $20 \times 20$  pixel) corresponds to 500 nm. Horizontal (circles) and vertical (squares) intensity cuts were fitted by a Gaussian profile shown as solid lines. The FWHM of vertical and horizontal cuts were averaged to the value  $\Gamma$  given in color. The gray value images are displayed in false color. Reprinted with permission from<sup>[129]</sup>. Copyright 2022 American Chemical Society.

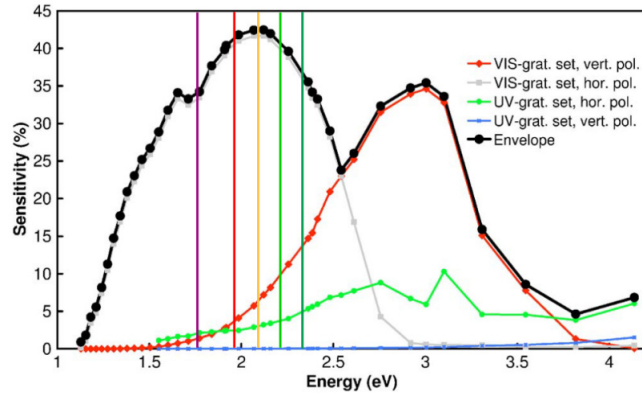
beam spot diameters given in Table 3.3. Beam spot diameters below  $d = 300$  nm were achieved for all excitation wavelengths except for the 560 nm diode laser. However, smaller beam spot diameters can be achieved when optimizing the spatial filter for this wavelength to fully illuminate the FO.

### Polarization selection

Depending on the chosen excitation wavelength, the sensitivity of the UT-3 spectrometer varies for certain laser polarizations.<sup>[126]</sup> To ensure a high sensitivity the most suitable polarization of the incoming laser is selected by a  $\lambda/2$  wave plate (WP) that is positioned in front of the micro-Raman unit (see Figure 3.8). An overview of the spectrometer sensitivities for the selected excitation wavelengths of the resonance study on single  $\text{Bi}_2\text{Se}_3$  NFs is given in Table 3.4 and Figure 3.10. Due to the low sensitivity of below 5% for vertically polarized light with energies less than 2 eV, the spectrometer itself can function as an analyzer when conducting polarization dependent measurements. For symmetry analysis of the recorded Raman modes the micro-Raman measurements can, therefore, be conducted in parallel or cross scattering configuration, as discussed in section 3.1.6, by changing the WP to select the incident laser polarization. For a 633 nm excitation line, corresponding to 1.96 eV, with an incoming vertical laser polarization the setup would operate in cross polarization configuration since the spectrometer mainly detects the horizontally polarized component of the scattered light. In turn, a horizontally polarized laser would resemble a parallel polarization configuration.

**Table 3.4:** UT-3 spectrometer sensitivity.

$\lambda$	Sens(%)	Pol
704.96 nm	33.0	hor
632.82 nm	41.0	hor
593.72 nm	42.0	ver
560.35 nm	39.7	ver
532.04 nm	36.0	ver

**Figure 3.10:** UT-3 spectrometer sensitivity with indicated excitation energies as vertical lines used for resonance Raman studies. Adapted from<sup>[126]</sup> with the permission of AIP Publishing. Copyrights 2005 American Institute of Physics.**The Micro-Setup enables**

- Raman studies on single NFs by sub- $\mu$  laser spot diameters between  $d = 211\text{--}389$  nm
- Resonance Raman studies by incoupling lasers in the spectral range of 400–705 nm
- Single spot or scan measurements by the piezo sample stage

**3.2.3 Ultimate Triple-Grating spectrometer**

For both macro- and micro-Raman measurements custom-made ultimate-triple grating spectrometers<sup>[126]</sup> were used to obtain the Raman spectra. A schematic illustration of the UT-3 spectrometer as employed in the micro-Raman measurements is given in Figure 3.11. Details on the original UT-1 system as employed in the magnetic field setup can be found in the thesis of M. Kang<sup>[122]</sup>. Further details on the later version of the UT-3 system are given in Schulz *et al.*<sup>[126]</sup>. Since both Raman setups are operating in a true backscattering configuration the reflected laser signal is also focused into the spectrometer and has to be removed from the Raman signal. This is achieved by the use of a first filtering stage and a second stage for spectral resolution. The first stage combines two monochromators (Mono 1 and Mono 2) connected via a relay stage and enables high stray light reduction. This first premonochromator is crucial to remove the excitation frequency from the Raman signal and therefore enables the detection of low-frequency Raman excitations. The second stage is a third monochromator (Mono 3) with a large grating that spectrally resolves the

Raman signal onto a CCD-chip and enables the high spectral resolution.

### Premonochromator

In the premonochromator all integrated mirrors in Mono1, the relay stage, and Mono2 are off-axis parabolic (OAP) mirrors. The use of OAPs, which are characterized by reduced spherical aberrations and create sharp focus points, is responsible for the excellent stray-light rejection. In Mono1 the collected Raman signal is dispersed by a first blazed grating G1 and focused into the first slit S1 of the relay stage as shown by the raytracing in Figure 3.11. The slits in the relay stage are each equipped with monolateral knife edges that can be inserted to function as a low or high frequency bandpass filter. As shown in Figure 3.11, the relay stage collimates and refocuses the dispersed Raman signal onto the second monochromator. In Mono2 the second grating G2 is set to recombine the spectrally resolved light again into one beam, which is finally focused into the entrance slit of Mono3. The strong stray light reduction in this first stage is especially important for the detection of the first low-frequency  $A_{1g}^1$  mode in the investigated  $\text{Bi}_2\text{Se}_3$  and  $\text{Bi}_2\text{Te}_3$  NFs.

### Spectrograph

In the final monochromator the beam is collimated onto a larger grating G3 that disperses the light even further. The spectrally resolved light is focused by an elliptical mirror onto the CCD array detector, which leads to a high photon flux and consequently low signal-to-noise ratio. Due to the larger grating and longer distances in Mono3 a high resolution is achieved. For the investigation of TI NFs this is of high importance to i) enable

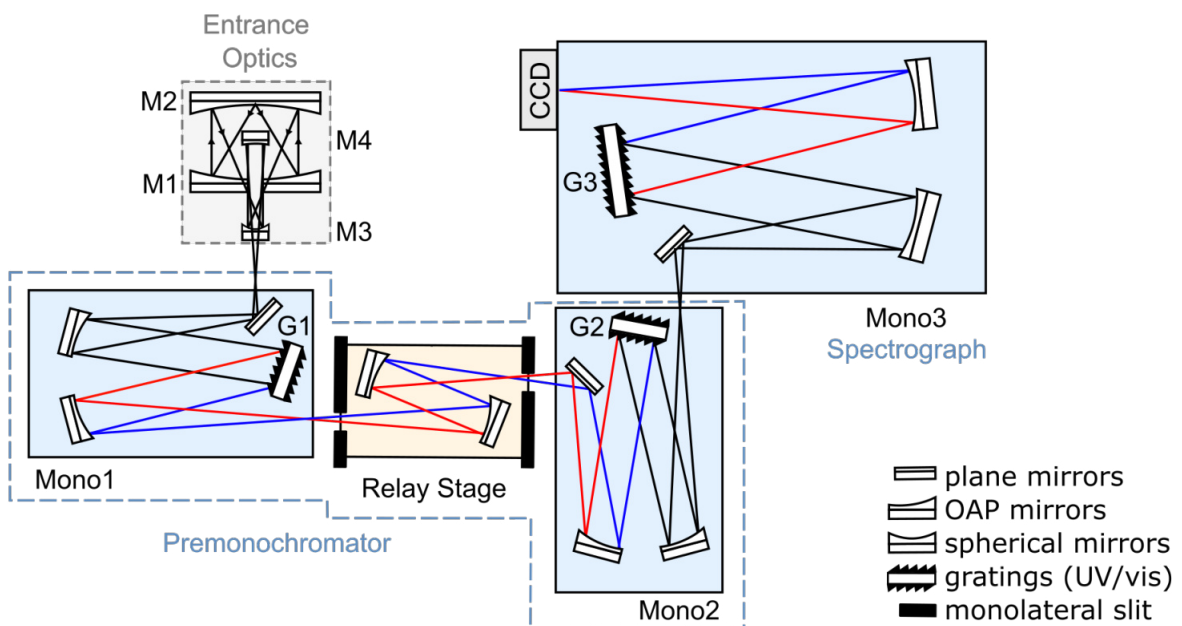


**Figure 3.11:** Schematic top view of the UT-3 system as employed in the micro-Raman measurements. Adapted from<sup>[126]</sup>.

### 3 Raman Response of Topological Insulator 2D Nanoflakes

a precise line shape analysis of the phonons and ii) allow for a distinction between neighboring phonons with very similar frequencies. This is especially important for ultrathin NF samples where additional surface modes are detected closely adjacent to the bulk modes.

#### Key advantages of the UT system

- low-frequency detection and strong stray-light rejection by using off-axis parabolic mirrors
- additional stray-light reduction by the use of a relay stage functioning as a low- or high- frequency adjustable bandpass filter
- fully achromatic due to reflective optics
- wide spectral range by employing double gratings (185–2000 nm)



# 4 Macro-Raman investigations of thin film samples

This chapter presents macro-Raman scattering studies on  $\text{Bi}_2\text{Se}_2$  and  $\text{Bi}_2\text{Te}_3$  NFs in a thin film geometry as a function of temperature and magnetic field strength. Section 4.1 describes the motivation for temperature and magnetic field dependent measurements. In section 4.2 all preparations regarding sample preparation and precharacterizations of the macro-Raman setup necessary for the investigation of ultra-thin films are included. The results of the temperature and magnetic field dependent studies are discussed in section 4.4 and section 4.5. The emerging electron-phonon interactions in  $\text{Bi}_2\text{Se}_3$  that become apparent in low temperature measurements are discussed and linked to interactions with the topological surface states, which are further validated by the magnetic field dependent phonon renormalizations. The results are concluded in section 4.6. The described work in this chapter is based upon research published in “Temperature and Magnetic field dependent Raman study of electron-phonon interactions in thin films of  $\text{Bi}_2\text{Se}_3$  and  $\text{Bi}_2\text{Te}_3$  nanoflakes”, S. Buchenau, S. Scheitz *et al.*, Phys. Rev. B 101, 245431 (2020).<sup>[78]</sup>

## 4.1 Motivation

The investigation of a manifold of overlapping NFs in the form of a thin film geometry was conducted to characterize the surface related properties of  $\text{Bi}_2\text{Se}_3$  and  $\text{Bi}_2\text{Te}_3$  NFs in the 2D limit. By studying the Raman response of the samples as a function of temperature, information about the phonon dynamics and present decay mechanisms in the materials can be gained. This helps to identify possible electron-phonon interactions that could limit the utilization of the Dirac surface states in the topological insulator 2D samples. By investigating the thin film samples a major reduction of the bulk properties is ensured. This allows to enhance the surface contribution and emphasize the influence of different decay channels with regard to the surface electrons. Temperature dependent studies have been conducted on  $\text{Bi}_2\text{Se}_3$  and  $\text{Bi}_2\text{Te}_3$  in the form of single crystals<sup>[81,101,102]</sup>, nanoplates<sup>[130]</sup> and  $\mu\text{m}$ -thick films<sup>[131]</sup>. Those previous works mainly focus on the phonon-phonon interactions with the aim of deducing the thermal conductivity properties, since  $\text{Bi}_2\text{Se}_3$  and  $\text{Bi}_2\text{Te}_3$  are prominent candidates for use as thermoelectrics.<sup>[132]</sup>

With respect to the existing works that identify different phonon-phonon decay channels, this work gives further insight on additional phonon-electron interactions. This was achieved by recording temperature dependent Raman spectra with a very high temperature

resolution especially at lower temperatures between 3 K to 120 K. This is, within the current knowledge, in contrast to all previous works that employed broad temperature increments of about 20 K. The high resolution at lower temperatures allows us to identify the electronic contributions to the phonon's self-energy corrections, since phonon-phonon interactions are expected to contribute less at lower temperatures due to decreasing phonon populations. By analyzing the temperature dependence of the phonon modes frequency and line width, corrections to the phonon's self-energy are deducted and interpreted in the form of electron-phonon interactions.

Moreover, the nature of the electron-phonon interactions can be further understood by the application of a magnetic field. The TSS are susceptible for magnetic fields that break time-reversal symmetry and subsequently the protection of Dirac states. Due to the confinement of the Dirac fermions on the surface the application of perpendicular magnetic fields leads to a formation of Landau levels that can be observed in forms of Shubnikov-de Haas oscillations in transport measurements.<sup>[50,133,134]</sup> It was suggested that the effects of a magnetic field oriented normal to the topological insulator surface plane will cause an opening of a small gap at the Dirac point.<sup>[28,135,136]</sup> Indeed, the prediction of the gap opening was observed in ARPES measurements when magnetic order was introduced into Bi<sub>2</sub>Se<sub>3</sub> after the deposition of magnetic elements like Fe<sup>[28,36,136]</sup> or by exchange coupling TIs to magnetic insulators.<sup>[79,137,138]</sup> In Bi<sub>2</sub>Te<sub>3</sub> the magnetic gap was observed for Mn-doped samples.<sup>[139,140]</sup> By studying the Raman response of Bi<sub>2</sub>Se<sub>3</sub> and Bi<sub>2</sub>Te<sub>3</sub> as a function of magnetic field the phonon self-energies are expected to reveal a manipulation of the Dirac surface states. The application of an external magnetic field, rather than the introduction of magnetic dopants, is also more versatile in the interpretation of magnetic fields induced effects since dopants also cause structural disorder that can lead to additional disruptive effects in the surface states.<sup>[141]</sup>

## 4.2 Sample Preparation of NF thin films

The Bi<sub>2</sub>Se<sub>3</sub> and Bi<sub>2</sub>Te<sub>3</sub> NFs employed for the macro-Raman studies were synthesized according to the wet-chemical synthesis routes explained in detail in chapter 2 and in the supporting information of Buchenau *et al.*<sup>[78]</sup> The exact synthesis parameters can be found in Table B.1. For the purification of the NFs in solvent, 200  $\mu$ L of the product were mixed with 1 mL isopropanol followed by centrifugation for 20 min at 4,000 rpm. The supernatant was disposed and the centrifugation step was repeated two times with isopropanol and one time with acetone. Lastly, the precipitated NFs were stored in isopropanol. For the preparation of samples with an effective thin film geometry, 10  $\mu$ L of each NF dispersion was drop cast on clean Si 100 wafers (1  $\times$  1 cm) repeatedly. The isopropanol was allowed to evaporate at room temperature between each drop casting load as schematically shown in Figure 4.1(a). This was repeated until the overlapping NFs formed a continuous film with only a few spaces of uncovered silica left as shown in optical microscope images of the

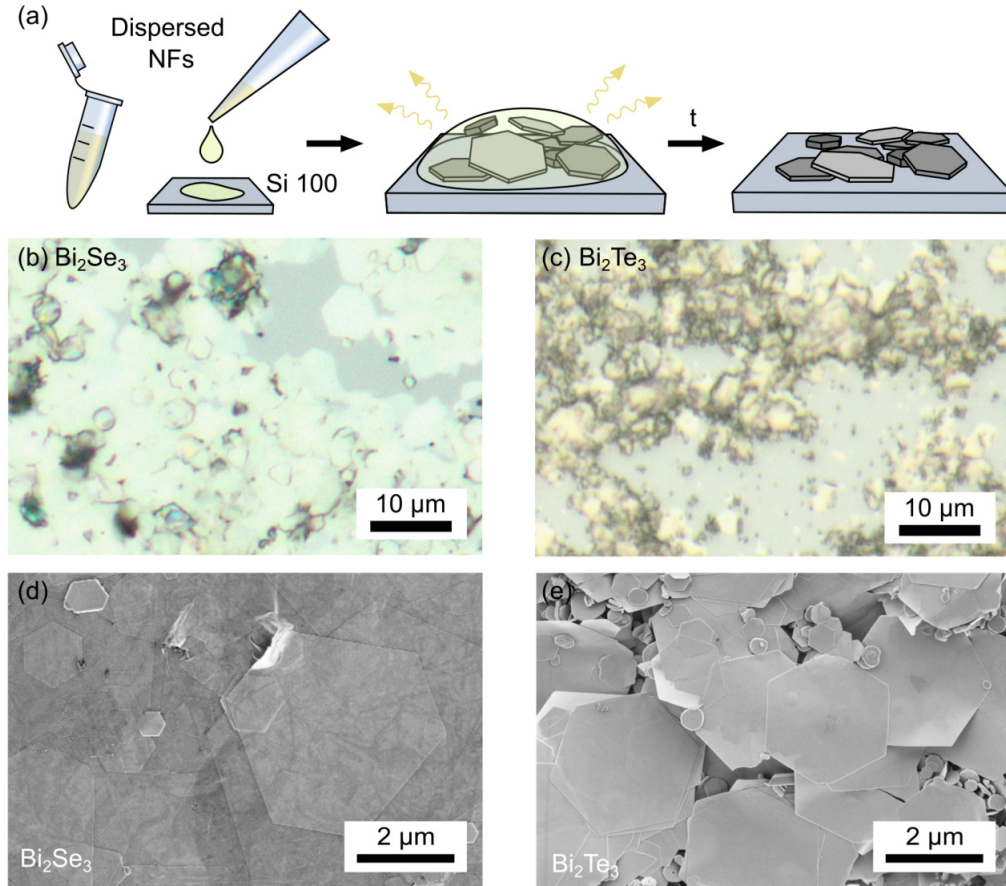


**Figure 4.1:** Preparation of thin film samples for macro-Raman measurements as a function of temperature and magnetic field strength. (a) Schematic illustration of the iterated drop casting process to create overlapping NFs in an effective thin film geometry. (b,c) Optical microscope images of the investigated  $\text{Bi}_2\text{Se}_3$  and  $\text{Bi}_2\text{Te}_3$  samples, respectively. The shown section approximately displays the sample area investigated by the macro-Raman laser ( $d \approx 50 \mu\text{m}$ ). Adapted with permission from [78]. Copyright 2020 by the American Physical Society. (d,e) SEM micrographs of the  $\text{Bi}_2\text{Se}_3$  and  $\text{Bi}_2\text{Te}_3$  thin film samples, respectively.

prepared films in Figure 4.1(b,c). Due to the subsequent drop casting, the NFs preferably attached to each other, which lead to the formation of clusters of NFs next to uncovered silicon areas. Since the macro-Raman setup presented in section 4.2 employs laser spot sizes of around  $50 \mu\text{m}$  a complete coverage of the silicon wafer was not necessary. Primarily, the prepared samples were aimed to give an average information about a manifold of overlapping NFs and correspondingly high amount of TSS .

To simultaneously investigate the samples as a function of temperature and magnetic field the prepared wafers were glued to the end of a thin rod using silver paint for good thermal conduction. The rod is inserted into the cryostat, which itself is mounted into the open bore of a super conducting magnet as explained in detail in section 3.2.1.

### 4.3 Measurement configuration and data analysis

To exclude laser induced sample damage a suitable laser power was determined by measuring the  $\text{Bi}_2\text{Te}_3$  thin film sample at various laser powers.  $\text{Bi}_2\text{Te}_3$  was chosen as a representative for both materials due to their similar thermal conductivities and hence ability to drain the heat induced by laser thermal heating.<sup>[142]</sup> The power dependent Raman spectra given in Figure 4.2(a) show no phonon frequency shifts and line width broadening with increasing power from 6.2 mW to 40 mW. However, at 50 mW an additional mode around  $120\text{cm}^{-1}$  appears, indicating that at this high laser powers structural changes are induced in the material. Since the lowest chosen power of 6.2 mW already gives Raman spectra with a good signal-to-noise ratio it was chosen for all further measurements. The choice of a low laser power is especially important for measurements at low temperatures because the incoming laser will lead to additional heating. To rule out any laser heating effects at 6.2 mW the  $\text{Bi}_2\text{Te}_3$  sample was measured for 1 h in the same sample position both at 3 K and at room temperature. The acquired spectra were analyzed in time periods of 5 min and no changes in frequency or line width are observed as shown in Figure 4.2(b). The stability of Raman spectra over these long integration times validates that the chosen laser power of 6.2 mW does not heat the sample and induces no sample damage in the NFs. Therefore, all obtained frequency shifts and line widths from data analysis can solely be assigned to change in temperature and magnetic field as we excluded any laser heating effects.

For all temperature and magnetic field dependent measurements Raman spectra were acquired with an integration time of 5 min and averaged over 5 acquisitions, leading to a total measurement time of 25 min per data point. The focus of the laser was verified and adjusted before each measurement.

Before analyzing the phonon modes all Raman spectra were Bose corrected as outlined in section 3.1.2 and a linear background was subtracted. The linear background varied slightly for different measurements and can be effected by the exact laser spot position on the sample and hence varying elastic stray light contributions. For the analysis of frequency and phonon life time as a function of temperature and magnetic field all phonon modes were fit by a Voigt profile function, if not stated otherwise:

$$V(\omega) = y_0 + \int_{-\infty}^{\infty} \text{Gauss}(\Gamma_G, \omega) \cdot \text{Lorentz}(\Gamma_L, \omega - \omega_0) d\omega \quad (4.1)$$

The Voigt profile represents the phonon Raman response function in form of a Lorentzian profile convoluted with a Gaussian profile accounting for the spectrometer resolution.<sup>[143]</sup>

$$\text{Gauss}(\Gamma_G, \omega) = \sqrt{\frac{4 \ln 2}{\pi}} \cdot \frac{\exp\left[-\frac{4 \ln 2}{\Gamma_G^2} \omega^2\right]}{\Gamma_G} \quad (4.2)$$

$$\text{Lorentz}(\Gamma_L, \omega - \omega_0) = \frac{2A}{\pi} \frac{\Gamma_L}{4(\omega - \omega_0)^2 + \Gamma_L^2} \quad (4.3)$$

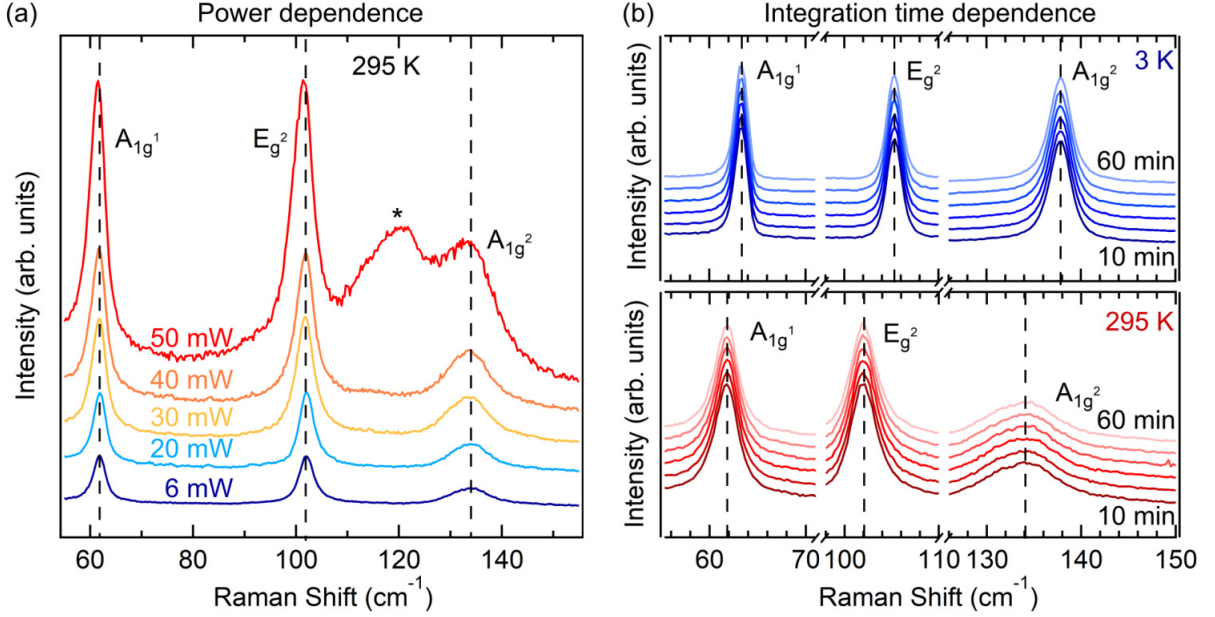


**Figure 4.2:** Exclusion of laser induced damage on the  $\text{Bi}_2\text{Te}_3$  thin film sample. (a) Laser power dependent Raman spectra acquired at room temperature. All spectra acquired with identical integration times and displayed with an offset. Dashed lines correspond to the modes frequencies acquired with 6 mW. An additional mode induced by sample damage is marked by an asterisk. (b) Raman spectra acquired with a laser power of 6.2 mW over 60 min at 3 K (upper panel) and 295 K (lower panel). Selected spectra of every 10 min increment are chosen and sorted from bottom to top with increasing integration time. Spectra are normalized to the  $A_{1g}^1$  mode and displayed with an offset. Adapted with permission from<sup>[78]</sup>. Copyright 2020 by the American Physical Society.

The profiles include the line width  $\Gamma_{G,L}$  of both Gaussian and Lorentzian profiles, as well as the phonon frequency  $\omega_0$  and integrated area  $A$  of the Lorentzian. Due to the narrow line widths of the Raman modes close to the spectrometer resolution of  $\Gamma_G = 1.44 \pm 0.1 \text{ cm}^{-1}$ <sup>[77]</sup> this deconvolution was necessary to accurately determine the contributing width of the Lorentzian and deduct correct phonon decay mechanisms. For the analysis of macro-Raman measurements, the Voigt profile was employed to fit all Raman and additional appearing IR-active modes. In the temperature dependent study, fitting of additional IR-active modes was included for spectra acquired up to temperatures of 220 K for  $\text{Bi}_2\text{Se}_3$  and 100 K for  $\text{Bi}_2\text{Te}_3$ . At higher temperatures only the bulk Raman modes were fit due to decreased intensity of the IR-active modes as explained in section 3.1.6. The coherent use of the Voigt fit function for  $\text{Bi}_2\text{Se}_3$  and  $\text{Bi}_2\text{Te}_3$  allows for a direct comparison between the two materials and application of similar models in temperature and magnetic field dependence. In addition, it has to be noted that a weak asymmetry in the Raman modes of  $\text{Bi}_2\text{Se}_3$  are recorded that are not sufficiently described using a Lorentzian response function. However, the asymmetry in the modes is very subtle as is discussed in detail in section 4.4 and, therefore, Voigt fits were employed to extract all mode frequencies and line widths and describe the renormalization with temperature and magnetic field strength.

## 4.4 Results - Temperature dependence

Temperature dependent Raman spectra of the  $\text{Bi}_2\text{Se}_3$  and  $\text{Bi}_2\text{Te}_3$  samples in thin film geometry were acquired for 30 different temperatures in the range between 3 K to 300 K. Particularly at low temperatures very narrow temperature increments of 3 K were chosen between 3 K to 30 K, followed by 10 K step sizes up to a temperature of 100 K. At higher temperatures up to room temperature broader step sizes of 20 K were sufficient to track the temperature dependence. In Figure 4.3(a) all acquired Raman spectra as a function of temperature are displayed. Figure 4.3(b) shows selected Raman spectra at 3 K, 120 K, and 300 K.

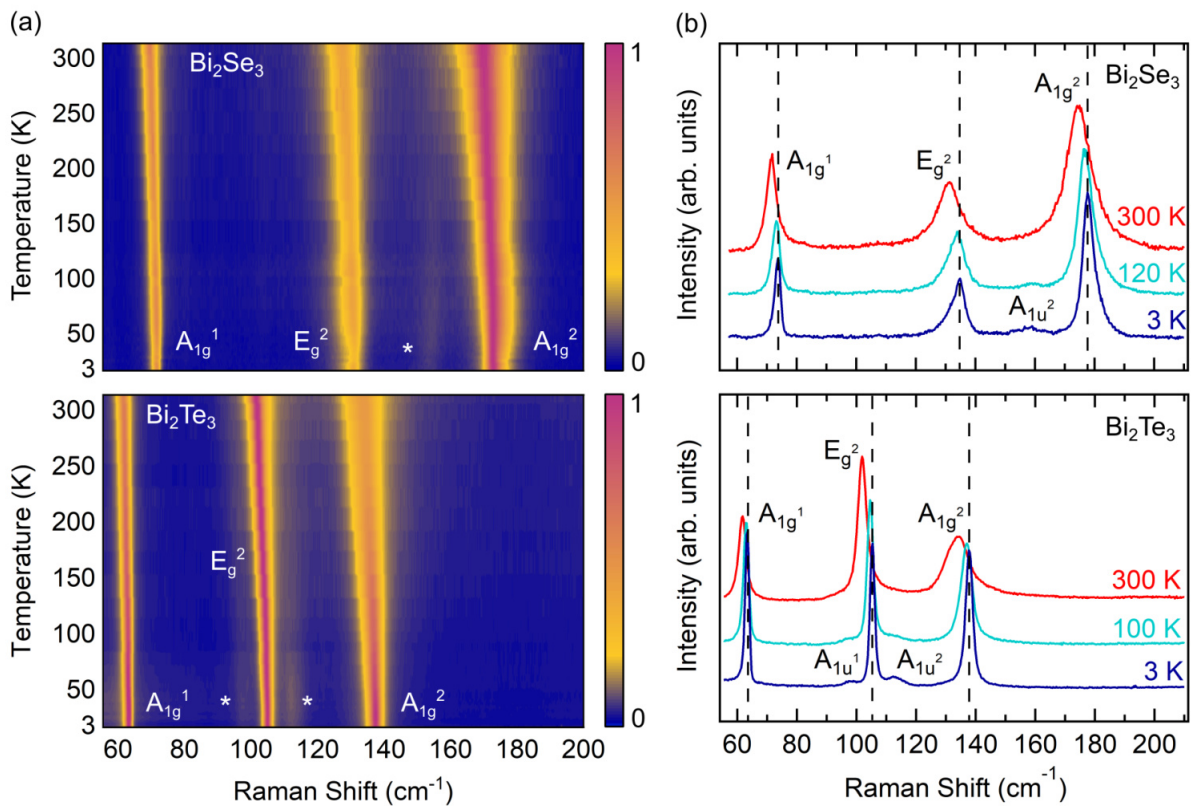


**Figure 4.3:** (a) Temperature dependent Raman spectra of the thin films samples acquired between 3 K to 300 K. Displayed spectra are normalized to the highest intensity mode, which was the  $A_{1g}^2$  and the  $E_g^2$  mode for  $\text{Bi}_2\text{Se}_3$  and  $\text{Bi}_2\text{Te}_3$ , respectively. IR-active modes are labeled by asterisks. (b) Raman spectra of three selected temperatures displayed with an offset to show the presence of the labeled IR-active  $A_{1u}^1$  and  $A_{1u}^2$  modes up to elevated temperatures.

### 4.4.1 Mode symmetry analysis

At all temperatures the three high energy bulk phonon modes of  $A_{1g}^1$ ,  $E_g^2$  and  $A_{1g}^2$  symmetry are detected as apparent from Figure 4.3(a). The symmetry of the modes was confirmed by polarization dependent measurements at 3 K that are shown in Figure 4.4. As



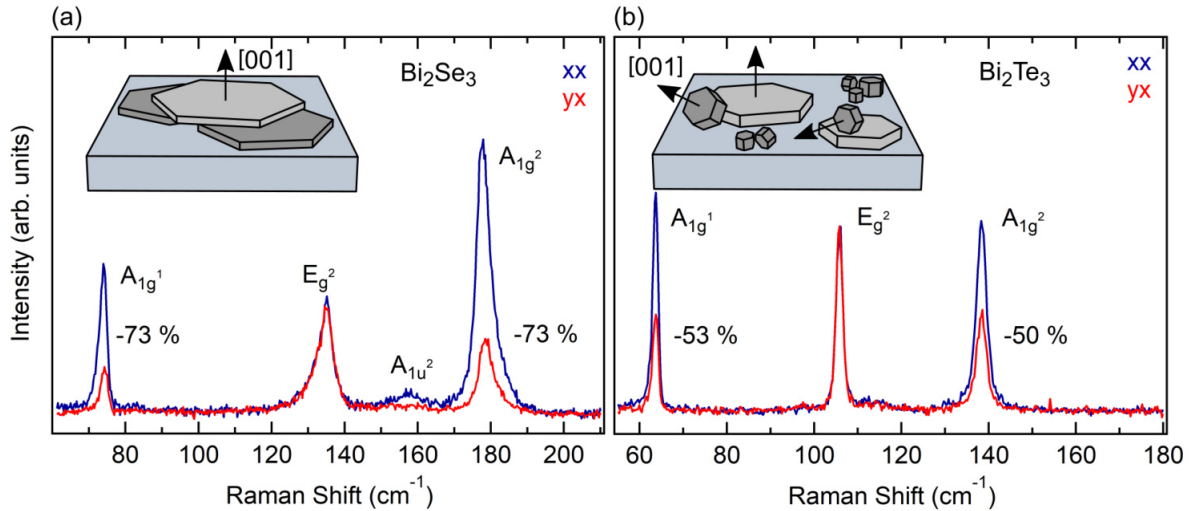


**Figure 4.4:** Polarization dependence of modes from (a)  $\text{Bi}_2\text{Se}_3$  and (b)  $\text{Bi}_2\text{Te}_3$  thin film samples recorded in parallel (xx) and cross (yx) polarization configuration. Spectra were normalized to the  $E_g^2$  mode. The insets give a schematic representation of the investigated NFs with the black arrows marking the [001] orientation of the crystal facets. The simplified illustration explains the higher residual intensities of  $A_{1g}$  modes in cross polarization configuration for  $\text{Bi}_2\text{Te}_3$  due to the stronger anisotropy in oriented NFs.

expected from the polarization dependence of the corresponding Raman tensors, explained in section 3.1.6, the intensity of modes with  $A_{1g}$  symmetry is decreased in cross polarization configuration, whereas the intensity of the  $E_g$  mode is constant for both configurations. This can be observed in the red graphs in Figure 4.4 for both materials with a reduction of the  $A_{1g}$  mode intensities of about 70% in  $\text{Bi}_2\text{Se}_3$  and about 50% in  $\text{Bi}_2\text{Te}_3$ . The residual signal of the  $A_{1g}$  modes in cross polarization is owed to the investigated sample geometry. The overlapping NFs of course differ in their relative orientation to the incoming laser polarization, which leads to the illumination of different crystal facets. However, the Raman selection rules given in section 3.1.6 were calculated for one particular orientation of the principal axes of the crystal relative to the incoming laser polarization.<sup>[85]</sup> The random orientation and tilted surfaces of the manifold of illuminated NFs hence are in part not subject to the given rules and lead to a leakage of Raman signal. The lower reduction of  $A_{1g}$  modes in  $\text{Bi}_2\text{Te}_3$  is caused by a higher amount of smaller bulk like cubes, see also Figure 4.1(e). The cube-like  $\text{Bi}_2\text{Te}_3$  NFs can be oriented in any direction due to their 3D nature as illustrated in the insets of Figure 4.4(b) and, therefore, contribute Raman intensity in both scattering geometries.

#### 4.4.2 Inversion symmetry breaking in 2D NFs observable at low temperatures

Besides the three bulk Raman modes, additional weaker modes are detected in both  $\text{Bi}_2\text{Se}_3$  and  $\text{Bi}_2\text{Te}_3$ . These are assigned to bulk IR-active phonons that become Raman-active in

ultrathin samples due to a broken inversion symmetry at the surfaces of the samples, as explained in section 3.1.6. In  $\text{Bi}_2\text{Te}_3$  additional modes at  $97.7\text{ cm}^{-1}$  and  $112.6\text{ cm}^{-1}$  are detected for all lower temperatures up to 100 K that show good agreement with the bulk IR modes of  $A_{1u}^1$  and  $A_{1u}^2$  symmetry, respectively, see Table A.1 and references therein. The assignment of the weaker modes to bulk IR modes of A symmetry was originally motivated by the idea that the out-of-plane  $A_{1u}$  vibrations would be affected more strongly by the reduced crystal symmetry in  $c$ -direction as argued in literature.<sup>[119]</sup> However, our recent studies have shown that also bulk IR modes of  $E_u$  symmetry are more strongly detected in ultrathin samples as shown in detail in section 5.5.<sup>[129]</sup> The bulk IR  $E_u^2$  mode in  $\text{Bi}_2\text{Te}_3$  has a very similar room temperature frequency of  $95\text{ cm}^{-1}$  in comparison to the  $A_{1u}^1$  mode at  $94\text{ cm}^{-1}$ <sup>[22]</sup>, see also the phonon dispersion curve in Figure 3.5(b) and Table A.1. This impedes the explicit assignment of the IR mode symmetry to the observed mode in our  $\text{Bi}_2\text{Te}_3$  thin film samples around  $97.7\text{ cm}^{-1}$ . Nevertheless, the distinction of the IR modes from the enclosed  $E_g^2$  mode at  $105.3\text{ cm}^{-1}$  is easily made due to the very narrow line width of the  $E_g^2$  bulk mode at 3 K (see orange graphs in Figure 4.5(b) for  $\text{Bi}_2\text{Te}_3$ ).

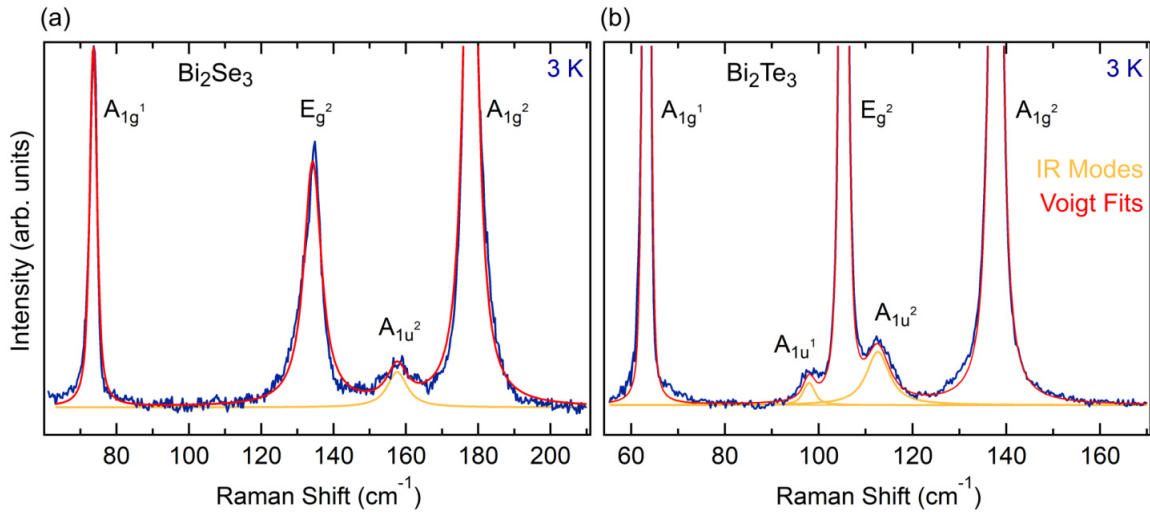


**Figure 4.5:** Enlarged view of the background subtracted Raman spectra showing the IR Modes in  $\text{Bi}_2\text{Se}_3$  and  $\text{Bi}_2\text{Te}_3$ . From the fit of Voigt profiles (red) for all modes the deconvoluted profiles corresponding to the IR modes (orange) are shown.

In the case of  $\text{Bi}_2\text{Se}_3$ , however, only one bulk IR mode of  $A_{1u}^2$  symmetry at  $158\text{ cm}^{-1}$  can be assigned with certainty, see Figure 4.5(a), and is detected up to even higher temperatures of 160 K. The  $E_u^2$  and  $A_{1u}^1$  mode cannot be identified for certain due to their very similar frequency compared to the bulk Raman  $E_g^2$  mode (see Table A.2). However, the detection of those modes in the  $\text{Bi}_2\text{Te}_3$  sample suggests that they in principle should also appear in the  $\text{Bi}_2\text{Se}_3$  spectra but might be covered by the much stronger bulk  $E_g^2$  phonon. This is supported by the fact that the IR active  $E_u^2$  mode has been recently identified in Raman measurements on ultrathin NFs, as shown in section 5.5.



The detection of IR active modes up to 160 K and 100 K in the  $\text{Bi}_2\text{Se}_3$  and  $\text{Bi}_2\text{Te}_3$  samples, respectively, underlines the high surface-to-bulk ratio of the examined NFs and shows how the surface properties of the NFs start to dominate at lower temperatures. The fact that the IR modes can be observed in  $\text{Bi}_2\text{Se}_3$  up to higher temperatures compared to  $\text{Bi}_2\text{Te}_3$  again shows the higher amount of bulk-like structures in  $\text{Bi}_2\text{Te}_3$ , whose bulk properties dominate earlier with respect to temperature over the surface contribution.

### 4.4.3 Temperature dependent self-energy effects

To investigate the phonon dynamics in  $\text{Bi}_2\text{Se}_3$  and  $\text{Bi}_2\text{Te}_3$  thin film samples the mode frequency shifts and line widths are analyzed as a function of temperature. The parameters extracted from Voigt fits are given in Figure 4.6 for the three bulk phonons of  $A_{1g}^1$ ,  $E_g^2$  and  $A_{1g}^2$  symmetry for  $\text{Bi}_2\text{Se}_3$  (left column) and  $\text{Bi}_2\text{Te}_3$  (right column).

All modes show a general softening of mode frequency and broadening in line width as the temperature increases. The frequency shift in the range between 3 K to 300 K is very subtle for both materials, with the low-frequency  $A_{1g}^1$  mode only experiencing a decrease of  $2 \text{ cm}^{-1}$ , and the  $E_g^2$  and  $A_{1g}^2$  mode shifting by  $3 \text{ cm}^{-1}$ . In first approximation, the high temperature behavior of mode frequencies is described by a linear decrease that accounts for the lattice thermal expansion according to section 3.1.5. To compare the temperature dependence of our thin film samples with reference literature, the linear frequency dependence between 90 K to 300 K is readily fit by Equation (3.26) to determine the first-order thermal expansion coefficient  $\chi^{\text{th}}(T)$ . The linear fits at elevated temperatures are shown in the appendix in Figure C.1 as solid red graphs. Our determined temperature coefficients for the thin film samples are in the same order of magnitude in comparison with values obtained from bulk crystals, thin films, and NF samples as shown in Table 4.1. However, in  $\text{Bi}_2\text{Se}_3$  for all three modes the frequency decreases about 40% slower than compared to ref.<sup>[81,130]</sup>. Since the first-order temperature coefficient can be related to the thermal conductivity<sup>[144]</sup> this indicates a reduced thermal conductivity as expected by the high amount of grain boundaries between the attached  $\text{Bi}_2\text{Se}_3$  2D NFs.

The linear change at higher temperatures is described by the thermal expansion of the volume crystal but is not sufficient to describe the low temperature ( $T < 120 \text{ K}$ ) frequency dependence. To get an accurate description of the frequency and line width across the entire temperature range additional contributions arising from phonon-phonon interactions via the anharmonic lattice potential have to be considered. Depending on the available decay channels for the phonon, there exist different models to account for the phonon-phonon interactions as described in detail in section 3.1.5. For the presented data the symmetrical three-phonon model is chosen that assumes a symmetric decay of the optical phonon into two acoustic phonons of equal frequency and opposite momenta. Within this anharmonic decay (AD) model, also referred to as the Klemens decay channel, the frequency and line width are modeled by Equation (3.34) and Equation (3.35).

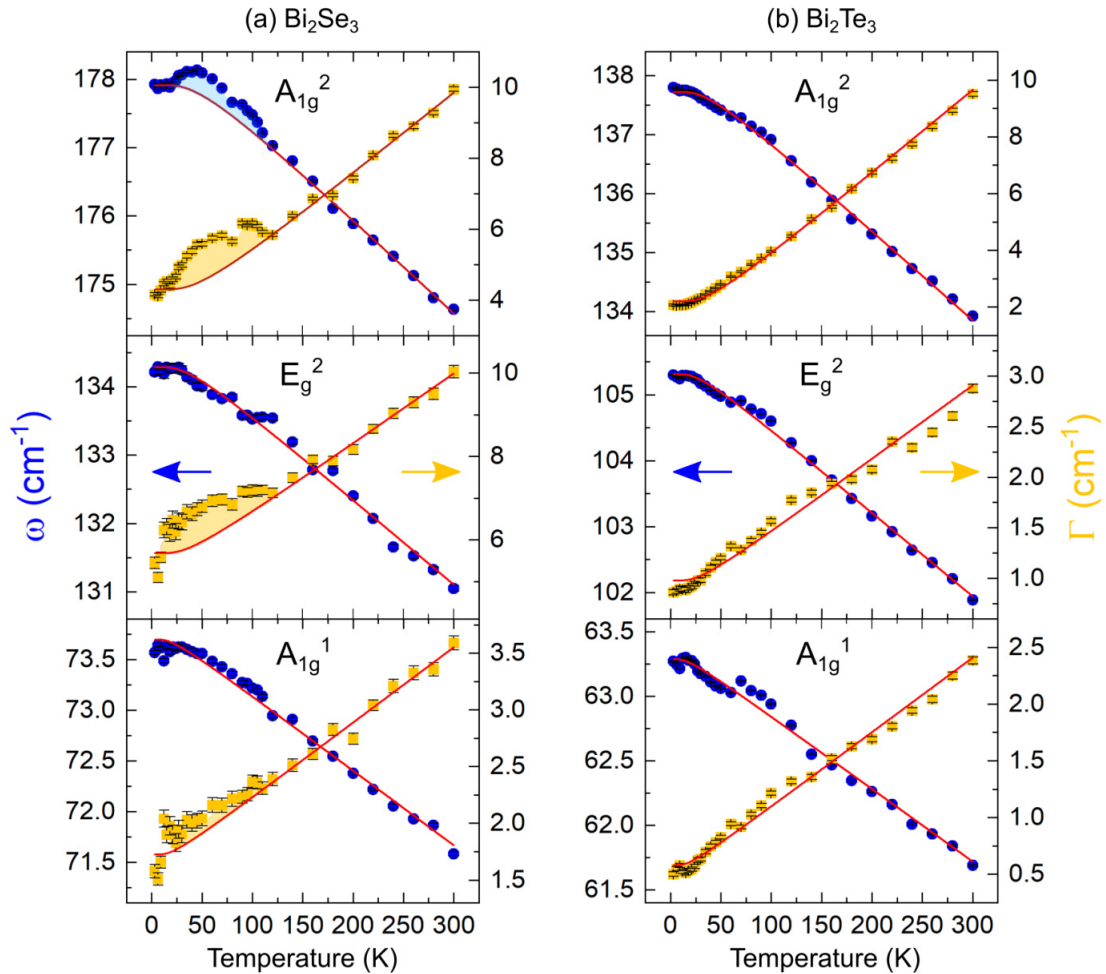


**Figure 4.6:** Temperature dependent self-energy effects of the three bulk Raman modes of the (a)  $\text{Bi}_2\text{Se}_3$  and (b)  $\text{Bi}_2\text{Te}_3$  sample. All modes experience a red-shift in frequency (left axes, blue circles) and broadening in line width (right axes, orange squares) with increasing temperature. The self-energy effects are fit by a symmetric anharmonic decay model, according to section 3.1.5, shown as red graphs. For  $\text{Bi}_2\text{Te}_3$  the model fits well to the data, whereas for  $\text{Bi}_2\text{Se}_3$  clear deviations are observed below 120 K especially for the high-energy modes. Adapted with permission from<sup>[78]</sup>. Copyright 2020 by the American Physical Society.

The AD fits, given as red graphs in Figure 4.6(b), show excellent agreement with the obtained data for  $\text{Bi}_2\text{Te}_3$ . The  $\text{Bi}_2\text{Te}_3$  data was fit in the whole temperature range and fit parameters are listed in Table C.1. This indicates that the phonon dynamics in  $\text{Bi}_2\text{Te}_3$  are readily described by the employed model and are thus dominated by phonon-phonon interactions as the prominent scattering mechanism. The resolution limited line widths down to  $0.5 \text{ cm}^{-1}$  for the  $A_{1g}^1$  mode represent long lifetimes of the phonons in  $\text{Bi}_2\text{Te}_3$  underlining the high crystallinity of the investigated sample. Together with the dominant phonon-phonon interactions and reduced polarization sensitivity, this demonstrates a more bulk-like behavior for the  $\text{Bi}_2\text{Te}_3$  sample. This is most likely induced by the high amount of smaller cubic NFs with a bulk character that are present in the sample next to the 2D NFs (see Figure 4.1(e) for comparison).

In comparison to  $\text{Bi}_2\text{Te}_3$ , the temperature dependence of mode frequencies and line widths in  $\text{Bi}_2\text{Se}_3$  is not well described by the chosen model regardless of different fit procedures and fit ranges as further detailed in appendix C.1.2. The fit parameters corresponding to the AD fits given in Figure 4.6(a) are listed in Table C.1. In particular, below 120 K the line widths of all Raman modes show higher values than anticipated by the symmetrical AD model as shown in Figure 4.6(a). For the low-energy  $A_{1g}^1$  mode the deviations are the smallest compared to the higher energy  $E_g^2$  and  $A_{1g}^2$  modes that show very strong discrepancies. For the  $A_{1g}^2$  phonon the deviations in line width are further mirrored in frequency that also exhibit higher values than described by the fit. The correlation between frequency and line width is expected for changes in the phonon-phonon coupling coefficient due to the Kramers-Kronig relation as explained in section 3.1.5. In comparison with literature, such significant deviations in the low temperature range have not been reported before when conducting temperature dependent measurement on single crystal samples.<sup>[81,101]</sup> This indicates to an origin of additional decay channels arising from the enhanced surface contribution of the investigated NFs. Especially the broad line widths at low temperatures show the need for an extended model that includes further possible decay channels.

**Table 4.1:** Thermal expansion coefficients  $\chi^{\text{th}}$  of  $\text{Bi}_2\text{Se}_3$  and  $\text{Bi}_2\text{Te}_3$  samples with various geometries. The temperature range for the linear fits is given in brackets.

Reference	sample	$\chi^{\text{th}} (10^{-2} \text{ cm}^{-1})$		
		$A_{1g}^1$	$E_g^2$	$A_{1g}^2$
<b><math>\text{Bi}_2\text{Se}_3</math></b>				
our work (90–300 K)	NFs in thin film geometry	-0.80	-1.28	-1.44
Kim <i>et al.</i> <sup>[101]</sup> (90–300 K)	bulk crystal			-1.5
Irfan <i>et al.</i> <sup>[81]</sup> (83–523 K)	bulk crystal	-1.44	-1.94	-1.95
Zhou <i>et al.</i> <sup>[130]</sup> (83–603 K)	single NF	-1.26	-1.39	-2.36
<b><math>\text{Bi}_2\text{Te}_3</math></b>				
our work	NFs in thin film geometry	-0.63	-1.34	-1.52
Li <i>et al.</i> <sup>[131]</sup> (240–513 K)	4 $\mu\text{m}$ films		-1.37	

#### 4.4.4 Self-energy corrections by electron-phonon interactions

Until now only anharmonic interactions between phonons were considered for the corrections in the phonon self-energy. However, according to the Matthiessen rule (Equation (3.31)), additional interactions to magnetic or electronic excitations can lead to further decay channels of the phonons and an increase in the phonons line width. Since  $\text{Bi}_2\text{Se}_3$  is a non-magnetic material this strongly suggests the presence of a low-energy electronic susceptibility coupling to the phonons and leading to the decay of phonons by the creation of electron-hole pairs.<sup>[145,146]</sup> This aspect is justified by the fact that the deviations in line width start to set in at temperatures below 120 K where phonons are frozen out. Therefore, contributions from additional anharmonic decay processes with the phonon decaying into various combinations of optical and acoustic phonons are ruled out. Secondly, an increased electronic density at the Fermi-level of the  $\text{Bi}_2\text{Se}_3$  thin films was verified using X-ray photoelectron spectroscopy (XPS)<sup>[78]</sup>, which indicates an available low-energy electronic susceptibility and verifies possible low-energy electron-phonon (el-ph) interactions.

The coupling of phonons to an electric susceptibility  $\chi_{el}$  in the phonons frequency range leads to an enhanced contribution of the non-resonant Raman matrix element as explained in section 3.1.2. The Raman response determined by el-ph interactions is given by Equation (3.19):

$$I(\omega) \propto T_{A_2}^2 g^2 \frac{\Gamma\omega - g^2\pi_{im}}{\underbrace{(\omega^2 - \omega_0^2 - g^2\pi_{re})^2}_{\omega_{0,\text{exp}}^2} + \underbrace{(\Gamma\omega - g^2\pi_{im})^2}_{\Gamma_{\text{exp}}\omega}}, \quad (4.4)$$

where Equation (3.16) and Equation (3.17) were inserted. This response describes a Lorentzian line shape with the phonon frequency  $\omega_0$  and line width  $\Gamma$  expected according to the AD model experiencing renormalization. Hereby, both the real and imaginary part of the susceptibility contribute to the phonons self-energy, where the real part  $\pi_{re}$  modifies the frequency and the imaginary part  $\pi_{im}$  modifies the line width. As a result, the frequencies  $\omega_{0,\text{exp}}$  and line widths  $\Gamma_{\text{exp}}$  determined experimentally via Lorentzian fits of the phonons, deviate from the values expected for mere anharmonic coupling,  $\omega_{0,\text{anh}}$  and  $\Gamma_{\text{anh}}$ . The self-energy corrections for values expected from an AD model are thereby given as:

$$\omega_{0,\text{exp}} = \sqrt{\omega_{0,\text{anh}}^2 + g^2\pi_{re}} \quad (4.5)$$

$$\Gamma_{\text{exp}} = \Gamma_{\text{anh}} - g^2 \frac{\pi_{im}}{\omega}. \quad (4.6)$$

where the indices *anh* have been introduced for the not-renormalized values corresponding to the anharmonic decay model. The renormalization of the phonons depends (a) on the frequency  $\omega_{el}$  of the electric susceptibility, which determines the relative positioning of  $\chi_{el}$  to the phonon, and (b) on the electron-phonon coupling strength  $g$ .

In Bi<sub>2</sub>Se<sub>3</sub> the extracted line widths at temperatures below 120 K are higher for all three phonons as anticipated by the AD model (see Figure 4.6(a)). These strong deviations, especially in the E<sub>g</sub><sup>2</sup> and A<sub>1g</sub><sup>2</sup> modes, indicate a coupling to the imaginary part of an electric susceptibility in the meV range. For a negative  $\pi_{im}$  the line widths are expected to broaden according to Equation (4.6), which is observed for all three modes. The pronounced line width corrections in the two higher frequency phonons compared to the low-frequency A<sub>1g</sub><sup>1</sup> mode indicate an enhanced contribution of  $\pi_{im}$  in the frequency range between 130 cm<sup>-1</sup> to 180 cm<sup>-1</sup> (16 meV to 22 meV, accordingly). Assuming that all phonons couple to the same electric susceptibility, the renormalization in frequency can be explained by examining the real part  $\pi_{re}$ . For the E<sub>g</sub><sup>2</sup> phonon the strong renormalization in line width but none in frequency can be explained by an electronic susceptibility with an energy around 16 meV as shown in Figure 4.7(a). The change of sign in  $\pi_{re}$  in the frequency range of the E<sub>g</sub><sup>2</sup> phonon would only lead to a vanishing renormalization in frequency but significant broadening of the line width by a finite  $\pi_{im}$ . For a vanishing contribution of  $\pi_{re}$  the E<sub>g</sub><sup>2</sup> frequency would show a temperature dependence readily described by the anharmonic interactions, as is indeed evident from Figure 4.6(b). Following this approach, the A<sub>1g</sub><sup>2</sup> mode around 22 meV would couple to a positive  $\pi_{re}$  and experience a frequency renormalization to higher frequencies according to Equation (4.5) and additional broadening due to coupling to  $\pi_{im}$ . These renormalizations fit to the observed deviations below 120 K for the A<sub>1g</sub><sup>2</sup> mode, shown in Figure 4.6(a). In Figure 4.7(a) the renormalization of the E<sub>g</sub><sup>2</sup> and A<sub>1g</sub><sup>2</sup> mode is shown exemplarily and was calculated using the renormalized Lorentzian function of Equation (4.4). The unperturbed phonons, depicted in gray, experience frequency shifts and broadening by coupling to an electric susceptibility around 16 meV.

To describe the deviations from the AD model as shown in Figure 4.6(a) we hence propose an electric susceptibility in the frequency range of 16 meV that couples to the E<sub>g</sub><sup>2</sup> and A<sub>1g</sub><sup>2</sup> phonons. The model of contributing el-ph interactions is strongly supported by the significant deviations setting in at lower temperatures, where possible phonon-phonon interactions can be ruled out. We can identify two temperature regions that are characterized by different dominant decay mechanisms as indicated in Figure 4.7(b). At higher temperatures above 120 K the number of available phonons leads to dominant phonon-phonon interactions. Therefore, the data follows the classic model of an anharmonic decay and shows good agreement with temperature behavior observed for bulk samples.<sup>[81,101,102]</sup> For temperatures below 120 K the el-ph coupling becomes significant and leads to additional phonon self-energy corrections. The coupling to a low-energy electric susceptibility is further justified by calculations of Heid *et al.* that reveal enhanced el-ph interactions for phonons within an energy range between 17 meV to 22 meV.<sup>[147]</sup> They identify dominant coupling for optical phonons with polar character, while Raman-active phonons in the same frequency range experience weaker coupling. However, due to our high resolution we were able to resolve even this coupling in our study. The determined coupling strengths are in good agreement with our measurements, where we identify no additional renormalizations for the low-energy A<sub>1g</sub><sup>1</sup> phonon at 9 meV but strong renormalizations in the higher energy

$E_g^2$  (16.7 meV) and  $A_{1g}^2$  (21.9 meV) phonons.

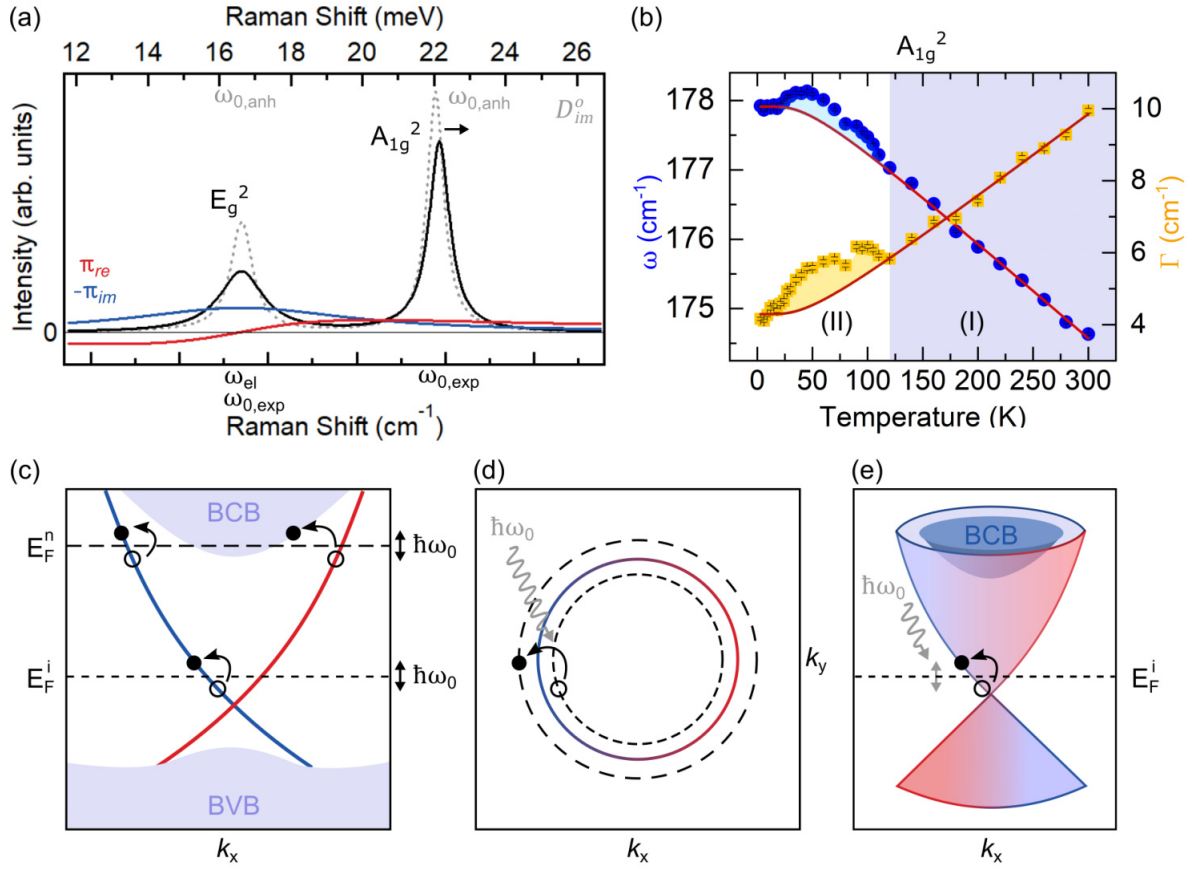


**Figure 4.7:** (a) Phonon renormalization of the  $E_g^2$  and  $A_{1g}^2$  modes by electron-phonon coupling to an overdamped low-frequency electric susceptibility  $\chi_{el}$ . The imaginary part of the bare phonon propagators  $D_{im}^o$  with frequencies and line widths as expected from the AD fits are shown. The black graphs show the renormalized phonon modes by coupling to the indicated real  $\pi_{re}$  and imaginary part  $\pi_{im}$  of  $\chi_{el}$ . (b) Renormalization of the  $A_{1g}^2$  phonon and indicated temperature ranges with different dominating decay channels. Adapted with permission from<sup>[78]</sup>. Copyright 2020 by the American Physical Society. (c) Schematic band structure of  $\text{Bi}_2\text{Se}_3$  with two possible low-energy electronic intraband transitions available for electron-phonon coupling. The decay process is shown for two possible locations of the Fermi level for intrinsic ( $E_F^i$ ) and  $n$ -doped ( $E_F^n$ )  $\text{Bi}_2\text{Se}_3$  nanoflakes. Excitation of an electron-hole pair by the absorption of a phonon. (d) Possible el-ph scattering mechanism in the  $k_{\parallel}$  plane for intrinsic  $\text{Bi}_2\text{Se}_3$  with  $E_F^i$ . (e) Low-energy electronic transitions in the Dirac cone coupling to the phonon.

In the following section, two possible low-energy electronic transitions available for el-ph scattering are discussed. Due to the low phonon energy in the range of 16 meV to 22 meV the decay via coupling to an electric susceptibility is strongly limited to intraband transitions as the energy of bulk interband transitions in  $\text{Bi}_2\text{Se}_3$  is at least 300 meV. The creation of an electron-hole pair by the emission (Stokes) or absorption (Anti-Stokes) of a phonon is, therefore, restricted to a narrow energy and momentum space provided by the phonon. Depending on the Fermi level position in  $\text{Bi}_2\text{Se}_3$  this results in two possible el-ph scattering processes as depicted in Figure 4.7(c). Firstly, for intrinsic single-crystalline  $\text{Bi}_2\text{Se}_3$  the

Fermi level lies within the bulk band gap and crosses the Dirac cone.<sup>[21]</sup> As long as the Fermi level is positioned in the gap, only intraband scattering of the topological surface states is allowed, as shown in Figure 4.7(e). In the Dirac cone the creation of electron-hole pairs further has to obey spin conservation due to the present spin-momentum locking. This restricts the probability for an el-ph scattering process involving the Dirac cone to a narrow momentum space as indicated in Figure 4.7(d).<sup>[148]</sup> Since the phonons involved in the Raman scattering process have very small momenta, as they are generated close to the Brillouin zone center, their probability for intraband scattering in the topological surface states is very likely. In addition, the el-ph coupling strength increases linearly with a rising energy distance of the Fermi level to the Dirac point. This is due to the increasing density of states in the topological surface states as expected for a 2D Dirac dispersion.<sup>[147]</sup>

The second possible el-ph scattering process is available for highly  $n$ -doped  $\text{Bi}_2\text{Se}_3$  samples where the Fermi level crosses the bulk conduction bands, also shown in Figure 4.7(c). A native  $n$ -doping is frequently reported for  $\text{Bi}_2\text{Se}_3$  that arises during crystal growth as a result of Se vacancies<sup>[33]</sup> or in ambient conditions by surface passivation<sup>[37,44,134]</sup>. In this condition, both intraband scattering of the topological surface states as well as decay into the trivial bulk states are possible. It was shown by Heid *et al.*<sup>[147]</sup> that the coupling constant of electronic states in the upper Dirac cone is enhanced once the Fermi level is raised into the BCB due to additional contributions from interband coupling. In addition to intra-cone scattering the states can then also decay into the first bulk conduction band as depicted in Figure 4.7(c).

The hypothesis of the  $\chi_{\text{el}}$  originating from the topological surface states is justified by the following aspects: (i) The enhanced surface contribution of the  $\text{Bi}_2\text{Se}_3$  NFs was verified by the detection of the IR modes in Raman spectra at low temperatures up to 120 K. (ii) In previous temperature dependent studies on bulk samples no el-ph self-energy corrections were identified. This can be related to the dominating bulk properties of the investigated samples, where the Fermi level residing in the bulk band gap, and the lack of any states within the gap, do not allow for any el-ph scattering processes. Therefore, our observed phonon renormalizations must be connected to the enhanced surface contribution, which in turn points to the connection of  $\chi_{\text{el}}$  to transitions involving the Dirac cone. The observation of el-ph interactions is thus a result of the increased amount of TSS by the manifold of high aspect ratio NFs.

In conclusion, additional phonon self-energy contributions below 120 K in  $\text{Bi}_2\text{Se}_3$  are ascribed to dominating el-ph interactions that can be explained by phonon renormalizations according to the model of coupling to electronic intraband transitions. The low-energy electric susceptibility is justified to be provided by the topological surface states, which is further validated in the following magnetic field dependent study.

## Temperature dependence reveals

- enhanced surface contribution identified by pronounced detection of Raman-active IR phonons in  $\text{Bi}_2\text{Te}_3$  and  $\text{Bi}_2\text{Se}_3$  for  $T < 100$  K and  $T < 160$  K, respectively
- dominant bulk character of  $\text{Bi}_2\text{Te}_3$  following the symmetric anharmonic decay model
- deviations from the anharmonic decay model in  $\text{Bi}_2\text{Se}_3$  for  $T < 120$  K
- additional self-energy corrections in  $\text{Bi}_2\text{Se}_3$  readily ascribed to el-ph coupling to a low-energy  $\chi_{\text{el}}$  between 15 meV to 22 meV, which can be related to the Dirac surface states

## 4.5 Results - Magnetic field dependence

To investigate the change in phonon behavior with magnetic field strength, Raman spectra of the  $\text{Bi}_2\text{Se}_3$  and  $\text{Bi}_2\text{Te}_3$  thin film samples were acquired while increasing the field strength from 0 T to 7 T in increments of 1 T. The measurements were conducted at a temperature of 3 K where the el-ph interactions are expected to dominate over the anharmonic interactions. The field was applied in Faraday geometry, as explained in section 3.2.1, and the incident laser was horizontally polarized (x-). In Figure 4.8 all background corrected spectra are displayed. Due to the sample environment of 3 K the bulk IR-active modes of  $A_{1u}$  symmetry are observed for both materials at all magnetic field strengths and were hence included during the fits.

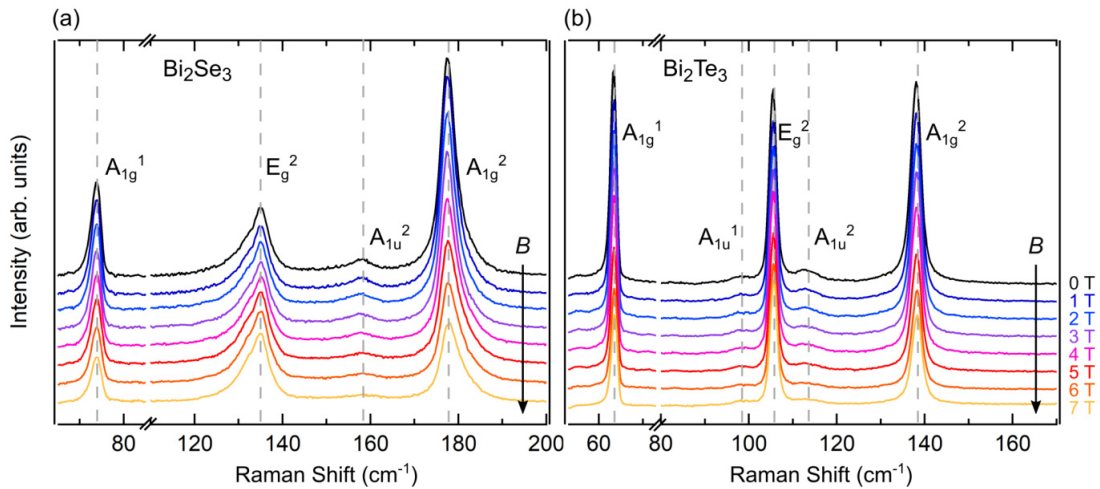


**Figure 4.8:** Background corrected Raman spectra acquired with magnetic field strengths from 0 T to 7 T of (a)  $\text{Bi}_2\text{Se}_3$  and (b)  $\text{Bi}_2\text{Te}_3$  nanoflake samples in thin film geometry. All spectra were recorded at 3 K in Faraday configuration and are displayed with an offset.



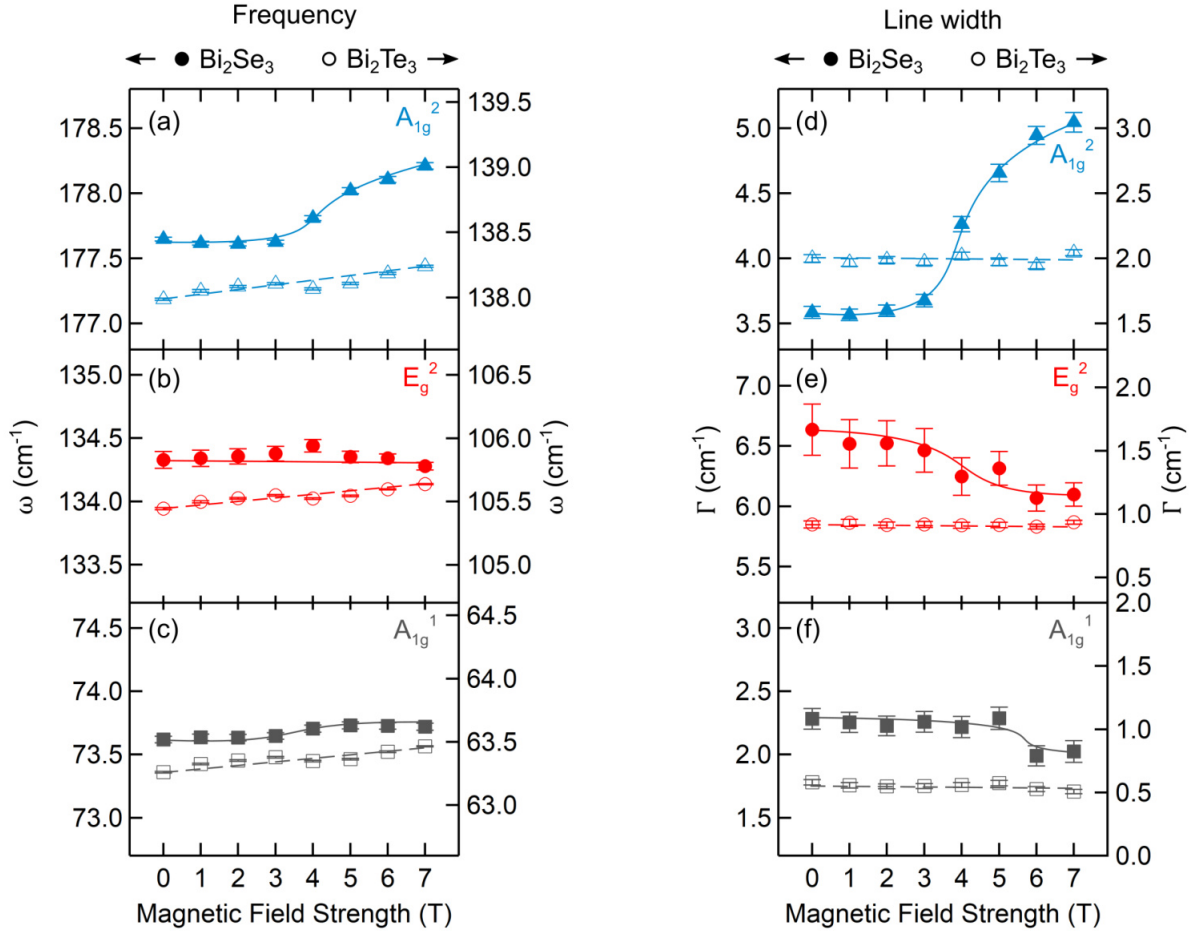


**Figure 4.9:** Magnetic field strength dependent self-energy effects of the frequency (a-c) and line width (d-f) of the three bulk phonon modes. Parameters were obtained from Voigt fits and are displayed as filled markers for  $\text{Bi}_2\text{Se}_3$  and open markers for  $\text{Bi}_2\text{Te}_3$ . The left and right  $y$ -axes in both diagrams correspond to the values for  $\text{Bi}_2\text{Se}_3$  and  $\text{Bi}_2\text{Te}_3$ , respectively, as indicated by the arrows. All  $y$ -axes are set to intervals of  $2\text{ cm}^{-1}$  for a direct comparison between the two materials.  $\text{Bi}_2\text{Te}_3$  modes (dashed guides) show no significant change with field strength.  $\text{Bi}_2\text{Se}_3$  modes (solid guides) exhibit pronounced renormalizations above 3 T especially in the  $A_{1g}^2$  mode in (a,d). Adapted with permission from<sup>[78]</sup>. Copyright 2020 by the American Physical Society.

To reveal any changes in the electronic band structure while tuning the field strength, especially in the Dirac cone, the phonon renormalizations of the three bulk Raman modes are analyzed in Figure 4.9. The frequencies and line widths were extracted from Voigt profiles of the  $A_{1g}^1$ ,  $E_g^2$  and  $A_{1g}^2$  modes. For  $\text{Bi}_2\text{Te}_3$  no changes in all phonon frequencies and line widths (open markers in Figure 4.9) are observed with minimal deviations of only  $0.2\text{ cm}^{-1}$  from the average values. The constant phonon self-energies with field strength demonstrate no changes or additional contributions from el-ph interactions. This again suggests a dominating bulk behavior for the phonons in  $\text{Bi}_2\text{Te}_3$ , as already evident from the temperature dependent data. The surface contribution of the  $\text{Bi}_2\text{Te}_3$  NF sample is not strong enough to resolve any modulations in the band structure with increasing field strengths. The here presented data cannot rule out a gap opening in the Dirac

cone in  $\text{Bi}_2\text{Te}_3$ , however, in accordance with the temperature dependent study, only bulk dominating effects are observed.

In contrast, there are strong phonon renormalizations clearly observed for  $\text{Bi}_2\text{Se}_3$  at field strengths above 3 T. Especially the  $A_{1g}^2$  mode again shows a simultaneous hardening by  $0.6 \text{ cm}^{-1}$  and broadening by  $1.5 \text{ cm}^{-1}$  (see closed markers in Figure 4.9(a,d)). The changing Raman response with magnetic field gives a clear indication that the self-energy corrections must origin from el-ph interactions as anharmonic interactions are not changed by the presence of a magnetic field. The pronounced renormalization observed in  $A_{1g}^2$  in turn verifies that the self-energy corrections observed at temperatures below 120 K in the temperature study origin from el-ph interactions.

The changing el-ph coupling in  $\text{Bi}_2\text{Se}_3$  with field strengths above 3 T further confirms that the interacting electric susceptibility is modified by the applied magnetic field. While the  $A_{1g}^1$  and  $E_g^2$  modes experience no frequency shift, the hardening and broadening in the  $A_{1g}^2$  phonon implies an increase of the coupling electric susceptibility's real and imaginary part. According to Equation (4.5) and Equation (4.6) the electric susceptibility contributing to the phonon's self-energy hence should experience a shift towards higher energies closer to the energy of the  $A_{1g}^2$  mode. In addition, the narrowing line width in  $E_g^2$  at field strengths above 3 T (Figure 4.9(e)) suggests a reduced coupling to the electric susceptibility and a decrease in  $\pi_{im}$  at the energy of the  $E_g^2$  phonon. It can therefore be argued that above fields of 3 T the electric susceptibility available for el-ph coupling corresponds to an electronic transition with an energy below 22 meV. It seems reasonable to assign this electronic transition to the gap opening in the Dirac cone, which has been previously observed in  $\text{Bi}_2\text{Se}_3$ .<sup>[28,79]</sup> According to the observed self-energy effects in the  $E_g^2$  and  $A_{1g}^2$  mode the energy of the gap opening is estimated to be around 16 meV to

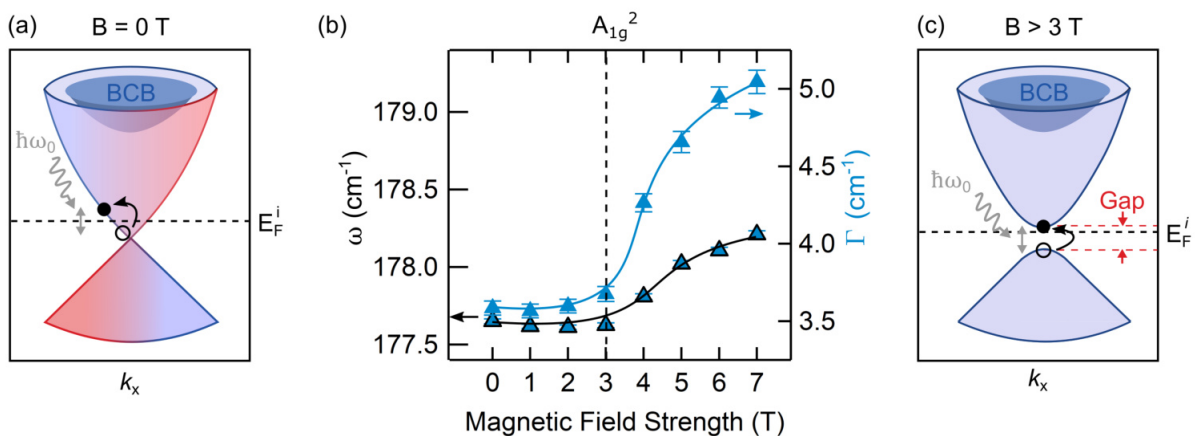


**Figure 4.10:** (a) Coupling of the  $A_{1g}^2$  phonon to the  $\chi_{el}$  of the intact Dirac cone. (b) Frequency  $\omega_0$  (black marker) and width  $\Gamma$  (blue marker) renormalization in the  $\text{Bi}_2\text{Se}_3$   $A_{1g}^2$  phonon mode at magnetic field strengths above 3 T. Solid lines are guides to the eye. (c) Change in the  $\chi_{el}$  related to the Dirac cone by the opening of a gap. The phonon decays by the creation of an electron-hole pair across the gap or vice versa a recombining electron-hole pair creates a phonon.

22 meV, which is in agreement with experimental observations in the order of tens of meV.<sup>[28,79]</sup> Consequently, the self-energy corrections incipient above 3 T are assigned to additional phonon decay channels by coupling to interband transitions across the gapped Dirac cone, as schematically proposed in Figure 4.10(c). The strong self-energy corrections in Bi<sub>2</sub>Se<sub>3</sub> provide clear evidence of the changing electric susceptibility that can only be assigned to the TSS and reinforces the claim of a gapped Dirac cone.

#### Magnetic field dependence reveals

- in Bi<sub>2</sub>Te<sub>3</sub> dominant bulk character with no renormalizations
- in Bi<sub>2</sub>Se<sub>3</sub> strong renormalizations in  $\omega_0$  and  $\Gamma$  for the  $A_{1g}^2$  mode for  $B > 3$  T
- in Bi<sub>2</sub>Se<sub>3</sub> change in the  $\chi_{el}$  coupling to  $A_{1g}^2$  mode, which can be related to a gap opening in the Dirac cone at high magnetic fields

## 4.6 Summary

Altogether, for the Bi<sub>2</sub>Te<sub>3</sub> NFs in thin film geometry prevailing bulk-like properties are detected. The temperature dependence of the three bulk phonon modes in the range of 300 K to 3 K shows very good agreement with the model of a symmetric anharmonic decay indicating dominating bulk phonon dynamics. It is presumed that the higher amount of smaller cube shaped Bi<sub>2</sub>Te<sub>3</sub> NFs in the sample lead to the strong contribution of bulk properties. These are already apparent from the diminished polarization dependence of the Raman spectra that can be explained by the random orientation of crystal facets to the incoming laser polarization. Likewise, the Bi<sub>2</sub>Te<sub>3</sub> phonons show no renormalization with increasing magnetic field strengths. It is therefore concluded, that the Bi<sub>2</sub>Te<sub>3</sub> NF sample properties are dominated by the smaller bulk-like NFs and reveal no additional surface related effects.

In contrast, for Bi<sub>2</sub>Se<sub>3</sub> the phonon mode behaviour with temperature is not fully described by the anharmonic decay model. The Bi<sub>2</sub>Se<sub>3</sub> NFs reveal strong phonon renormalizations at temperatures below 120 K that can be related to additional el-ph interactions. The coupling of a low-energy electric susceptibility with an energy around 16 meV can explain the observed frequency shifts and line width broadening with decreasing temperature. For this, the phonon renormalizations are successfully described employing the renormalized Lorentzian model for phononic Raman scattering via electronic intraband transitions. The nature of the electric susceptibility can be assigned to the enhanced contribution of the topological states on the NFs surface, which is further modified by the application of a magnetic field. The topological surface states provide an additional channel for the phonons to decay via the creation of electron-hole pairs. At magnetic fields above 3 T the

#### *4 Macro-Raman investigations of thin film samples*

related electric susceptibility coupling to the phonons is modified, which is apparent in the observed frequency and line widths renormalizations of the  $A_{1g}^2$  phonon. The phonon renormalization at fields above 3 T is unprecedented for a non-magnetic system like  $\text{Bi}_2\text{Se}_3$ , and strongly indicates the modification of the TSS's electric susceptibility by the proposed gap opening in the Dirac cone.

## 4.7 Paper I






# Temperature and magnetic field dependent Raman study of electron-phonon interactions in thin films of $\text{Bi}_2\text{Se}_3$ and $\text{Bi}_2\text{Te}_3$ nanoflakes

Sören Buchenau\*, Sarah Scheitz, Astha Sethi, John E. Slimak, Tomke E. Glier, Pranab K. Das, Torben Dankwort, Lewis Akinsinde, Lorenz Kienle, Andrivo Rusydi, Clemens Ulrich, S. Lance Cooper and Michael Rübhausen

Published in: Physical Review B - 22 June 2020  
<https://doi.org/10.1103/PhysRevB.101.245431>

Reprinted with permission from S. Buchenau, S. Scheitz *et al.*, *Physical Review B*, **2020**, 101, 245431. Copyright 2020 by the American Physical Society.

## Temperature and magnetic field dependent Raman study of electron-phonon interactions in thin films of $\text{Bi}_2\text{Se}_3$ and $\text{Bi}_2\text{Te}_3$ nanoflakes

Sören Buchenau <sup>1,\*</sup>, Sarah Scheitz <sup>1</sup>, Astha Sethi,<sup>2</sup> John E. Slimak,<sup>2</sup> Tomke Eva Glier <sup>1</sup>, Pranab Kumar Das <sup>3</sup>,  
Torben Dankwort,<sup>4</sup> Lewis Akinsinde,<sup>1</sup> Lorenz Kienle,<sup>4</sup> Andriwo Rusydi,<sup>3</sup> Clemens Ulrich <sup>5</sup>, S. Lance Cooper,<sup>2</sup>  
and Michael Rübhausen<sup>1</sup>

<sup>1</sup>CFEL, University Hamburg, Luruper Chaussee 175, 22761 Hamburg, Germany

<sup>2</sup>Department of Physics and Materials Research Laboratory, University of Illinois, Urbana, Illinois 61801, USA

<sup>3</sup>Singapore Synchrotron Light Source, National University of Singapore, Singapore 117603, Singapore

<sup>4</sup>Institute for Materials Science, Kiel University, Kaiserstrasse 2, 24143 Kiel, Germany

<sup>5</sup>School of Physics, The University of New South Wales, New South Wales 2052, Sydney, Australia



(Received 8 October 2019; accepted 26 May 2020; published 22 June 2020)

We have investigated two-dimensional nanostructures of the topological insulators  $\text{Bi}_2\text{Se}_3$  and  $\text{Bi}_2\text{Te}_3$  by means of temperature and magnetic field dependent Raman spectroscopy. The surface contribution of our samples was increased by using thin films of dropcasted nanoflakes with the aim of enhancing their topological properties. Raman spectroscopy provides a contact-free method to investigate the behavior of topological properties with temperature and magnetic fields at lower dimensions. The temperature dependent Raman study reveals anharmonic phonon behavior for  $\text{Bi}_2\text{Te}_3$  indicative of a two-phonon relaxation mechanism in this material. Contrary to this,  $\text{Bi}_2\text{Se}_3$  shows clear deviations from a two-phonon anharmonic decay model at temperatures below 120 K exhibiting a hardening and broadening, especially of the  $A_{1g}^2$  mode. Similarly, the magnetic field dependent self-energy effects are only observed for the  $A_{1g}^2$  mode of  $\text{Bi}_2\text{Se}_3$ , showing a broadening and hardening with increasing field. We interpret our results in terms of corrections to the phonon self-energy for  $\text{Bi}_2\text{Se}_3$  at temperatures below 120 K and magnetic fields above 4 T due to electron-hole pair excitations associated with the conducting surface states. The phonon renormalization with increasing magnetic field is explained by a gap opening in the Dirac cone that enables phonon coupling to the changing electric susceptibility.

DOI: [10.1103/PhysRevB.101.245431](https://doi.org/10.1103/PhysRevB.101.245431)

### I. INTRODUCTION

Topological insulators (TIs) are a new class of materials, which are insulating in the bulk and host conducting surface states (CSSs) at the interface between the TI and conventional insulators [1]. The idea of topological states was strongly promoted during the aftermath of the discovery of the quantum Hall effect by von Klitzing [2], who identified specific quantized changes in the Hall conductance, which turn out to be topological quantum numbers. After several incremental steps, modern three-dimensional (3D) TIs were predicted in 2007 by Fu *et al.* [3]. The strong spin-orbit coupling leads, in specific materials, to a band inversion of two  $p$  bands [4], which is essential for the CSSs. In addition, the electron transport is characterized by spin-momentum locking and a linear dispersion relation, known as a Dirac cone, superimposed on the bulk bands [5].  $\text{Bi}_2\text{X}_3$  ( $X=\text{Se}, \text{Te}$ ) belongs to the most frequently studied 3D TI with a single Dirac cone at the  $\Gamma$  point of the Brillouin zone [6,7] and bulk band gaps of 0.3 eV [8] and 0.1 eV [9] for  $\text{Bi}_2\text{Se}_3$  and  $\text{Bi}_2\text{Te}_3$ , respectively.

To explicitly study the CSSs and reduce contributions from the bulk, we have examined dropcasted nanoflakes with high aspect ratios that lead to an increased surface contribution.

In order to evaluate the fundamental limit of the conductivity of electrons in the CSSs at lower dimensions, it is

important to study the electron-phonon interactions of these 2D materials [10,11].

A unique technique to study phononic and electronic properties of solids simultaneously is Raman scattering, which has been widely applied to investigate bulk samples and conventional 2D films of  $\text{Bi}_2\text{Se}_3$  [12–15] and  $\text{Bi}_2\text{Te}_3$  [14,16,17].  $\text{Bi}_2\text{Se}_3$  and  $\text{Bi}_2\text{Te}_3$  are layered materials with a rhombohedral crystal structure that grow in multiples of so-called quintuple layers (QLs) consisting of alternating Bi and Se or Te layers, as depicted in Fig. 1(a) [18]. The primitive unit cell consists of five atoms, which results in 15 lattice dynamical modes that are classified in three acoustic and 12 optical modes. The optical modes are further grouped into four Raman-active modes with two modes each of  $A_{1g}$  and  $E_g$  symmetry and four infrared(IR)-active modes with two modes each of  $A_{1u}$  and  $E_u$  symmetry according to group theory [18]. Due to the inversion symmetry of the crystal structure, these phonon modes are exclusively either Raman or IR active [18]. Of the Raman-active phonons, the  $A_{1g}$  modes are out-of-plane vibrations, whereas the  $E_g$  modes vibrate in-plane.

Systematic temperature dependent Raman studies have been conducted before on  $\text{Bi}_2\text{Se}_3$  single crystals [19,20] and nanoplates [21], and on  $\text{Bi}_2\text{Te}_3$  thin films [22]. In this work, we report on a temperature and magnetic field dependent high-energy-resolution Raman study of thin films of individual  $\text{Bi}_2\text{Se}_3$  and  $\text{Bi}_2\text{Te}_3$  nanoflakes with average heights in the range of 8 and 14 QLs, respectively.

\*Corresponding author: sbuchena@physnet.uni-hamburg.de



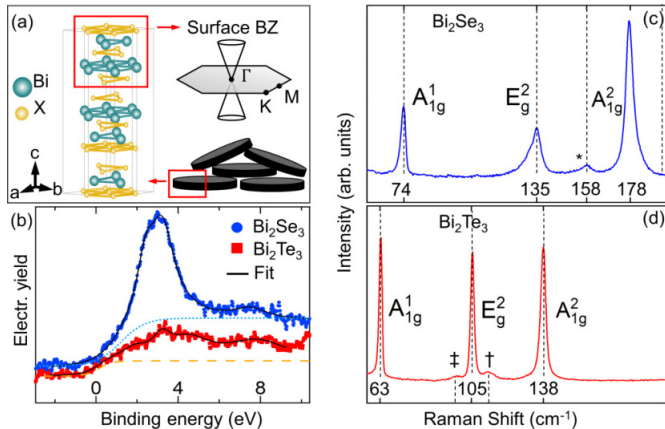


FIG. 1. (a) Schematic illustration of a thin film of  $\text{Bi}_2\text{X}_3$  ( $X=\text{Se}, \text{Te}$ ) nanoflakes. This configuration greatly enhances the amount of surface, which hosts massless Dirac electrons due to the linear Dirac cone at the  $\Gamma$  point [29], as shown in the surface Brillouin zone in the upper right corner. The figure further shows the crystal structure with blue spheres representing Bi atoms and yellow spheres representing either Se or Te atoms. (b) Valence-band emission spectra extracted from XPS spectra of both materials. The Fermi edge modeled by a step function shows a highly increased electron density for  $\text{Bi}_2\text{Se}_3$  (light-blue, dotted graph) compared to  $\text{Bi}_2\text{Te}_3$  (orange, dashed graph). (c),(d) Raman spectra at 3 K in  $z(xx)\bar{z}$  geometry showing three labeled bulk modes for  $\text{Bi}_2\text{Se}_3$  and  $\text{Bi}_2\text{Te}_3$ , respectively. The asterisk, dagger, and double dagger mark Raman-forbidden infrared modes.

Magnetic field dependent Raman measurements are of utmost importance as they allow for investigations of the destruction of the CSSs by gapping of the Dirac cone induced by the presence of a magnetic field [1]. It was theoretically predicted that the CSSs are sensitive to the application of a magnetic field [23] and an opening of the Dirac cone has indeed been observed in magnetically doped TIs [24,25] or by exchange coupling TIs to magnetic insulators [26–28]. The tuning of the CSSs with an applied magnetic field is expected to display a spectroscopic signature, which is amplified due to the highly increased surface contributions of our nanoflakes. We therefore interpret our results by means of self-energy corrections of the phonons due to electron-phonon interactions.

## II. EXPERIMENTAL PART

Figure 1(a) shows an illustration of strongly anisotropic nanoflakes. The  $\text{Bi}_2\text{Se}_3$  nanoflakes were grown with the chemical polyol method following our earlier work [30]. The  $\text{Bi}_2\text{Te}_3$  nanoflakes were synthesized using a slightly modified route according to Zhang *et al.* [31]. Details on the synthesis are presented in Ref. [30] and in the Supplemental Material [32]. The clean flakes were dropcasted on a Si substrate and the solvent evaporated. It should be noted that the structures are not damaged by these preparatory steps, as can be seen in Fig. S-2 of the Supplemental Material [32]. The required stoichiometry, single crystallinity, and morphology of both samples were confirmed using energy dispersive x-ray spectroscopy (EDX), x-ray photoelectron spectroscopy (XPS), transmission electron microscopy (TEM), selected area electron diffraction (SAED), and atomic

force microscopy (AFM). A detailed characterization of the nanoflakes can be found in the Supplemental Material [32].

The topological insulator  $\text{Bi}_2\text{X}_3$  ( $X=\text{Se}, \text{Te}$ ) features Dirac states at the interface with conventional insulators, but not at the interface of every QL [28]. It has furthermore been shown for  $\text{Bi}_2\text{Se}_3$ , that the CSS wave functions hybridize below a critical flake thickness of 6 QLs, which results in a gap opening in the Dirac cone [33]. To investigate the intact CSSs, it is hence necessary to grow flakes of certain thicknesses and maintain enough space between dropcasted flakes to prevent hybridization of the CSSs from neighboring flake surfaces. With average heights of 8 and 14 QLs for our  $\text{Bi}_2\text{Se}_3$  and  $\text{Bi}_2\text{Te}_3$  flakes, respectively, we expect our samples to host unperturbed CSSs. In addition, our flakes were grown covered with the ligand polyvinylpyrrolidone (PVP) to facilitate a 2D growth. The PVP layers act as conventional insulators and thus provide sufficient spacing between neighboring flakes. It is known that the CSSs are robust against different kinds of adsorbates and are maintained even under ambient environmental conditions [24,34]. However, adsorbates are known to induce a band bending of the bulk bands near the surface due to charge accumulation [6,35]. This leads to the creation of additional surface quantum well states originating from the bulk bands coexisting next to the CSSs. Nonetheless, the CSSs stay intact, but are pushed deeper into the bulk separating them from the surface defects [36]. Thus, for volume scattering techniques, the CSSs stay detectable as Raman scattering is able to probe the whole volume including the deeper-lying CSSs, in contrast to surface sensitive techniques such as angle-resolved photoemission spectroscopy (ARPES). In fact, Raman scattering probes the complete thickness of a flake of about 10 nm. Therefore, probing a thin film of dropcasted nanoflakes is expected to contain a manifold of topologically nontrivial contributions, as illustrated in Fig. 1(a), making it easier to observe phenomena that have their origin in those exotic states.

We conducted Raman measurements on films of dropcasted nanoflakes using the 647.1 nm excitation line of a continuous-wave  $\text{Kr}^+$  gas laser. The incident laser power was limited to 6.2 mW and focused on a 50- $\mu\text{m}$ -diameter spot size to prevent laser induced heating or damage of the sample, which is shown in detail in the Supplemental Material [32]. The sample was mounted so that the incident light impinged on the flakes perpendicular to their surfaces. The scattered light from the sample was collected in a backscattering configuration, dispersed through a triple-stage spectrometer, and then detected with a liquid-nitrogen-cooled charged-coupled-device detector. The horizontal polarization of the incident light with regard to the setup was selected with a polarization rotator and the scattered light was analyzed by the triple-stage gratings of the spectrometer that is primarily sensitive to horizontally polarized light [37]. Our scattering configuration denoted in Porto notation is hence  $z(xx)\bar{z}$  [38]. The samples were inserted into a continuous He-flow cryostat, which itself was horizontally mounted in the open bore of a superconducting magnet. This setup allowed for simultaneous temperature (3–295 K) and magnetic field (0–7 T) dependent measurements. Magnetic field dependent measurements were performed in Faraday geometry with the wave vector of the incident light  $\vec{q}$  parallel to the applied field  $\vec{H}$ .

### III. RESULTS AND DISCUSSION

Figure 1(b) shows the valence-band spectra extracted from XPS measurements of the  $\text{Bi}_2\text{Se}_3$  and  $\text{Bi}_2\text{Te}_3$  films. The indicated Fermi edges modeled by step functions reveal, for  $\text{Bi}_2\text{Se}_3$ , a highly increased electron density near the Fermi edge compared to  $\text{Bi}_2\text{Te}_3$ . Differences in the two samples are also reflected in their phononic properties measured by Raman spectroscopy. The implication of the enhanced surface contribution of our flakes is already observable in the representative Raman spectra shown in Figs. 1(c) and 1(d). Next to the three identified bulk phonon modes that are in good agreement with previous experiments [18,39,40], additional IR-active modes at  $158\text{ cm}^{-1}$  in  $\text{Bi}_2\text{Se}_3$  and at  $98\text{ cm}^{-1}$  and  $113\text{ cm}^{-1}$  in  $\text{Bi}_2\text{Te}_3$  are detected [14,15,41]. The IR-active modes become Raman active because of the breaking of the crystal's inversion symmetry at the surface of the nanoflakes [15]. This aspect is a direct manifestation of the enhanced surface-to-volume ratio of the dropcasted nanoflakes compared to the bulk material. The bulk material crystallizes in the  $D_{3d}$  space group with inversion symmetry, whereas the symmetry at the surface is reduced to  $C_{3v}$  [15]. Gnezdilov *et al.* [15] reported that the  $A_{2u}^2$  mode at  $158\text{ cm}^{-1}$  in the case of  $\text{Bi}_2\text{Se}_3$  is only observable at temperatures below 10 K for their bulk crystalline sample. In contrast, for our nanoflake samples, we were able to observe this mode even at elevated temperatures up to  $\sim 160\text{ K}$  (see Fig. S-9 in the Supplemental Material [32]), indicating enhanced surface contributions with respect to the scattering volume at lower temperatures. Likewise, the IR modes in the  $\text{Bi}_2\text{Te}_3$  films are detected for temperatures up to 100 K (see Fig. S-9 in the Supplemental Material [32]). Furthermore, the high single crystalline quality of our flakes is indicated by the nearly resolution-limited linewidths of the  $\text{Bi}_2\text{Te}_3$  phonons. In Sec. 5 in the Supplemental Material [32], we discuss in detail that the narrow linewidths and high quality of the  $\text{Bi}_2\text{Se}_3$  spectra suggest nearly stoichiometric samples with only a few Se vacancies. Furthermore, a sensitivity of the phonons to band-bending effects due to adsorbates at the surface and consequent localized electronic surface states cannot be seen. Since Raman is a volume scattering technique, we do not expect to observe any contributions from possible highly localized electronic states at the sample surface. This leads us to conclude that the phonons track the CSSs and electronic states associated to the Fermi level of our sample. Furthermore, we conclude from the low number of Se vacancies that the Fermi level in our sample lies indeed between the bulk valence and conduction band.

We conducted a detailed temperature dependent Raman study by acquiring 30 spectra for each material system in a temperature range from 3 to 295 K. To investigate the phonon dynamics, we extracted the values of the frequency  $\omega$  and the linewidth  $\Gamma$  [full width at half maximum (FWHM)] from the respective Voigt fits to the phonon modes. The Voigt profile is represented by a Lorentz profile broadened by a Gaussian that accounts for the spectral resolution of the spectrometer, and is given as

$$V(\omega) = y_0 + A \frac{2 \ln 2}{\pi^{3/2}} \frac{\Gamma_L}{\Gamma_G^2} \times \int_{-\infty}^{\infty} \frac{e^{-t^2}}{(\sqrt{\ln 2} \frac{\Gamma_L}{\Gamma_G})^2 + (\sqrt{4 \ln 2} \frac{\omega - \omega_0}{\Gamma_G} - t)^2} dt. \quad (1)$$

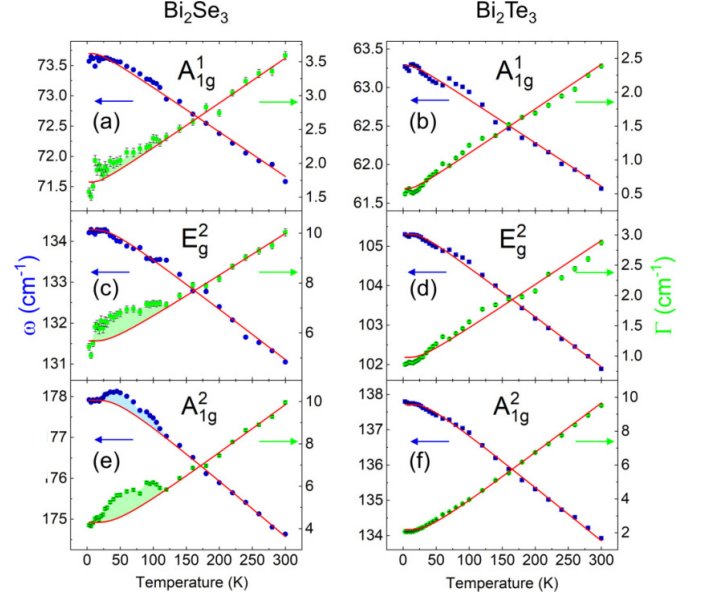


FIG. 2. Self-energy effects from Voigt fits of the temperature dependent Raman response for  $\text{Bi}_2\text{Se}_3$  (left column) and  $\text{Bi}_2\text{Te}_3$  (right column). (a),(b) The  $A_{1g}^1$  phonons, (c),(d) the  $E_g^2$  phonons, and (e),(f) the  $A_{1g}^2$  phonons. The red lines are fits using the model of an anharmonic decay with a symmetric decay channel into two acoustic phonons. The data show the general trend of an anharmonic decay consisting of broadening and softening with increasing temperature. Clear deviations from the model are present for the high-energy modes in  $\text{Bi}_2\text{Se}_3$  [(c) and (e)], which are mirrored in energy and linewidth. Below  $\sim 120\text{ K}$ , the phonons exhibit higher energies and linewidths than expected from the usual anharmonic phonon decay, as an indication for additional phonon interactions with the electronic system.

Hereby,  $\Gamma_{G,L}$  denotes the linewidth of both convoluted peaks, with a spectral resolution of the setup of  $\Gamma_G = 1.4\text{ cm}^{-1}$ ,  $\omega_0$  is the peak center,  $A$  is the integrated area of the Lorentzian peak, and  $y_0$  is the offset.

We have analyzed the three higher-energy modes of the commonly known [14,39] four bulk modes in  $\text{Bi}_2\text{X}_3$  ( $X = \text{Se}, \text{Te}$ ) because the lowest-energy  $E_g^1$  mode was covered by the strong Rayleigh background due to the enhanced elastic scattering from the nanoflakes. Figure 2 shows the behavior of the frequency  $\omega_0$  and linewidth  $\Gamma_L$  of the  $A_{1g}^1$ ,  $E_g^2$ , and  $A_{1g}^2$  modes for  $\text{Bi}_2\text{Se}_3$  (left column) and  $\text{Bi}_2\text{Te}_3$  (right column). The frequencies and linewidths show a general trend of phonon softening and broadening with increasing temperature by several wave numbers. This phonon behavior can be described by the model of an anharmonic decay (AD) assuming a symmetric decay of the optical phonon into two acoustic phonons [42]. Within this model, the temperature dependences of the phonon frequency and linewidth are given by

$$\omega_{\text{anh}}(T) = \omega_0 - \frac{a}{e^{\frac{\hbar\omega_0}{2k_B T}} - 1}, \quad (2)$$

$$\Gamma_{\text{anh}}(T) = \Gamma_0 + \frac{a}{e^{\frac{\hbar\omega_0}{2k_B T}} - 1}, \quad (3)$$



with  $T$  as the temperature,  $\omega_{\text{anh}}$  and  $\Gamma_{\text{anh}}$  as the modulated frequency and linewidth, respectively, and  $\omega_0$  and  $\Gamma_0$  as the bare phonon frequency and linewidth of a particular phonon, respectively.  $a$  contains the transition matrix element and the two-phonon density of states of the anharmonic decay. Fits of the data according to the AD model are shown as red lines in Fig. 2. For  $\text{Bi}_2\text{Te}_3$ , the anharmonic fits show very good agreement with the data, especially for the highest-energy  $A_{1g}^2$  mode in Fig. 2(f). This indicates a more bulklike behavior typical for semiconductors and insulators with phonon-phonon interactions as the dominant scattering mechanism in the  $\text{Bi}_2\text{Te}_3$  sample. Compared to  $\text{Bi}_2\text{Te}_3$ , the linewidths for all Raman modes in  $\text{Bi}_2\text{Se}_3$  show clear deviations from the AD model at temperatures below 120 K; see Figs. 2(a), 2(c) and 2(e). The linewidth of the  $A_{1g}^1$  mode exhibits only weak deviations from the AD model, whereas the higher-energy modes deviate more strongly. For the  $A_{1g}^2$  mode, the deviation in linewidth is mirrored in frequency, illustrated in Fig. 2(e), as expected by the Kramers-Kronig relation. In previous temperature dependent Raman investigations on  $\text{Bi}_2\text{Se}_3$  crystals [19,20], no phonon anomalies were observed. This hints to an origin of these deviations stemming from the increased electronic surface contributions of the investigated flakes at lower temperatures. This aspect is supported by the enhanced electron density near the Fermi edge in  $\text{Bi}_2\text{Se}_3$ , shown in Fig. 1(b).

Since the AD model is not sufficient to describe the low-temperature behavior of phonons, additional scattering mechanisms need to be taken into consideration. As  $\text{Bi}_2\text{Se}_3$  is nonmagnetic, additional scattering channels could stem from electron-phonon interactions since the only available states at these energies and low temperatures must be of an electronic nature. The coupling of phonons to available electronic susceptibilities would result in a decay of the phonons by creating electron-hole pairs [43,44]. The possibility of this interaction is plausible since our XPS data show a higher electron density near the Fermi edge for  $\text{Bi}_2\text{Se}_3$ . The coupling of phonons to an electric susceptibility  $\chi^{\text{el}}(\omega)$  leads to a correction in the phonon self-energy, which manifests itself in a modified Raman response. This response  $I^{\text{ph}}(\omega)$  of a phonon coupled to an electric susceptibility  $\chi^{\text{el}}(\omega)$ ,

$$\chi^{\text{el}}(\omega) = R(\omega) + i\rho(\omega), \quad (4)$$

with its real  $R(\omega)$  and imaginary part  $\rho(\omega)$ , is expressed by [45,46]

$$I^{\text{ph}}(\omega) \propto \frac{[g^2\rho(\omega) + \Gamma_{\text{anh}}]\omega_{\text{anh}}}{\underbrace{\left\{ \omega^2 - \omega_{\text{anh}}^2 \left[ 1 - g^2 \frac{R(\omega)}{\omega_{\text{anh}}} \right] \right\}^2}_{\omega_{\text{exp}}^2} + \omega_{\text{anh}}^2 \underbrace{[\Gamma_{\text{anh}} + g^2\rho(\omega)]^2}_{\Gamma_{\text{exp}}^2}}. \quad (5)$$

Here,  $\omega_{\text{anh}}$  and  $\Gamma_{\text{anh}}$  correspond to the frequency and linewidth expected from the AD model, and  $g$  is a coupling constant determining the coupling strength between the phonon and the electric susceptibility. Equation (5) describes a Lorentz profile with a phonon frequency  $\omega_{\text{anh}}$  that is modified by coupling to the real part  $R(\omega)$  of the electric susceptibility and a linewidth  $\Gamma_{\text{anh}}$  modified by coupling to the imaginary part  $\rho(\omega)$ . As a result, the values for the frequency  $\omega_{\text{exp}}$  and

linewidth  $\Gamma_{\text{exp}}$  extracted from Voigt fits of the phonons differ from the values expected for an anharmonic decay due to corrections from the electric susceptibility. We hence interpret the deviations in linewidth and frequency expected from the AD model as arising from additional contributions caused by the decay of phonons coupling to an available electronic transition. When the electron-phonon coupling  $g$  is strong enough, the extracted phonon linewidths and frequencies are therefore given as follows:

$$\omega_{\text{exp}} = \sqrt{\omega_{\text{anh}}(T)^2 - \omega_{\text{anh}}(T) \cdot g^2 R(\omega)}, \quad (6)$$

$$\Gamma_{\text{exp}} = \Gamma_{\text{anh}}(T) + g^2 \rho(\omega). \quad (7)$$

The deviations from the AD model could be caused by an interaction of the phonons with an electric susceptibility with an energy in the meV range. The lack of any electronic renormalization in  $\text{Bi}_2\text{Te}_3$  is thus indicating that there are no available electronic states in this energy range. This is further verified by the strongly diminished electronic density near the Fermi edge in  $\text{Bi}_2\text{Te}_3$  compared to  $\text{Bi}_2\text{Se}_3$  seen by XPS, as shown in Fig. 1(b).

Since the  $A_{1g}^2$ - and  $E_g^2$ -symmetry phonons show deviations from the AD model, it can be argued that both phonons couple to a close-lying electronic transition. The different energies of the two phonons lead to different corrections from the real and imaginary parts of the electric susceptibility according to Eqs. (6) and (7).

The strong electronic renormalization in  $\text{Bi}_2\text{Se}_3$  for the  $E_g^2$  mode in linewidth but none in frequency, shown in Fig. 2(c), leads to the assumption that the  $E_g^2$  phonon couples to an electric susceptibility with an energy identical to the  $E_g^2$  energy, as visualized in Fig. 3(a). In that way, the  $E_g^2$  phonon would get a strong correction from the imaginary part  $\rho(\omega)$  since it is located at the maximum, resulting in an increased linewidth  $\Gamma_{\text{exp}}$  according to Eq. (7). On the other hand, there would not be any corrections in frequency because at  $\omega_{\text{ph}}$  the real part  $R(\omega)$  is zero and thus  $\omega_{\text{exp}}$  corresponds to  $\omega_{\text{anh}}$  according to Eq. (6). The temperature dependence of the  $E_g^2$  frequency is then sufficiently well described by the AD model, as evident in Fig. 2(c). Following this hypothesis, the  $A_{1g}^2$  phonon with an energy of 22 meV would couple to  $\rho(\omega)$  and a negative  $R(\omega)$  of the same electric susceptibility, as illustrated in Fig. 3(b). This would again result in increased linewidths and additionally in increased frequencies according to Eqs. (6) and (7). Our hypothesis agrees well with the observed deviations in frequency and linewidth at lower temperatures for the  $A_{1g}^2$  phonon shown in Fig. 2(e). In this picture, we expect to observe these effects at lower temperatures where phonons are frozen out and the scattering mechanism is dominated by the electron-phonon coupling. This is again in good agreement with our data, where we observe deviations from the AD model setting in at temperatures below 120 K. Heid *et al.* have calculated the coupling strengths of the  $\text{Bi}_2\text{Se}_3$  CSSs to optical modes as a function of phonon energy [47]. They show that enhanced coupling occurs to phonons within an energy range of 17 to 22 meV with a reduced coupling for modes below 10 meV [47]. Even though Heid *et al.* state that the dominant coupling occurs via polar-type optical modes, significant coupling to Raman-active modes of the electron-

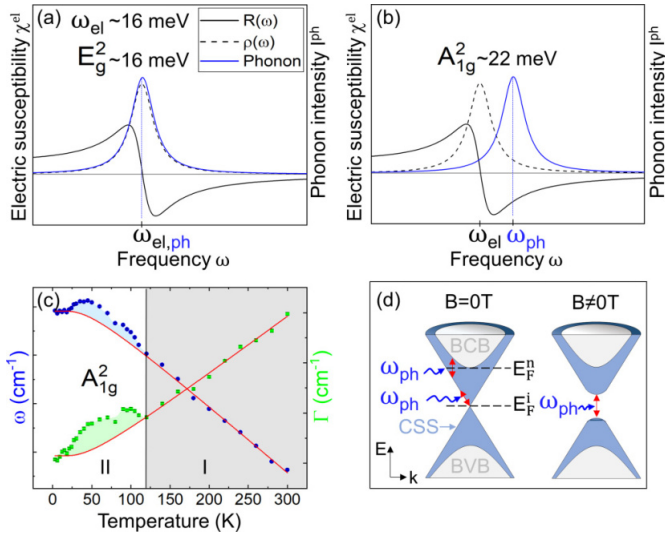


FIG. 3. (a),(b) The real  $R(\omega)$  and imaginary  $\rho(\omega)$  parts of the electric susceptibility are plotted together with the discrete state of a phonon modeled by a simple Lorentzian with a phonon frequency  $\omega_{ph}$ . An overlap of both states is shown for the  $E_g^2$  mode in (a) and the  $A_{1g}^2$  mode in (b). (c) Temperature dependence of frequency and linewidth of the Bi<sub>2</sub>Se<sub>3</sub>  $A_{1g}^2$  phonon. Two areas are indicated that account for different decay mechanisms of the phonon. (d) Schematic band structure of Bi<sub>2</sub>Se<sub>3</sub> with two possible locations of the Fermi level in an intrinsic ( $E_F^i$ ) and  $n$ -doped ( $E_F^n$ ) Bi<sub>2</sub>Se<sub>3</sub> nanoflake. The bulk conduction band (BCB) and bulk valence band (BVB) are labeled. Red arrows illustrate creations of electron-hole pairs by a Raman phonon  $\omega_{ph}$ . The gapped Dirac cone is shown when a magnetic field  $B \neq 0$  T is applied.

phonon interaction is still present, as suggested in several studies [11,48]. Thus, our observations are in good agreement with the calculated coupling strengths, which support our findings for only very weak renormalizations in the  $A_{1g}^1$  mode at 9 meV and strong renormalizations in the  $E_g^2$  (16.7 meV) and  $A_{1g}^2$  (21.9 meV) modes. The preceding analysis leads to the identification of two temperature regions with different dominant scattering mechanisms that are shown in Fig. 3(c). In region I, at higher temperatures, phonon-phonon coupling dominates the phonon decay by the anharmonic interaction and additional contributions from electron-phonon coupling are no longer evident. Therefore, we observe good agreement with the classic AD model in region I, where the bulk properties mask all surface-related effects. In region II, electron-phonon coupling is significant and phonon renormalization can be observed when the surface contribution is high enough.

So far, we discussed the electron-phonon coupling from an energetic point of view. The  $A_{1g}^1$  phonon with an energy of around 9 meV should interfere with the electric susceptibility around 16 meV by coupling to the positive imaginary and real part. However, we do not observe electronic renormalizations for this mode. Hence, an additional aspect has to be considered that affects the coupling strength  $g$  between the phonons and the electric susceptibility. The eigenvectors of the phonons show significantly different displacement vectors for the  $A_{1g}^1$  phonon compared to the  $E_g^2$  and  $A_{1g}^2$  phonons.

The atomic displacements for the  $E_g^2$  and  $A_{1g}^2$  modes modulate the electric susceptibility related to the CSSs in the following way: For both modes, the partially negatively charged chalcogen (Se, Te) atoms terminating each QL vibrate opposite to the positively charged Bi atoms [18,49], whereas they vibrate in phase for the  $A_{1g}^1$  mode. The electronic polarizability is, therefore, affected more strongly by the  $E_g^2$  and  $A_{1g}^2$  phonons, resulting in a stronger electron-phonon coupling and enhanced self-energy effects.

In a perfect single-crystalline Bi<sub>2</sub>Se<sub>3</sub> sample the Fermi level is expected to be located at the Dirac point [7], as indicated in Fig. 3(d). In this case, intracone electronic transitions in the upper Dirac cone are available. The electron-phonon coupling strength increases linearly with the energy distance from the Dirac point due to the linear increase of the density of states expected for the 2D Dirac dispersion [47]. It is also possible that the Fermi level lies closer to the bulk conduction band due to inherent  $n$  doping that is often reported for naturally grown Bi<sub>2</sub>Se<sub>3</sub> [33] and is also shown in Fig. 3(d). In that case, transitions of the Dirac fermions into the bulk conduction band become possible and add to the intracone contributions. The coupling strength is expected to be enhanced when additional interband transitions are available [47], which explains our observed strong phonon renormalizations. We, therefore, expect the Fermi level in our Bi<sub>2</sub>Se<sub>3</sub> samples to lie within the bulk gap but closer to the bulk conduction bands.

The assumption of  $\chi^{el}$  being related to the CSSs is justified by two aspects. First, we were able to show the enhanced surface contributions of our flakes by the detection of IR modes up to high temperatures. Second, the electric susceptibility in the meV range can be associated with transitions involving Dirac cone states. Additional insight can be gained by manipulating the Dirac cone and the associated electric susceptibility by means of a magnetic field. Since the Dirac cone determines the low-energy electric susceptibility, its modification is also indicative of the presence of the CSSs. The changes in frequency and linewidth of the phonons as a function of magnetic field for Bi<sub>2</sub>Se<sub>3</sub> and Bi<sub>2</sub>Te<sub>3</sub> are shown in Figs. 4(a) to 4(f).

In agreement with our temperature dependent study and XPS results, we observe a magnetic field dependent renormalization of phonon energies and linewidths in Bi<sub>2</sub>Se<sub>3</sub>, but not in Bi<sub>2</sub>Te<sub>3</sub>. The absence of any phonon renormalization in Bi<sub>2</sub>Te<sub>3</sub> is again consistent with the reduced electronic density near the Fermi edge compared to the Bi<sub>2</sub>Se<sub>3</sub> sample. For Bi<sub>2</sub>Se<sub>3</sub>, however, magnetic field dependent self-energy corrections are observed in frequency and linewidth for the  $A_{1g}^2$  mode at 177 cm<sup>-1</sup>. At fields above 3 T, we find a simultaneous hardening and broadening of about 0.6 cm<sup>-1</sup> and 1.5 cm<sup>-1</sup>, respectively. Since it is known that in topological insulators a gap opening in the Dirac cone occurs in the presence of a magnetic field [23], our results point to a change in the electric susceptibility of the Dirac cone by the magnetic field. The change in the electric susceptibility would lead to a renormalization in the  $A_{1g}^2$  mode in Bi<sub>2</sub>Se<sub>3</sub>. A gap opening would shift and redistribute the electric susceptibility. The hardening and broadening of the  $A_{1g}^2$  mode with increasing field strengths indicate the coupling to an electric

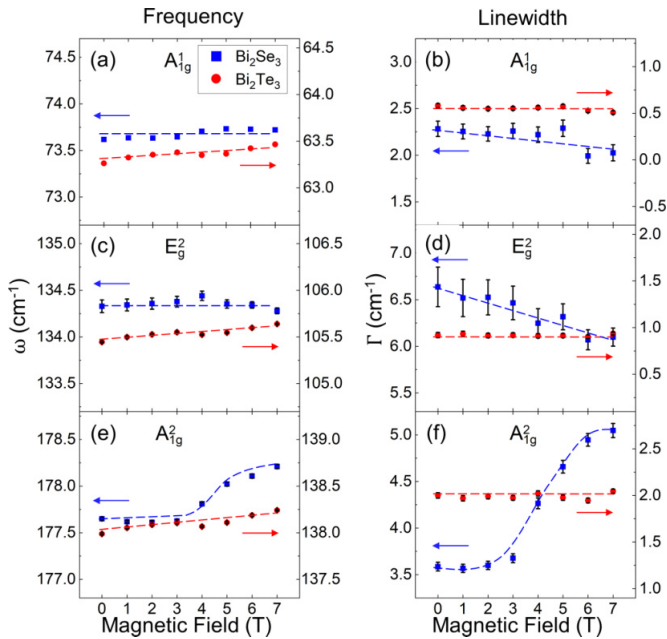


FIG. 4. Magnetic field dependent self-energy effects for  $\text{Bi}_2\text{Se}_3$  and  $\text{Bi}_2\text{Te}_3$  nanoflakes at 3 K in ( $X$ -)scattering geometry and Faraday configuration. The dependency of the three Raman modes in energy (left column) and linewidth (right column) with magnetic field is shown. All y axes are set to intervals of  $2.0 \text{ cm}^{-1}$  for easier comparability.  $\text{Bi}_2\text{Te}_3$  phonons (red curves) show no significant change in energy and linewidth over the applied magnetic field range. For the  $\text{Bi}_2\text{Se}_3$  phonons (blue curves), clear changes in energy and linewidth can be observed for magnetic fields above 3 T. The dashed lines represent guides to the eye.

susceptibility with a lower energy than the phonon according to Eqs. (6) and (7). The decreasing linewidth of the  $E_g^2$  mode, on the other hand, shows a reduced coupling to the electric susceptibility. We can therefore estimate the energy of a gap opening in the Dirac cone to be in the range of 16 to 22 meV, which would explain the phonon renormalizations. This finding is in agreement with results of Gooth *et al.* [50], who report a gap opening in the order of tens of meV by magnetic interactions in TI. According to our model, the phonons decay by coupling to interband transitions from the lower gapped Dirac cone to the upper one, as visualized in Fig. 3(d). The strong phonon self-energy corrections due to the electron-phonon interactions provide direct evidence

for the changes in the electric susceptibility in the CSSs at magnetic field strengths above 3 T.

#### IV. CONCLUSION

In conclusion, we have investigated thin films of drop-casted  $\text{Bi}_2\text{Se}_3$  and  $\text{Bi}_2\text{Te}_3$  nanoflakes by means of temperature and magnetic field dependent Raman spectroscopy. The temperature dependence of the phonon dynamics in our  $\text{Bi}_2\text{Te}_3$  sample is readily described by the anharmonic phonon-phonon interaction, indicating a dominant bulk behavior. For  $\text{Bi}_2\text{Se}_3$ , we observe deviations from the AD model, which can be linked to additional contributions from the electron-phonon interaction originating from the increased surface contribution. Our study suggests that the Dirac fermions contribute significantly to the electron-phonon interactions, which manifest in the strong phonon renormalizations in  $\text{Bi}_2\text{Se}_3$  at temperatures below 120 K. Additional magnetic field dependent Raman spectroscopy reveals strong phonon self-energy corrections in  $\text{Bi}_2\text{Se}_3$ , indicating the renormalization of the phonons by the continuum free carriers and a significant magnetoelectric coupling. The self-energy changes in the  $\text{Bi}_2\text{Se}_3$  phonons provide direct evidence for the manipulation of the CSSs by an applied magnetic field, which can be associated with a gap opening in the Dirac cone.

#### ACKNOWLEDGMENTS

This work was funded by the Deutsche Forschungsgemeinschaft (DFG; German Research Foundation), DFG RU 773/8-1. Work at the University of Illinois was supported by the National Science Foundation under Grant No. NSF DMR 1800982. S.B., C.U., and M.R. would like to acknowledge the support from the Australian Research Council (ARC) through Grant No. DP170100415. The work at National University of Singapore is supported by the Ministry of Educations of Singapore AcRF Tier-2 (Grants No. MOE2017-T2-1-135, No. 323 MOE2018-T2-2-117, and No. MOE2018-T2-2-117), and Ministry of Education AcRF-1 (Grant No. R-144-000-423-114) and is acknowledged by the support of the Singapore Synchrotron Light Source (SSLS), which is a National Research Infrastructure under the National Research Foundation Singapore via NUS Core Support Grant No. C-380-003-003-001. We thank Robert Frömter and Dorota Koziej for the use of their scanning electron microscopes. We are further thankful for Robert Zierold and Stephan Martens for helpful discussions and magnetization measurements of our samples.

- [1] M. Z. Hasan and C. L. Kane, *Colloquium: Topological insulators*, *Rev. Mod. Phys.* **82**, 3045 (2010).
- [2] K. Von Klitzing, The quantized Hall effect, *Rev. Mod. Phys.* **58**, 519 (1986).
- [3] L. Fu, C. L. Kane, and E. J. Mele, Topological Insulators in Three Dimensions, *Phys. Rev. Lett.* **98**, 106803 (2007).
- [4] J. Betancourt, S. Li, X. Dang, J. Burton, E. Tsymlal, and J. Velez, Complex band structure of topological insulator  $\text{Bi}_2\text{Se}_3$ , *J. Phys.: Condens. Matter* **28**, 395501 (2016).

- [5] Y. Ando, Topological insulator materials, *J. Phys. Soc. Jpn.* **82**, 102001 (2013).
- [6] J. G. Analytis, J.-H. Chu, Y. Chen, F. Corredor, R. D. McDonald, Z. X. Shen, and I. R. Fisher, Bulk Fermi surface coexistence with Dirac surface state in  $\text{Bi}_2\text{Se}_3$ : A comparison of photoemission and Shubnikov-de Haas measurements, *Phys. Rev. B* **81**, 205407 (2010).
- [7] H. Zhang, C.-X. Liu, X.-L. Qi, X. Dai, Z. Fang, and S.-C. Zhang, Topological insulators in  $\text{Bi}_2\text{Se}_3$ ,  $\text{Bi}_2\text{Te}_3$  and  $\text{Sb}_2\text{Te}_3$



- with a single Dirac cone on the surface, *Nat. Phys.* **5**, 438 (2009).
- [8] Y. Xia, D. Qian, D. Hsieh, L. Wray, A. Pal, H. Lin, A. Bansil, D. Grauer, Y. S. Hor, R. J. Cava, and M. Z. Hasan, Observation of a large-gap topological-insulator class with a single Dirac cone on the surface, *Nat. Phys.* **5**, 398 (2009).
- [9] Y. L. Chen, J. G. Analytis, J.-H. Chu, Z. K. Liu, S.-K. Mo, X. L. Qi, H. J. Zhang, D. H. Lu, X. Dai, Z. Fang, S. C. Zhang, I. R. Fisher, Z. Hussain, and Z.-X. Shen, Experimental realization of a three-dimensional topological insulator,  $\text{Bi}_2\text{Te}_3$ , *Science* **325**, 178 (2009).
- [10] D. Kim, Q. Li, P. Syers, N. P. Butch, J. Paglione, S. D. Sarma, and M. S. Fuhrer, Intrinsic Electron-Phonon Resistivity of  $\text{Bi}_2\text{Se}_3$  in the Topological Regime, *Phys. Rev. Lett.* **109**, 166801 (2012).
- [11] C. Chen, Z. Xie, Y. Feng, H. Yi, A. Liang, S. He, D. Mou, J. He, Y. Peng, X. Liu *et al.*, Tunable Dirac fermion dynamics in topological insulators, *Sci. Rep.* **3**, 2411 (2013).
- [12] M. Eddrief, P. Atkinson, V. Etgens, and B. Jusserand, Low-temperature Raman fingerprints for few-quintuple layer topological insulator  $\text{Bi}_2\text{Se}_3$  films epitaxied on GaAs, *Nanotechnology* **25**, 245701 (2014).
- [13] S. Zhao, C. Beekman, L. Sandilands, J. Bashucky, D. Kwok, N. Lee, A. LaForge, S.-W. Cheong, and K. Burch, Fabrication and characterization of topological insulator  $\text{Bi}_2\text{Se}_3$  nanocrystals, *Appl. Phys. Lett.* **98**, 141911 (2011).
- [14] K. Shahil, M. Hossain, V. Goyal, and A. Balandin, Micro-Raman spectroscopy of mechanically exfoliated few-quintuple layers of  $\text{Bi}_2\text{Te}_3$ ,  $\text{Bi}_2\text{Se}_3$ , and  $\text{Sb}_2\text{Te}_3$  materials, *J. Appl. Phys.* **111**, 054305 (2012).
- [15] V. Gnezdilov, Y. G. Pashkevich, H. Berger, E. Pomjakushina, K. Conder, and P. Lemmens, Helical fluctuations in the Raman response of the topological insulator  $\text{Bi}_2\text{Se}_3$ , *Phys. Rev. B* **84**, 195118 (2011).
- [16] D. Teweldebrhan, V. Goyal, and A. A. Balandin, Exfoliation and characterization of bismuth telluride atomic quintuples and quasi-two-dimensional crystals, *Nano Lett.* **10**, 1209 (2010).
- [17] K. M. F. Shahil, M. Hossain, D. Teweldebrhan, and A. Balandin, Crystal symmetry breaking in few-quintuple  $\text{Bi}_2\text{Te}_3$  films: Applications in nanometrology of topological insulators, *Appl. Phys. Lett.* **96**, 153103 (2010).
- [18] W. Richter, C. R. Becker, and H. Köhler, A Raman and far-infrared investigation of phonons in the rhombohedral  $\text{V}_2\text{-VI}_3$  compounds, *Phys. Status Solidi (b)* **84**, 619 (1977).
- [19] B. Irfan, S. Sahoo, A. P. S. Gaur, M. Ahmadi, M. J.-F. Guinel, R. S. Katiyar, and R. Chatterjee, Temperature dependent Raman scattering studies of three dimensional topological insulators  $\text{Bi}_2\text{Se}_3$ , *J. Appl. Phys.* **115**, 173506 (2014).
- [20] Y. Kim, X. Chen, Z. Wang, J. Shi, I. Miotkowski, Y. P. Chen, P. A. Sharma, A. L. Lima Sharma, M. A. Hekmaty, Z. Jiang, and D. Smirnov, Temperature dependence of Raman-active optical phonons in  $\text{Bi}_2\text{Se}_3$  and  $\text{Sb}_2\text{Te}_3$ , *Appl. Phys. Lett.* **100**, 071907 (2012).
- [21] F. Zhou, Y. Zhao, W. Zhou, and D. Tang, Temperature-dependent Raman scattering of large size hexagonal  $\text{Bi}_2\text{Se}_3$  single-crystal nanoplates, *Appl. Sci.* **8**, 1794 (2018).
- [22] D. Li, L. Li, D.-W. Liu, and J.-F. Li, Temperature dependence of the Raman spectra of  $\text{Bi}_2\text{Te}_3$  and  $\text{Bi}_{0.5}\text{Sb}_{1.5}\text{Te}_3$  thermoelectric films, *Phys. Status Solidi RRL* **6**, 268 (2012).
- [23] X.-L. Qi, T. L. Hughes, and S.-C. Zhang, Topological field theory of time-reversal invariant insulators, *Phys. Rev. B* **78**, 195424 (2008).
- [24] Y. Chen, J.-H. Chu, J. Analytis, Z. Liu, K. Igarashi, H.-H. Kuo, X. Qi, S.-K. Mo, R. Moore, D. Lu *et al.*, Massive Dirac fermion on the surface of a magnetically doped topological insulator, *Science* **329**, 659 (2010).
- [25] P. Sessi, R. R. Biswas, T. Bathon, O. Storz, S. Wilfert, A. Barla, K. A. Kokh, O. E. Tereshchenko, K. Fauth, M. Bode *et al.*, Dual nature of magnetic dopants and competing trends in topological insulators, *Nat. Commun.* **7**, 12027 (2016).
- [26] W. Luo and X.-L. Qi, Massive Dirac surface states in topological insulator/magnetic insulator heterostructures, *Phys. Rev. B* **87**, 085431 (2013).
- [27] P. Wei, F. Katmis, B. A. Assaf, H. Steinberg, P. Jarillo-Herrero, D. Heiman, and J. S. Moodera, Exchange-Coupling-Induced Symmetry Breaking in Topological Insulators, *Phys. Rev. Lett.* **110**, 186807 (2013).
- [28] S. Buchenau, P. Sergelius, C. Wiegand, R. Zierold, H. S. Shin, M. Rübhausen, J. Gooth, K. Nielsch *et al.*, Symmetry breaking of the surface mediated quantum Hall effect in  $\text{Bi}_2\text{Se}_3$  nanoplates using  $\text{Fe}_3\text{O}_4$  substrates, *2D Mater.* **4**, 015044 (2017).
- [29] D. Biswas, S. Thakur, K. Ali, G. Balakrishnan, and K. Maiti, Anomalies of a topologically ordered surface, *Sci. Rep.* **5**, 10260 (2015).
- [30] S. Buchenau, L. O. Akinsinde, M. Zocher, D. Rukser, U. Schürmann, L. Kienle, B. Grimm-Lebsanft, and M. Rübhausen, Scalable polyol synthesis for few quintuple layer thin and ultra high aspect ratio  $\text{Bi}_2\text{Se}_3$  structures, *Solid State Commun.* **281**, 49 (2018).
- [31] Y. Zhang, L. P. Hu, T. J. Zhu, J. Xie, and X. B. Zhao, High yield  $\text{Bi}_2\text{Te}_3$  single crystal nanosheets with uniform morphology via a solvothermal synthesis, *Crystal Growth Des.* **13**, 645 (2013).
- [32] See Supplemental Material at <http://link.aps.org/supplemental/10.1103/PhysRevB.101.245431> for details of the nanoflake synthesis and characterization, additional Raman measurements, and  $n$ -doping study of the  $\text{Bi}_2\text{Se}_3$  nanoflakes.
- [33] Y. Zhang, K. He, C.-Z. Chang, C.-L. Song, L.-L. Wang, X. Chen, J.-F. Jia, Z. Fang, X. Dai, W.-Y. Shan, S.-Q. Shen, Q. Niu, X.-L. Qi, S.-C. Zhang, X.-C. Ma, and Q.-K. Xue, Crossover of the three-dimensional topological insulator  $\text{Bi}_2\text{Se}_3$  to the two-dimensional limit, *Nat. Phys.* **6**, 584 (2010).
- [34] H. M. Benia, C. Lin, K. Kern, and C. R. Ast, Reactive Chemical Doping of the  $\text{Bi}_2\text{Se}_3$  Topological Insulator, *Phys. Rev. Lett.* **107**, 177602 (2011).
- [35] D. Kong, J. J. Cha, K. Lai, H. Peng, J. G. Analytis, S. Meister, Y. Chen, H.-J. Zhang, I. R. Fisher, Z.-X. Shen *et al.*, Rapid surface oxidation as a source of surface degradation factor for  $\text{Bi}_2\text{Se}_3$ , *ACS Nano* **5**, 4698 (2011).
- [36] B. Yan, D. Zhang, and C. Felser, Topological surface states of  $\text{Bi}_2\text{Se}_3$  coexisting with Se vacancies, *Phys. Status Solidi RRL* **7**, 148 (2013).
- [37] B. Schulz, J. Bäckström, D. Budelmann, R. Maeser, M. Rübhausen, M. V. Klein, E. Schoeffel, A. Mihill, and S. Yoon, Fully reflective deep ultraviolet to near infrared spectrometer and entrance optics for resonance Raman spectroscopy, *Rev. Sci. Instrum.* **76**, 073107 (2005).

- [38] C. Arguello, D. L. Rousseau, and S. P. d. S. Porto, First-order Raman effect in wurtzite-type crystals, *Phys. Rev.* **181**, 1351 (1969).
- [39] J. Zhang, Z. Peng, A. Soni, Y. Zhao, Y. Xiong, B. Peng, J. Wang, M. S. Dresselhaus, and Q. Xiong, Raman spectroscopy of few-quintuple layer topological insulator  $\text{Bi}_2\text{Se}_3$  nanoplatelets, *Nano Lett.* **11**, 2407 (2011).
- [40] Y. Liang, W. Wang, B. Zeng, G. Zhang, J. Huang, J. Li, T. Li, Y. Song, and X. Zhang, Raman scattering investigation of  $\text{Bi}_2\text{Te}_3$  hexagonal nanoplates prepared by a solvothermal process in the absence of naoh, *J. Alloys Compd.* **509**, 5147 (2011).
- [41] R. He, Z. Wang, R. L. J. Qiu, C. Delaney, B. Beck, T. E. Kidd, C. C. Chancey, and X. P. A. Gao, Observation of infrared-active modes in Raman scattering from topological insulator nanoplates, *Nanotechnology* **23**, 455703 (2012).
- [42] P. G. Klemens, Anharmonic decay of optical phonons, *Phys. Rev.* **148**, 845 (1966).
- [43] N. Bonini, M. Lazzeri, N. Marzari, and F. Mauri, Phonon Anharmonicities in Graphite and Graphene, *Phys. Rev. Lett.* **99**, 176802 (2007).
- [44] E. H. Hasdeo, A. R. T. Nugraha, M. S. Dresselhaus, and R. Saito, Breit-Wigner-Fano line shapes in Raman spectra of graphene, *Phys. Rev. B* **90**, 245140 (2014).
- [45] M. A. Rübhausen, Electronic correlations in cuprate superconductors - An inelastic light scattering study, Ph.D. thesis, Universität Hamburg, 1998.
- [46] M. Cardona, *Light Scattering in Solids I - Introductory Concepts*, edited by M. Cardona (Springer-Verlag, Berlin, 1983).
- [47] R. Heid, I. Yu. Sklyadneva, and E. V. Chulkov, Electron-phonon coupling in topological surface states: The role of polar optical modes, *Sci. Rep.* **7**, 1095 (2017).
- [48] T. Kondo, Y. Nakashima, Y. Ota, Y. Ishida, W. Malaeb, K. Okazaki, S. Shin, M. Kriener, S. Sasaki, K. Segawa *et al.*, Anomalous Dressing of Dirac Fermions in the Topological Surface State of  $\text{Bi}_2\text{Se}_3$ ,  $\text{Bi}_2\text{Te}_3$ , and Cu-Doped  $\text{Bi}_2\text{Se}_3$ , *Phys. Rev. Lett.* **110**, 217601 (2013).
- [49] S. Mishra, S. Satpathy, and O. Jepsen, Electronic structure and thermoelectric properties of bismuth telluride and bismuth selenide, *J. Phys.: Condens. Matter* **9**, 461 (1997).
- [50] J. Gooth, R. Zierold, P. Sergeius, B. Hamdou, J. Garcia, C. Damm, B. Rellinghaus, H. J. Pettersson, A. Pertsova, C. Canali *et al.*, Local magnetic suppression of topological surface states in  $\text{Bi}_2\text{Te}_3$  nanowires, *ACS Nano* **10**, 7180 (2016).



# 5

## Micro-Raman investigations of the TI-gold interface

In this chapter Raman investigations of single  $\text{Bi}_2\text{Se}_3$  and  $\text{Bi}_2\text{Te}_3$  nanoflakes (NFs) on gold substrates employing a micro-Raman setup are presented. The study of single NFs allows to investigate the influence of a gold substrate. Tuning the thickness of the NFs is used to identify the effect of carrier injection from the gold. The motivation for these studies is given in section 5.1. In section 5.2 details are given on the sample preparation to obtain single NF samples and section 5.3 contains all relevant information of measurement configurations and data analysis. As a preliminary study, the resonance Raman profile of  $\text{Bi}_2\text{Se}_3$  is characterized in section 5.4. Finally, the main results of the thickness dependent studies of single  $\text{Bi}_2\text{Se}_3$  and  $\text{Bi}_2\text{Te}_3$  NFs on a gold substrate revealing carrier injection and pronounced band bending at the flake-gold interface are discussed in section 5.5. A summary of the single flake investigations are given in section 5.6. The results of this chapter were published in "Carrier injection observed by interface-enhanced Raman scattering from topological insulators on gold substrates", S. Scheitz *et al.*, ACS Appl. Materials & Interfaces 14, 32625–32633 (2022).<sup>[129]</sup>

### 5.1 Motivation

As outlined in section 1.3 one of the main obstacles in exploiting the TSS for device applications is the suppression of significant contributions arising from trivial bulk electrons. Progress has been made in positioning the Fermi level of TIs within the bulk band gap and enhancing the contribution of the Dirac electrons (see section 1.3). However, enabling the charge transport solely through the Dirac surface states is especially difficult in real devices, where the deposition of electrical contacts or abutting interfaces to substrates may affect the electronic band structure of the TI. Depending on the choice of contact metal charge transfer can occur that leads to band bending at the TI/metal interface and population of bulk states.<sup>[149,150]</sup> The positioning of the Fermi level at the interface is hence relevant in the determination of the topological properties of the device. Due to  $\text{Bi}_2\text{Se}_3$  largest bulk band gap within the bismuth chalcogenides TIs, which in principle allows access to the Dirac cone over a broad energy range, the interface of  $\text{Bi}_2\text{Se}_3$  to several contact metals is of high interest. Here, the study was conducted with the focus on the TI interface to gold, since gold is among the most commonly used contact metals in TI-based devices.<sup>[151–153]</sup> Additionally, gold is expected to show chemical inertness and no hybridization with the TSS, which was confirmed experimentally in XPS measurements<sup>[149]</sup> and theoretically via *ab initio* calculations.<sup>[150]</sup> However, the significant carrier injection from Au into  $\text{Bi}_2\text{Se}_3$

is predicted<sup>[150]</sup>, which has to be considered for ultrathin TI layers as the band bending might consume the topmost TI QLs and impede their application. Therefore, the effect of band bending at the interface of gold to ultrathin Bi<sub>2</sub>Se<sub>3</sub> and Bi<sub>2</sub>Te<sub>3</sub> is of high importance to study, with the aim to determine possible limitations in the TI thickness.

An exclusive study of the TI/gold interface is difficult to perform as the contact is often obscured. Here, Raman scattering of thin TI NFs on gold substrates enables a non-contact experimental technique to study the sole influence of the metal interface. Furthermore, Raman spectroscopy is a volume scattering technique and allows to study the concealed TI/Au interface, which is the main challenge for surface sensitive techniques like ARPES<sup>[154]</sup> or scanning tunneling spectroscopy (STS).<sup>[155]</sup> By tuning the thickness of the NFs placed on Au substrate the dimensions of band bending effects due to carrier injection are identified. Additionally, by analyzing the phonon line shapes the interactions between the lattice and available electrons are studied.

To increase the low Raman intensity expected from measurements of ultrathin single NFs, and detect possibly subtle line shape changes as a function of NF thickness, the most suitable excitation wavelength was determined. For the preliminary resonance Raman study five excitation wavelengths were chosen in the visible frequency range. In this spectral range Bi<sub>2</sub>Se<sub>3</sub> shows the largest absorption coefficient,<sup>[64]</sup> which is expected to originate from resonant electronic interband transitions. The resonance Raman study allows the identification of resonance conditions where a high signal is expected. The high intensities enable a high accuracy for the analysis of Raman spectra in the subsequent thickness dependent study.

## 5.2 Sample Preparation of single NFs

The NFs used for the micro-Raman study were synthesized using the wet-chemical process as explained in chapter 2 and the exact synthesis parameters are given in Table B.1. To remove solvent and precursor residues the Bi<sub>2</sub>Se<sub>3</sub> and Bi<sub>2</sub>Te<sub>3</sub> NFs were washed in isopropanol and acetone equivalent to procedure presented in the macro-Raman chapter section 4.2 and finally stored in isopropanol. To investigate single NFs the solutions were further diluted by mixing 250  $\mu$ L of the purified NF solution with 750  $\mu$ L isopropanol. Samples of individual NFs on silicon and sputtered gold substrates were prepared by drop casting 5  $\mu$ L of the diluted NFs onto the substrates and the isopropanol was allowed to evaporate at room temperature. In Figure 5.1 the schematic sample preparation on Si and Au substrates is shown as well as light microscopy and SEM images of the produced samples.

The used Si and Au substrates featured a micro-grid that allowed for the identification of individual NFs and measure the same NFs with several techniques like micro-Raman spectroscopy, AFM, and SEM. For the Si substrates commercially bought Bor-doped Si(100) substrates (EM-Tec FG1 silicon finder grid substrate) were used that featured



a 1000  $\mu\text{m}$  pitch chromium grid (25 mesh) as schematically shown in Figure 5.1(b). The silicon substrate has a native oxide layer of about 2 nm and was used without further purification.

Gold substrates were prepared via RF-sputtering, where a 10 nm chromium adhesion layer was coated on Si(100) substrate followed by a 100 nm layer of gold. Both metals were deposited in a Cressington 308R coating system equipped with two DC sputter sources (Au,Cr) without vacuum break at 40 mA current for 2 min and 10 min, respectively. The base pressure was 1E-6 mbar and was adjusted to 0.01 mbar during deposition. A finder grid on the Au substrate was custom fashioned by scratching a grid with a 500  $\mu\text{m}$  pitch into the gold layer, as schematically shown in Figure 5.1(a), using a custom-made setup employing a scalpel blade. A photograph of the setup and detailed explanation on the grid manufacturing is given in Appendix C.2.1. As apparent from the SEM micrograph in Figure 5.1(e) the sputtered gold films exhibit a rough surface with grain sizes in the range of 40 nm.

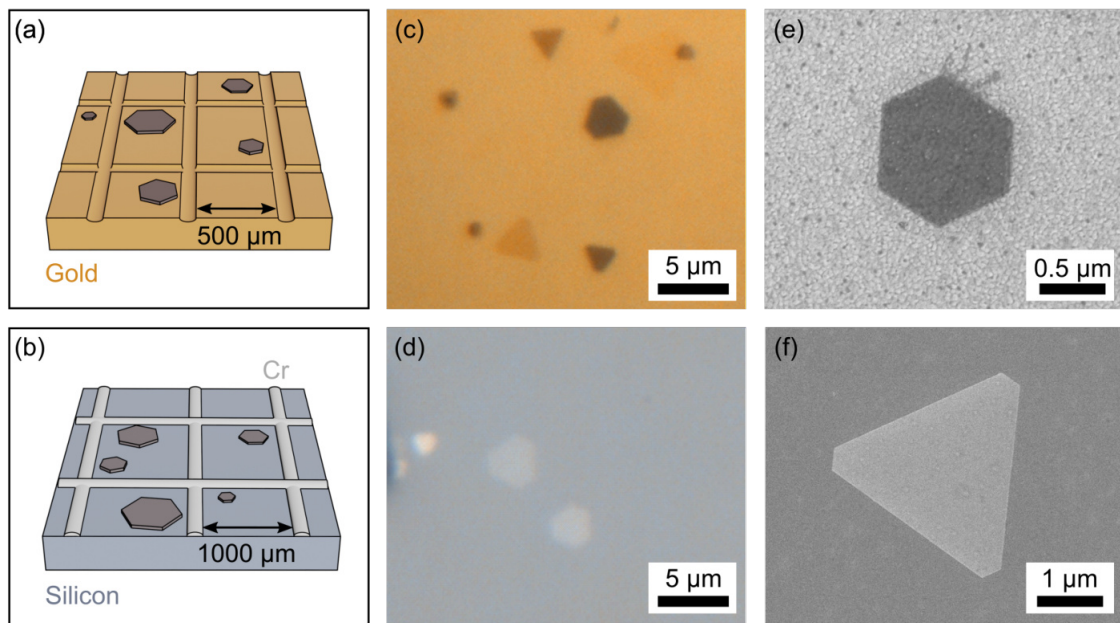


**Figure 5.1:** Preparation of single  $\text{Bi}_2\text{Se}_3$  and  $\text{Bi}_2\text{Te}_3$  NF samples on Au and Si substrates for micro-Raman measurements in the top and bottom row, respectively. (a,b) Schematic illustration of the drop cast single NFs on Au and Si finder grid substrates, respectively. The NFs size is strongly exaggerated for better visibility. (c,d) Optical microscope images of the investigated  $\text{Bi}_2\text{Se}_3$  NFs on Au and Si substrates, respectively.  $\text{Bi}_2\text{Te}_3$  samples look similarly. (e,f) SEM micrographs of the NFs on Au and Si substrates, respectively. On the Au substrate the rough surface due to grain formation during the sputtering process is visible.

### 5.3 Measurement configuration and data analysis

Raman spectroscopy on single Bi<sub>2</sub>Se<sub>3</sub> and Bi<sub>2</sub>Te<sub>3</sub> NFs was conducted using the custom-made micro-Raman setup presented in section 3.2.1. For the study of the resonance Raman profile of individual Bi<sub>2</sub>Se<sub>3</sub> NFs on Si and Au substrate five excitation wavelengths in the visible range were employed. The laser source specifications for each excitation line are given in Table 3.3.

#### Employed laser powers

The surface laser power densities employed for the single NF measurements on Si and Au substrates at all wavelengths are presented in Table 5.1. The power densities and suitable integration times were determined via an iterative trial and error process. The here presented measurement configurations allowed for a detection of Raman spectra with a good signal to noise ratio and at least three accumulations per measured NF. In general, for all measurements the exclusion of beam damage was verified by (i) visual review of the investigated NF after every accumulation and (ii) stability of the Raman signal regarding identical intensities and phonon positions. In addition, to further increase the distribution of laser energy in the NFs the laser spot was scanned over the NF surface in areas of 2  $\mu\text{m}^2$  to 4  $\mu\text{m}^2$  during the measurement.

**Table 5.1:** Surface laser power densities  $PD$  in kW/cm<sup>2</sup> and integration times  $t_{\text{int}}$  in min for single NF measurements.

wavelength	705 nm		633 nm		594 nm		560 nm		532 nm	
	$PD$	$t_{\text{int}}$	$PD$	$t_{\text{int}}$	$PD$	$t_{\text{int}}$	$PD$	$t_{\text{int}}$	$PD$	$t_{\text{int}}$
Bi <sub>2</sub> Se <sub>3</sub> /Si	167	30	175	30	223	20	50	30	106	30
Bi <sub>2</sub> Se <sub>3</sub> /Au	167	10	114	20	223	5	18	10	106	10
Bi <sub>2</sub> Te <sub>3</sub> /Au	-	-	255	30	-	-	-	-	-	-

#### General data treatment

Acquired Raman spectra were normalized to the used integration time and laser power. The laser power at the sample position was measured with a Si photodiode power meter (PM160, Thorlabs). Furthermore, all normalized spectra were background corrected by subtraction of a pure substrate (Si or Au, respectively) measurement. The substrate measurements were also normalized to integration time and power and usually measured under the same conditions as the associated NF measurements.

#### Spectral analysis in the resonance Raman study

In the resonance Raman study all phonon modes were modeled by Lorentzian profiles

according to Equation (3.13) given by

$$I(\omega) = \frac{A\omega\Gamma}{(\omega^2 - \omega_0^2)^2 + (\Gamma\omega)^2}, \quad (5.1)$$

with a scaling prefactor  $A$ . The Raman susceptibilities of the modes were determined by calculating the maximum mode intensities as  $I^{\max} = A/\omega_0\Gamma$ . Since several NFs were measured within the scope of the resonance Raman study, the extracted mode intensities were further corrected for the varying thicknesses of the NFs and varying optical response due to the use of the different excitation energies. To include all factors regarding the specific NF properties at each excitation wavelength a correction factor  $CF$  was determined. The Raman correction factors for each measured NF included an effective scattering volume  $V_i^{\text{eff}}$  and the effective transmission  $T_i^{\text{eff}}$  of laser signal into the NFs.

First, the effective transmission  $T_i^{\text{eff}}$  is given by the fraction of laser signal  $T_i^{\text{eff}} = |1 - R(\nu_i)|^2$  transmitted into the NF and contributing to the Raman process, with  $R(\nu_i)$  being the reflectivity as a function of excitation energy  $\nu_i$ . The reflectivity  $R(\nu_i)$  of  $\text{Bi}_2\text{Se}_3$  is given as

$$R(\nu_i) = \left| \frac{n_1 - n_2}{n_1 + n_2} \right|^2,$$

with  $n_{1,2}(\nu_i)$  being the real refractive index of air ( $n_1 = 1$ ) and  $\text{Bi}_2\text{Se}_3$ , respectively. The laser energy dependent refractive index  $n_2$  and absorption coefficient  $k$  of  $\text{Bi}_2\text{Se}_3$  were obtained from the dielectric function calculated by Zhang *et al.*<sup>[64]</sup> and selected values for the used excitation energies in this study are given in Table 5.2. The effective transmission as a function of excitation energy is given in Figure 5.2(b).

Secondly, the effective scattering volume  $V_i^{\text{eff}}$  of each measured NF is determined by the illuminated volume as schematically shown in Figure 5.2(a) that changes with the diffraction angle  $\theta'_i$ . The contributing NF volume estimated by a cone will have a penetration depth dependent radius  $r_i(z)$  due to the dispersion of the laser, which is calculated by  $r_i(z) = r_0 + z \cdot \tan\theta'_i$ . Here,  $r_0$  is the laser spot radius, which was determined during the characterization of the micro-Raman setup in Figure 3.9, and  $\theta'_i$  is the laser energy dependent diffraction angle as shown in Figure 5.2(a).  $\theta'_i$  is calculated via Snellius' law,  $\sin\theta'_i = \frac{1}{n_1} \sin\theta$ , where  $\sin\theta = 0.75$  is determined by the used focusing objective.

Lastly, due to the absorption of laser signal with increasing penetration depth in the NF, each atomic layer will be exposed to a different laser intensity and hence contribute less to the overall Raman signal. The change in laser intensity is given by Lambert-Beer's law,  $I(z) = e^{-\alpha_i z}$ , with the NF thickness  $z$  and absorption coefficient  $\alpha_i = \frac{2k_i\nu_i}{c}$ , where  $c$  is the speed of light in vacuum. Please note, that the penetration depth  $\alpha_i^{-1}$  of all used lasers for  $\text{Bi}_2\text{Se}_3$  is around 9 nm as shown in Figure 5.2(c), with only the 705 nm excitation line having a slightly larger penetration depth of 12 nm.

Similarly, the generated Raman signal is reabsorbed before exiting the NF depending on the depth. The reabsorption is also accounted for in again applying Lambert-Beer's law,

where the same frequency of excitation and Raman frequency  $\nu_i \approx \omega_i$  is assumed. The effective scattering volume is hence calculated by the laser intensity integrated over the NF thickness and reabsorption of the Raman signal as

$$V_i^{\text{eff}} = \int_0^z e^{2\frac{-2k_i\nu_i}{c}z} \cdot \pi r_i(z)^2 dz,$$

with values of all measured NFs given in Figure 5.2(d,e). The integration range was adapted to the investigated NF thickness respectively. In Table 5.2 the thickness of each NF measured for the resonance Raman study on silicon and gold is given. For a reference bulk sample an integration range of 20 nm was selected for all energies, as the effective laser intensity for all  $\nu_i$  has decreased below 20 %. The resulting correction factors  $CF$  for each measurement are shown in Table 5.2 and calculated by

$$CF_i = T_i^{\text{eff}} \cdot V_i^{\text{eff}}.$$

The Raman susceptibilities  $\chi^{\text{max}}$  of the  $\text{Bi}_2\text{Se}_3$  phonon modes for all excitation energies and investigated NFs are finally obtained by dividing the maximum peak intensities by the associated correction factors:

$$\chi^{\text{max}}(\nu_i) = \frac{I^{\text{max}}(\nu_i)}{CF_i}. \quad (5.2)$$

**Table 5.2:** Optical properties and parameters critical for the calculation of resonance Raman correction factors.

Laser wavelength $\lambda_i$ (nm)	Laser energy $\nu_i$ (eV)	$\text{Bi}_2\text{Se}_3$ $n_2$	$\text{Bi}_2\text{Se}_3$ $k_i$	Diffraction angle $\theta'_i$ (°)	Laser spot $r_0$ (nm)	NF thickness $z$ on Si (nm)	NF thickness $z$ on Au (nm)
704.96	1.76	5.78	4.59	7.46	141.5	11.8	15.1
632.82	1.96	4.26	5.47	10.14	106.0	11.8	15.1
593.72	2.09	3.51	5.30	12.34	134.5	17.1	15.1
560.35	2.21	2.87	4.92	15.15	194.0	11.3	15.1
532.04	2.33	2.42	4.70	18.05	127.5	15.8	14.5

### Spectral analysis in the NF thickness dependent Raman study on gold

The thickness dependent Raman study of  $\text{Bi}_2\text{Se}_3$  and  $\text{Bi}_2\text{Te}_3$  NFs on Au substrates was conducted with the 633 nm excitation line. To analyze the phonon mode line shapes different fit functions were employed for the  $A_{1g}$  and  $E_{g,u}$  modes. Due to their asymmetric profile the two  $A_{1g}$  modes were fit by a Fano profile<sup>[96]</sup> according to

$$I(\omega) = A \cdot \frac{(q + \frac{\omega - \omega_0}{\Gamma})^2}{1 + (\frac{\omega - \omega_0}{\Gamma})^2}, \quad (5.3)$$

where the maximum Raman susceptibilities of the modes were determined as  $I^{\max} = Aq^2$ . The  $E_g^2$  mode and an adjacent mode were fit with the Lorentzian profile given by Equation (5.1) since the two modes showed strong overlap.

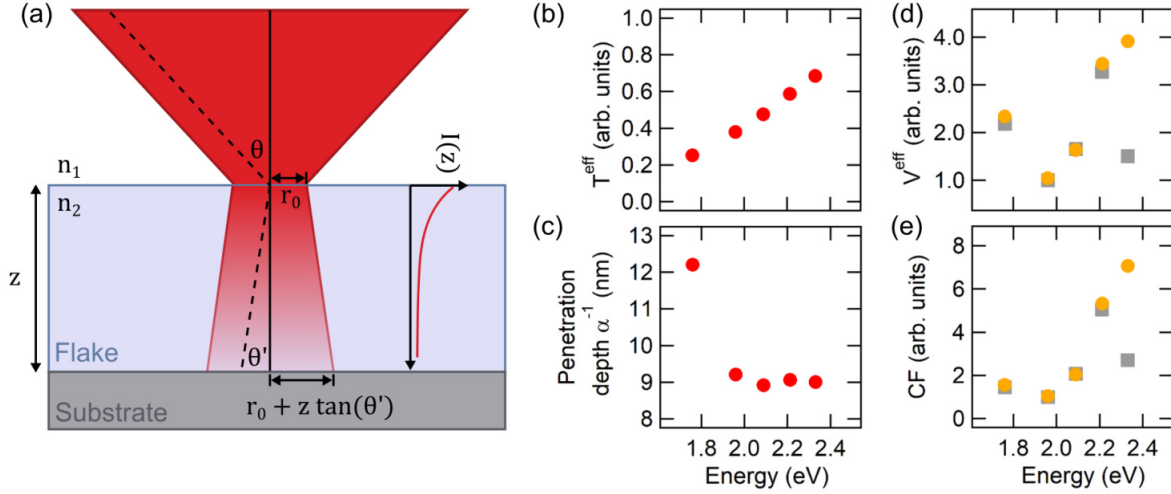


**Figure 5.2:** Effective scattering volume of NFs measured for the resonance Raman study. (a) Schematic cross section of a  $\text{Bi}_2\text{Se}_3$  NF illuminated by the focused laser beam. The laser (red cone) is focused onto the NF resulting in a beam spot radius of  $r_0$ . The laser disperses into the NF according to the laser energy dependent refractive index  $n_2$ . The scattering volume of the NF contributing to the Raman signal, indicated by the faded red area, is estimated by a truncated cone. The decreasing laser intensity  $I(z)$  with NF thickness according to Lambert-Beer's law is shown as an inset on the right side of the NF. (b-d) Excitation energy dependent values for the effective transmission  $T_i^{\text{eff}}$ , penetration depth  $\alpha_i^{-1}$ , effective scattering volume  $V_i^{\text{eff}}$ , and correction factor  $CF_i$ , respectively. In (d,e) values depicted by gray squares correspond to the measured NFs on silicon and yellow circles correspond to NFs on gold, respectively. The values in (d,e) are normalized to the smallest value of all investigated NFs. Reprinted with permission from<sup>[129]</sup>. Copyright 2022 American Chemical Society.

## 5.4 Results - Resonance Raman study of Bi<sub>2</sub>Se<sub>3</sub> on Si and Au substrates

The resonance Raman spectra for single Bi<sub>2</sub>Se<sub>3</sub> NFs on silicon and gold substrates for excitation wavelengths of 532 nm, 560 nm, 594 nm, 633 nm, and 705 nm are presented in Figure 5.3(a). On both Si and Au substrates the Bi<sub>2</sub>Se<sub>3</sub> spectra show the two bulk E<sub>g</sub><sup>2</sup> and A<sub>1g</sub><sup>2</sup> phonon modes for all excitation wavelengths. Depending on the wavelength the resolution of the spectrometer on the CCD sensor changes, which leads to lower resolutions and a shift of the lowest bulk A<sub>1g</sub><sup>1</sup> mode closer to the elastic Rayleigh signal for decreasing wavelengths. As a result, the lowest bulk A<sub>1g</sub><sup>1</sup> mode was cut from the spectra by the relay stage for lower excitation wavelengths and, therefore, this study focuses on the analysis of the two higher frequency modes. As apparent from the spectra in Figure 5.3(a) the Raman signals for all measurements of NFs on the gold substrate are significantly enhanced in comparison

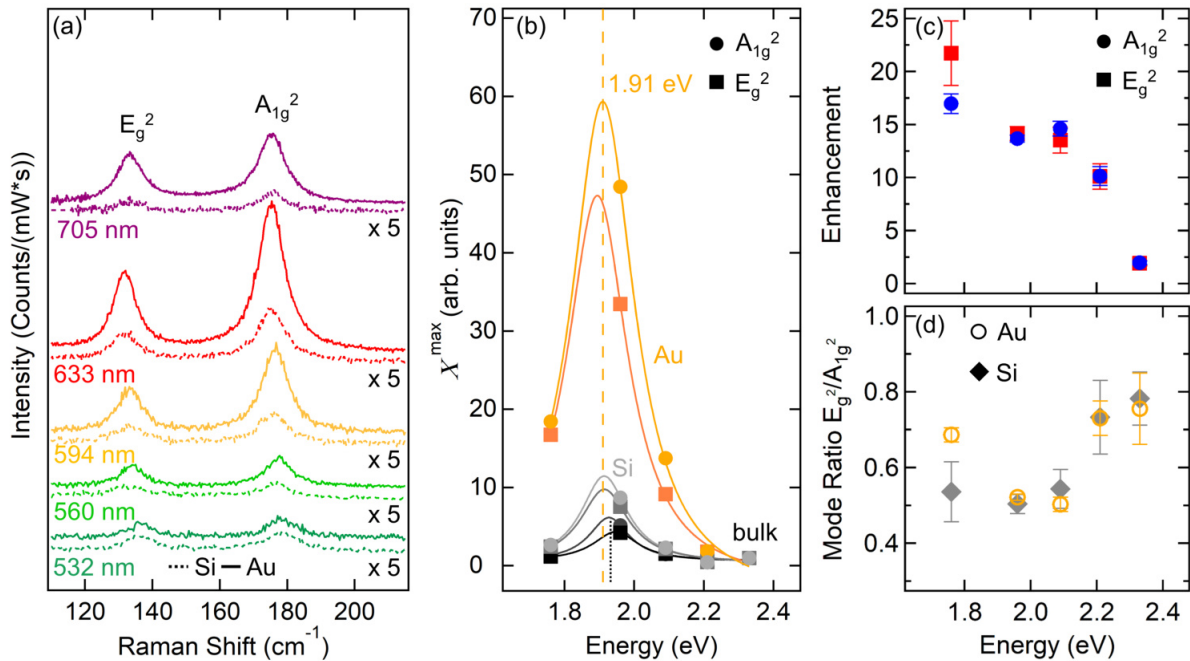


**Figure 5.3:** Resonance Raman spectra of single Bi<sub>2</sub>Se<sub>3</sub> NFs on Si and Au substrates. (a) Raman spectra of single NFs on silicon (dotted) and gold (solid) substrates for five selected excitation energies given next to the graphs. All spectra normalized to laser power and integration time and displayed with an offset. Spectra acquired on Si are multiplied by a factor of five. (b) Resonance Raman profiles of the E<sub>g</sub><sup>2</sup> (squares) and A<sub>1g</sub><sup>2</sup> (circles) phonon susceptibilities as a function of energy corresponding to the excitation wavelength given in (a). Gray and yellow markers refer to the spectra of the NFs on Si and Au, respectively. Black markers correspond to a reference Bi<sub>2</sub>Se<sub>3</sub> bulk sample. All values are normalized to 532 nm (2.33 eV). Lorentzian fits of the profiles are shown and dashed and dotted lines indicate the resonance energies of the NFs on Au and the bulk sample, respectively. (c) Enhancement of the E<sub>g</sub><sup>2</sup> (squares) and A<sub>1g</sub><sup>2</sup> (circles) susceptibilities for NFs on Au in comparison with NFs on Si. (d) Susceptibility ratios of the E<sub>g</sub><sup>2</sup> to A<sub>1g</sub><sup>2</sup> modes for the NFs on Si (gray diamonds) and Au (yellow open circles). Adapted with permission from<sup>[129]</sup>. Copyright 2022 American Chemical Society.

with the signal obtained from NFs on silicon.

The Raman susceptibilities of the  $E_g^2$  and  $A_{1g}^2$  were extracted from Lorentzian fits to the data and are corrected for the dielectric properties of  $\text{Bi}_2\text{Se}_3$  as well as the scattering volume of each NF. Details on the correction factors and investigated NFs are given in section 5.3. The Raman susceptibility resonance profiles for the NFs on Au and Si substrates as well as a reference bulk sample are shown in Figure 5.3(b). For all three sample configurations the Raman signal shows the strongest intensity for the 633 nm excitation line. Hereby, the bulk sample shows a moderate signal increase when tuning into resonance, whereas the Raman signal of NFs on silicon increases by a factor of 10. This resonance of  $\text{Bi}_2\text{Se}_3$  has been observed before<sup>[118,156]</sup> and can be assigned to an electronic interband transition at the  $\Gamma$  point in resonance with the incoming excitation laser at 1.96 eV.<sup>[157–159]</sup> An even more remarkable effect is observed for the NFs on gold substrate that give a stronger signal for all energies in comparison with NFs on silicon. Additionally, they show an enhanced resonance profile with a signal increase by even a factor of 50 when tuning into the red. The resonance profiles were fit by a Lorentzian function given in Figure 5.3(b) and clearly reveal similar sharp resonance positions at  $1.94 \pm 0.06$  eV (bulk) and  $1.91 \pm 0.03$  eV (NFs), both of which are close to the 1.96 eV (633 nm) excitation line. The similar resonance positions indicate that in all three  $\text{Bi}_2\text{Se}_3$  sample geometries the intrinsic resonance due to electronic interband transitions is available.

We now turn to the observed signal enhancement and pronounced resonance profiles for NFs on silicon and especially gold substrates. At all energies the extracted Raman susceptibilities of the bulk sample is the smallest in comparison with the NF samples. This effect has been observed before in few nm thick  $\text{Bi}_2\text{Se}_3$  and  $\text{Bi}_2\text{Te}_3$  nanoplate samples but was not addressed further.<sup>[64,117,160]</sup> Due to the penetration depth of around 9 nm in the visible spectra range, see also Figure 5.2(c), the bulk and NF samples actually yield similar scattering volumes. Yet, the thin NFs on gold substrate show a strongly enhanced Raman response. The enhancement of the Raman susceptibilities of both phonon modes is quantified by comparing the peak susceptibilities of the silicon and gold measurements. The determined enhancement factor  $EF = \chi_{\text{Au}}^{\text{max}} / \chi_{\text{Si}}^{\text{max}}$  is given in Figure 5.3(c) and shows an increasing enhancement as the incident photon energy is tuned to lower energies. The strongest relative signal enhancement by a factor of about 20 is found for the 1.76 eV excitation energy, which is at slightly lower energies compared to the resonance position at 1.91 eV.

To understand the origin of the signal enhancement by the gold substrate the relative Raman susceptibilities of the  $E_g^2$  to the  $A_{1g}^2$  modes are examined. The mode ratio decreases when approaching the resonance energy as shown in Figure 5.3(d). At the resonant excitation energy of 1.96 eV the  $A_{1g}^2$  mode shows a stronger enhancement, which results in a decreasing susceptibility ratio of  $E_g^2$  to  $A_{1g}^2$ . This trend is observed for NFs on both, silicon and gold substrates. The observations of identical resonance energies and mode ratios for NFs on silicon and gold lead to the conclusion that the

resonance is intrinsic to the  $\text{Bi}_2\text{Se}_3$  NFs. However, for the NFs on a gold substrate this intrinsic resonance is strongly enhanced by a factor of 14 (see Figure 5.3(c)). The pronounced enhancement of the resonance profile is a first indicator that the Au substrate modifies the conditions for resonant interband transitions in  $\text{Bi}_2\text{Se}_3$ . In order to further characterize the influence of the gold substrate on the NFs and determine the origin of the resonance enhancement, a systematic study of NFs with varying thicknesses was conducted. The change of the resonant interband transitions in  $\text{Bi}_2\text{Se}_3$  due to the gold interface is, therefore, fully discussed in the following sections. As a preliminary result the resonance energy of the  $\text{Bi}_2\text{Se}_3$  NFs was determined to lie around 1.91 eV. Therefore, all following measurements of single NFs ( $\text{Bi}_2\text{Se}_3$  and  $\text{Bi}_2\text{Te}_3$ ) were conducted with the 1.96 eV excitation line corresponding to 633 nm.

## 5.5 Results - Carrier injection by Au substrate

The influence of a gold interface to the intrinsic properties of the ultrathin TI  $\text{Bi}_2\text{Se}_3$  and  $\text{Bi}_2\text{Te}_3$  NFs was investigated by systematically varying the thickness of the NFs on the same gold substrate. The study of NFs on the same gold substrate allows to assign all changes in the Raman spectra to the changing NF thickness. Figure 5.4(a) shows selected Raman spectra of  $\text{Bi}_2\text{Se}_3$  NFs with decreasing thicknesses between 12.5 nm to 7.7 nm. Even though the NFs vary only by a few nanometer in thickness, this change is already evident in the optical microscope images given next to the spectra. With decreasing thickness the NFs show a drastic change in their optical contrast (OC). In fact, it can be shown that the thickness  $d$  of investigated NFs shows a linear correlation to their OC. The OC is defined by the ratio of average grayscale values of the NF compared to the values obtained from the gold substrate. Since the thickness of the NFs determined by AFM measurements typically gives uncertainties of about  $\pm 1$  nm the quantification of the NFs OC was used to precisely study the changes in Raman spectra as a function of thickness. The correlation of the OC to the measured NF thickness via AFM is described in detail in appendix C.2.2. For  $\text{Bi}_2\text{Se}_3$  thick NFs obtain high OCs with values above 50 (corresponding to  $d > 12$  nm) that decrease down to a value of 32 for thinner NFs of around 8 nm. The OC values obtained for the investigated NFs are given next to the spectra in Figure 5.3(a).

### NF thickness dependent phonon renormalizations

The Raman spectra obtained from thicker NFs ( $OC > 50$ ) show the expected three bulk modes of  $A_{1g}^1$  ( $63.18 \pm 0.02 \text{ cm}^{-1}$ ),  $E_g^2$  ( $123.08 \pm 0.04 \text{ cm}^{-1}$ ) and  $A_{1g}^2$  ( $166.41 \pm 0.02 \text{ cm}^{-1}$ ) symmetry, with the frequencies obtained from the thickest measured NF given in parentheses. As the NFs get thinner all three bulk phonon modes experience renormalization that is clearly observed from the recorded spectra. In particular, the two  $A_{1g}$  modes shift in frequency and the  $E_g^2$  mode splits into a double peak feature. The mode frequencies and line widths extracted from the fits, as explained in section 5.3, are



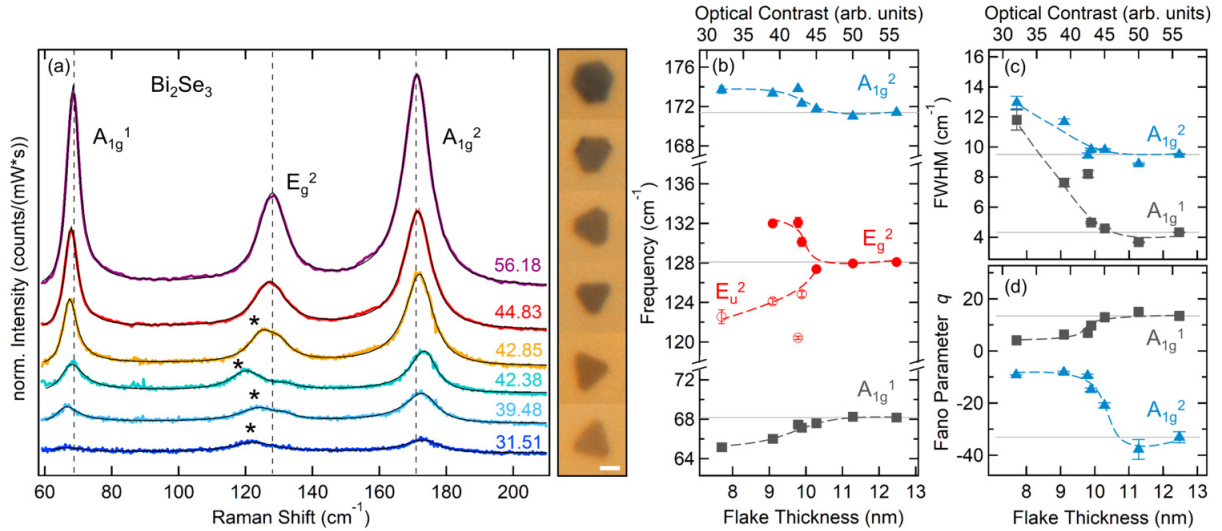


**Figure 5.4:** Phonon renormalization in Bi<sub>2</sub>Se<sub>3</sub> NFs with varying thickness on the same gold substrate. (a) Raman spectra of six individual NFs with decreasing thicknesses from 12.5 nm ( $OC = 56.18$ ) to 7.7 nm ( $OC = 31.51$ ) (see Table C.3 in the appendix). Corresponding microscope images of the measured NFs are shown to the right of the spectra. The scale bar is 2  $\mu\text{m}$ . The three bulk phonon modes  $A_{1g}^1$ ,  $E_g^2$ , and  $A_{1g}^2$  are labeled as well as a growing IR mode marked by asterisks. Vertical dashed lines are given as a guide to the eye corresponding to the mode frequencies for the thickest NF. The OCs of the NFs is given next to their corresponding spectra. Renormalization of (b) mode frequencies, (c) FWHM, and (d) extracted Fano parameters with NF thickness. Dashed lines represent guides to the eye. For reference, phonon frequencies, FWHM, and Fano parameters measured from the thickest NF are given as solid gray lines in (b-d). Reprinted with permission from<sup>[129]</sup>. Copyright 2022 American Chemical Society.

shown in Figure 5.4(b,c). In the range of thicker NFs the extracted bulk phonon mode frequencies are constant. However, when the NFs reach a critical OC of 45 ( $d < 10$  nm) the mode frequencies show abrupt and strong renormalizations. The  $A_{1g}^1$  mode softens by  $3 \text{ cm}^{-1}$ , whereas the  $A_{1g}^2$  hardens by  $2.6 \text{ cm}^{-1}$  in the investigated range of NF thicknesses. This frequency renormalization is accompanied by a broadening of the mode's FWHM of  $8 \text{ cm}^{-1}$  and  $4 \text{ cm}^{-1}$ , respectively, as shown in Figure 5.4(c). The frequencies and line widths of the  $A_{1g}$  modes were extracted from Fano fits to account for the asymmetric line shapes. By examining the asymmetry parameter, or Fano parameter,  $q$  as a function of NF thickness, an increased asymmetry in the  $A_{1g}$  mode line shapes is detected as shown in Figure 5.4(d). The low-energy  $A_{1g}^1$  mode exhibits an asymmetric line shape with additional spectral weight at higher energies yielding positive values of  $q$ , whereas the  $A_{1g}^2$  mode is more asymmetric to its low energy side and yields negative  $q$  values. In agreement with the strong phonon renormalizations, the asymmetry is pronounced for NFs at a critical OC of 45 corresponding to a thickness of 10 nm. In addition to the renormalization of the  $A_{1g}$  phonons, the appearance of a new mode at the low energy side of the  $E_g^2$  phonon is observed.

An equivalent study on Bi<sub>2</sub>Te<sub>3</sub> NFs with varying thicknesses on gold reveals the same

critical phonon behaviour with thickness as in  $\text{Bi}_2\text{Se}_3$ . Figure 5.5(a) shows the thickness dependent Raman spectra acquired for single  $\text{Bi}_2\text{Te}_3$  NFs in the range of 18 nm to 9 nm. The optical micrographs of the investigated NFs are shown next to the spectra. Also in  $\text{Bi}_2\text{Te}_3$  NFs the thickness can be correlated to the OC, which is shown in detail in appendix C.2.2. The thickness dependence of the recorded Raman spectra of  $\text{Bi}_2\text{Te}_3$  contains the same features as the  $\text{Bi}_2\text{Se}_3$  study. Firstly, for all NFs the three bulk phonon modes of  $A_{1g}^1$  ( $61.53 \pm 0.03 \text{ cm}^{-1}$ ),  $E_g^2$  ( $101.80 \pm 0.02 \text{ cm}^{-1}$ ) and  $A_{1g}^2$  ( $133.49 \pm 0.11 \text{ cm}^{-1}$ ) symmetry are detected. The frequencies of the thickest investigated NF given in parentheses show good agreement with literature values (see also Table A.1). Secondly, a critical NF thickness can be identified that leads to phonon renormalizations equivalent to  $\text{Bi}_2\text{Se}_3$ . In  $\text{Bi}_2\text{Te}_3$  NFs with OCs below 34 the phonons experience similar deviations in frequency, line width and Fano parameter (see Figure 5.5(b-d)) in comparison with the values obtained for the thickest investigated NFs. In detail, the  $A_{1g}^1$  and  $A_{1g}^2$  modes show a strong softening by  $6.9 \text{ cm}^{-1}$  and a hardening by  $3 \text{ cm}^{-1}$ , respectively, accompanied by an increase in FWHM of  $6 \text{ cm}^{-1}$  and even  $13 \text{ cm}^{-1}$ . Both  $A_{1g}$  modes again show a slight asymmetry, which is better described by the employed Fano profile and yields for thin NFs ( $d < 12 \text{ nm}$ ) positive and negative  $q$  values for the  $A_{1g}^1$  and  $A_{1g}^2$  modes, respectively (Figure 5.5(d)).

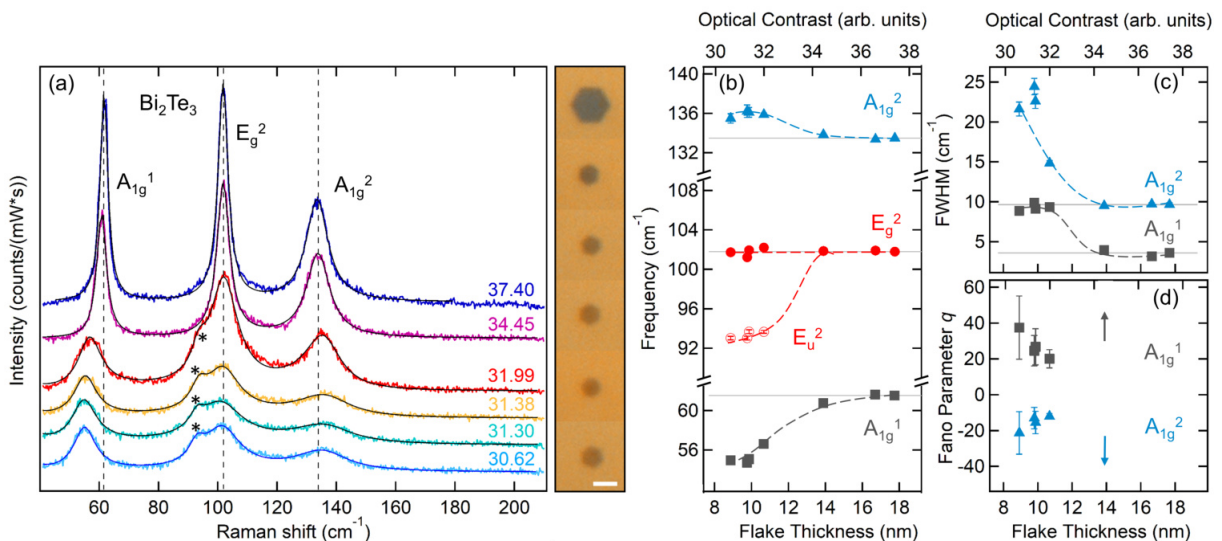


**Figure 5.5:** Phonon renormalization in  $\text{Bi}_2\text{Te}_3$  NFs with varying thickness on the same gold substrate. (a) Raman spectra of six individual NFs with decreasing thicknesses from 17.7 nm ( $OC = 37.40$ ) to 8.9 nm ( $OD = 30.62$ ) (see Table C.3 in the appendix). Corresponding microscope images of the measured NFs are shown to the right of the spectra with a  $2 \mu\text{m}$  scale bar. The three bulk phonon modes  $A_{1g}^1$ ,  $E_g^2$ , and  $A_{1g}^2$  are labeled as well as a growing IR mode marked by asterisks. Dashed lines are given as a guide to the eye corresponding to the mode frequencies for the thickest NF. Renormalization of (b) mode frequencies, (c) FWHM, and (d) Fano parameter with NF thickness. Dashed lines represent guides to the eye. For reference, phonon frequencies and FWHM measured from the thickest NF are given as solid gray lines in (b,c). In (d) the Fano parameters for the  $A_{1g}$  modes in thick NFs ( $d < 14 \text{ nm}$ ), which obtained very high values due to their symmetrical line shape, are indicated by arrows. Reprinted with permission from<sup>[129]</sup>. Copyright 2022 American Chemical Society.

Furthermore, the same appearance of an additional mode at the low energy side of the  $E_g^2$  phonon is detected in NFs with OCs below the critical value. The mode is marked by an asterisk in Figure 5.5(a).

Before analyzing the phonon renormalizations in both  $\text{Bi}_2\text{Se}_3$  and  $\text{Bi}_2\text{Te}_3$  the identification and origin of the additional modes in thin NFs is discussed in the next paragraph.

### Inversion symmetry breaking in thin $\text{Bi}_2\text{Se}_3$ and $\text{Bi}_2\text{Te}_3$ NFs on Au substrate

As the thickness of the  $\text{Bi}_2\text{Se}_3$  NFs reduces below 11 nm an additional mode is recorded in the Raman spectra that splits from the bulk  $E_g^2$  mode by as much as  $10\text{ cm}^{-1}$  as shown in Figure 5.4(b). The emerging phonon in thin NFs is marked by an asterisk in Figure 5.4(a) and can be assigned to a bulk IR-active mode that becomes Raman-active due to pronounced inversion symmetry breaking at the surface of thin NFs. The mode appearing at  $124\text{ cm}^{-1}$  fits well to the in-plane vibrational IR mode of  $E_u^2$  symmetry. As explained in section 3.1.6 the reduction of inversion symmetry for thin NFs leads to altered Raman selection rules that allow for the detection of previously exclusive IR-active modes. In comparison with literature the  $E_u^2$  mode has been identified in Raman measurements on bulk samples at cryogenic temperatures of below 13 K<sup>[62,113]</sup> and for thin film samples below 9 nm thickness at slightly elevated temperatures of 80 K.<sup>[115]</sup> (see also Table A.2). The appearance of this mode even at room temperature Raman measurements again highlights the strong enhancement by the underlying gold substrate. Assigning the mode to the  $E_u^2$  phonon is justified by polarization dependent measurements of several NFs with varying thickness, shown in Figure C.6. The constant Raman intensity measured in both xx and xy geometry confirms the E symmetry of the emerging mode, which is shown for an exemplary thin  $\text{Bi}_2\text{Se}_3$  NF in Figure 5.6(a).

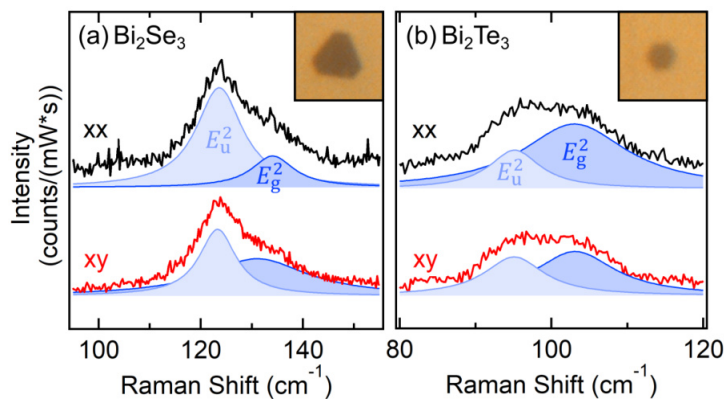


**Figure 5.6:** Inversion symmetry breaking in thin 2D NFs on Au substrates. Polarization dependent measurements of (a) a thin  $\text{Bi}_2\text{Se}_3$  ( $OC = 39.0$ ) and (b)  $\text{Bi}_2\text{Te}_3$  ( $OC = 29.5$ ) NF, with optical micrographs of the NFs shown in the insets. In both polarization configurations of xx (black) and xy (red) geometry the Raman intensity is constant confirming the E symmetry. The blue graphs show the deconvoluted profiles obtained from Lorentzian fits to the spectra. Adapted with permission from<sup>[129]</sup>. Copyright 2022 American Chemical Society.

Equivalently, in thin  $\text{Bi}_2\text{Te}_3$  NFs with thicknesses below 11 nm, corresponding to OCs below 34, the emerging mode with frequency around  $93.5\text{ cm}^{-1}$  can also be identified as the bulk IR  $E_u^2$  mode (see modes marked by asterisks in Figure 5.5(a)). The E symmetry of this mode is also verified in the polarization configuration independent Raman intensity as shown in Figure 5.6(b). Additional measurements are presented in appendix C.2.3. In contrast to  $\text{Bi}_2\text{Se}_3$ , this surface mode has been experimentally observed before in room temperature measurements on thin film samples with  $40\text{ }\mu\text{m}$  thickness,<sup>[116]</sup> and nanoplates with thicknesses below 7 nm.<sup>[119,121]</sup> (see also Table A.1).

The detection of the IR-active phonons originating from the inversion symmetry breaking at the surface underlines the high surface-to-bulk ratio of the investigated NFs. The pronounced detection of the  $E_u^2$  mode at room temperature shows the strong enhancement of the Raman response due to the Au substrate.

### Interface-enhanced Raman scattering by carrier injection

The strong phonon renormalizations observed in the NF thickness dependent Raman studies on Au substrate are the result of changing self-energy corrections in the NFs. Especially the observation of Fano profiles for the two  $A_{1g}$  modes hints to the presence of a low-energy electric susceptibility coupling to the phonons. In the following section it is argued how the Au substrate leads to an accumulation of free carriers at the contacted NF surface that can explain both the strong Raman signal enhancement as well as the observed phonon renormalizations by changing el-ph interactions.

First, the phonon renormalizations solely caused by the change in NF thickness are considered. In comparison with literature, an equivalent thickness dependent study of  $\text{Bi}_2\text{Se}_3$  NFs on silicon substrate conducted by Zhang *et al.* revealed much weaker phonon renormalizations.<sup>[64]</sup> The  $A_{1g}^1$  phonon for NFs on Si showed a frequency shift of only  $1.2\text{ cm}^{-1}$  in the decreasing NF thickness range of 13 nm to 8 nm. In contrast, the NFs placed on Au substrate investigated here show a substantially stronger frequency shift in the same thickness range, with the  $A_{1g}^1$  mode shifting by  $3\text{ cm}^{-1}$  in  $\text{Bi}_2\text{Se}_3$  and even  $5.8\text{ cm}^{-1}$  in  $\text{Bi}_2\text{Te}_3$  NFs (see Figure 5.4(b) and Figure 5.5(b)). The thickness dependent change in frequency was explained to origin from a phenomenological phonon confinement in  $c$ -direction that lifts the bulk Raman selection rule ( $q = 0$ ) and allows for the creation of phonons around the Brillouin zone center.<sup>[64]</sup> However, examining the phonon dispersion curves of  $\text{Bi}_2\text{Se}_3$  and  $\text{Bi}_2\text{Te}_3$  presented in Figure 3.5 it cannot explain the strong red shifts of the  $A_{1g}^1$  and especially blue shifts of the  $A_{1g}^2$  modes. Therefore, in agreement with the concomitant changes in line width and Fano parameter, self-energy corrections by additional el-ph interactions have to be considered for the NFs on Au substrate.

It was shown by ab initio calculations that the interface between  $\text{Bi}_2\text{Se}_3$  to an Au substrate leads to the transfer of electrons from gold into the  $\text{Bi}_2\text{Se}_3$  because of its electron affinity of 5.3 eV, which results in substantial band bending at the contacted side.<sup>[150]</sup> Due to the insulating bulk properties of  $\text{Bi}_2\text{Se}_3$  the injected electrons are accumulated at the  $\text{Bi}_2\text{Se}_3$

surface in contact. In Figure 5.7(a) the band bending in  $\text{Bi}_2\text{Se}_3$  is schematically shown and indicates how the charge accumulation in the first 2 nm leads to a build up of an electric field across the NF. The electric field enhances the Raman scattering cross section. This explains the strongly increased Raman susceptibilities obtained at all wavelengths for the NFs on Au in comparison with similarly thick NFs placed on silicon substrate (Figure 5.3(a,c)). On Si substrate with an additional insulating  $\text{SiO}_2$  layer reduced carrier transfer is expected. Indeed, band bending at the interface of  $\text{Bi}_2\text{Se}_3$  nanoribbons to an  $\text{SiO}_2$  interface was identified by Veyrat *et al.* leading to a downward band bending by about 400 meV and the creation of 2D quantum well states originating from the bulk.<sup>[40]</sup> The similar but weaker band bending at an  $\text{SiO}_2$  interface can equivalently explain the higher Raman intensities obtained from NFs on Si in comparison to bulk signals. The enhanced Raman signal for thin NFs placed on Si or Au substrates can hence be linked to the band bending induced build up of an electric field across the NFs (see Figure 5.7(b)). Depending on the charge transfer and band bending potential different enhancements are observed. The minor band bending effects for NFs placed on silicon explains the by a factor of around 15 weaker Raman susceptibilities (Figure 5.3(c)) and comparatively small phonon renormalizations observed by Zhang *et al.* due to reduced el-ph interactions.

### Reduction of bulk resonance conditions due to band bending effects

In contrast, the injected carriers for NFs in contact to gold can explain the NF thickness dependent renormalizations and Raman intensities. The phonon renormalizations by el-ph interactions are discussed in detail in the last paragraph of this section. Beforehand, the Raman intensities changing with the NF thickness are considered. In Figure 5.7(c,d) the extracted phonon intensities corrected for the NF scattering volume are given as a function of  $\text{Bi}_2\text{Se}_3$  and  $\text{Bi}_2\text{Te}_3$  NF thickness, respectively. Surprisingly, the Raman intensities show a stronger thickness dependence than anticipated by the linear change in scattering volume. Similar to the phonon renormalizations, the thicker NFs show a constant enhanced Raman signal that quickly collapses below a critical thickness of about 10 nm ( $OC < 45$ ) in  $\text{Bi}_2\text{Se}_3$  and 12 nm ( $OC < 35$ ) in  $\text{Bi}_2\text{Te}_3$ . The reduced signal enhancement in thin NFs becomes again apparent when analyzing the band bending effects induced by the Au interface. For  $\text{Bi}_2\text{Se}_3$  in contact to gold the carrier transfer leads to a downward band bending by as much as 1 eV as predicted by Spataru *et al.*,<sup>[150]</sup> schematically shown in Figure 5.7(a). For stoichiometric  $\text{Bi}_2\text{Se}_3$  this corresponds to a population of the bulk conduction band at the contacted NF surface. The band bending affects the electronic band structure up to a depth of 5.5 nm into the NF surface.<sup>[150]</sup> For the only few nm thin  $\text{Bi}_2\text{Se}_3$  NFs the contact to gold and carrier injection hence significantly reduces the insulating bulk region inside the NF. With decreasing NF thicknesses the band bending would finally extend across the entire NF as illustrated in Figure 5.7(a). In thick  $\text{Bi}_2\text{Se}_3$  NFs ( $d > 11$  nm) the electronic structure in the bulk allows for the resonant interband transitions from the valence into the first conduction band, as discussed in the previous sections.

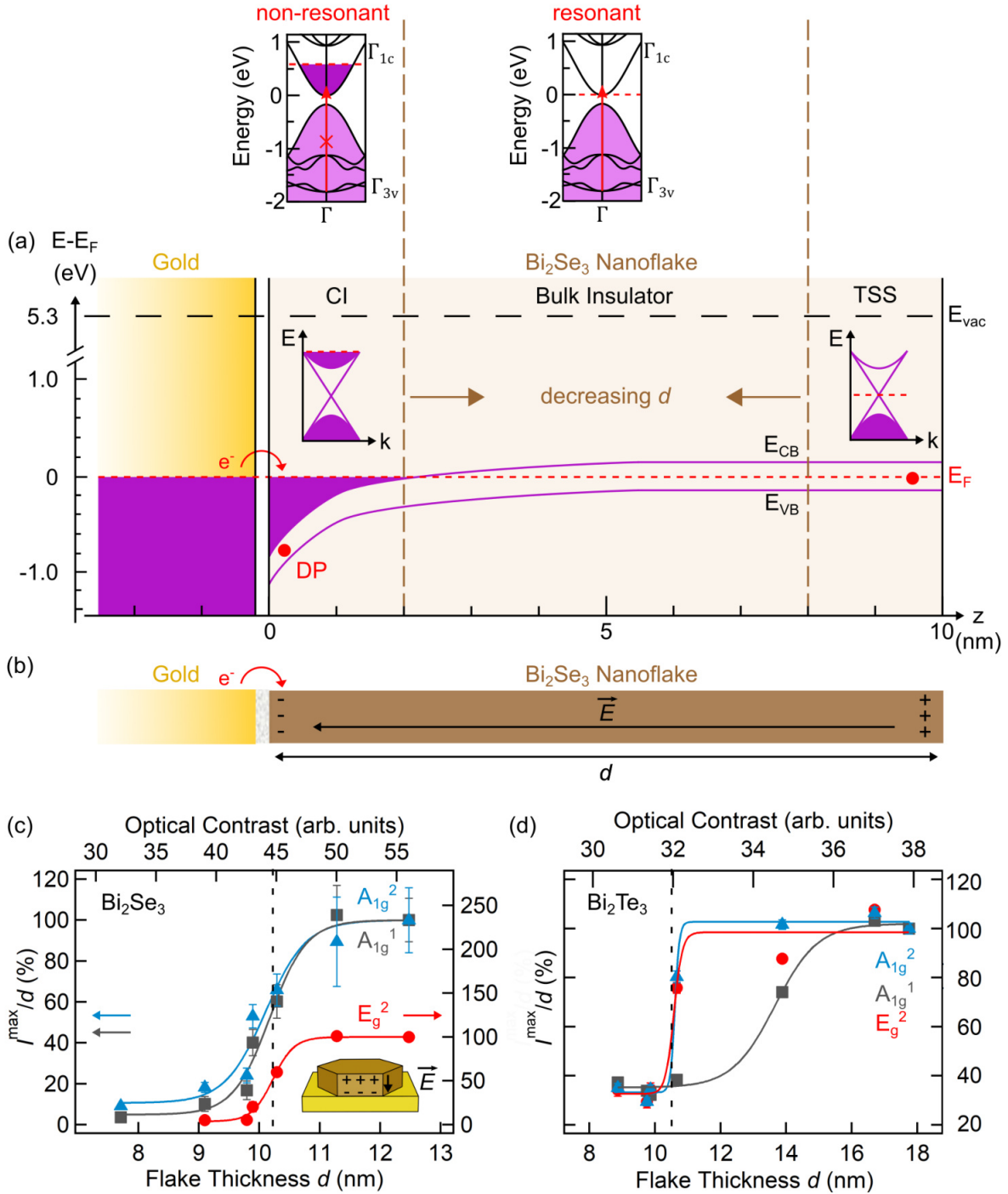


**Figure 5.7:** Carrier injection induced Raman enhancement and phonon renormalizations. (a) Schematic model of the band bending effects in a Bi<sub>2</sub>Se<sub>3</sub> NF in contact to gold. The band bending potential was depicted according to the calculations of Spataru *et al.*<sup>[150]</sup> Band structures above the respective flake area give the band fillings and depict resonant conditions in bulk and non-resonant conditions in the band bending area. Bands dispersions are depicted along the  $\Gamma L$  direction according to<sup>[21]</sup> (b) Schematic carrier transfer from the gold substrate into the contacted bottom surface of the NF and creation of an electric field. (c,d) Scattering volume corrected intensities of the three bulk phonon modes of Bi<sub>2</sub>Se<sub>3</sub> and Bi<sub>2</sub>Te<sub>3</sub>, respectively. Intensities are normalized to the value of the thickest measured NF and solid lines correspond to sigmoidal fits. Dashed lines indicate the threshold thickness for bulk resonance contributions. Adapted with permission from<sup>[129]</sup>. Copyright 2022 American Chemical Society.



The bulk resonance conditions together with the electric field across the NF lead to the strongly observed signal enhancement. The scattering-volume corrected intensities for thicker NFs are hence constant. For thin NFs ( $d < 10$  nm) the extending band bending effects quickly lead to a tuning out of the resonance bulk conditions. By the population of the first bulk conduction band the probability for the resonant interband transitions is reduced as schematically depicted in the band structures of Figure 5.7(a). This is evident in the drastically reduced signal by 80 % when the NF thickness is only reduced from 11 nm to 9 nm.

The abrupt change in Raman signal while reducing the thickness below a critical value of 10 nm is assigned to the collapsing bulk resonance conditions. The sigmoidal fits of the thickness dependent phonon intensities in Figure 5.7(c) reveal for Bi<sub>2</sub>Se<sub>3</sub> a threshold thickness of  $10.2 \pm 0.02$  nm. Additionally, the surface of Bi<sub>2</sub>Se<sub>3</sub> is known to be prone to the formation of Se vacancies leading to the formation of localized two-dimensional trivial surface states.<sup>[33]</sup> The exposure of Bi<sub>2</sub>Se<sub>3</sub> to ambient conditions can hence result in an inherent band bending similar to a gold substrate, that typically extends up to about 2 nm below the surface<sup>[45,134,161]</sup>. In Figure 5.7(a) we have depicted for the sake of simplicity a native Bi<sub>2</sub>Se<sub>3</sub> surface with the Fermi level inside the bulk band gap. However, under ambient conditions the native *n*-doping effect would yield for a 10 nm thick NF an effective bulk contribution of 6 nm. In contact to gold this bulk contribution is further reduced by the strong band bending effects explaining the sudden reduced Raman intensities for NFs below a thickness of 10 nm.

Since Bi<sub>2</sub>Te<sub>3</sub> exhibits a similar electron affinity of 5.3 eV as Bi<sub>2</sub>Se<sub>3</sub>,<sup>[38]</sup> the prediction of equivalent carrier injection from a gold substrate is made. With a slightly smaller bulk band gap Bi<sub>2</sub>Te<sub>3</sub> is also expected to experience band bending effects. Indeed, the scattering volume corrected Raman intensities shown in Figure 5.7(d) similarly show a constant value for thick NFs ( $d > 11$  nm) and reduce abruptly by about 65 % in thin NFs. Here, the sigmoidal fits determine a critical thickness of  $10.6 \pm 0.8$  nm for the E<sub>g</sub><sup>2</sup> and A<sub>1g</sub><sup>2</sup> modes. The identification of a critical Bi<sub>2</sub>Te<sub>3</sub> NF thickness of about 11 nm indicates similar band bending effects induced by the TI/gold interface.

### Electron-phonon coupling

The pronounced band bending effects and growing contribution of injected carriers in thinner NFs are further evident in the strong phonon renormalizations. In accordance with the band bending induced changes in phonon mode intensities, phonon renormalizations are setting in at the same critical NF thicknesses (Figure 5.4, Figure 5.5,(b,c)). The injected carriers populate the upper Dirac cone and bulk conduction bands in the TI NFs as schematically depicted in Figure 5.7(a). The available carriers provide a low-energy electric susceptibility that interacts with the phonons. The el-ph interaction is clearly evident in the changing Fano parameter of the A<sub>1g</sub> modes and significant renormalizations in frequency and line width. As explained in section 3.1.2, the Fano profile indicates

a Raman response that is determined by coupling to a low-energy electric susceptibility  $\chi^{\text{el}}$ . The Fano profile given in Equation (3.20) describes the resulting phonon self-energy corrections that can be used to derive the change in the el-ph interaction with decreasing NF thickness. Here, specifically the change in the modes line width, given by Equation (3.17), is used to analyze the el-ph interaction and is rewritten to

$$g\sqrt{\pi_{im}} = \sqrt{\Gamma\omega - \tilde{\Gamma}\omega}. \quad (5.4)$$

The renormalization in line width is determined by the el-ph coupling strength  $g$  as well as the imaginary part of the electric susceptibility  $\pi_{im}$ . Furthermore,  $\pi_{im}$  also determines the electronic background leading to the Fano interference. To study the possible change in the electronic background with NF thickness the Bose corrected background after the subtraction of the phonon modes is examined in Figure 5.8(a,c). For the investigated

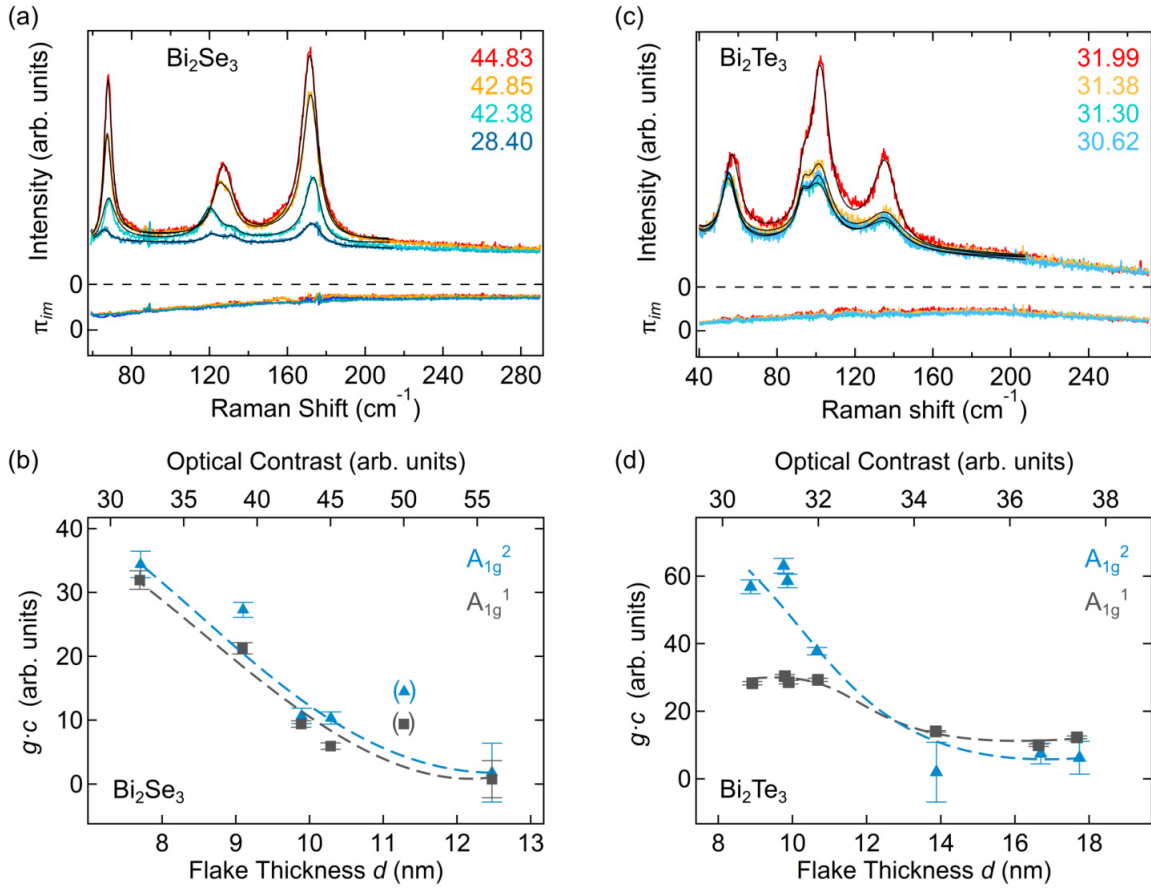


**Figure 5.8:** Electronic background and changes in el-ph coupling strength as a function of NF thickness. (a,c) Raw Raman spectra of Bi<sub>2</sub>Se<sub>3</sub> and Bi<sub>2</sub>Te<sub>3</sub> NFs with varying OCs and their Bose corrected backgrounds after phonon subtraction, respectively. Black graphs correspond to the phonons fit function. The backgrounds correspond to the imaginary part  $\pi_{im}$  of a low-energy electric susceptibility and are constant for NFs of varying thickness. (b,d) Electron-phonon coupling strength  $g \cdot c$  derived from line width renormalizations in the Bi<sub>2</sub>Se<sub>3</sub> and Bi<sub>2</sub>Te<sub>3</sub> bulk phonons as function of NF thickness, respectively. Dashed lines give guides to the eye. Adapted with permission from<sup>[129]</sup>. Copyright 2022 American Chemical Society.



$\text{Bi}_2\text{Se}_3$  and  $\text{Bi}_2\text{Te}_3$  NFs, respectively, there is no change in background observed, strongly suggesting a constant electronic background  $\pi_{im}$  independent of the NFs thicknesses. This is reasonable as all NFs are in contact with the same gold substrate and should experience carrier injection to the same extent leading to identical accumulations of electron densities at the contacted surface. Accordingly, Equation (5.4) can be applied to investigate the change in el-ph coupling strength  $g$  with NF thickness. Assuming  $\pi_{im}$  is constant its contribution can be summarized in a constant  $c$ . The results presented in Figure 5.8(b,d) for  $\text{Bi}_2\text{Se}_3$  and  $\text{Bi}_2\text{Te}_3$ , respectively, reveal an increasing el-ph coupling as the NFs get thinner. This is again plausible as the relative contribution of the constant electric susceptibility to the possible phonon decay channels increases as the NFs get thinner. In summary, the concomitant changes in phonon intensity and el-ph interaction at the same critical thickness demonstrate how both can be related to band bending effects at the NF surface in contact to a gold substrate.

#### The Au/TI interface leads to

- carrier injection from Au into the TI NFs induces band bending
- enhancement of Raman susceptibility via electric field across the NFs
- reduction of resonance bulk condition with decreasing NF thickness
- increasing electron-phonon interactions in thin NFs due to the injected carriers occupying the bulk conduction bands

## 5.6 Summary

In a preliminary study to obtain the highest possible Raman signal of single Flake measurements, the resonance Raman conditions at excitation energies of 1.96 eV were identified for  $\text{Bi}_2\text{Se}_3$  NFs placed on Si and Au substrates, as well as a reference bulk sample. The resonance corresponds to electronic interband transitions and is intrinsic to  $\text{Bi}_2\text{Se}_3$ .

The influence of a gold substrate on ultrathin  $\text{Bi}_2\text{Se}_3$  and  $\text{Bi}_2\text{Te}_3$  NFs was studied by investigating NFs with decreasing thicknesses of 12.5–7.7 nm and 17.7–8.9 nm, respectively. The use of thin NFs enabled the access of the TI-gold interface via Raman spectroscopy. The obtained results reveal carrier injection from the gold substrate into the contacted NF surface resulting in downward band bending in the TI band structure. The carrier accumulation and band bending effects are reflected in several properties of the Raman spectra that are equivalent for both TI materials.

Firstly, the Raman susceptibility and resonance profile of  $\text{Bi}_2\text{Se}_3$  NFs on gold is strongly enhanced by a factor of 14 in comparison with silicon substrate that are explained by the

build up of an electric field across the NF. Secondly, the  $\text{Bi}_2\text{Se}_3$  and  $\text{Bi}_2\text{Te}_3$  phonons show strong renormalizations below critical thicknesses of 10 nm and 12 nm, respectively. These can be related to self-energy corrections by coupling to a low-energy electric susceptibility provided by the injected carriers. The electron-phonon interaction is apparent in the incipient renormalizations and asymmetric Fano line shapes in thin NFs. Analyzing the electronic background of Raman spectra reveals a constant electric susceptibility for decreasing NF thicknesses. This is expected since all NFs were in contact with the same gold substrate and identical carrier transfer is expected at all interfaces. However, the electron-phonon coupling strength increases in thin NFs due to the higher contribution to the overall NF volume. This is reflected in strong Fano parameters and increased line widths. Lastly, the carrier injection leads to a population of the bulk conduction bands in the TI NFs, which reduces the bulk resonance conditions and leads to a tuning out of resonance with decreasing NF thickness.

## 5.7 Paper II

# Carrier injection observed by interface-enhanced Raman scattering from topological insulators on gold substrates

Sarah Scheitz\*, Tomke E. Glier, Christian Nweze, Malte van Heek, Isa Moch, Robert Zierold, Robert H. Blick, Nils Huse and Michael Rübhausen\*

Published in: ACS Applied Materials & Interfaces - 11 July 2022  
<https://doi.org/10.1021/acsami.2c04380>

Reprinted with permission from S. Scheitz, T. E. Glier, C. Nweze *et al.*, *ACS Applied Materials & Interfaces* **2022**, 14, 32625–32633. Copyright 2022 The Authors. Published by American Chemical Society.

# Carrier Injection Observed by Interface-Enhanced Raman Scattering from Topological Insulators on Gold Substrates

Sarah Scheitz,\* Tomke Eva Glier, Christian Nweze, Malte van Heek, Isa Moch, Robert Zierold, Robert Blick, Nils Huse, and Michael Rübhausen\*



Cite This: *ACS Appl. Mater. Interfaces* 2022, 14, 32625–32633



Read Online

ACCESS |



Metrics & More



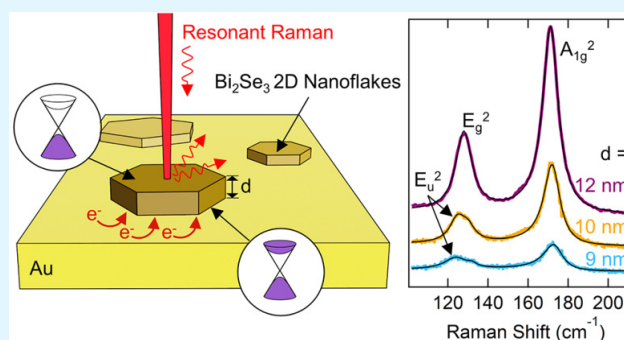
Article Recommendations



Supporting Information

**ABSTRACT:** The electron-phonon interaction at the interface between topological insulator (TI), namely,  $\text{Bi}_2\text{Se}_3$  and  $\text{Bi}_2\text{Te}_3$  two-dimensional (2D) nanoflakes, to a gold substrate as a function of TI flake thickness is studied by means of Raman scattering. We reveal the presence of interface-enhanced Raman scattering and a strong phonon renormalization induced by carriers injected from the gold substrate to the topological surface in contact. We derive the change of the electron-phonon coupling showing a nearly linear behavior as a function of layer thickness. The strongly nonlinear change of the Raman scattering cross section as a function of flake thickness can be associated with band bending effects at the metal-TI interface. Our results provide spectroscopic evidence for a strongly modified band structure in the first few quintuple layers of  $\text{Bi}_2\text{Se}_3$  and  $\text{Bi}_2\text{Te}_3$  in contact with gold.

**KEYWORDS:** topological insulator gold contact,  $\text{Bi}_2\text{Se}_3$ ,  $\text{Bi}_2\text{Te}_3$ , Raman spectroscopy, carrier injection, band bending, electron-phonon coupling



## 1. INTRODUCTION

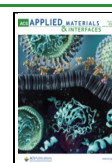
Spin-polarized surface states hosting quasi-relativistic electrons are a key characteristic of topological insulator (TI) nanostructures.<sup>1,2</sup> Most importantly, novel, robust, and highly conductive electronic channels can form at interfaces between systems with different topological character. These surface states are topologically protected by time-reversal symmetry and are the result of a strong spin-orbit coupling (SOC) term in the Hamiltonian. Due to the spin-momentum locking of the topological surface states (TSS) leading to reduced back-scattering and high carrier mobilities, TIs have become promising candidates for spin-transfer torque memory devices,<sup>3–6</sup> high-performance photodetectors,<sup>7</sup> and fiber lasers.<sup>8</sup> At interfaces of systems with different topological character, one would expect that the TSS are robust.<sup>1,9</sup> Yet, the response of the TSS to a contact or substrate is critical for the development of electronic devices with consequences for their applications. Furthermore, the relevance of topological physics depends on the Fermi-level position at the interfaces due to possible charge transfer across the interface.<sup>10</sup> Even though detailed theoretical predictions on the metal-TI band structure exist,<sup>11</sup> these obscured interfaces are rarely studied. Especially the contact to gold is of high interest in TI-based devices.<sup>7,12,13</sup> Important representatives for three-dimensional TIs are  $\text{Bi}_2\text{Se}_3$  and  $\text{Bi}_2\text{Te}_3$  featuring a single Dirac Cone in the Brillouin zone center with different bulk band gaps.<sup>14</sup> The narrow-gap

semiconductor  $\text{Bi}_2\text{Se}_3$  is one of the most intensively studied three-dimensional (3D) TIs due to its comparably large bulk band gap of 0.3 eV with the Dirac point positioned within the bulk band gap.<sup>15,16</sup> In contrast, the band gap of 0.16 eV in  $\text{Bi}_2\text{Te}_3$  is substantially smaller and the Dirac point is shifted close to the valence band.<sup>17,18</sup> Despite many studies on the electronic properties of  $\text{Bi}_2\text{Se}_3$  and  $\text{Bi}_2\text{Te}_3$  by means of transport measurements,<sup>19–22</sup> only a very limited number of studies exist that explicitly focus on the local properties of the Au-TI interface. The interface chemistry between gold and  $\text{Bi}_2\text{Se}_3$  has been studied both theoretically<sup>11</sup> and experimentally,<sup>23,24</sup> revealing chemical inertness and no hybridization with the TSS. However, ab initio calculations have predicted the injection of carriers into the TI leading to substantial band bending at the Au-TI interface of about 1 eV.<sup>11</sup> Often the metal-to-insulator contact is not directly accessible for experiments that study the topological state from the side of the vacuum. However, Raman scattering on thin flakes has already been proven to be a valuable tool to reveal quasi-

Received: March 10, 2022

Accepted: June 30, 2022

Published: July 11, 2022



relativistic electrons and their interactions with phonons of the TSS.<sup>25–27</sup> Note that Raman scattering is a contact-free, local, and direct measurement of the interface properties. Furthermore, Raman spectroscopy is a volume scattering technique and allows us to study TSS that are not directly accessible or covered, which is the main challenge for highly surface-sensitive techniques like angle-resolved photoemission spectroscopy (ARPES)<sup>21</sup> and scanning tunneling spectroscopy (STS).<sup>28</sup> In particular, Raman spectroscopy allows for understanding the interplay between electronic degrees of freedom and the lattice.

In this paper, we study the interface between a gold substrate and topological insulator nanoflakes (NFs) of Bi<sub>2</sub>Se<sub>3</sub> and Bi<sub>2</sub>Te<sub>3</sub> of varying thickness by employing spatially resolved high-resolution Raman scattering. Tuning the thickness of the NFs allows for controlling (a) the bulk contribution, which is used to identify contributions originating from the surface, and (b) the effective charge transfer from the substrate. We investigate the changes in the electronic susceptibility of the NFs and its influence on the phonon line shapes as a function of the NF's thickness and optical contrast, thereby identifying carrier injection at the interface. We discuss the implications of band bending on the observed Raman spectra and determine the changes in the electron-phonon interaction as a function of NF thickness.

## 2. EXPERIMENTAL SECTION

Bi<sub>2</sub>Se<sub>3</sub> and Bi<sub>2</sub>Te<sub>3</sub> NFs were synthesized using a wet-chemical polyol method, which is described in detail in ref<sup>26</sup> and the Supporting Information (SI-Section 1). The single crystallinity, growth direction, and correct stoichiometry were thoroughly verified using transmission electron microscopy (TEM), selected area electron diffraction (SAED), and energy-dispersive X-ray spectroscopy (EDX), respectively.<sup>26</sup> For the investigation of individual NFs, the dispersed flakes were drop-cast onto silicon and gold substrates and their thicknesses were determined using atomic force microscopy (AFM) (see SI-Section 4). Raman measurements on individual NFs were acquired employing a custom-made micro-Raman setup<sup>29,30</sup> creating diffraction-limited laser spot diameters varying between 211 to 398 nm depending on wavelength (see SI-Section 2). All spectra were collected in an effective backscattering configuration with the polarization configuration  $z(xx)\bar{z}$  denoted in Porto notation.<sup>31</sup> The micro-Raman setup enables the use of various excitation wavelengths in the visible range of 400–700 nm. Details on the used laser sources and data treatment are given in SI-Sections 2 and 3. Due to the low thermal conductivity of both Bi<sub>2</sub>Se<sub>3</sub> and Bi<sub>2</sub>Te<sub>3</sub>,<sup>32</sup> extensive prestudies on laser powers and integration times were conducted to determine appropriate measurement configurations that exclude laser heating effects on the Raman spectra. With the employed conditions, we ensure damage-free measurements (see SI-Section 2.2). We found that for a 633 nm excitation wavelength with a spot diameter of 211 nm, a power of 40  $\mu$ W (leading to a power density of 114 kW/cm<sup>2</sup> on the sample) results in low noise Raman signals without damaging the NFs. The spectra were acquired while scanning over the NF surfaces by about 2–4  $\mu$ m<sup>2</sup>. All data have been normalized to power and integration time and are corrected for the spectral response of the instrument.<sup>29</sup>

## 3. RESULTS AND DISCUSSION

**3.1. Resonance Raman Study on Bi<sub>2</sub>Se<sub>3</sub>.** We first investigate Bi<sub>2</sub>Se<sub>3</sub> NFs on gold and silicon substrates as a function of wavelength to determine the Raman resonance profile. By measuring under resonant conditions, the collected Raman signal of individual NFs is increased by an order of magnitude, which enables higher accuracy in the data analysis

of NFs differing by only a few nanometers in thickness. Figure 1a shows the collected Raman spectra of single Bi<sub>2</sub>Se<sub>3</sub> NFs on

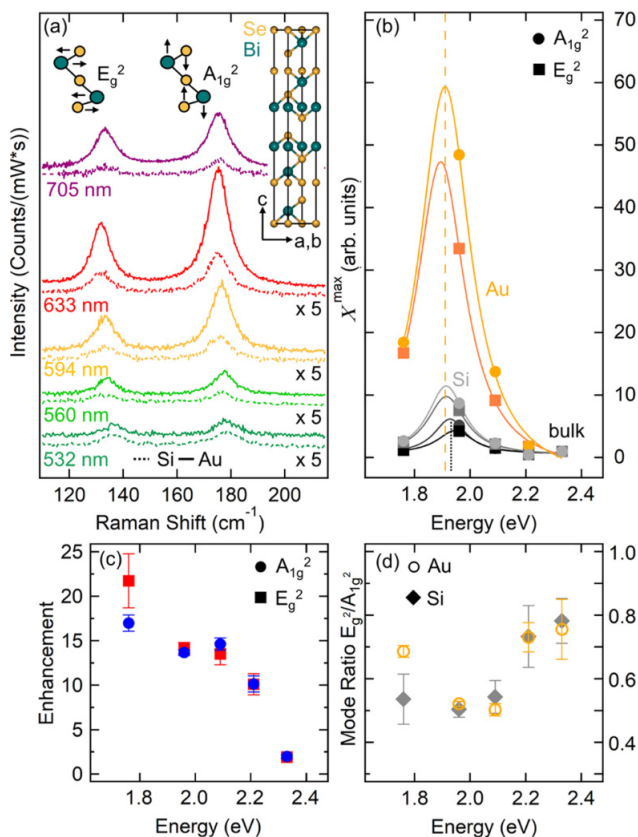


**Figure 1.** Resonance studies on Bi<sub>2</sub>Se<sub>3</sub> NF Raman signal on gold compared to silicon substrates and a bulk single crystal. (a) Comparison of Raman spectra from single NFs on silicon (dotted) and sputtered gold substrate (solid) for different excitation wavelengths as indicated. The thicknesses of the NFs are given in Table S4 in the SI. All spectra are normalized to laser power as well as integration time and are displayed with an offset for clarity. The measurements on silicon substrates are all multiplied by a factor of 5. The insets show the crystal structure of a conventional Bi<sub>2</sub>Se<sub>3</sub> unit cell and the atomic displacement vectors for the two observed phonon modes. (b) Resonance profiles of the E<sub>g</sub><sup>2</sup> (squares) and A<sub>1g</sub><sup>2</sup> (circles) phonon susceptibilities as a function of energy corresponding to the excitation wavelength shown in (a). Gray and yellow markers correspond to the spectra of the NFs on silicon and gold substrate, respectively. Lorentzian fits are given as solid lines for the NFs on Au and Si. Black markers show the resonance behavior of a Bi<sub>2</sub>Se<sub>3</sub> bulk sample. Values are normalized to 532 nm (2.33 eV). The dashed and dotted lines indicate the resonance frequency of the NFs on Au and bulk sample, respectively. (c) Enhancement between the NF Raman signal on gold and silicon at the corresponding energy of the E<sub>g</sub><sup>2</sup> (squares) and A<sub>1g</sub><sup>2</sup> (circles) phonons. (d) Susceptibility ratios of the E<sub>g</sub><sup>2</sup> to A<sub>1g</sub><sup>2</sup> modes for the NFs on Si (gray diamonds) and Au (yellow open circles).

silicon and gold for excitation wavelengths of 532, 560, 594, 633, and 705 nm. For all NFs, regardless of the substrate, the characteristic bulk phonon modes of E<sub>g</sub><sup>2</sup> and A<sub>1g</sub><sup>2</sup> symmetry were identified.<sup>33,34</sup> In Figure 1b, we show the peak susceptibilities extracted from Lorentzian fits for both phonons for all incident photon energies. To obtain the resonance behavior, we have corrected the peak intensities for the dielectric properties of Bi<sub>2</sub>Se<sub>3</sub> as well as the scattering volume



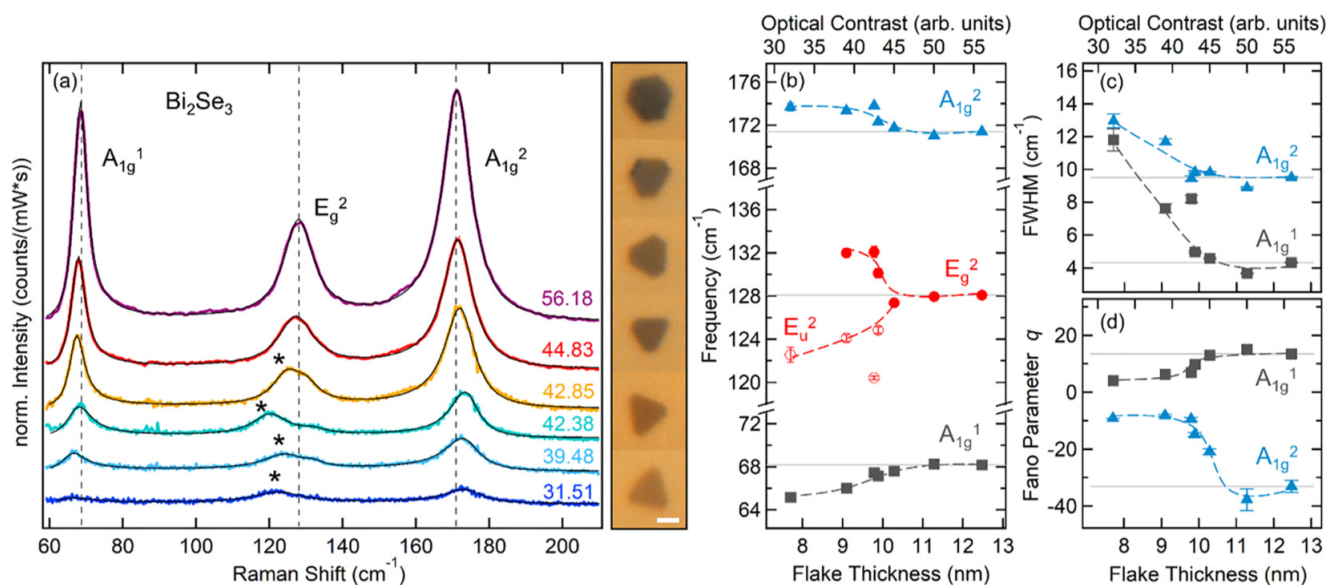


**Figure 2.** Phonon renormalization in Bi<sub>2</sub>Se<sub>3</sub> NFs with varying thickness on the same gold substrate. (a) Raman spectra of six individual NFs with decreasing thicknesses from 12.5 nm (OC = 56.18) to 7.7 nm (OC = 31.51) (see Table S5 in the SI). Corresponding microscope images of the measured NFs are shown to the right of the spectra. The scale bar is 2  $\mu$ m. In the diagram, the three main phonon modes A<sub>1g</sub><sup>1</sup>, E<sub>g</sub><sup>2</sup>, and A<sub>1g</sub><sup>2</sup> of Bi<sub>2</sub>Se<sub>3</sub> are labeled as well as a growing IR mode marked by asterisks. Vertical dashed lines are given as a guide to the eye and correspond to the mode frequencies for the thickest NF. The optical contrasts of the NFs are given next to their corresponding spectra. Renormalization of (b) mode frequencies, (c) FWHM, and (d) extracted Fano parameters with NF thickness. Dashed lines are a guide to the eye. For reference, phonon frequencies, FWHM, and Fano parameters measured from the thickest NF are given as solid gray lines in (b–d).

of each measured NF. Details on the correction factors used to obtain the Raman susceptibilities are given in SI-Section 3.2. Already on the silicon substrate, we obtain a signal increase by a factor of 10 when tuning the excitation wavelength into resonance. For a reference bulk sample, a similar but weaker resonance is observed (see Figure 1b). This resonance of Bi<sub>2</sub>Se<sub>3</sub> has been previously reported<sup>35,36</sup> and is generally assigned to a resonant interband transition.<sup>37,38</sup> However, for the measurements on gold substrate, a substantially larger signal is obtained for all wavelengths in comparison with the silicon substrate. Furthermore, we observe an enhanced resonance profile on gold with a signal increase by a factor of 50 when tuning the excitation energy into the red. Note that the Raman susceptibility of the bulk sample is significantly smaller than the NF susceptibilities, an effect that has been observed before for Bi<sub>2</sub>Se<sub>3</sub> and Bi<sub>2</sub>Te<sub>3</sub> thin-film samples.<sup>27,39</sup> Due to the penetration depth of around 9 nm in the visible spectra range (see SI-Figure S2c), the bulk and NF samples actually yield similar scattering volumes. Yet, the thin NFs show a strongly enhanced Raman response, which we discuss in the final part of this study. Figure 1b clearly indicates a sharp resonance of the phonons in the Bi<sub>2</sub>Se<sub>3</sub> NFs on the gold substrate at 633 nm corresponding to 1.96 eV. The resonance profiles for bulk samples and NFs on silicon and gold were fitted by a Lorentzian profile. They exhibit similar resonance positions at  $1.94 \pm 0.06$  eV (bulk) and  $1.91 \pm 0.03$  eV (NFs), both of which are close to the 1.96 eV (633 nm) excitation line. By comparing the peak susceptibilities of the silicon and gold measurements, we determine an increasing enhancement for both phonons on the gold substrate,  $E = X^{\text{Au}}/X^{\text{Si}}$ , which is shown in Figure 1c. The enhancement on the gold substrate is increasing when tuning the incident photon energy to smaller energies. The strongest relative signal enhancement by a factor of  $\sim 20$  is found for 1.76 eV, which is at slightly lower energies compared to the resonance position at 1.90 eV. We further

observe a change in the relative susceptibilities of the E<sub>g</sub><sup>2</sup> to the A<sub>1g</sub><sup>2</sup> modes when approaching the resonance as shown in Figure 1d. The A<sub>1g</sub><sup>2</sup> mode shows a stronger enhancement around the resonant excitation energy, which results in a decreasing susceptibility ratio of E<sub>g</sub><sup>2</sup> to A<sub>1g</sub><sup>2</sup>. This trend is observed for NFs on both, silicon and gold substrates. Our observations of identical resonance profiles and mode ratios for NFs on silicon and gold show that the resonance is intrinsic to the Bi<sub>2</sub>Se<sub>3</sub> NFs. The enhanced Bi<sub>2</sub>Se<sub>3</sub> resonance on Au provides first indications that the conditions for a resonant interband transition are changed. We show in the final part of this work how the interband transitions are affected by band bending effects as a possible consequence of carrier injection from the gold substrate. Carriers injected into the bottom NF side in contact with gold increase the number of available electrons for resonant interband transitions and lead to an enhanced Raman response. This view is also supported by changes in the resonance positions in the NF samples compared to the bulk, where the occupation of bands responsible for the resonant transitions leads to a slight change in resonance energy. All further measurements have been conducted under resonant conditions with an excitation wavelength of 633 nm.

**3.2. Thickness Dependence of Bi<sub>2</sub>Se<sub>3</sub> and Bi<sub>2</sub>Te<sub>3</sub> NFs on Au.** In Figure 2, we study the thickness dependence of the Raman signal from Bi<sub>2</sub>Se<sub>3</sub> NFs on the same gold substrate. Figure 2a shows selected Raman spectra of Bi<sub>2</sub>Se<sub>3</sub> NFs with decreasing thicknesses from 12.5 to 7.7 nm. The change in NF thickness of only a few nanometers is already apparent in optical microscope images, where the optical contrast (OC) of the NFs changes drastically with thickness. The OC is defined by the ratio of the averaged greyscale values on the NF compared to the values on the gold substrate (see SI-Section 4.1). NFs with thicknesses above 12 nm appear dark on the gold substrate with OCs above 50, whereas the OC decreases

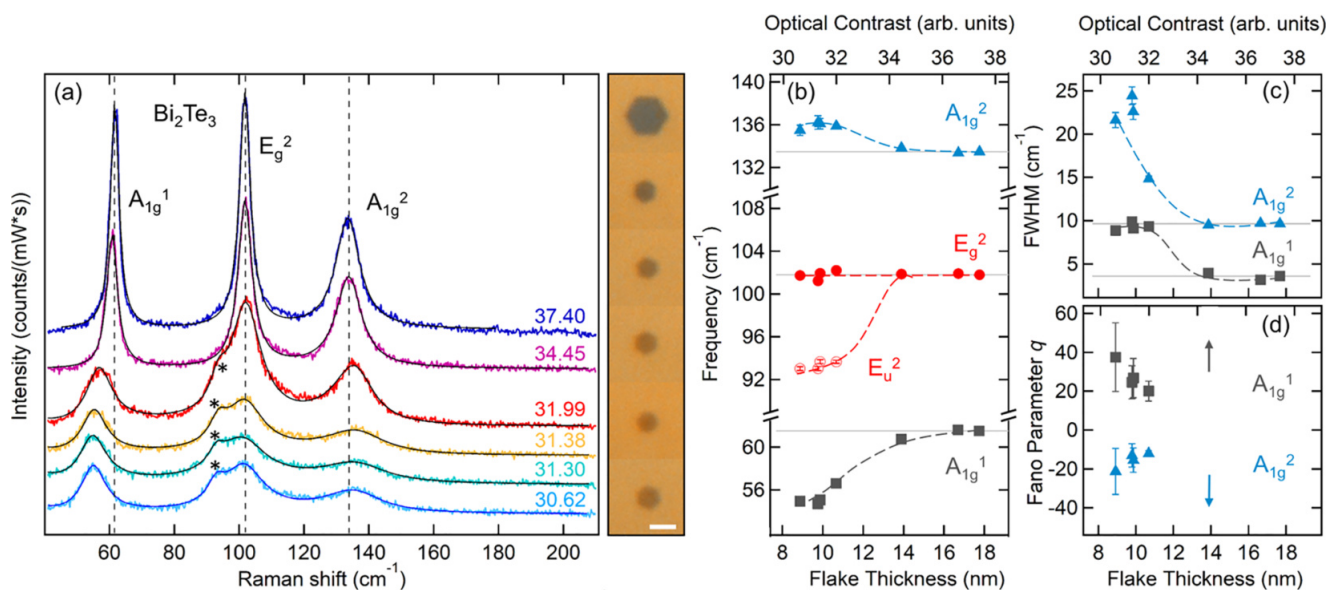


**Figure 3.** Phonon renormalization in Bi<sub>2</sub>Te<sub>3</sub> NFs with varying thickness on the same gold substrate. (a) Raman spectra of six individual NFs with decreasing thicknesses from 17.7 nm (OC = 37.40) to 8.9 nm (OD = 30.62) (see Table S5 in the SI). Corresponding microscope images of the measured NFs are shown to the right of the spectra. The scale bar is 2  $\mu$ m. In the diagram, the three main phonon modes A<sub>1g</sub><sup>1</sup>, E<sub>g</sub><sup>2</sup>, and A<sub>1g</sub><sup>2</sup> of Bi<sub>2</sub>Te<sub>3</sub> are labeled as well as a growing IR mode marked by asterisks. Dashed lines are given as a guide to the eye and correspond to the mode frequencies for the thickest NF. Renormalization of (b) mode frequencies, (c) FWHM, and (d) Fano parameter with NF thickness. Dashed lines are a guide to the eye. For reference, phonon frequencies and FWHM measured from the thickest NF are given as solid gray lines in (b,c). In (d), the Fano parameters for A modes in thick NFs ( $d > 14$  nm), which obtained very high values due to their symmetrical line shape, are indicated by arrows.

for thinner NFs of around 8 nm down to a value of 32. Indeed, in this range of thicknesses, the OC is directly proportional to the NF thickness as shown in the SI-Section 4.1, thus allowing for a direct experimental control of the NF thickness in the Raman measurement. For Bi<sub>2</sub>Se<sub>3</sub> NFs with high OCs above 50 (corresponding to  $d > 12$  nm), Raman spectra show the three well-known bulk phonons of A<sub>1g</sub><sup>1</sup> ( $63.18 \pm 0.02$  cm<sup>-1</sup>), E<sub>g</sub><sup>2</sup> ( $123.08.18 \pm 0.04$  cm<sup>-1</sup>), and A<sub>1g</sub><sup>2</sup> ( $166.41 \pm 0.02$  cm<sup>-1</sup>) symmetries,<sup>33</sup> with the frequencies obtained for the thickest NF given in parentheses. Intriguingly, for thinner NFs close to a critical OC of 45 ( $d < 10$  nm), the three bulk phonons experience a strong renormalization. In particular, with decreasing OC, the A<sub>1g</sub> modes are shifted in frequency and the E-mode splits into a double peak feature. Furthermore, for the lowest OC, we observe a substantial decrease in Raman intensity that we cannot exclusively attribute to the decreased thickness of the NF.

By fitting the E<sub>g</sub> modes with Lorentzian and the A<sub>1g</sub> modes with Fano profiles, we show in Figure 2b the extracted mode frequencies that reveal a softening of the low-energy A<sub>1g</sub><sup>1</sup> mode by 3 cm<sup>-1</sup> and a hardening of the A<sub>1g</sub><sup>2</sup> mode by 2.6 cm<sup>-1</sup> in the investigated range of NF thicknesses. This frequency renormalization is accompanied by an increase of the full width at half-maximum (FWHM) by 8 and 4 cm<sup>-1</sup>, respectively, as shown in Figure 2c. Moreover, for thin NFs on gold, the bulk E<sub>g</sub><sup>2</sup> phonon splits into two modes. The split low-energy mode separates from the E<sub>g</sub><sup>2</sup> bulk mode by about 10 cm<sup>-1</sup>, as shown in Figure 2b. The emerging phonon on the low-energy side of the bulk E<sub>g</sub><sup>2</sup> phonon in NFs with low thicknesses is related to a surface vibrational mode. At the surface, the crystalline symmetry is perturbed, which results in a reduction of the bulk point group symmetry D<sub>3d</sub><sup>5</sup> to the surface point group C<sub>3v</sub>.<sup>40,41</sup> The C<sub>3v</sub> point group contains irreducible representations that include infrared (IR) active

bulk phonons, which become Raman-active upon the breaking of inversion symmetry at the surface. For Bi<sub>2</sub>Se<sub>3</sub>, the mode around 124 cm<sup>-1</sup> can be assigned to the in-plane bulk IR mode of E<sub>u</sub><sup>2</sup> symmetry.<sup>33</sup> This surface mode has been observed for bulk samples at very low temperatures <13 K<sup>25,41</sup> and thin-film samples below 9 nm thickness at 80 K.<sup>42</sup> We have confirmed the E-symmetry of the emerging surface vibrational mode by conducting Raman measurements with parallel (xx) and crossed (xy) polarization. A thorough analysis of the symmetry is given in the SI-Section 4.3. The significant thickness dependence of the A<sub>1g</sub> modes becomes further apparent when analyzing the line shape of the phonons. For the A<sub>1g</sub> modes, we find an asymmetric Fano profile yielding information on the electron-phonon coupling. This line shape encodes a coupling of discrete phonon states to electronic degrees of freedom in the system.<sup>43</sup> The Fano parameter *q* determines the asymmetry of the profile, where the negative or positive sign of *q* specifies whether the electronic susceptibility constructively interferes with the phonon on its low- or high-energy side, respectively. In agreement with the observed renormalizations of mode frequencies and FWHM, we find a strong decrease in the Fano parameter for NFs below an OC of 45 and corresponding thickness below 10 nm, as shown in Figure 2d. This observation shows the presence of a low-energy electronic susceptibility interacting with the phonons. Since the phonon frequency is renormalized by the real part of an electronic susceptibility,<sup>26,44</sup> the softening of the A<sub>1g</sub><sup>1</sup> mode can be explained by coupling to a positive real part and the hardening of the A<sub>1g</sub><sup>2</sup> mode by coupling to a negative real part of the electric susceptibility. Furthermore, taking the opposite signs of the Fano parameter *q* for the two A<sub>1g</sub> modes into account, this spectral behavior indicates the coupling of these modes to an electronic susceptibility in a frequency range between 60 and 130 cm<sup>-1</sup>.

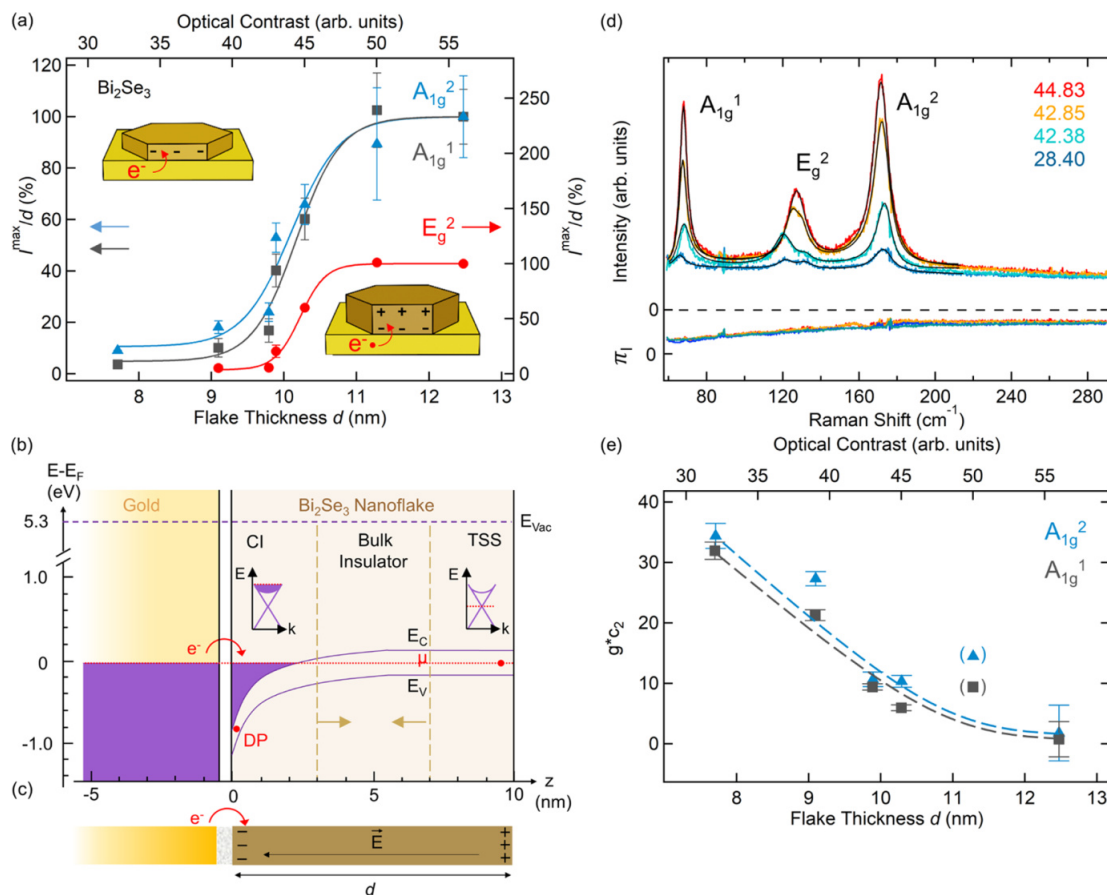


**Figure 4.** Carrier injection-induced Raman enhancement and phonon renormalizations. (a) Scattering volume-corrected intensities of the three measured phonon modes in  $Bi_2Se_3$  as a function of NF thickness. Intensities were normalized to the value of the thickest NF. The right axis corresponds to the  $E_g^2$  intensities. The insets show a model of a thin NF with band bending effects across the entire NF (left) and a thick NF with band bending localized to the bottom surface (right). (b) Model of the band structure for a contacted  $Bi_2Se_3$  NF on gold with values for the band bending potential according to ref 11. Bulk bands experience downward bending due to carrier injection (CI) into the contacted surface. Three different regions in the NF are indicated by vertical dashed lines corresponding to the strongly bent contact surface, the bulk insulator region, and the top surface with the native topological surface state (TSS) in contact with air. The relative position of the Dirac point (DP) for the bottom and top TSS are marked as red dots. Top insets illustrate the relative Fermi position in the top and bottom Dirac Cone. (c) Illustration of charge injection from gold into the contacted  $Bi_2Se_3$  surface and development of an electric field across a thick NF. (d) Raman spectra of  $Bi_2Se_3$  NFs with varying OCs and their Bose-corrected extracted background corresponding to the imaginary part of a low-energy electronic susceptibility. (e) Electron-phonon coupling strength determined from line width renormalization with dashed lines as a guide to the eye.

In Figure 3, we present data from the equivalent experiment on the 3D TI  $Bi_2Te_3$ , which exhibits a smaller bulk band gap of 0.16 eV. The OC of  $Bi_2Te_3$  NFs is also proportional to the NF thickness, as shown in SI-Section 4.1. The thickness-dependent Raman measurements on gold for  $Bi_2Te_3$  NFs from around 18 to 9 nm are presented in Figure 3a. For all NFs, the bulk Raman modes of  $A_{1g}^1$  ( $61.53 \pm 0.03 \text{ cm}^{-1}$ ),  $E_g^2$  ( $101.80 \pm 0.02 \text{ cm}^{-1}$ ), and  $A_{1g}^2$  ( $133.49 \pm 0.11 \text{ cm}^{-1}$ ) symmetries are detected with frequencies of the thickest measured NF given in parentheses. In comparison with  $Bi_2Se_3$ , the Raman modes of  $Bi_2Te_3$  are shifted to lower frequencies due to the higher mass of Te atoms compared to Se atoms.<sup>33</sup> When evaluating the Raman spectra as a function of NF thickness, the phonons show a behavior similar to  $Bi_2Se_3$  with respect to phonon renormalizations as the NFs get thinner. For NFs with OCs below 34, we find strong deviations in frequency, FWHM, and Fano parameter from the Raman spectra of thicker NFs. Namely, a stronger softening by  $6.9 \text{ cm}^{-1}$  compared to  $Bi_2Se_3$  and a comparable hardening by  $3 \text{ cm}^{-1}$  of the respective  $A_{1g}^1$  and  $A_{1g}^2$  phonon modes as shown in Figure 3b is observed. We

find increasing FWHMs by about 6 and  $13 \text{ cm}^{-1}$ , respectively, which is accompanied by a decreased Fano parameter for thin NFs (Figure 3c,d), indicating incipient electron-phonon interactions also in these thin  $Bi_2Te_3$  NFs. In particular, a similar mode splitting of the  $E_g^2$  mode is clearly apparent. In  $Bi_2Te_3$ , the split emerging mode at  $93.5 \text{ cm}^{-1}$  can again be assigned to the bulk IR-active  $E_u^2$  mode<sup>33</sup> (see SI-Section 4.3). This surface mode has been experimentally observed at room temperature in thin-film samples and nanoplates with thicknesses below  $7 \text{ nm}$ <sup>45–47</sup> as well as in films of drop-cast NFs below  $100 \text{ K}$ .<sup>26</sup>

**3.3. Interface-Enhanced Raman Scattering by Carrier Injection.** Our observation of strong renormalizations of the phonons in metal-contacted TIs is a result of an enhanced electron-phonon interaction that can be associated with carrier injection and corresponding band bending at the contacted side of the NF as we will detail below. In comparison, Zhang et al. have measured  $Bi_2Se_3$  NFs of differing thicknesses placed on silicon substrates and observed a much weaker frequency shift in the  $A_{1g}^1$  phonon of only  $1.2 \text{ cm}^{-1}$  for decreasing NF



thicknesses between 13 and 8 nm.<sup>34</sup> This was assigned to a phenomenological phonon confinement model of the out-of-plane vibrations leading to a relaxed bulk Raman selection rule ( $q = 0$ ). However, our measurements on NFs placed on gold reveal a substantially stronger renormalization for the  $A_{1g}^1$  mode of up to  $3 \text{ cm}^{-1}$  for  $\text{Bi}_2\text{Se}_3$  and even  $5.8 \text{ cm}^{-1}$  for  $\text{Bi}_2\text{Te}_3$  NFs in the same thickness range. Hence, the strong redshifts of the  $A_{1g}^1$  modes and especially the blueshifts of the  $A_{1g}^2$  modes cannot only be attributed to a confined phonon state. Furthermore, the observation of concomitant changes in the line width and Fano parameter hint very strongly toward the presence of a low-energy electronic susceptibility. *Ab initio* calculations have predicted the injection of carriers from gold into  $\text{Bi}_2\text{Se}_3$ , leading to a substantial band bending<sup>11</sup> and accumulation of free carriers on the interface side of the contacted NF. The charge accumulation yields an electric field across the NF due to the insulating bulk as illustrated in Figure 4c. This leads to the conclusion that the build-up field in combination with the induced band bending effect enhances the Raman scattering cross section in contrast to the weaker signal obtained from NFs on Si (see Figure 1b). The strong interface enhancement induced by carrier injection is further supported by the observation of the usually weak bulk IR modes in both  $\text{Bi}_2\text{Se}_3$  and  $\text{Bi}_2\text{Te}_3$ . Additionally, the presence of free carriers injected in the bottom side of the NFs explains both the thickness-dependent phonon renormalizations and intensities. In Figure 4a, we show the dependence of the  $\text{Bi}_2\text{Se}_3$  phonon mode intensities corrected for the NF scattering volume as a function of NF thickness. We find a stronger thickness dependence of the Raman intensities than anticipated by the linear change in scattering volume. For thicker NFs, an enhanced Raman signal is observed that quickly collapses below a critical thickness of about 10 nm. In this range of thinner NFs, we also observe the strongest phonon renormalization indicating a strongly enhanced electron-phonon interaction. In Figure 4b, we schematically display the band bending effects predicted by Spataru et al.<sup>11</sup> for  $\text{Bi}_2\text{Se}_3$  on gold. The injected carriers at the contacted NF surface lead to a downward bending by 1 eV changing the electronic band structure to a depth of 5 nm from the interface of the Au film and the NF<sup>11</sup> and populating the bulk conduction bands. With decreasing NF thickness, this carrier injection reduces the insulating bulk region until the band bending reaches across the entire NF as illustrated in Figure 4b. For thick NFs ( $d > 11 \text{ nm}$ ), the electronic band structure meets the conditions of resonant interband transitions leading to strong Raman susceptibilities. The scattering volume-corrected intensities for thicker NFs are, therefore, constant. However, with decreasing NF thicknesses below  $d < 10 \text{ nm}$ , the band bending quickly leads to tuning out of the resonance conditions in accordance with the drastically reduced Raman signal by more than 80% when reducing the NF thickness from 11 to 9 nm. The scattering volume-corrected intensities for the three phonon modes are readily fit by a sigmoidal function revealing a critical thickness of  $10.2 \pm 0.2 \text{ nm}$ , as shown in Figure 4a. For the sake of clarity, we have depicted a native  $\text{Bi}_2\text{Se}_3$  in Figure 4b with the Fermi level positioned in the center of the bulk band gap at the uncontacted side. However, it is known that the surface of  $\text{Bi}_2\text{Se}_3$  samples is typically *n*-doped after sample preparation due to electron doping by local Se vacancies.<sup>48</sup> The accumulated charges induce a downward band bending similarly to a gold substrate, typically reaching  $\sim 2 \text{ nm}$  below the surface and leading to the formation of trivial

surface states.<sup>49–51</sup> For a 10 nm thick NF, this would give an effective bulk contribution of 6 nm, which is further modified by the strong band bending effects induced by the Au substrate. Hence, only a small region inside an NF would contribute to the resonant Raman scattering signal, which explains the abruptly decreasing Raman intensity for NFs thinner than 10 nm that is caused by tuning the bulk conduction bands out of resonance.

**3.4. Electron-Phonon Interaction.** The growing contribution of injected carriers for decreasing NF thicknesses is further mirrored in the continuous phonon renormalizations. The additional free carriers provide a low-energy electronic susceptibility that couples to the lattice. The resulting electron-phonon interaction can be derived from the phonon self-energy effects,<sup>44</sup> in particular the change of the widths of the phonon line shape can be used to estimate the change in the electron-phonon interaction. The change in the width of the phonon is given by

$$gc_2 = \sqrt{|2\tilde{\Gamma}\omega_0 - 2\Gamma_0\omega_0|} \quad (1)$$

where  $\omega_0$  and  $\Gamma_0$  are the native frequency and not renormalized width of the phonon,  $\tilde{\Gamma}$  is the renormalized width, and  $C_2$  is proportional to the imaginary part of the electronic susceptibility  $\pi_i$ . It is only possible to derive a quantity that is proportional to the electron-phonon coupling  $g$ , and its changes can be derived only if the imaginary part of the electronic susceptibility  $\pi_i$  is constant. However,  $\pi_i$  also determines the electronic background required for the Fano interference. Therefore, we study the changes in the observed electronic susceptibility, i.e., the Bose-corrected background after subtraction of the phonons in Figure 4d. Indeed, we find no changes in the electronic susceptibility, strongly suggesting that  $c_2$  is indeed constant. Accordingly, we can apply eq 1 to derive the change of the electron-phonon coupling as a function of NF thickness, as shown in Figure 4e. We find that the electron-phonon coupling is enhanced at the same critical thickness at which the phonon intensity is reduced, demonstrating that both observations can be related to the band bending effects. For  $\text{Bi}_2\text{Te}_3$  with a reduced bulk band gap and a similar electron affinity of 5.3 eV,<sup>52</sup> one would expect analogous band bending and qualitatively identical effects on Raman enhancement, which is indeed the case as shown in the SI-Section 4.5. This provides evidence that the observed effects seem to be intrinsic for topological insulators of this class of materials.

## 4. CONCLUSIONS

In conclusion, we have studied the interface between a gold substrate and 2D nanoflakes (NFs) of the topological insulators  $\text{Bi}_2\text{Se}_3$  and  $\text{Bi}_2\text{Te}_3$  as a function of NF thickness by means of Raman scattering under resonant excitation with 633 nm. By reducing the thickness of the NFs an increasing surface contribution becomes apparent in the detection of the bulk IR  $E_u^2$  mode in both  $\text{Bi}_2\text{Se}_3$  and  $\text{Bi}_2\text{Te}_3$  at room temperature. We reveal the presence of interface-enhanced Raman scattering and strong phonon renormalization induced by carriers injected from the gold substrate to the TI NF in contact. This carrier injection results in band bending, which leads to the formation of an intrinsic field enhancement for NFs thicker than 11 nm. In turn, the charge accumulation at the contacted side of the NF yields strong phonon renormalization for thinner NFs due to an enhanced

electron-phonon coupling and simultaneous reduction of the resonant Raman conditions. The abrupt reduction in Raman intensity and incipient phonon renormalizations at a transition thickness of 10.5 nm show the implications of band bending effects. This creates a fundamental understanding of TI/gold contacts that should be considered for TI applications and experiments in the ultrathin limit. Our results outline the capability of Raman spectroscopy to study the carrier injection and subsequent electron-phonon interaction in obscured interfaces between a TI and metal contact and pave the way for further investigations on different TI/metal contacts.

## ■ ASSOCIATED CONTENT

### SI Supporting Information

The Supporting Information is available free of charge at <https://pubs.acs.org/doi/10.1021/acsami.2c04380>.

Sample preparation; Raman setup; data treatment; correction factors for resonance Raman study; quantification of NF optical contrast; influence of NF lateral dimensions; symmetry properties of phonons; estimated carrier density in Bi<sub>2</sub>Se<sub>3</sub>; interface enhancement of Bi<sub>2</sub>Te<sub>3</sub> NFs on gold, and ellipsometry data of Au substrate (PDF)

## ■ AUTHOR INFORMATION

### Corresponding Authors

**Sarah Scheitz** – Institut für Nanostruktur- und Festkörperphysik, Center for Free Electron Laser Science (CFEL), Universität Hamburg, 22761 Hamburg, Germany; [orcid.org/0000-0002-0305-5512](https://orcid.org/0000-0002-0305-5512); Email: [sscheitz@physnet.uni-hamburg.de](mailto:sscheitz@physnet.uni-hamburg.de)

**Michael Rübhausen** – Institut für Nanostruktur- und Festkörperphysik, Center for Free Electron Laser Science (CFEL), Universität Hamburg, 22761 Hamburg, Germany; Email: [mruebhu@physnet.uni-hamburg.de](mailto:mruebhu@physnet.uni-hamburg.de)

### Authors

**Tomke Eva Glier** – Institut für Nanostruktur- und Festkörperphysik, Center for Free Electron Laser Science (CFEL), Universität Hamburg, 22761 Hamburg, Germany; [orcid.org/0000-0001-8943-1509](https://orcid.org/0000-0001-8943-1509)

**Christian Nweze** – Institut für Nanostruktur- und Festkörperphysik, Center for Free Electron Laser Science (CFEL), Universität Hamburg, 22761 Hamburg, Germany; [orcid.org/0000-0002-4569-4902](https://orcid.org/0000-0002-4569-4902)

**Malte van Heek** – Institut für Nanostruktur- und Festkörperphysik, Center for Free Electron Laser Science (CFEL), Universität Hamburg, 22761 Hamburg, Germany

**Isa Moch** – Institut für Nanostruktur- und Festkörperphysik, Center for Free Electron Laser Science (CFEL), Universität Hamburg, 22761 Hamburg, Germany

**Robert Zierold** – Institut für Nanostruktur- und Festkörperphysik, Center for Hybrid Nanostructures (CHyN), Universität Hamburg, Hamburg 22761, Germany; [orcid.org/0000-0003-0292-0970](https://orcid.org/0000-0003-0292-0970)

**Robert Blick** – Institut für Nanostruktur- und Festkörperphysik, Center for Hybrid Nanostructures (CHyN), Universität Hamburg, Hamburg 22761, Germany

**Nils Huse** – Institut für Nanostruktur- und Festkörperphysik, Center for Free Electron Laser Science (CFEL), Universität Hamburg, 22761 Hamburg, Germany; [orcid.org/0000-0002-3281-7600](https://orcid.org/0000-0002-3281-7600)

Complete contact information is available at: <https://pubs.acs.org/doi/10.1021/acsami.2c04380>

## Notes

The authors declare no competing financial interest.

## ■ ACKNOWLEDGMENTS

The authors thank Stephan Martens for the support on ellipsometry measurements.

## ■ ABBREVIATIONS

TI, topological insulator  
SOC, spin-orbit coupling  
TSS, topological surface states  
NF, nanoflake  
TEM, transmission electron microscopy  
SAED, selected area electron diffraction  
EDX, energy-dispersive X-ray spectroscopy  
AFM, atomic force microscopy  
OC, optical contrast  
FWHM, full width at half-maximum  
IR, infrared  
DP, Dirac point

## ■ REFERENCES

- (1) Hasan, M. Z.; Kane, C. L. Colloquium: Topological Insulators. *Rev. Mod. Phys.* **2010**, *82*, 3045–3067.
- (2) Qi, X. L.; Zhang, S. C. Topological Insulators and Superconductors. *Rev. Mod. Phys.* **2011**, *83*, 1057–1110.
- (3) Mellnik, A. R.; Lee, J. S.; Richardella, A.; Grab, J. L.; Mintun, P. J.; Fischer, M. H.; Vaezi, A.; Manchon, A.; Kim, E.-A.; Samarth, N.; Ralph, D. C. Spin-Transfer Torque Generated by a Topological Insulator. *Nature* **2014**, *511*, 449–451.
- (4) Fan, Y.; Upadhyaya, P.; Kou, X.; Lang, M.; Takei, S.; Wang, Z.; Tang, J.; He, L.; Chang, L.-T.; Montazeri, M.; Yu, G.; Jiang, W.; Nie, T.; Schwartz, R. N.; Tserkovnyak, Y.; Wang, K. L. Magnetization Switching through Giant Spin-Orbit Torque in a Magnetically Doped Topological Insulator Heterostructure. *Nat. Mater.* **2014**, *13*, 699–704.
- (5) Jamali, M.; Lee, J. S.; Jeong, J. S.; Mahfouzi, F.; Lv, Y.; Zhao, Z.; Nikolić, B. K.; Mkhoyan, K. A.; Samarth, N.; Wang, J.-P. Giant Spin Pumping and Inverse Spin Hall Effect in the Presence of Surface and Bulk Spin-Orbit Coupling of Topological Insulator Bi<sub>2</sub>Se<sub>3</sub>. *Nano Lett.* **2015**, *15*, 7126–7132.
- (6) Pesin, D.; MacDonald, A. H. Spintronics and Pseudospintronics in Graphene and Topological Insulators. *Nat. Mater.* **2012**, *11*, 409–416.
- (7) Zhang, H.; Zhang, X.; Liu, C.; Lee, S.-T.; Jie, J. High-Responsivity, High-Detectivity, Ultrafast Topological Insulator Bi<sub>2</sub>Se<sub>3</sub>/Silicon Heterostructure Broadband Photodetectors. *ACS Nano* **2016**, *10*, 5113–5122.
- (8) Zhao, C.; Zou, Y.; Chen, Y.; Wang, Z.; Lu, S.; Zhang, H.; Wen, S.; Tang, D. Wavelength-Tunable Picosecond Soliton Fiber Laser with Topological Insulator: Bi<sub>2</sub>Se<sub>3</sub> as a Mode Locker. *Opt. Express* **2012**, *20*, 27888–27895.
- (9) Kane, C. L.; Mele, E. J. Z<sub>2</sub> Topological Order and the Quantum Spin Hall Effect. *Phys. Rev. Lett.* **2005**, *95*, No. 146802.
- (10) Kondou, K.; Yoshimi, R.; Tsukazaki, A.; Fukuma, Y.; Matsuno, J.; Takahashi, K. S.; Kawasaki, M.; Tokura, Y.; Otani, Y. Fermi-Level-Dependent Charge-to-Spin Current Conversion by Dirac Surface States of Topological Insulators. *Nat. Phys.* **2016**, *12*, 1027–1031.
- (11) Spataru, C. D.; Léonard, F. Fermi-Level Pinning, Charge Transfer, and Relaxation of Spin-Momentum Locking at Metal Contacts to Topological Insulators. *Phys. Rev. B* **2014**, *90*, No. 085115.

- (12) Yeh, Y. C.; Ho, P. H.; Wen, C. Y.; Shu, G. J.; Sankar, R.; Chou, F. C.; Chen, C. W. Growth of the  $\text{Bi}_2\text{Se}_3$  Surface Oxide for Metal-Semiconductor-Metal Device Applications. *J. Phys. Chem. C* **2016**, *120*, 3314–3318.
- (13) Litvinov, V. *Magnetism in Topological Insulators*; Springer, 2020. <https://doi.org/10.1007/978-3-030-12053-5>.
- (14) Zhang, H.; Liu, C. X.; Qi, X. L.; Dai, X.; Fang, Z.; Zhang, S. C. Topological Insulators in  $\text{Bi}_2\text{Se}_3$ ,  $\text{Bi}_2\text{Te}_3$  and  $\text{Sb}_2\text{Te}_3$  with a Single Dirac Cone on the Surface. *Nat. Phys.* **2009**, *5*, 438–442.
- (15) Hsieh, D.; Xia, Y.; Qian, D.; Wray, L.; Dil, J. H.; Meier, F.; Osterwalder, J.; Patthey, L.; Checkelsky, J. G.; Ong, N. P.; Fedorov, A. V.; Lin, H.; Bansil, A.; Grauer, D.; Hor, Y. S.; Cava, R. J.; Hasan, M. Z. A Tunable Topological Insulator in the Spin Helical Dirac Transport Regime. *Nature* **2009**, *460*, 1101–1105.
- (16) Xia, Y.; Qian, D.; Hsieh, D.; Wray, L.; Pal, A.; Lin, H.; Bansil, A.; Grauer, D.; Hor, Y. S.; Cava, R. J.; Hasan, M. Z. Observation of a Large-Gap Topological-Insulator Class with a Single Dirac Cone on the Surface. *Nat. Phys.* **2009**, *5*, 398–402.
- (17) Chen, Y. L.; Analytis, J. G.; Chu, J.-H.; Liu, Z. K.; et al. Experimental Realization of a Three-Dimensional Topological Insulator,  $\text{Bi}_2\text{Te}_3$ . *Science* **2009**, *325*, 178–181.
- (18) Hsieh, D.; Xia, Y.; Qian, D.; Wray, L.; Meier, F.; Dil, J. H.; Osterwalder, J.; Patthey, L.; Fedorov, A. V.; Lin, H.; Bansil, A.; Grauer, D.; Hor, Y. S.; Cava, R. J.; Hasan, M. Z. Observation of Time-Reversal-Protected Single-Dirac-Cone Topological-Insulator States in  $\text{Bi}_2\text{Te}_3$  and  $\text{Sb}_2\text{Te}_3$ . *Phys. Rev. Lett.* **2009**, *103*, No. 146401.
- (19) Steinberg, H.; Gardner, D. R.; Lee, Y. S.; Jarillo-Herrero, P. Surface State Transport and Ambipolar Electric Field Effect in  $\text{Bi}_2\text{Se}_3$  Nanodevices. *Nano Lett.* **2010**, *10*, 5032–5036.
- (20) Chiatti, O.; Riha, C.; Lawrenz, D.; Busch, M.; Dusari, S.; Sánchez-Barriga, J.; Mogilatenko, A.; Yashina, L. V.; Valencia, S.; Ūnal, A. A.; Rader, O.; Fischer, S. F. 2D Layered Transport Properties from Topological Insulator  $\text{Bi}_2\text{Se}_3$  Single Crystals and Micro Flakes. *Sci. Rep.* **2016**, *6*, No. 27483.
- (21) Hofer, K.; Becker, C.; Rata, D.; Swanson, J.; Thalmeier, P.; Tjeng, L. H. Intrinsic Conduction through Topological Surface States of Insulating  $\text{Bi}_2\text{Te}_3$  Epitaxial Thin Films. *Proc. Natl. Acad. Sci. U.S.A.* **2014**, *111*, 14979–14984.
- (22) Qu, D. X.; Hor, Y. S.; Xiong, J.; Cava, R. J.; Ong, N. P. Quantum Oscillations and Hall Anomaly of Surface States in the Topological Insulator  $\text{Bi}_2\text{Te}_3$ . *Science* **2010**, *329*, 821–824.
- (23) Fanetti, M.; Mikulska, I.; Ferfolja, K.; Moras, P.; Sheverdyeva, P. M.; Panighel, M.; Lodi-Rizzini, A.; Piš, I.; Nappini, S.; Valant, M.; Gardonio, S. Growth, Morphology and Stability of Au in Contact with the  $\text{Bi}_2\text{Se}_3(0001)$  Surface. *Appl. Surf. Sci.* **2019**, *471*, 753–758.
- (24) Walsh, L. A.; Smyth, C. M.; Barton, A. T.; Wang, Q.; Che, Z.; Yue, R.; Kim, J.; Kim, M. J.; Wallace, R. M.; Hinkle, C. L. Interface Chemistry of Contact Metals and Ferromagnets on the Topological Insulator  $\text{Bi}_2\text{Se}_3$ . *J. Phys. Chem. C* **2017**, *121*, 23551–23563.
- (25) Gnezdilov, V.; Pashkevich, Y. G.; Berger, H.; Pomjakushina, E.; Conder, K.; Lemmens, P. Helical Fluctuations in the Raman Response of the Topological Insulator  $\text{Bi}_2\text{Se}_3$ . *Phys. Rev. B* **2011**, *84*, No. 195118.
- (26) Buchenau, S.; Scheitz, S.; Sethi, A.; Slimak, J. E.; Glier, T. E.; Das, P. K.; Dankwort, T.; Akinsinde, L.; Kienle, L.; Rusydi, A.; Ulrich, C.; Cooper, S. L.; Rübhausen, M. Temperature and Magnetic Field Dependent Raman Study of Electron-Phonon Interactions in Thin Films of  $\text{Bi}_2\text{Se}_3$  and  $\text{Bi}_2\text{Te}_3$  Nanoflakes. *Phys. Rev. B* **2020**, *101*, No. 245431.
- (27) Zhang, J.; Peng, Z.; Soni, A.; Zhao, Y.; Xiong, Y.; Peng, B.; Wang, J.; Dresselhaus, M. S.; Xiong, Q. Raman Spectroscopy of Few-Quintuple Layer Topological Insulator  $\text{Bi}_2\text{Se}_3$  nanoplatelets. *Nano Lett.* **2011**, *11*, 2407–2414.
- (28) Mann, C.; West, D.; Miotkowski, I.; Chen, Y. P.; Zhang, S.; Shih, C. K. Mapping the 3D Surface Potential in  $\text{Bi}_2\text{Se}_3$ . *Nat. Commun.* **2013**, *4*, No. 2277.
- (29) Schulz, B.; Bäckström, J.; Budelmann, D.; Maeser, R.; Rübhausen, M.; Klein, M. V.; Schoeffel, E.; Mihill, A.; Yoon, S. Fully Reflective Deep Ultraviolet to near Infrared Spectrometer and Entrance Optics for Resonance Raman Spectroscopy. *Rev. Sci. Instrum.* **2005**, *76*, No. 073107.
- (30) Glier, T. E. *Applications of Functional One-Dimensional Nanostructures Studied by Light Scattering Dissertation*; Universität Hamburg, 2021.
- (31) Arguello, C. A.; Rousseau, D. L.; Porto, S. P. S. First-Order Raman Effect in Wurtzite-Type Crystals. *Phys. Rev.* **1969**, *181*, 1351–1363.
- (32) Majumdar, A. Thermoelectricity in Semiconductor Nanostructures. *Science* **2004**, *303*, 777–778.
- (33) Richter, W.; Becker, C. R. A Raman and Far-Infrared Investigation of Phonons in the Rhombohedral  $\text{V}_2\text{VI}_3$  Compounds. *Phys. Status Solidi (b)* **1977**, *84*, 619–628.
- (34) Zhang, J.; Peng, Z.; Soni, A.; Zhao, Y.; Xiong, Y.; Peng, B.; Wang, J.; Dresselhaus, M. S.; Xiong, Q. Raman Spectroscopy of Few-Quintuple Layer Topological Insulator  $\text{Bi}_2\text{Se}_3$  Nanoplatelets. *Nano Lett.* **2011**, *11*, 2407–2414.
- (35) Shahil, K. M. F.; Hossain, M. Z.; Goyal, V.; Balandin, A. A. Micro-Raman Spectroscopy of Mechanically Exfoliated Few-Quintuple Layers of  $\text{Bi}_2\text{Te}_3$ ,  $\text{Bi}_2\text{Se}_3$ , and  $\text{Sb}_2\text{Te}_3$  Materials. *J. Appl. Phys.* **2012**, *111*, No. 054305.
- (36) Humlíček, J.; Hemzal, D.; Dubroka, A.; Caha, O.; Steiner, H.; Bauer, G.; Springholz, G. Raman and Interband Optical Spectra of Epitaxial Layers of the Topological Insulators  $\text{Bi}_2\text{Te}_3$  and  $\text{Bi}_2\text{Se}_3$  on  $\text{BaF}_2$  substrates. *Phys. Scr.* **2014**, *T162*, No. 014007.
- (37) Mishra, S. K.; Satpathy, S.; Jepsen, O. Electronic Structure and Thermoelectric Properties of Bismuth Telluride and Bismuth Selenide. *J. Phys.: Condens. Matter* **1997**, *9*, 461–470.
- (38) Sharma, Y.; Srivastava, P.; Dashora, A.; Vadkhiya, L.; Bhayani, M. K.; Jain, R.; Jani, A. R.; Ahuja, B. L. Electronic Structure, Optical Properties and Compton Profiles of  $\text{Bi}_2\text{S}_3$  and  $\text{Bi}_2\text{Se}_3$ . *Solid State Sci.* **2012**, *14*, 241–249.
- (39) Shahil, K. M. F.; Hossain, M. Z.; Teweldebrhan, D.; Balandin, A. A. Crystal Symmetry Breaking in Few-Quintuple  $\text{Bi}_2\text{Te}_3$  Films: Applications in Nanometrology of Topological Insulators. *Appl. Phys. Lett.* **2010**, *96*, No. 153103.
- (40) Li, J.; Tu, J. J.; Birman, J. L. Symmetry Predicted Transitions in 3D Topological Insulators. *Solid State Commun.* **2013**, *163*, 11–14.
- (41) Kung, H. H.; Salehi, M.; Boulares, I.; Kemper, A. F.; Koirala, N.; Brahlek, M.; Lošťák, P.; Uher, C.; Merlin, R.; Wang, X.; Cheong, S. W.; Oh, S.; Blumberg, G. Surface Vibrational Modes of the Topological Insulator  $\text{Bi}_2\text{Se}_3$  Observed by Raman Spectroscopy. *Phys. Rev. B* **2017**, *95*, No. 245406.
- (42) Eddrief, M.; Atkinson, P.; Etgens, V.; Jusserand, B. Low-Temperature Raman Fingerprints for Few-Quintuple Layer Topological Insulator  $\text{Bi}_2\text{Se}_3$  films Epitaxied on GaAs. *Nanotechnology* **2014**, *25*, No. 245701.
- (43) Fano, U. Effects of Configuration Interaction on Intensities and Phase Shifts. *Phys. Rev.* **1961**, *124*, 1866–1878.
- (44) Bock, A.; Ostertun, S.; Sharma, R. D.; Rübhausen, M.; Subke, K. O.; Rieck, C. T. Anomalous Self-Energy Effects of the  $\text{B}_{1g}$  Phonon in  $\text{Y}_{1-x}(\text{Pr}, \text{Ca})_x\text{Ba}_2\text{Cu}_3\text{O}_7$  Films. *Phys. Rev. B* **1999**, *60*, 3532–3537.
- (45) Wang, C.; Zhu, X.; Nilsson, L.; Wen, J.; Wang, G.; Shan, X.; Zhang, Q.; Zhang, S.; Jia, J.; Xue, Q. In Situ Raman Spectroscopy of Topological Insulator  $\text{Bi}_2\text{Te}_3$  Films with Varying Thickness. *Nano Res.* **2013**, *6*, 688–692.
- (46) He, R.; Wang, Z.; Qiu, R. L. J.; Delaney, C.; Beck, B.; Kidd, T. E.; Chancey, C. C.; Gao, X. P. A. Observation of Infrared-Active Modes in Raman Scattering from Topological Insulator Nanoplates. *Nanotechnology* **2012**, *23*, No. 455703.
- (47) Yuan, J.; Zhao, M.; Yu, W.; Lu, Y.; Chen, C.; Xu, M.; Li, S.; Loh, K. P.; Bao, Q. Raman Spectroscopy of Two-Dimensional  $\text{Bi}_2\text{Te}_3\text{Se}_{3-x}$  Platelets Produced by Solvothermal Method. *Materials* **2015**, *8*, 5007–5017.
- (48) Hor, Y. S.; Richardella, A.; Roushan, P.; Xia, Y.; Checkelsky, J. G.; Yazdani, A.; Hasan, M. Z.; Ong, N. P.; Cava, R. J. p-type  $\text{Bi}_2\text{Se}_3$  for topological insulator and low-temperature thermoelectric applications. *Phys. Rev. B* **2009**, *79*, No. 195208.

(49) Analytis, J. G.; Chu, J. H.; Chen, Y.; Corredor, F.; McDonald, R. D.; Shen, Z. X.; Fisher, I. R. Bulk Fermi Surface Coexistence with Dirac Surface State in  $\text{Bi}_2\text{Se}_3$ : A Comparison of Photoemission and Shubnikov-de Haas Measurements. *Phys. Rev. B* **2010**, *81*, No. 205407.

(50) Yan, B.; Zhang, D.; Felser, C. Topological surface states of  $\text{Bi}_2\text{Se}_3$  coexisting with Se vacancies. *Phys. Status Solidi RRL* **2013**, *7*, 148–150.

(51) Rakyta, P.; Ujfalussy, B.; Szunyogh, L. Band Bending at the Surface of  $\text{Bi}_2\text{Se}_3$  Studied from First Principles. *New J. Phys.* **2015**, *17*, No. 123011.

(52) Suh, J.; Fu, D.; Liu, X.; Furdyna, J. K.; Yu, K. M.; Walukiewicz, W.; Wu, J. Fermi-Level Stabilization in the Topological Insulators  $\text{Bi}_2\text{Se}_3$  and  $\text{Bi}_2\text{Te}_3$ : Origin of the Surface Electron Gas. *Phys. Rev. B* **2014**, *89*, No. 115307.



## Chapter 6

# 6 Conclusion and Outlook

---

In this work, the significantly enhanced surface contribution of wet-chemically synthesized  $\text{Bi}_2\text{Se}_3$  and  $\text{Bi}_2\text{Te}_3$  nanoflakes was identified by means of Raman spectroscopy. The investigation of 2D NFs under different environmental conditions like low temperatures, high magnetic fields, and in contact to a gold interface was conducted to reveal spectroscopic signatures of the topological surface electrons and their possible interactions with the crystal lattice.

The surface signature is firstly evident in the detection of Raman-forbidden infrared-active modes arising from the broken inversion symmetry at the flakes surfaces. These modes are detected while investigating a manifold of overlapping nanoflakes forming thin film samples at low temperatures of  $< 160$  K and  $< 100$  K for  $\text{Bi}_2\text{Se}_3$  and  $\text{Bi}_2\text{Te}_3$ , respectively. The reduced temperatures are needed to resolve the surface modes as their weak signal is covered by the much stronger Raman response of bulk phonons at elevated temperatures. However, for single NFs placed on a gold substrate a substantial enhancement of the Raman signal is apparent. This enables the detection of IR modes even at room temperature when the NFs thickness is below a critical threshold of around 11 nm.

The high contribution of surface modes suggests a strongly increased presence of the surface related properties, such as the topological surface states, that are expected to result in spectroscopic features. Indeed, the  $\text{Bi}_2\text{Se}_3$  phonon modes show temperature dependent phonon dynamics that cannot solely be described by a symmetric anharmonic decay of the phonons into acoustic modes, which would typically dominate in bulk samples. The phonon modes show additional self-energy corrections. These are successfully described using a model for non-resonant Raman scattering including the coupling of a phonon to a low-energy electric susceptibility. This susceptibility can be assigned to electronic intraband transitions involving the topological Dirac fermions. This is further verified in the modulation of mentioned susceptibility under the application of magnetic fields above 3 T. The influence of a magnetic field parallel to the crystals  $c$ -axis is expected to break time-reversal symmetry, which leads to the acquisition of mass and lifting of the spin helicity in the TSS. This causes a gap opening in the Dirac cone with an energy of several meV. In this thesis, the model of Raman scattering via coupling to low-energy electronic transitions is able to describe the observed phonon renormalizations. We identify an available broad electronic continuum with energies between 16 meV to 22 meV connected to the quasi-relativistic Dirac states. Our results give complementary evidence of the surprisingly strong coupling of the TSS to phonons in  $\text{Bi}_2\text{Se}_3$  that has been identified in ARPES measurements<sup>[148]</sup> and demonstrates a particularly strong interaction with the  $A_{1g}^2$  mode.

In contrast, we find for the  $\text{Bi}_2\text{Te}_3$  thin film sample dominating bulk properties, where the

## 6 Conclusion and Outlook

phonon dynamics are readily described by the anharmonic decay model and no further renormalizations under the influence of a magnetic field are detected. This is primarily assigned to the high amount of smaller cube like NFs that contribute stronger bulk properties and mask possible surface related effects from the NFs present in the sample. Furthermore, the isotropic orientation of the cubes  $c$ -axis to the applied  $\vec{B}$  field impedes the observation of a manipulation in the Dirac states.

The observation of strong modifications in the  $\text{Bi}_2\text{Se}_3$  TSS at fields above 3 T motivates further investigations on the nature of the coupling between phonons and electrons. In future experiments, by applying the magnetic field in-plane of the NFs, the TSS origin could be further verified as the Dirac cone is expected to stay in tact<sup>[162]</sup> and no phonon renormalization as a function of field should occur. On the other hand, to obtain conclusive results of the Dirac cone modulations in  $\text{Bi}_2\text{Te}_3$  a more homogeneous sample is necessary containing only two-dimensional NFs that lie flat on the substrate and enable an orientation of the crystals  $c$ -axis parallel to an external field. The optimization of the  $\text{Bi}_2\text{Te}_3$  NF sample has been started by tuning the synthesis parameters in the wet-chemical synthesis.<sup>[76]</sup> In particular, the choice of polyol solvent and alkaline environment lead to  $\text{Bi}_2\text{Te}_3$  batches solely containing two-dimensional NFs with average thicknesses of  $d = 25$  nm and rather small diameters of around  $1 \mu\text{m}$ .<sup>[76]</sup> However, we are already investigating the influence of the protecting capping agent PVP, where the molecular weight influences the thickness and lateral dimensions. This holds great promise to synthesize  $\text{Bi}_2\text{Te}_3$  NFs with similar dimensions as the  $\text{Bi}_2\text{Se}_3$  NFs.<sup>[76]</sup>

As an outlook for possible future experiments the topological surface structure could be locally manipulated by decorating single  $\text{Bi}_2\text{Se}_3$  or  $\text{Bi}_2\text{Te}_3$  NFs with ferromagnetic nanoparticles (NP) such as  $\text{Fe}_3\text{O}_4$ . Aligning the NP magnetic moments perpendicular to the NF's surfaces by e.g. the application of a weak magnetic field or ferromagnetic substrate, could lead to a strong local field in proximity to the NP. By switching of the magnetic field the reversible breaking of TRS at the  $\text{Fe}_3\text{O}_4$  NP could be studied as a function of time.

While temperature and magnetic field dependent Raman studies discussed in this thesis reveal the presence of electron-phonon coupling related to the topological surface states, an additional surface related electric susceptibility was identified by measurements of single NFs on gold substrates. By measuring  $\text{Bi}_2\text{Se}_3$  and  $\text{Bi}_2\text{Te}_3$  NFs with varying thicknesses our results reveal the transfer of carriers from the gold substrate into the contacted NF surface. The carriers are accumulated at the contacted side, inducing downward band bending due to the population of both the TSS and trivial bulk conduction bands. The strong phonon renormalizations evident in Raman measurements on thin NFs ( $d < 11$  nm) on gold are the result of interactions with the non-topological surface electric susceptibility originating from the bent bulk bands. The discussed results highlight the importance of the choice of contact metals for the exclusive access to the TSS. While our study does not conclude a destruction of the TSS in the thin TI samples, it nevertheless demonstrates the strong

local band bending effects that influence the electronic band structures of NFs below 11 nm thickness. For useful practical devices exploiting the topological transport regime these band bending effects have to be prevented or at least compensated by an appropriate choice of mediating contact layers. The common processing issues with gold, like poor adhesion, are typically counteracted by the use of adhesion layers of Cr<sup>[163,164]</sup>, Ti,<sup>[165]</sup> or Pd,<sup>[166]</sup>. However, the lower work function of these metals between 4.33-5.12 eV<sup>[167]</sup> in comparison to the electron affinity of Bi<sub>2</sub>X<sub>3</sub> around 5.3 eV<sup>[38,150]</sup> has also been shown to give rise to *n*-type doping and additionally chemical reaction and formation of interfacial layers upon direct metal deposition.<sup>[149]</sup> Band bending and intermixing effects with deposited metal contacts lead to a consumption of the topmost quintuple layers and might lead to a hybridization of opposing TSS especially in devices employing ultrathin TI layers. The study of band bending effects could be expanded to further typical contact or adhesion metals mentioned above. Thereby, different results could be gained e.g. (i) in terms of experimental optimization: the most suitable substrate for high-resolution micro-Raman investigations on single nanoflakes or even nanowires could be determined. Or (ii) in terms of fundamental physics: understanding of the influence of band bending effects by the choice of substrate. This could help to tune the surface band structure of 3D TI thin films or NFs, which has to be considered in all other experimental techniques aiming to exclusively study the TSS.

The main issue of utilizing the topological properties in Bi<sub>2</sub>Se<sub>3</sub> and Bi<sub>2</sub>Te<sub>3</sub> applications is, therefore, the reduction of the contribution from topologically trivial surface electron gases. These are, on the one hand, induced by native defects in the material occurring during growth or after exposition to ambient conditions and, on the other hand, formed by carrier transfer from metal contacts. As a consequence the TSS are best accessed when the surface of the TIs is protected by an interface to a suitable ordinary insulator rather than the interface to vacuum or air. The configuration of such heterostructures or the passivation by an amorphous Se/Te layer has been shown to greatly facilitate the access of the topological transport regime.<sup>[168,169]</sup> In the case of the here studied NFs, the passivation of the surface is already dealt with during growth by the adhesion of the polymer ligand.

Additionally, the formation of defects and vacancies during growth can be antagonized by use of counter-dopants, which has been shown to work for Ca<sup>[50]</sup> However, other works show that the counteracting dopants introduce disorder leading to reduced carrier mobilities.<sup>[33]</sup> Since the peculiar topological properties of the 3D TIs form at the interface to trivial insulators, extensive care has to be taken in suitable passivation. The results presented in this work highlight this aspect especially in the only few nm thin Bi<sub>2</sub>Se<sub>3</sub> and Bi<sub>2</sub>Te<sub>3</sub>, which will help in the sample preparation and analysis in future experiments exploring the topological surface states.





# Bibliography

- [1] M. Z. Hasan and C. L. Kane, “Colloquium: Topological insulators,” *Rev. Mod. Phys.*, vol. 82, pp. 3045–3067, 2010.
- [2] X.-L. Qi and S.-C. Zhang, “Topological insulators and superconductors,” *Reviews of Modern Physics*, vol. 83, no. 4, p. 1057, 2011.
- [3] J. E. Moore, “The birth of topological insulators,” *Nature*, vol. 464, no. 7286, p. 194, 2010.
- [4] Y. Ando, “Topological insulator materials,” *Journal of the Physical Society of Japan*, vol. 82, no. 10, p. 102001, 2013.
- [5] K. v. Klitzing, G. Dorda, and M. Pepper, “New method for high-accuracy determination of the fine-structure constant based on quantized Hall resistance,” *Physical review letters*, vol. 45, no. 6, p. 494, 1980.
- [6] M. Nakahara, *Geometry, topology and physics*. CRC press, 2018.
- [7] Y. Tokura, M. Kawasaki, and N. Nagaosa, “Emergent functions of quantum materials,” *Nature Physics*, vol. 13, no. 11, pp. 1056–1068, 2017.
- [8] R. Gross and A. Marx, *Festkörperphysik*, ch. 14 Topologische Quantenmaterie, pp. 929–956. De Gruyter, third ed., 2018.
- [9] D. J. Thouless, M. Kohmoto, M. P. Nightingale, and M. den Nijs, “Quantized Hall conductance in a two-dimensional periodic potential,” *Physical review letters*, vol. 49, no. 6, p. 405, 1982.
- [10] M. V. Berry, “Quantal phase factors accompanying adiabatic changes,” *Proceedings of the Royal Society of London. A. Mathematical and Physical Sciences*, vol. 392, no. 1802, pp. 45–57, 1984.
- [11] C. L. Kane and E. J. Mele, “Z<sub>2</sub> topological order and the quantum spin Hall effect,” *Phys. Rev. Lett.*, vol. 95, p. 146802, 2005.
- [12] B. A. Bernevig, T. L. Hughes, and S.-C. Zhang, “Quantum spin Hall effect and topological phase transition in HgTe quantum wells,” *science*, vol. 314, no. 5806, pp. 1757–1761, 2006.
- [13] L. Fu, C. L. Kane, and E. J. Mele, “Topological insulators in three dimensions,” *Physical review letters*, vol. 98, no. 10, p. 106803, 2007.
- [14] J. E. Moore and L. Balents, “Topological invariants of time-reversal-invariant band structures,” *Physical Review B*, vol. 75, no. 12, p. 121306, 2007.

## BIBLIOGRAPHY

- [15] A. Altland and M. R. Zirnbauer, “Nonstandard symmetry classes in mesoscopic normal-superconducting hybrid structures,” *Physical Review B*, vol. 55, no. 2, p. 1142, 1997.
- [16] B. A. Bernevig, *Topological Insulators and Topological Superconductors*. Princeton University Press, 2013.
- [17] A. H. Castro Neto, F. Guinea, N. M. R. Peres, K. S. Novoselov, and A. K. Geim, “The electronic properties of graphene,” *Reviews of Modern Physics*, vol. 81, pp. 109–162, 2009.
- [18] V. Litvinov, *Magnetism in Topological Insulators*, ch. 8 Device Applications, pp. 143–154. Springer Nature Switzerland AG, 2020.
- [19] Y. Xia, D. Qian, D. Hsieh, L. Wray, A. Pal, H. Lin, A. Bansil, D. Grauer, Y. S. Hor, R. J. Cava, and M. Z. Hasan, “Observation of a large-gap topological-insulator class with a single Dirac cone on the surface,” *Nature Physics*, vol. 5, pp. 398–402, 2009.
- [20] Y.-L. Chen, J. G. Analytis, J.-H. Chu, Z. K. Liu, S.-K. Mo, X. L. Qi, H. J. Zhang, D. H. Lu, X. Dai, Z. Fang, S. C. Zhang, I. R. Fisher, Z. Hussain, and Z.-X. Shen, “Experimental realization of a three-dimensional topological insulator,  $\text{Bi}_2\text{Te}_3$ ,” *Science*, vol. 325, no. 5937, pp. 178–181, 2009.
- [21] H. Zhang, C.-X. Liu, X.-L. Qi, X. Dai, Z. Fang, and S.-C. Zhang, “Topological insulators in  $\text{Bi}_2\text{Se}_3$ ,  $\text{Bi}_2\text{Te}_3$  and  $\text{Sb}_2\text{Te}_3$  with a single Dirac cone on the surface,” *Nature Physics*, vol. 5, pp. 438–442, 2009.
- [22] W. Richter, C. R. Becker, and H. Köhler, “A Raman and far-infrared investigation of phonons in the rhombohedral  $\text{V}_2\text{-VI}_3$  compounds,” *physica status solidi (b)*, vol. 84, pp. 619 – 628, 1977.
- [23] B. A. Bernevig, *Topological Insulators and Topological Superconductors*, ch. 4 Time-Reversal Symmetry, pp. 33–40. Princeton University Press, 2013.
- [24] M. Bianchi, D. Guan, S. Bao, J. Mi, B. B. Iversen, P. D. King, and P. Hofmann, “Coexistence of the topological state and a two-dimensional electron gas on the surface of  $\text{Bi}_2\text{Se}_3$ ,” *Nature communications*, vol. 1, no. 1, pp. 1–5, 2010.
- [25] A. D. LaForge, A. Frenzel, B. C. Pursley, T. Lin, X. Liu, J. Shi, and D. N. Basov, “Optical characterization of  $\text{Bi}_2\text{Se}_3$  in a magnetic field: Infrared evidence for magnetoelectric coupling in a topological insulator material,” *Phys. Rev. B*, vol. 81, p. 125120, 2010.
- [26] Y.-Y. Li, G. Wang, X.-G. Zhu, M.-H. Liu, C. Ye, X. Chen, Y.-Y. Wang, K. He, L.-L. Wang, X.-C. Ma, *et al.*, “Intrinsic topological insulator  $\text{Bi}_2\text{Te}_3$  thin films on Si and their thickness limit,” *Advanced materials*, vol. 22, no. 36, pp. 4002–4007, 2010.
- [27] G. Jnawali, S. Linser, I. A. Shojaei, S. Pournia, H. E. Jackson, L. M. Smith, R. F. Need, and S. D. Wilson, “Revealing optical transitions and carrier recombination

- dynamics within the bulk band structure of  $\text{Bi}_2\text{Se}_3$ ,” *Nano letters*, vol. 18, no. 9, pp. 5875–5884, 2018.
- [28] Y. Chen, J.-H. Chu, J. Analytis, Z. Liu, K. Igarashi, H.-H. Kuo, X. Qi, S.-K. Mo, R. Moore, D. Lu, *et al.*, “Massive Dirac fermion on the surface of a magnetically doped topological insulator,” *Science*, vol. 329, no. 5992, pp. 659–662, 2010.
- [29] R. Yu, W. Zhang, H.-J. Zhang, S.-C. Zhang, X. Dai, and Z. Fang, “Quantized anomalous Hall effect in magnetic topological insulators,” *science*, vol. 329, no. 5987, pp. 61–64, 2010.
- [30] S.-Y. Xu, M. Neupane, C. Liu, D. Zhang, A. Richardella, L. Andrew Wray, N. Alidoust, M. Leandersson, T. Balasubramanian, J. Sánchez-Barriga, *et al.*, “Hedgehog spin texture and Berry’s phase tuning in a magnetic topological insulator,” *Nature Physics*, vol. 8, no. 8, pp. 616–622, 2012.
- [31] D. Hsieh, Y. Xia, D. Qian, L. Wray, F. Meier, J. Dil, J. Osterwalder, L. Patthey, A. Fedorov, H. Lin, *et al.*, “Observation of time-reversal-protected single-Dirac-cone topological-insulator states in  $\text{Bi}_2\text{Te}_3$  and  $\text{Sb}_2\text{Te}_3$ ,” *Physical review letters*, vol. 103, no. 14, p. 146401, 2009.
- [32] H. Steinberg, D. R. Gardner, Y. S. Lee, and P. Jarillo-Herrero, “Surface state transport and ambipolar electric field effect in  $\text{Bi}_2\text{Se}_3$  nanodevices,” *Nano letters*, vol. 10, no. 12, pp. 5032–5036, 2010.
- [33] Y. Hor, A. Richardella, P. Roushan, Y. Xia, J. Checkelsky, A. Yazdani, M. Hasan, N. P. Ong, and R. J. Cava, “p-type  $\text{Bi}_2\text{Se}_3$  for topological insulator and low-temperature thermoelectric applications,” *Physical Review B*, vol. 79, no. 19, p. 195208, 2009.
- [34] H.-J. Noh, H. Koh, S.-J. Oh, J.-H. Park, H.-D. Kim, J. Rameau, T. Valla, T. Kidd, P. Johnson, Y. Hu, *et al.*, “Spin-orbit interaction effect in the electronic structure of  $\text{Bi}_2\text{Te}_3$  observed by angle-resolved photoemission spectroscopy,” *EPL (Europhysics Letters)*, vol. 81, no. 5, p. 57006, 2008.
- [35] C. Chen, S. He, H. Weng, W. Zhang, L. Zhao, H. Liu, X. Jia, D. Mou, S. Liu, J. He, *et al.*, “Robustness of topological order and formation of quantum well states in topological insulators exposed to ambient environment,” *Proceedings of the National Academy of Sciences*, vol. 109, no. 10, pp. 3694–3698, 2012.
- [36] D. Hsieh, Y. Xia, D. Qian, L. Wray, F. Meier, J. Osterwalder, L. Patthey, J. G. Checkelsky, N. Ong, A. V. Fedorov, *et al.*, “A tunable topological insulator in the spin helical Dirac transport regime,” *Nature*, vol. 460, no. 7259, pp. 1101–1105, 2009.
- [37] M. Bianchi, R. C. Hatch, D. Guan, T. Planke, J. Mi, B. B. Iversen, and P. Hofmann, “The electronic structure of clean and adsorbate-covered  $\text{Bi}_2\text{Se}_3$ : an angle-resolved photoemission study,” *Semiconductor Science and Technology*, vol. 27, no. 12, p. 124001, 2012.

## BIBLIOGRAPHY

- [38] J. Suh, D. Fu, X. Liu, J. K. Furdyna, K. M. Yu, W. Walukiewicz, and J. Wu, “Fermi-level stabilization in the topological insulators  $\text{Bi}_2\text{Se}_3$  and  $\text{Bi}_2\text{Te}_3$ : Origin of the surface electron gas,” *Physical Review B*, vol. 89, no. 11, p. 115307, 2014.
- [39] E. De Vries, S. Pezzini, M. Meijer, N. Koirala, M. Salehi, J. Moon, S. Oh, S. Wiedmann, and T. Banerjee, “Coexistence of bulk and surface states probed by Shubnikov–de Haas oscillations in  $\text{Bi}_2\text{Se}_3$  with high charge-carrier density,” *Physical Review B*, vol. 96, no. 4, p. 045433, 2017.
- [40] L. Veyrat, F. Iacovella, J. Dufouleur, C. Nowka, H. Funke, M. Yang, W. Escoffier, M. Goiran, B. Eichler, O. G. Schmidt, *et al.*, “Band bending inversion in  $\text{Bi}_2\text{Se}_3$  nanostructures,” *Nano Letters*, vol. 15, no. 11, pp. 7503–7507, 2015.
- [41] O. Chiatti, C. Riha, D. Lawrenz, M. Busch, S. Dusari, J. Sánchez-Barriga, A. Mogilatenko, L. V. Yashina, S. Valencia, A. A. Ünal, *et al.*, “2D layered transport properties from topological insulator  $\text{Bi}_2\text{Se}_3$  single crystals and micro flakes,” *Scientific Reports*, vol. 6, no. 1, pp. 1–11, 2016.
- [42] H. Cao, R. Venkatasubramanian, C. Liu, J. Pierce, H. Yang, M. Zahid Hasan, Y. Wu, and Y. P. Chen, “Topological insulator  $\text{Bi}_2\text{Te}_3$  films synthesized by metal organic chemical vapor deposition,” *Applied Physics Letters*, vol. 101, no. 16, p. 162104, 2012.
- [43] M. Brahlek, Y. S. Kim, N. Bansal, E. Edrey, and S. Oh, “Surface versus bulk state in topological insulator  $\text{Bi}_2\text{Se}_3$  under environmental disorder,” *Applied Physics Letters*, vol. 99, no. 1, p. 012109, 2011.
- [44] H. M. Benia, C. Lin, K. Kern, and C. R. Ast, “Reactive chemical doping of the  $\text{Bi}_2\text{Se}_3$  topological insulator,” *Physical Review Letters*, vol. 107, no. 17, p. 177602, 2011.
- [45] B. Yan, D. Zhang, and C. Felser, “Topological surface states of  $\text{Bi}_2\text{Se}_3$  coexisting with Se vacancies,” *physica status solidi (RRL)–Rapid Research Letters*, vol. 7, no. 1-2, pp. 148–150, 2013.
- [46] J. G. Analytis, R. D. McDonald, S. C. Riggs, J.-H. Chu, G. Boebinger, and I. R. Fisher, “Two-dimensional surface state in the quantum limit of a topological insulator,” *Nature Physics*, vol. 6, no. 12, pp. 960–964, 2010.
- [47] A. Taskin, Z. Ren, S. Sasaki, K. Segawa, and Y. Ando, “Observation of Dirac holes and electrons in a topological insulator,” *Physical Review Letters*, vol. 107, no. 1, p. 016801, 2011.
- [48] D. Kong, Y. Chen, J. J. Cha, Q. Zhang, J. G. Analytis, K. Lai, Z. Liu, S. S. Hong, K. J. Koski, S.-K. Mo, *et al.*, “Ambipolar field effect in the ternary topological insulator  $\text{Bi}_x\text{Sb}_{1-x}\text{Te}_3$  by composition tuning,” *Nature nanotechnology*, vol. 6, no. 11, pp. 705–709, 2011.

- [49] J. Chen, H. Qin, F. Yang, J. Liu, T. Guan, F. Qu, G. Zhang, J. Shi, X. Xie, C. Yang, *et al.*, “Gate-voltage control of chemical potential and weak antilocalization in  $\text{Bi}_2\text{Se}_3$ ,” *Physical Review Letters*, vol. 105, no. 17, p. 176602, 2010.
- [50] J. Checkelsky, Y. Hor, R. Cava, and N. Ong, “Bulk band gap and surface state conduction observed in voltage-tuned crystals of the topological insulator  $\text{Bi}_2\text{Se}_3$ ,” *Physical review letters*, vol. 106, no. 19, p. 196801, 2011.
- [51] P. Wei, Z. Wang, X. Liu, V. Aji, and J. Shi, “Field-effect mobility enhanced by tuning the Fermi level into the band gap of  $\text{Bi}_2\text{Se}_3$ ,” *Physical Review B*, vol. 85, no. 20, p. 201402, 2012.
- [52] F. Xiu, L. He, Y. Wang, L. Cheng, L.-T. Chang, M. Lang, G. Huang, X. Kou, Y. Zhou, X. Jiang, *et al.*, “Manipulating surface states in topological insulator nanoribbons,” *Nature nanotechnology*, vol. 6, no. 4, pp. 216–221, 2011.
- [53] Y. Wang, F. Xiu, L. Cheng, L. He, M. Lang, J. Tang, X. Kou, X. Yu, X. Jiang, Z. Chen, *et al.*, “Gate-controlled surface conduction in Na-doped  $\text{Bi}_2\text{Te}_3$  topological insulator nanoplates,” *Nano letters*, vol. 12, no. 3, pp. 1170–1175, 2012.
- [54] R. Yoshimi, A. Tsukazaki, Y. Kozuka, J. Falson, K. Takahashi, J. Checkelsky, N. Nagaosa, M. Kawasaki, and Y. Tokura, “Quantum Hall effect on top and bottom surface states of topological insulator  $(\text{Bi}_{1-x}\text{Sb}_x)_2\text{Te}_3$  films,” *Nature communications*, vol. 6, no. 1, pp. 1–6, 2015.
- [55] T. P. Ginley, Y. Wang, and S. Law, “Topological insulator film growth by molecular beam epitaxy: A review,” *Crystals*, vol. 6, no. 11, p. 154, 2016.
- [56] Y. Zhang, K. He, C.-Z. Chang, C.-L. Song, L.-L. Wang, X. Chen, J.-F. Jia, Z. Fang, X. Dai, W.-Y. Shan, S.-Q. Shen, Q. Niu, X.-L. Qi, S.-C. Zhang, X.-C. Ma, and Q.-K. Xue, “Crossover of the three-dimensional topological insulator  $\text{Bi}_2\text{Se}_3$  to the two-dimensional limit,” *Nature Physics*, vol. 6, p. 584, 2010.
- [57] F. Vidal, M. Eddrief, B. R. Salles, I. Vobornik, E. Velez-Fort, G. Panaccione, and M. Marangolo, “Photon energy dependence of circular dichroism in angle-resolved photoemission spectroscopy of  $\text{Bi}_2\text{Se}_3$  Dirac states,” *Physical Review B*, vol. 88, no. 24, p. 241410, 2013.
- [58] M. Neupane, A. Richardella, J. Sánchez-Barriga, S. Xu, N. Alidoust, I. Belopolski, C. Liu, G. Bian, D. Zhang, D. Marchenko, *et al.*, “Observation of quantum-tunnelling-modulated spin texture in ultrathin topological insulator  $\text{Bi}_2\text{Se}_3$  films,” *Nature communications*, vol. 5, no. 1, pp. 1–7, 2014.
- [59] W. Zhang, R. Yu, H.-J. Zhang, X. Dai, and Z. Fang, “First-principles studies of the three-dimensional strong topological insulators  $\text{Bi}_2\text{Te}_3$ ,  $\text{Bi}_2\text{Se}_3$  and  $\text{Sb}_2\text{Te}_3$ ,” *New Journal of Physics*, vol. 12, no. 6, p. 065013, 2010.
- [60] Z.-H. Wang, X. P. Gao, and Z.-D. Zhang, “Transport properties of doped  $\text{Bi}_2\text{Se}_3$

## BIBLIOGRAPHY

- and  $\text{Bi}_2\text{Te}_3$  topological insulators and heterostructures,” *Chinese Physics B*, vol. 27, no. 10, p. 107901, 2018.
- [61] L. Malard, M. A. Pimenta, G. Dresselhaus, and M. Dresselhaus, “Raman spectroscopy in graphene,” *Physics reports*, vol. 473, no. 5-6, pp. 51–87, 2009.
- [62] V. Gnezdilov, Y. G. Pashkevich, H. Berger, E. Pomjakushina, K. Conder, and P. Lemmens, “Helical fluctuations in the Raman response of the topological insulator  $\text{Bi}_2\text{Se}_3$ ,” *Phys. Rev. B*, vol. 84, p. 195118, 2011.
- [63] Y. D. Glinka, S. Babakiray, T. A. Johnson, and D. Lederman, “Thickness tunable quantum interference between surface phonon and Dirac plasmon states in thin films of the topological insulator  $\text{Bi}_2\text{Se}_3$ ,” *Journal of Physics: Condensed Matter*, vol. 27, no. 5, p. 052203, 2015.
- [64] J. Zhang, Z. Peng, A. Soni, Y. Zhao, Y. Xiong, B. Peng, J. Wang, M. S. Dresselhaus, and Q. Xiong, “Raman spectroscopy of few-quintuple layer topological insulator  $\text{Bi}_2\text{Se}_3$  nanoplatelets,” *Nano Letters*, vol. 11, no. 6, pp. 2407–2414, 2011.
- [65] Y. D. Glinka, S. Babakiray, and D. Lederman, “Plasmon-enhanced electron-phonon coupling in Dirac surface states of the thin-film topological insulator  $\text{Bi}_2\text{Se}_3$ ,” *Journal of Applied Physics*, vol. 118, no. 13, p. 135713, 2015.
- [66] M. Brahlek, N. Koirala, M. Salehi, J. Moon, W. Zhang, H. Li, X. Zhou, M.-G. Han, L. Wu, T. Emge, *et al.*, “Disorder-driven topological phase transition in  $\text{Bi}_2\text{Se}_3$  films,” *Physical Review B*, vol. 94, no. 16, p. 165104, 2016.
- [67] F. Fievet, J. Lagier, and M. Figlarz, “Preparing monodisperse metal powders in micrometer and submicrometer sizes by the polyol process,” *MRS Bulletin*, vol. 14, no. 12, pp. 29–34, 1989.
- [68] C. Bock, C. Paquet, M. Couillard, G. A. Botton, and B. R. MacDougall, “Size-selected synthesis of PtRu nano-catalysts: Reaction and size control mechanism,” *Journal of the American Chemical Society*, vol. 126, no. 25, pp. 8028–8037, 2004.
- [69] Y. Holade, N. E. Sahin, K. Servat, T. W. Napporn, and K. B. Kokoh, “Recent advances in carbon supported metal nanoparticles preparation for oxygen reduction reaction in low temperature fuel cells,” *Catalysts*, vol. 5, no. 1, pp. 310–348, 2015.
- [70] Y. Min, G. D. Moon, B. S. Kim, B. Lim, J.-S. Kim, C. Y. Kang, and U. Jeong, “Quick, controlled synthesis of ultrathin  $\text{Bi}_2\text{Se}_3$  nanodiscs and nanosheets,” *Journal of the American Chemical Society*, vol. 134, no. 6, pp. 2872–2875, 2012.
- [71] M. Hong, Z.-G. Chen, L. Yang, G. Han, and J. Zou, “Enhanced thermoelectric performance of ultrathin  $\text{Bi}_2\text{Se}_3$  nanosheets through thickness control,” *Advanced Electronic Materials*, vol. 1, no. 6, p. 1500025, 2015.
- [72] Y. Zhang, L. P. Hu, T. J. Zhu, J. Xie, and X. B. Zhao, “High yield  $\text{Bi}_2\text{Te}_3$  single crystal nanosheets with uniform morphology via a solvothermal synthesis,” *Crystal Growth & Design*, vol. 13, no. 2, pp. 645–651, 2013.

- [73] X. He, H. Zhang, W. Lin, R. Wei, J. Qiu, M. Zhang, and B. Hu, “PVP-assisted solvothermal synthesis of high-yielded  $\text{Bi}_2\text{Te}_3$  hexagonal nanoplates: application in passively Q-switched fiber laser,” *Scientific reports*, vol. 5, no. 1, pp. 1–10, 2015.
- [74] W. Shi, L. Zhou, S. Song, J. Yang, and H. Zhang, “Hydrothermal synthesis and thermoelectric transport properties of impurity-free antimony telluride hexagonal nanoplates,” *Advanced Materials*, vol. 20, no. 10, pp. 1892–1897, 2008.
- [75] J. Dilling, “Growth and characterization of growth and characterization of two-dimensional  $\text{Sb}_2\text{Te}_3$  nanoflakes,” Bachelor thesis, University of Hamburg, 2020.
- [76] M.-C. Dalchow, “Synthesis and characterization of topological insulator  $\text{Bi}_2\text{Te}_3$  2D hexagonal nanoflakes,” Bachelor thesis, University of Hamburg, 2021.
- [77] S. Scheitz, “Temperature and magnetic field dependent Raman spectroscopy of topological insulator  $\text{Bi}_2\text{Se}_3$  and  $\text{Bi}_2\text{Te}_3$  2D nanostructures,” Master thesis, University of Hamburg, 2019.
- [78] S. Buchenau, S. Scheitz, A. Sethi, J. E. Slimak, T. E. Glier, P. K. Das, T. Dankwort, L. Akinsinde, L. Kienle, A. Rusydi, *et al.*, “Temperature and magnetic field dependent Raman study of electron-phonon interactions in thin films of  $\text{Bi}_2\text{Se}_3$  and  $\text{Bi}_2\text{Te}_3$  nanoflakes,” *Physical Review B*, vol. 101, no. 24, p. 245431, 2020.
- [79] S. Buchenau, P. Sergelius, C. Wiegand, R. Zierold, H. S. Shin, M. Rübhausen, J. Gooth, K. Nielsch, *et al.*, “Symmetry breaking of the surface mediated quantum Hall effect in  $\text{Bi}_2\text{Se}_3$  nanoplates using  $\text{Fe}_3\text{O}_4$  substrates,” *2D Materials*, vol. 4, no. 1, p. 015044, 2017.
- [80] L. Akinsinde, S. Scheitz, L. Zimoch, J. Sierck, L. Siebert, R. Adelung, U. Schürmann, M. Rübhausen, T. Dankwort, and L. Kienle, “Resistivity response to stress and strain of a flexible  $\text{Bi}_2\text{Te}_3$  based thermoelectric material,” in *International Conference on Nanotechnologies and Biomedical Engineering*, pp. 57–60, Springer, 2019.
- [81] B. Irfan, S. Sahoo, A. P. S. Gaur, M. Ahmadi, M. J.-F. Guinel, R. S. Katiyar, and R. Chatterjee, “Temperature dependent Raman scattering studies of three dimensional topological insulators  $\text{Bi}_2\text{Se}_3$ ,” *Journal of Applied Physics*, vol. 115, p. 173506, 2014.
- [82] Q. Yao, Y. Zhu, L. Chen, Z. Sun, and X. Chen, “Microwave-assisted synthesis and characterization of  $\text{Bi}_2\text{Te}_3$  nanosheets and nanotubes,” *Journal of Alloys and Compounds*, vol. 481, pp. 91–95, 2009.
- [83] A. Pinczuk and E. Burstein, *Light Scattering in Solids I*, vol. 8, ch. 2 Fundamentals of inelastic light scattering in semiconductors and insulators, pp. 23–78. Springer-Verlag Berlin Heidelberg New York, 1983.
- [84] M. Cardona, *Light Scattering in Solids II: Basic Concepts and Instrumentation*, ch. 2.1 Classical Theory: Elastic Scattering by Molecules, Liquids, and Solids, pp. 22–98. Springer-Verlag Berlin Heidelberg New York, 1982.

## BIBLIOGRAPHY

- [85] R. Loudon, “The Raman effect in crystals,” *Advances in Physics*, vol. 13, no. 52, pp. 423–482, 1964.
- [86] A. Jorio, R. Saito, G. Dresselhaus, and M. Dresselhaus, *Raman Spectroscopy in Graphene Related Systems*, ch. 5 Quantum Description of Raman Scattering, pp. 103–119. John Wiley & Sons, 2011.
- [87] R. Loudon, *The Quantum Theory of Light*, ch. 4 .3.1 First order transition and Fermi’s golden rule, pp. 133–136. Oxford University Press, 1973.
- [88] W. Hayes and L. Rodney, *Scattering of Light by Crystals*. J. Wiley and Sons, New York, 1978.
- [89] R. D. Mattuck, *A guide to Feynman diagrams in the many-body problem*. Courier Corporation, 1992.
- [90] A. Kawabata, “Green function theory of Raman scattering,” *Journal of the Physical Society of Japan*, vol. 30, no. 1, pp. 68–85, 1971.
- [91] M. A. Rübhausen, *Electronic Correlations in Cuprate Superconductors - An Inelastic Light Scatterin Study*. PhD thesis, Universität Hamburg, 1998.
- [92] T. E. Glier, S. Scheitz, C. Nweze, and M. Rübhausen, “Inelastic light scattering to study electron-phonon interactions in topological insulators.” unpublished manuscript, Feb. 2022.
- [93] J. Kim, T. E. Glier, B. Grimm-Lebsanft, S. Buchenau, M. Teubner, F. Biebl, N.-J. Kim, H. Kim, G.-C. Yi, M. Rübhausen, *et al.*, “Quantum confinement induced excitonic mechanism in zinc-oxide-nanowalled microrod arrays for UV–vis surface-enhanced Raman scattering,” *The Journal of Physical Chemistry C*, vol. 123, no. 40, pp. 24957–24962, 2019.
- [94] A. Bock, S. Ostertun, R. D. Sharma, M. Rübhausen, K.-O. Subke, and C. Rieck, “Anomalous self-energy effects of the  $B_{1g}$  phonon in  $Y_{1-x}(\text{Pr}, \text{Ca})_x\text{Ba}_2\text{Cu}_3\text{O}_7$  films,” *Physical Review B*, vol. 60, no. 5, p. 3532, 1999.
- [95] T. Devereaux, A. Virosztek, and A. Zawadowski, “Charge-transfer fluctuation, d-wave superconductivity, and the  $B_{1g}$  Raman phonon in cuprates,” *Physical Review B*, vol. 51, no. 1, p. 505, 1995.
- [96] U. Fano, “Effects of configuration interaction on intensities and phase shifts,” *Phys. Rev.*, vol. 124, pp. 1866–1878, 1961.
- [97] J. F. Nye, *physical properties of crystals*. Oxford, Clarendon Press, 1957.
- [98] G. F. Koster, J. O. Dimmock, and R. G. Wheeler, *Properties of the thirty-two point groups*, vol. 24. MIT press, 1963.
- [99] R. Cowley, “Raman scattering from crystals of the diamond structure,” *Journal de Physique*, vol. 26, no. 11, pp. 659–667, 1965.



- [100] J. Menéndez and M. Cardona, “Temperature dependence of the first-order Raman scattering by phonons in Si, Ge, and  $\alpha$ -Sn: Anharmonic effects,” *Physical Review B*, vol. 29, no. 4, p. 2051, 1984.
- [101] Y. Kim, X. Chen, Z. Wang, J. Shi, I. Miotkowski, Y. Chen, P. Sharma, A. Lima Sharma, M. Hekmaty, Z. Jiang, *et al.*, “Temperature dependence of Raman-active optical phonons in  $\text{Bi}_2\text{Se}_3$  and  $\text{Sb}_2\text{Te}_3$ ,” *Applied Physics Letters*, vol. 100, no. 7, p. 071907, 2012.
- [102] Y. Tian, S. Jia, R. J. Cava, R. Zhong, J. Schneeloch, G. Gu, and K. S. Burch, “Understanding the evolution of anomalous anharmonicity in  $\text{Bi}_2\text{Te}_{3-x}\text{Se}_x$ ,” *Physical Review B*, vol. 95, no. 9, p. 094104, 2017.
- [103] A. Maradudin, A. Fein, and G. Vineyard, “On the evaluation of phonon widths and shifts,” *physica status solidi (b)*, vol. 2, no. 11, pp. 1479–1492, 1962.
- [104] P. G. Klemens, “Anharmonic decay of optical phonons,” *Phys. Rev.*, vol. 148, pp. 845–848, 1966.
- [105] J. Zhang, H. J. Liu, L. Cheng, J. Wei, J. Shi, X. F. Tang, and C. Uher, “Enhanced thermoelectric performance of a quintuple layer of  $\text{Bi}_2\text{Te}_3$ ,” *Journal of Applied Physics*, vol. 116, no. 2, p. 023706, 2014.
- [106] H. Köhler and C. R. Becker, “Optically active lattice vibrations in  $\text{Bi}_2\text{Se}_3$ ,” *physica status solidi (b)*, vol. 61, no. 2, pp. 533–537, 1974.
- [107] V. Wagner, G. Dolling, B. Powell, and G. Landweher, “Lattice vibrations of  $\text{Bi}_2\text{Te}_3$ ,” *physica status solidi (b)*, vol. 85, no. 1, pp. 311–317, 1978.
- [108] B.-T. Wang and P. Zhang, “Phonon spectrum and bonding properties of  $\text{Bi}_2\text{Se}_3$ : Role of strong spin-orbit interaction,” *Applied Physics Letters*, vol. 100, no. 8, p. 082109, 2012.
- [109] H. Rauh, R. Geick, H. Kohler, N. Nucker, and N. Lehner, “Generalized phonon density of states of the layer compounds  $\text{Bi}_2\text{Se}_3$ ,  $\text{Bi}_2\text{Te}_3$ ,  $\text{Sb}_2\text{Te}_3$  and  $\text{Bi}_2(\text{Te}_{0.5}\text{Se}_{0.5})_3$ ,  $(\text{Bi}_{0.5}\text{Sb}_{0.5})_2\text{Te}_3$ ,” *Journal of Physics C: Solid State Physics*, vol. 14, no. 20, p. 2705, 1981.
- [110] V. Chis, I. Y. Sklyadneva, K. A. Kokh, V. Volodin, O. Tereshchenko, and E. Chulkov, “Vibrations in binary and ternary topological insulators: First-principles calculations and Raman spectroscopy measurements,” *Physical Review B*, vol. 86, no. 17, p. 174304, 2012.
- [111] W. Cheng and S.-F. Ren, “Phonons of single quintuple  $\text{Bi}_2\text{Te}_3$  and  $\text{Bi}_2\text{Se}_3$  films and bulk materials,” *Physical Review B*, vol. 83, no. 9, p. 094301, 2011.
- [112] R. Vilaplana, D. Santamaría-Pérez, O. Gomis, F. Manjón, J. González, A. Segura, A. Muñoz, P. Rodríguez-Hernández, E. Pérez-González, V. Marín-Borrás, *et al.*, “Structural and vibrational study of  $\text{Bi}_2\text{Se}_3$  under high pressure,” *Physical Review B*, vol. 84, no. 18, p. 184110, 2011.

## BIBLIOGRAPHY

- [113] H.-H. Kung, M. Salehi, I. Boulares, A. F. Kemper, N. Koirala, M. Brahlek, P. Lošťák, C. Uher, R. Merlin, X. Wang, S.-W. Cheong, S. Oh, and G. Blumberg, “Surface vibrational modes of the topological insulator  $\text{Bi}_2\text{Se}_3$  observed by Raman spectroscopy,” *Phys. Rev. B*, vol. 95, p. 245406, 2017.
- [114] I. Boulares, G. Shi, E. Kioupakis, P. Lošťák, C. Uher, and R. Merlin, “Surface phonons in the topological insulators  $\text{Bi}_2\text{Se}_3$  and  $\text{Bi}_2\text{Te}_3$ ,” *Solid State Communications*, vol. 271, pp. 1–5, 2018.
- [115] M. Eddrief, P. Atkinson, V. Etgens, and B. Jusserand, “Low-temperature Raman fingerprints for few-quintuple layer topological insulator  $\text{Bi}_2\text{Se}_3$  films epitaxied on GaAs,” *Nanotechnology*, vol. 25, no. 24, p. 245701, 2014.
- [116] C. Wang, X. Zhu, L. Nilsson, J. Wen, G. Wang, X. Shan, Q. Zhang, S. Zhang, J. Jia, and Q. Xue, “In situ Raman spectroscopy of topological insulator  $\text{Bi}_2\text{Te}_3$  films with varying thickness,” *Nano Research*, vol. 6, no. 9, pp. 688–692, 2013.
- [117] K. Shahil, M. Hossain, D. Teweldebrhan, and A. Balandin, “Crystal symmetry breaking in few-quintuple  $\text{Bi}_2\text{Te}_3$  films: Applications in nanometrology of topological insulators,” *Applied physics letters*, vol. 96, no. 15, p. 153103, 2010.
- [118] K. Shahil, M. Hossain, V. Goyal, and A. Balandin, “Micro-Raman spectroscopy of mechanically exfoliated few-quintuple layers of  $\text{Bi}_2\text{Te}_3$ ,  $\text{Bi}_2\text{Se}_3$ , and  $\text{Sb}_2\text{Te}_3$  materials,” *Journal of Applied Physics*, vol. 111, no. 5, p. 054305, 2012.
- [119] R. He, Z. Wang, R. L. J. Qiu, C. Delaney, B. Beck, T. E. Kidd, C. C. Chancey, and X. P. A. Gao, “Observation of infrared-active modes in Raman scattering from topological insulator nanoplates,” *Nanotechnology*, vol. 23, no. 45, p. 455703, 2012.
- [120] Y. Liang, W. Wang, B. Zeng, G. Zhang, J. Huang, J. Li, T. Li, Y. Song, and X. Zhang, “Raman scattering investigation of  $\text{Bi}_2\text{Te}_3$  hexagonal nanoplates prepared by a solvothermal process in the absence of NaOH,” *Journal of Alloys and Compounds*, vol. 509, no. 16, pp. 5147 – 5151, 2011.
- [121] J. Yuan, M. Zhao, W. Yu, Y. Lu, C. Chen, M. Xu, S. Li, K. P. Loh, and B. Qiao-liang, “Raman spectroscopy of two-dimensional  $\text{Bi}_2\text{Te}_x\text{Se}_{3-x}$  platelets produced by solvothermal method,” *Materials*, vol. 8, no. 8, pp. 5007–5017, 2015.
- [122] M. Kang, *Low energy electronic Raman scattering in cuprate high temperature superconductors*. PhD thesis, University of Illinois at Urbana-Champaign, 1997.
- [123] T. Byrum, *Raman scattering studies of spinels  $\text{CoV}_2\text{O}_4$  and  $\text{MnV}_2\text{O}_4$* . PhD thesis, University of Illinois at Urbana-Champaign, 2016.
- [124] A. Sethi, *Inelastic light scattering studies of novel magnetodielectric mechanisms in transition metal  $\text{CoCr}_2\text{O}_4$  and rare earth  $\text{Ce}_2\text{O}_3$* . PhD thesis, University of Illinois at Urbana-Champaign, 2020.
- [125] M. Kim, X. M. Chen, X. Wang, C. S. Nelson, R. Budakian, P. Abbamonte, and S. L.

- Cooper, “Pressure and field tuning the magnetostructural phases of  $\text{Mn}_3\text{O}_4$ : Raman scattering and X-ray diffraction studies,” *Phys. Rev. B*, vol. 84, p. 174424, 2011.
- [126] B. Schulz, J. Bäckström, D. Budelmann, R. Maeser, M. Rübhausen, M. V. Klein, E. Schoeffel, A. Mihill, and S. Yoon, “Fully reflective deep ultraviolet to near infrared spectrometer and entrance optics for resonance Raman spectroscopy,” *Review of Scientific Instruments*, vol. 76, no. 7, p. 073107, 2005.
- [127] L. Westphal, “Mikro-raman-charakterisierung von nanostrukturierten proben,” 2020.
- [128] T. E. Glier, *Applications of Functional One-Dimensional Nanostructures Studied by Light Scattering*. PhD thesis, University of Hamburg, 2021.
- [129] S. Scheitz, T. E. Glier, C. Nweze, M. van Heek, I. Moch, R. Zierold, R. H. Blick, N. Huse, and M. Rübhausen, “Carrier injection observed by interface-enhanced Raman scattering from topological insulators on gold substrates,” *ACS Applied Materials & Interfaces*, 2022.
- [130] F. Zhou, Y. Zhao, W. Zhou, and D. Tang, “Temperature-dependent Raman scattering of large size hexagonal  $\text{Bi}_2\text{Se}_3$  single-crystal nanoplates,” *Applied Sciences*, vol. 8, no. 10, p. 1794, 2018.
- [131] D. Li, L. Li, D.-W. Liu, and J.-F. Li, “Temperature dependence of the raman spectra of  $\text{Bi}_2\text{Te}_3$  and  $\text{Bi}_{0.5}\text{Sb}_{1.5}\text{Te}_3$  thermoelectric films,” *physica status solidi (RRL)–Rapid Research Letters*, vol. 6, no. 6, pp. 268–270, 2012.
- [132] M. M. Alsalama, H. Hamoudi, A. Abdala, Z. K. Ghouri, and K. M. Youssef, “Enhancement of thermoelectric properties of layered chalcogenide materials,” *Reviews on Advanced Materials Science*, vol. 59, no. 1, pp. 371–378, 2020.
- [133] Y. Xu, I. Miotkowski, C. Liu, J. Tian, H. Nam, N. Alidoust, J. Hu, C.-K. Shih, M. Z. Hasan, and Y. P. Chen, “Observation of topological surface state quantum Hall effect in an intrinsic three-dimensional topological insulator,” *Nature Physics*, vol. 10, no. 12, pp. 956–963, 2014.
- [134] J. G. Analytis, J.-H. Chu, Y. Chen, F. Corredor, R. D. McDonald, Z. Shen, and I. R. Fisher, “Bulk Fermi surface coexistence with Dirac surface state in  $\text{Bi}_2\text{Se}_3$ : A comparison of photoemission and Shubnikov–de Haas measurements,” *Physical Review B*, vol. 81, no. 20, p. 205407, 2010.
- [135] Y. Hor, P. Roushan, H. Beidenkopf, J. Seo, D. Qu, J. Checkelsky, L. Wray, D. Hsieh, Y. Xia, S.-Y. Xu, *et al.*, “Development of ferromagnetism in the doped topological insulator  $\text{Bi}_{2-x}\text{Mn}_x\text{Te}_3$ ,” *Physical Review B*, vol. 81, no. 19, p. 195203, 2010.
- [136] L. A. Wray, S.-Y. Xu, Y. Xia, D. Hsieh, A. V. Fedorov, Y. S. Hor, R. J. Cava, A. Bansil, H. Lin, and M. Z. Hasan, “A topological insulator surface under strong Coulomb, magnetic and disorder perturbations,” *Nature Physics*, vol. 7, no. 1, pp. 32–37, 2011.

## BIBLIOGRAPHY

- [137] W. Luo and X.-L. Qi, “Massive Dirac surface states in topological insulator/magnetic insulator heterostructures,” *Physical Review B*, vol. 87, no. 8, p. 085431, 2013.
- [138] P. Wei, F. Katmis, B. A. Assaf, H. Steinberg, P. Jarillo-Herrero, D. Heiman, and J. S. Moodera, “Exchange-coupling-induced symmetry breaking in topological insulators,” *Physical review letters*, vol. 110, no. 18, p. 186807, 2013.
- [139] E. D. Rienks, S. Wimmer, J. Sánchez-Barriga, O. Caha, P. S. Mandal, J. Růžička, A. Ney, H. Steiner, V. V. Volobuev, H. Groß, *et al.*, “Large magnetic gap at the Dirac point in  $\text{Bi}_2\text{Te}_3/\text{MnBi}_2\text{Te}_4$  heterostructures,” *Nature*, vol. 576, no. 7787, pp. 423–428, 2019.
- [140] R. Lu, H. Sun, S. Kumar, Y. Wang, M. Gu, M. Zeng, Y.-J. Hao, J. Li, J. Shao, X.-M. Ma, *et al.*, “Half-magnetic topological insulator with magnetization-induced Dirac gap at a selected surface,” *Physical Review X*, vol. 11, no. 1, p. 011039, 2021.
- [141] L. Zhang, D. Zhao, Y. Zang, Y. Yuan, G. Jiang, M. Liao, D. Zhang, K. He, X. Ma, and Q. Xue, “Ferromagnetism in vanadium-doped  $\text{Bi}_2\text{Se}_3$  topological insulator films,” *APL Materials*, vol. 5, no. 7, p. 076106, 2017.
- [142] W. Tian, W. Yu, J. Shi, and Y. Wang, “The property, preparation and application of topological insulators: a review,” *Materials*, vol. 10, no. 7, p. 814, 2017.
- [143] D. Posener, “The shape of spectral lines: Tables of the Voigt profile,” *Australian Journal of Physics*, vol. 12, no. 2, pp. 184–196, 1959.
- [144] S. Sahoo, A. P. Gaur, M. Ahmadi, M. J.-F. Guinel, and R. S. Katiyar, “Temperature-dependent Raman studies and thermal conductivity of few-layer  $\text{MoS}_2$ ,” *The Journal of Physical Chemistry C*, vol. 117, no. 17, pp. 9042–9047, 2013.
- [145] N. Bonini, M. Lazzeri, N. Marzari, and F. Mauri, “Phonon anharmonicities in graphite and graphene,” *Phys. Rev. Lett.*, vol. 99, p. 176802, 2007.
- [146] E. H. Hasdeo, A. R. Nugraha, M. S. Dresselhaus, and R. Saito, “Breit-Wigner-Fano line shapes in Raman spectra of graphene,” *Physical Review B*, vol. 90, no. 24, p. 245140, 2014.
- [147] R. Heid, I. Y. Sklyadneva, and E. V. Chulkov, “Electron-phonon coupling in topological surface states: The role of polar optical modes,” *Scientific reports*, vol. 7, no. 1, pp. 1–9, 2017.
- [148] R. C. Hatch, M. Bianchi, D. Guan, S. Bao, J. Mi, B. B. Iversen, L. Nilsson, L. Hornekær, and P. Hofmann, “Stability of the  $\text{Bi}_2\text{Se}_3$  (111) topological state: Electron-phonon and electron-defect scattering,” *Physical Review B*, vol. 83, no. 24, p. 241303, 2011.
- [149] L. A. Walsh, C. M. Smyth, A. T. Barton, Q. Wang, Z. Che, R. Yue, J. Kim, M. J. Kim, R. M. Wallace, and C. L. Hinkle, “Interface chemistry of contact metals and ferromagnets on the topological insulator  $\text{Bi}_2\text{Se}_3$ ,” *The Journal of Physical Chemistry C*, vol. 121, no. 42, pp. 23551–23563, 2017.

- [150] C. D. Spataru and F. Léonard, “Fermi-level pinning, charge transfer, and relaxation of spin-momentum locking at metal contacts to topological insulators,” *Physical Review B*, vol. 90, no. 8, p. 085115, 2014.
- [151] H. Zhang, X. Zhang, C. Liu, S.-T. Lee, and J. Jie, “High-responsivity, high-detectivity, ultrafast topological insulator  $\text{Bi}_2\text{Se}_3$ /silicon heterostructure broadband photodetectors,” *ACS nano*, vol. 10, no. 5, pp. 5113–5122, 2016.
- [152] Y.-C. Yeh, P.-H. Ho, C.-Y. Wen, G.-J. Shu, R. Sankar, F.-C. Chou, and C.-W. Chen, “Growth of the  $\text{Bi}_2\text{Se}_3$  surface oxide for metal–semiconductor–metal device applications,” *The Journal of Physical Chemistry C*, vol. 120, no. 6, pp. 3314–3318, 2016.
- [153] V. Litvinov, *Magnetism in Topological Insulators*. Springer, 2020.
- [154] K. Hofer, C. Becker, D. Rata, J. Swanson, P. Thalmeier, and L. H. Tjeng, “Intrinsic conduction through topological surface states of insulating  $\text{Bi}_2\text{Te}_3$  epitaxial thin films,” *Proceedings of the National Academy of Sciences*, vol. 111, no. 42, pp. 14979–14984, 2014.
- [155] C. Mann, D. West, I. Miotkowski, Y. P. Chen, S. Zhang, and C.-K. Shih, “Mapping the 3D surface potential in  $\text{Bi}_2\text{Se}_3$ ,” *Nature communications*, vol. 4, no. 1, pp. 1–6, 2013.
- [156] J. Humlíček, D. Hemzal, A. Dubroka, O. Caha, H. Steiner, G. Bauer, and G. Springholz, “Raman and interband optical spectra of epitaxial layers of the topological insulators  $\text{Bi}_2\text{Te}_3$  and  $\text{Bi}_2\text{Se}_3$  on  $\text{BaF}_2$  substrates,” *Physica Scripta*, vol. 2014, no. T162, p. 014007, 2014.
- [157] Y. Sharma, P. Srivastava, A. Dashora, L. Vadkhiya, M. Bhayani, R. Jain, A. Jani, and B. Ahuja, “Electronic structure, optical properties and Compton profiles of  $\text{Bi}_2\text{S}_3$  and  $\text{Bi}_2\text{Se}_3$ ,” *Solid State Sciences*, vol. 14, no. 2, pp. 241–249, 2012.
- [158] S. Mishra, S. Satpathy, and O. Jepsen, “Electronic structure and thermoelectric properties of bismuth telluride and bismuth selenide,” *Journal of Physics: Condensed Matter*, vol. 9, no. 2, p. 461, 1997.
- [159] M. Eddrief, F. Vidal, and B. Gallas, “Optical properties of  $\text{Bi}_2\text{Se}_3$ : from bulk to ultrathin films,” *Journal of Physics D: Applied Physics*, vol. 49, no. 50, p. 505304, 2016.
- [160] W. Dang, H. Peng, H. Li, P. Wang, and Z. Liu, “Epitaxial heterostructures of ultrathin topological insulator nanoplate and graphene,” *Nano letters*, vol. 10, no. 8, pp. 2870–2876, 2010.
- [161] P. Rakyta, B. Ujfalussy, and L. Szunyogh, “Band bending at the surface of  $\text{Bi}_2\text{Se}_3$  studied from first principles,” *New Journal of Physics*, vol. 17, no. 12, p. 123011, 2015.

## BIBLIOGRAPHY

- [162] J. Honolka, A. Khajetoorians, V. Sessi, T. Wehling, S. Stepanow, J.-L. Mi, B. Iversen, T. Schlenk, J. Wiebe, N. Brookes, *et al.*, “In-plane magnetic anisotropy of Fe atoms on Bi<sub>2</sub>Se<sub>3</sub> (111),” *Physical review letters*, vol. 108, no. 25, p. 256811, 2012.
- [163] S. Xu, Y. Han, X. Chen, Z. Wu, L. Wang, T. Han, W. Ye, H. Lu, G. Long, Y. Wu, *et al.*, “Van der Waals epitaxial growth of atomically thin Bi<sub>2</sub>Se<sub>3</sub> and thickness-dependent topological phase transition,” *Nano letters*, vol. 15, no. 4, pp. 2645–2651, 2015.
- [164] H. Liu and P. D. Ye, “Atomic-layer-deposited Al<sub>2</sub>O<sub>3</sub> on Bi<sub>2</sub>Te<sub>3</sub> for topological insulator field-effect transistors,” *Applied Physics Letters*, vol. 99, no. 5, p. 052108, 2011.
- [165] M. Lang, L. He, F. Xiu, X. Yu, J. Tang, Y. Wang, X. Kou, W. Jiang, A. V. Fedorov, and K. L. Wang, “Revelation of topological surface states in Bi<sub>2</sub>Se<sub>3</sub> thin films by in situ Al passivation,” *ACS nano*, vol. 6, no. 1, pp. 295–302, 2012.
- [166] S. Cho, N. P. Butch, J. Paglione, and M. S. Fuhrer, “Insulating behavior in ultrathin bismuth selenide field effect transistors,” *Nano letters*, vol. 11, no. 5, pp. 1925–1927, 2011.
- [167] H. B. Michaelson, “The work function of the elements and its periodicity,” *Journal of applied physics*, vol. 48, no. 11, pp. 4729–4733, 1977.
- [168] M. Salehi, M. Brahlek, N. Koirala, J. Moon, L. Wu, N. Armitage, and S. Oh, “Stability of low-carrier-density topological-insulator Bi<sub>2</sub>Se<sub>3</sub> thin films and effect of capping layers,” *APL Materials*, vol. 3, no. 9, p. 091101, 2015.
- [169] K. Hofer, C. Becker, S. Wirth, and L. Hao Tjeng, “Protective capping of topological surface states of intrinsically insulating bi<sub>2</sub>te<sub>3</sub>,” *AIP Advances*, vol. 5, no. 9, p. 097139, 2015.
- [170] L. Goncalves, C. Couto, P. Alpuim, A. G. Rolo, F. Völklein, and J. Correia, “Optimization of thermoelectric properties on Bi<sub>2</sub>Te<sub>3</sub> thin films deposited by thermal co-evaporation,” *Thin Solid Films*, vol. 518, no. 10, pp. 2816–2821, 2010.
- [171] D. Teweldebrhan, V. Goyal, and A. A. Balandin, “Exfoliation and characterization of bismuth telluride atomic quintuples and quasi-two-dimensional crystals,” *Nano letters*, vol. 10, no. 4, pp. 1209–1218, 2010.
- [172] Y. Yan, X. Zhou, H. Jin, C.-Z. Li, X. Ke, G. Van Tendeloo, K. Liu, D. Yu, M. Dressel, and Z.-M. Liao, “Surface-facet-dependent phonon deformation potential in individual strained topological insulator Bi<sub>2</sub>Se<sub>3</sub> nanoribbons,” *Acs Nano*, vol. 9, no. 10, pp. 10244–10251, 2015.



# Abbreviations

2DEG	Two-dimensional electron gas
AD	Anharmonic decay
AFM	Atomic force microscopy
ARPES	Angle-resolved photoelectron spectroscopy
BP	Bandpass filter
BCB	Bulk conduction band
BS	Beam splitter
BVB	Bulk valence band
CCD	Charged-coupled device
CW	Continuous wave
DP	Dirac point
EDX	Energy dispersive X-ray spectroscopy
EO	Entrance optics
FO	Focusing objective
FWHM	Full width at half maximum
HRTEM	High-resolution transmission electron microscopy
IR	Infrared
MBE	Molecular beam epitaxy
NA	Numerical aperture
NF	Nanoflakes
OAP	Off-axis parabolic
OC	Optical contrast
OD	Optical density
PM	Prism monochromator
QAHE	Quantum anomalous Hall effect
QHE	Quantum Hall effect
QHS	Quantum Hall state
QL	Quintuple layer
SAED	Selected area electron diffraction
SEM	Scanning electron microscopy
SOC	spin-orbit coupling
SSB	Surface state band
STS	Scanning tunneling spectroscopy
TEM	Transmission electron microscopy
TI	Topological insulator
TKNN	Thouless, Kohmoto, Nightingale, and den Nijs
TRS	Time-reversal symmetry
TSS	Topological surface state
UT	Ultimate triple
WAL	Weak anti-localization
WP	Wave plate
XPS	X-ray photoelectron spectroscopy



# List of Figures

1.1	Topological phases in condensed matter systems. . . . .	2
1.2	Surface electronic band structure of $\text{Bi}_2\text{Se}_3$ and $\text{Bi}_2\text{Te}_3$ . . . . .	5
2.1	Morphology and thickness characterization by AFM of the $\text{Bi}_2\text{X}_3$ nanoflakes. . . . .	12
2.2	TEM and SAED characterization of investigated nanoflakes confirming rhombohedral crystal structure. . . . .	13
3.1	General Raman spectra for phononic Raman scattering. . . . .	16
3.2	Feynman diagrams representing the phononic Raman scattering process. . . . .	21
3.3	Typical Raman line shapes obtained from resonant and non-resonant electronic Raman scattering. . . . .	23
3.4	Rhombohedral crystal structure and lattice vibration modes of $\text{Bi}_2\text{Se}_3$ and $\text{Bi}_2\text{Te}_3$ . . . . .	30
3.5	Phonon dispersion relations of $\text{Bi}_2\text{Se}_3$ and $\text{Bi}_2\text{Te}_3$ in $\Gamma\text{Z}$ direction. . . . .	31
3.6	Schematic illustration of the macro-Raman setup for temperature and magnetic field dependent measurements. . . . .	34
3.7	Sample preparation and configurations for temperature and magnetic field dependent Raman measurements. . . . .	35
3.8	Schematic illustration of the micro-Raman setup for single nanoflake measurements. . . . .	37
3.9	Laser spot diameter characterization for micro-Raman measurements. . . . .	39
3.10	UT-3 spectrometer sensitivity for horizontally and vertically polarized light. . . . .	40
3.11	Schematic illustration of the 'ultimate triple' UT-3 spectrometer. . . . .	41
4.1	Preparation of thin film samples for macro-Raman measurements as a function of temperature and magnetic field strength. . . . .	45
4.2	Laser power and integration time dependence. . . . .	47
4.3	Temperature dependent Raman spectra of $\text{Bi}_2\text{Se}_3$ and $\text{Bi}_2\text{Te}_3$ thin film samples. . . . .	48
4.4	Polarization dependence of modes detected in measurements of nanoflake samples in thin film geometry. . . . .	49
4.5	Detection of infrared active modes in Raman measurements at low temperatures. . . . .	50
4.6	Temperature dependent self-energy effects in $\text{Bi}_2\text{Se}_3$ and $\text{Bi}_2\text{Te}_3$ . . . . .	52

## LIST OF FIGURES

4.7	Phonon renormalization in $\text{Bi}_2\text{Se}_3$ due to enhanced electron-phonon coupling at low temperatures. . . . .	56
4.8	Magnetic field strength dependent Raman spectra of $\text{Bi}_2\text{Se}_3$ and $\text{Bi}_2\text{Te}_3$ thin film samples. . . . .	58
4.9	Magnetic field strength dependent self-energy effects in $\text{Bi}_2\text{Se}_3$ and $\text{Bi}_2\text{Te}_3$	59
4.10	Phonon renormalization in $\text{Bi}_2\text{Se}_3$ for magnetic fields above 3 T related to a gap opening in the Dirac cone. . . . .	60
5.1	Preparation of single $\text{Bi}_2\text{Se}_3$ and $\text{Bi}_2\text{Te}_3$ nanoflake samples on Au and Si substrates for micro-Raman measurements. . . . .	75
5.2	Resonance Raman correction factors. . . . .	79
5.3	Resonance Raman profile of single $\text{Bi}_2\text{Se}_3$ nanoflakes on Si and Au substrates.	80
5.4	Phonon renormalization of $\text{Bi}_2\text{Se}_3$ nanoflakes on Au substrate with decreasing nanoflake thickness. . . . .	83
5.5	Phonon renormalization of $\text{Bi}_2\text{Te}_3$ nanoflakes on gold substrate with decreasing nanoflake thickness. . . . .	84
5.6	Inversion symmetry breaking in thin 2D nanoflakes on Au substrates. . . .	85
5.7	Schematic band bending model due to carrier injection from the gold substrate into the nanoflake surface in contact. . . . .	88
5.8	Electronic background and changes in the electron-phonon coupling strength for nanoflakes on gold substrate. . . . .	90
C.1	Thermal expansion coefficients obtained from high temperature frequency renormalization in $\text{Bi}_2\text{Se}_3$ and $\text{Bi}_2\text{Te}_3$ . . . . .	133
C.2	Anharmonic decay fits of $\text{Bi}_2\text{Se}_3$ phonon frequency and line width between 120 K to 300 K. . . . .	135
C.3	Blade setup for the fabrication of gold finder grid substrates. . . . .	137
C.4	Correlation between nanoflake thickness and optical contrast to gold and AFM measurements of all investigated single nanoflakes. . . . .	139
C.5	Infrared-active modes detected in Raman spectra of thin nanoflakes on gold substrate. . . . .	141
C.6	Polarization dependence of IR-active modes detected in Raman spectra of thin nanoflakes on gold substrate. . . . .	142

# List of Tables

3.1	Average Raman mode frequencies in $\text{cm}^{-1}$ at room temperature for bulk samples reported in literature. . . . .	32
3.2	Raman selection rules for the different point groups applicable in the bulk and at the surface for the bismuth chalcogenides. <sup>[85,113]</sup> . . . . .	32
3.3	Laser sources employed for resonance micro-Raman measurements. . . . .	38
3.4	UT-3 spectrometer sensitivity. . . . .	40
4.1	Thermal expansion coefficients $\chi^{\text{th}}$ of $\text{Bi}_2\text{Se}_3$ and $\text{Bi}_2\text{Te}_3$ samples with various geometries. The temperature range for the linear fits is given in brackets. . . . .	53
5.1	Surface laser power densities $PD$ in $\text{kW}/\text{cm}^2$ and integration times $t_{\text{int}}$ in min for single NF measurements. . . . .	76
5.2	Optical properties and parameters critical for the calculation of resonance Raman correction factors. . . . .	78
A.1	Experimentally determined phonon mode frequencies of $\text{Bi}_2\text{Te}_3$ bulk, film, and 2D nanostructured samples. All frequencies are given in units of $\text{cm}^{-1}$ and the precisions are reported as given in the corresponding references. . .	129
A.2	Experimentally determined phonon mode frequencies of $\text{Bi}_2\text{Se}_3$ bulk, film, and 2D nanostructured samples. All frequencies are given in units of $\text{cm}^{-1}$ and the precisions are reported as given in the corresponding references. . .	130
B.1	Quantities of chemicals used in the synthesis for $\text{Bi}_2\text{Se}_3$ and $\text{Bi}_2\text{Te}_3$ nanoflakes.	131
C.1	Fit-parameters for the symmetric anharmonic decay model according to Equation (3.34) with $\chi^{\text{th}}(\text{T})$ set to zero and Equation (3.35). $\text{Bi}_2\text{Se}_3$ was fit in the temperature range between 3–21 K and 140–300 K. The $\text{Bi}_2\text{Te}_3$ data was fit in the whole temperature range. . . . .	134
C.2	Fit-Parameters for the symmetric anharmonic decay model according to Equation (3.34) with $\chi^{\text{th}}(\text{T})$ set to zero and Equation (3.35). $\text{Bi}_2\text{Se}_3$ was fit in the elevated temperature range between 120 K to 300 K. . . . .	136
C.3	Measured optical contrasts and NF thicknesses for NFs measured in the thickness dependent Raman study. . . . .	140



# APPENDIX

*LIST OF TABLES*

# A Reference Raman literature on $\text{Bi}_2\text{Se}_3$ and $\text{Bi}_2\text{Te}_3$

**Table A.1:** Experimentally determined phonon mode frequencies of  $\text{Bi}_2\text{Te}_3$  bulk, film, and 2D nanostructured samples. All frequencies are given in units of  $\text{cm}^{-1}$  and the precisions are reported as given in the corresponding references.

Ref.	sample	T (K)	Raman active				IR active			
			$E_g^1$	$A_{1g}^1$	$E_g^2$	$A_{1g}^2$	$E_u^1$	$A_{1u}^1$	$E_u^2$	$A_{1u}^2$
[22]	bulk	300	36.5	62.5	103	134.0	50	94	95	120
[107]	bulk	300	34.0	60.4	100.7	133.4	55.4	101.7	-	-
[110]	bulk	300	-	61.5	101.5	133.5	-	-	-	-
[114]	bulk	10	-	64	106	139	-	-	-	114
[116]	film 40 $\mu\text{m}$	300	37	62	102	135	54	-	95	111
[170]	film 1 $\mu\text{m}$	300	-	62.3	103.7	134.2	-	-	-	-
[131]	film 4 $\mu\text{m}$	300	-	60	99.4	135	-	-	-	-
[117]	ribbon 40 nm	300	38.9	61.3	101.3	133.0	-	-	-	116.2
[118]	ribbon 50 nm	300	39	61.1	101.5	132.4	-	-	-	116
[171]	ribbon few nm	300	-	62	104	137	-	-	-	120
[119]	NF 11 nm	300	39	60.5	102	130	-	93	-	113
[120]	NFs	300	-	61	102	134	-	-	-	119
[73]	NFs 10 nm	300	-	61.1	100.8	139.7	-	-	-	119
[121]	NFs 6- 25 nm	300	-	62	102	137	-	92	-	115
[78]	NFs	300	-	61.7	101.9	133.9	-	-	-	-

**Table A.2:** Experimentally determined phonon mode frequencies of  $\text{Bi}_2\text{Se}_3$  bulk, film, and 2D nanostructured samples. All frequencies are given in units of  $\text{cm}^{-1}$  and the precisions are reported as given in the corresponding references.

Ref.	sample	T (K)	Raman active				IR active			
			$E_g^1$	$A_{1g}^1$	$E_g^2$	$A_{1g}^2$	$E_u^1$	$A_{1u}^1$	$E_u^2$	$A_{1u}^2$
[22]	bulk	300	-	72.0	131.5	174.5	65	-	129	-
[112]	bulk	300	-	72.3	131.5	174.1	-	-	-	-
[25]	bulk	300	-	-	-	-	61	-	133	-
[62]	bulk	3	38.9	73.3	132.9	175.4	68	129	125	160
[110]	bulk	300	-	72.5	131.5	176.5	-	-	-	-
[113]	bulk	13	39	75	137	180	67	136	126	158
[114]	bulk	10	38.5	75.5	135.8	178.2	-	-	-	159
[101]	bulk	300	-	-	131.5	175.5	-	-	-	-
[81]	bulk	300	37.0	72.0	131.0	175.0	-	-	-	-
[115]	film 18 nm	80	39	74	135	177	-	-	134	159
[63]	film 40 nm	300	-	73	130	173	-	-	-	-
[160]	NF 9 nm	300	-	-	131	174	-	-	-	-
[130]	NF	300	-	68	127	170	-	-	-	-
[64]	NF 20 nm	300	37	72	131	174	-	-	-	-
[118]	ribbon 15 nm	300	-	72.4	132	174.7	-	-	-	-
[121]	NF 5- 50 nm	300	-	72	130	172	110	-	-	-
[172]	ribbon > 70 nm	300	37.3	70.4	131.9	171.2	-	-	-	-
[78]	NFs	300	-	71.6	131.0	174.6	-	-	-	-



# B Appendix B

## Nanoflake synthesis parameters

For the Raman studies presented in this thesis in total three batches of nanoflake syntheses were used. For the preparation of thin film samples (macro) investigated in chapter 4 the nanoflakes were synthesized with quantities as indicated in Table B.1. For the preparation of single nanoflake samples (micro) investigated in chapter 5 the same batch of  $\text{Bi}_2\text{Te}_3$  was used but a new batches of  $\text{Bi}_2\text{Se}_3$  nanoflakes was synthesized. The synthesis of  $\text{Bi}_2\text{Se}_3$  NFs used for the micro-Raman studies was identical to the  $\text{Bi}_2\text{Se}_3$ -macro synthesis but only half the quantities were used to save resources as apparent from Table B.1.

**Table B.1:** Quantities of chemicals used in the synthesis for  $\text{Bi}_2\text{Se}_3$  and  $\text{Bi}_2\text{Te}_3$  nanoflakes.

Chemical	Properties	Company	Quantity
<b><math>\text{Bi}_2\text{Se}_3</math> - Macro</b> <sup>[78]</sup>			
Ethylene glycol ( $\text{C}_2\text{H}_4(\text{OH})_2$ )	99.8 %	Sigma Aldrich	60 mL
Bismuth nitrate pentahydrate ( $\text{Bi}(\text{NO}_3)_3 \cdot 5\text{H}_2\text{O}$ )	98 %	Sigma Aldrich	0.3 g, 0.0103 mol/L
Sodium selenite ( $\text{Na}_2\text{SeO}_3$ )	99 %	Sigma Aldrich	0.15 g, 0.0145 mol/L
Polyvinylpyrrolidone (PVP)	$M_w=55,000$	Sigma Aldrich	0.66 g
<b><math>\text{Bi}_2\text{Se}_3</math> - Micro</b> <sup>[129]</sup>			
Ethylene glycol ( $\text{C}_2\text{H}_4(\text{OH})_2$ )	99.7 %	VWR	30 mL
Bismuth nitrate pentahydrate ( $\text{Bi}(\text{NO}_3)_3 \cdot 5\text{H}_2\text{O}$ )	98 %	Sigma Aldrich	0.1397 g, 0.0096 mol/L
Sodium selenite ( $\text{Na}_2\text{SeO}_3$ )	99 %	Sigma Aldrich	0.0747 g, 0.0144 mol/L
Polyvinylpyrrolidone (PVP)	$M_w=55,000$	Sigma Aldrich	0.33 g
<b><math>\text{Bi}_2\text{Te}_3</math> -Macro &amp; Micro</b> <sup>[78,129]</sup>			
Ethylene glycol ( $\text{C}_2\text{H}_4(\text{OH})_2$ )	99 %	Carl Roth	50 mL
Bismuth nitrate pentahydrate ( $\text{Bi}(\text{NO}_3)_3 \cdot 5\text{H}_2\text{O}$ )	98 %	Sigma Aldrich	0.485 g, 0.02 mol/L
Potassium tellurite monohydrate ( $\text{K}_2\text{TeO}_3 \cdot \text{H}_2\text{O}$ )	97 %	Alfa Aesar	0.415 g, 0.03 mol/L
Polyvinylpyrrolidone (PVP)	$M_w=30,000$	Carl Roth	0.5 g
Sodium hydroxide (NaOH)	98 %	Merck	0.4 g, 0.2 mol/L



# C Appendix C

## Supplementary analysis of Raman investigations

### C.1 Temperature & Magnetic field strength dependence

#### C.1.1 Thermal coefficients of $\text{Bi}_2\text{Se}_3$ and $\text{Bi}_2\text{Te}_3$ NFs in thin film geometry

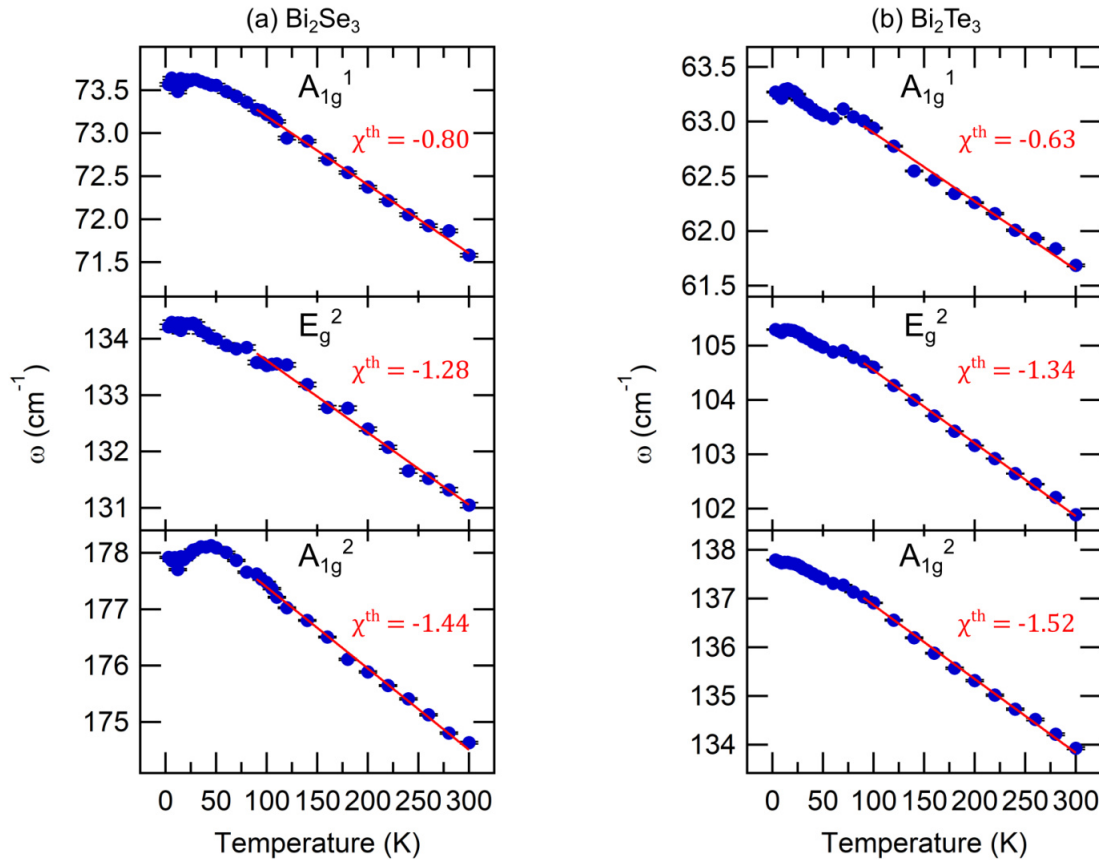


**Figure C.1:** Temperature dependent mode frequencies for (a)  $\text{Bi}_2\text{Se}_3$  and (b)  $\text{Bi}_2\text{Te}_3$  with a linear fit of the extracted frequencies between 90 K and 300 K shown as red graphs. The linear frequency dependence at elevated temperatures is readily described by the thermal expansion of the crystal. Extracted thermal expansion coefficients  $\chi^{\text{th}}$  given in units of  $10^{-2} \text{ cm}^{-1}$ .

### C.1.2 Anharmonic decay fits of Bi<sub>2</sub>Se<sub>3</sub> and Bi<sub>2</sub>Te<sub>3</sub> NFs in thin film geometry

To fit the temperature dependent frequencies and line widths presented in Figure 4.6 the model of a symmetric anharmonic decay according to Equation (3.34) and Equation (3.35) was used. The fit procedure was as follows: (i) Fit of the frequency dependence to determine  $\omega_0$ . Hereby, the first order thermal coefficient  $\chi^{\text{th}}(\text{T})$  was set to zero due to the very high dependency with the anharmonic term. (ii) Fit of the line width dependence with the previously determined  $\omega_0$  fixed.

The Bi<sub>2</sub>Te<sub>3</sub> data was readily fit in the whole temperature range. For the Bi<sub>2</sub>Se<sub>3</sub> data strong deviations in the temperature range between 21 K to 120 K were apparent that hindered a good fit by the AD model in the whole T range. For this reason different fit ranges were used to obtain the best description of the temperature dependence. The AD fits presented in Figure 4.6(a) were obtained by fitting the Bi<sub>2</sub>Se<sub>3</sub> data in the temperature range between 3–21 K and 140–300 K. The data points between 24 K to 120 K were masked for the AD fit. The corresponding fit parameters are listed in Table C.1.

**Table C.1:** Fit-parameters for the symmetric anharmonic decay model according to Equation (3.34) with  $\chi^{\text{th}}(\text{T})$  set to zero and Equation (3.35). Bi<sub>2</sub>Se<sub>3</sub> was fit in the temperature range between 3–21 K and 140–300 K. The Bi<sub>2</sub>Te<sub>3</sub> data was fit in the whole temperature range.

Mode	$\omega_0(\text{cm}^{-1})$	$\Gamma_0(\text{cm}^{-1})$	<b>A</b>	<b>A*</b>
<b>Bi<sub>2</sub>Se<sub>3</sub></b>				
A <sub>1g</sub> <sup>1</sup>	73.89 ± 0.02	1.54 ± 0.06	-0.197	0.177
E <sub>g</sub> <sup>2</sup>	134.89 ± 0.04	4.93 ± 0.17	-0.607	0.808
A <sub>1g</sub> <sup>2</sup>	178.81 ± 0.02	2.84 ± 0.08	-0.894	1.478
<b>Bi<sub>2</sub>Te<sub>3</sub></b>				
A <sub>1g</sub> <sup>1</sup>	63.41 ± 0.02	0.43 ± 0.02	-0.129	0.151
E <sub>g</sub> <sup>2</sup>	105.79 ± 0.02	0.70 ± 0.03	-0.486	0.278
A <sub>1g</sub> <sup>2</sup>	138.48 ± 0.02	0.72 ± 0.04	-0.761	1.471

#### Anharmonic decay fits of Bi<sub>2</sub>Se<sub>3</sub> between 120 K to 300 K

Another attempt in describing the temperature dependence by the AD fit was made by fitting only the data points from 120 K to 300 K as the AD model is expected to give a good description of the high temperature behaviour. The obtained fits, shown in Figure C.2, were extrapolated down to 3 K and give for both the A<sub>1g</sub><sup>1</sup> and A<sub>1g</sub><sup>2</sup> modes similar results compared to the results obtained with fits between 3–21 K and 140–300 K (Figure 4.6(a)). Again, the A<sub>1g</sub><sup>1</sup> and E<sub>g</sub><sup>2</sup> phonons deviate in line widths and the A<sub>1g</sub><sup>2</sup> phonon in both frequency in line widths at temperatures below 120 K. The only difference in the fit results is apparent for the frequency of the E<sub>g</sub><sup>2</sup> mode: The AD fit shows generally higher frequencies for T < 120 K than the actual data points. This is in contrast to the fit results shown in Figure 4.6 where the E<sub>g</sub><sup>2</sup> frequencies are well modeled by the AD fit.

According to our model of the phonon renormalization by el-ph coupling, Equation (3.19), the here observed broader line widths and lower frequencies for the  $E_g^2$  phonon would be the result of coupling to an electric susceptibility with an energy higher than the energy of the phonon mode ( $\omega_{el} > 16$  meV). Therefore, the main results of an electric susceptibility in the energy range between 16 meV to 22 meV still holds. In the main result section the AD fits for the temperature range of 3–21 K and 140–300 K were chosen due to the lower error bars, compare Table C.1 and Table C.2.

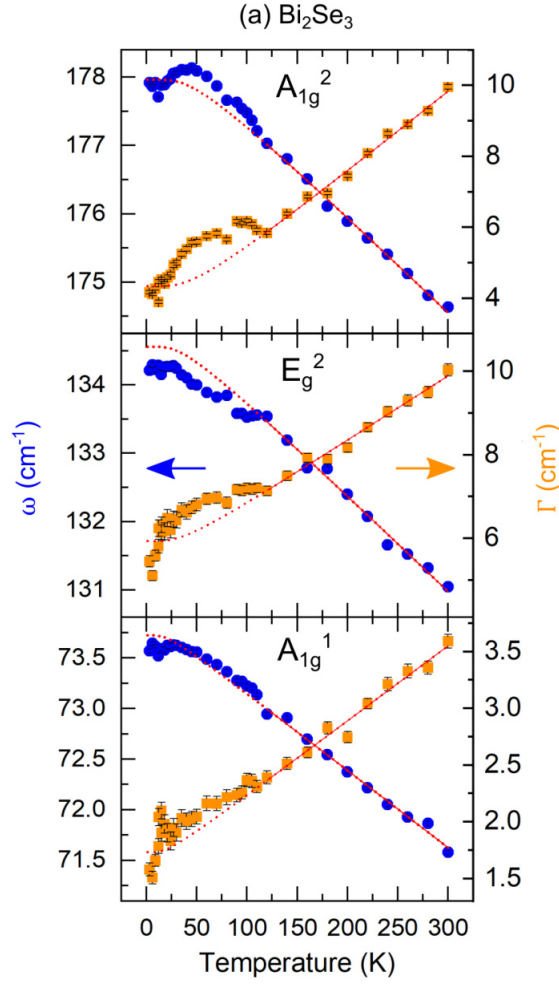


**Figure C.2:** Anharmonic decay (AD) fits at elevated temperatures between 120 K to 300 K of  $\text{Bi}_2\text{Se}_3$ . The AD fits, given as red solid lines, were extrapolated down to 3 K, which is displayed by the red dotted graphs.

**Table C.2:** Fit-Parameters for the symmetric anharmonic decay model according to Equation (3.34) with  $\chi^{\text{th}}(\text{T})$  set to zero and Equation (3.35).  $\text{Bi}_2\text{Se}_3$  was fit in the elevated temperature range between 120 K to 300 K.

Mode	$\omega_0(\text{cm}^{-1})$	$\Gamma_0(\text{cm}^{-1})$	<b>A</b>	<b>A*</b>
<b><math>\text{Bi}_2\text{Se}_3</math></b>				
$\text{A}_{1g}^1$	$73.93 \pm 0.06$	$1.55 \pm 0.09$	-0.203	0.176
$\text{E}_g^2$	$135.24 \pm 0.13$	$5.17 \pm 0.16$	-0.686	0.758
$\text{A}_{1g}^2$	$178.88 \pm 0.07$	$2.87 \pm 0.17$	-0.914	1.470

## C.2 Single nanoflake measurements

### C.2.1 Blade setup for the fabrication of the Au finder grids

The setup shown in Figure C.3 was built up of two translation stages (Thorlabs, PT1/M-25.0 mm) that were fixed perpendicular to each other. The gold coated wafer was fixed onto the stage and brought into contact with a scalpel blade whose height was adjusted by a coarse translation stage. In contact, the wafer was moved along under the blade by operating the  $y$ -stage, which created a vertical groove in the Au layer. For adjacent grooves the wafer was moved horizontally in steps of  $500 \mu\text{m}$  by operating the  $x$ -stage to obtain evenly spaced lines as shown in Figure C.3(b). To create the grid the wafer was turned by  $90^\circ$  and another set of grooves was fashioned.

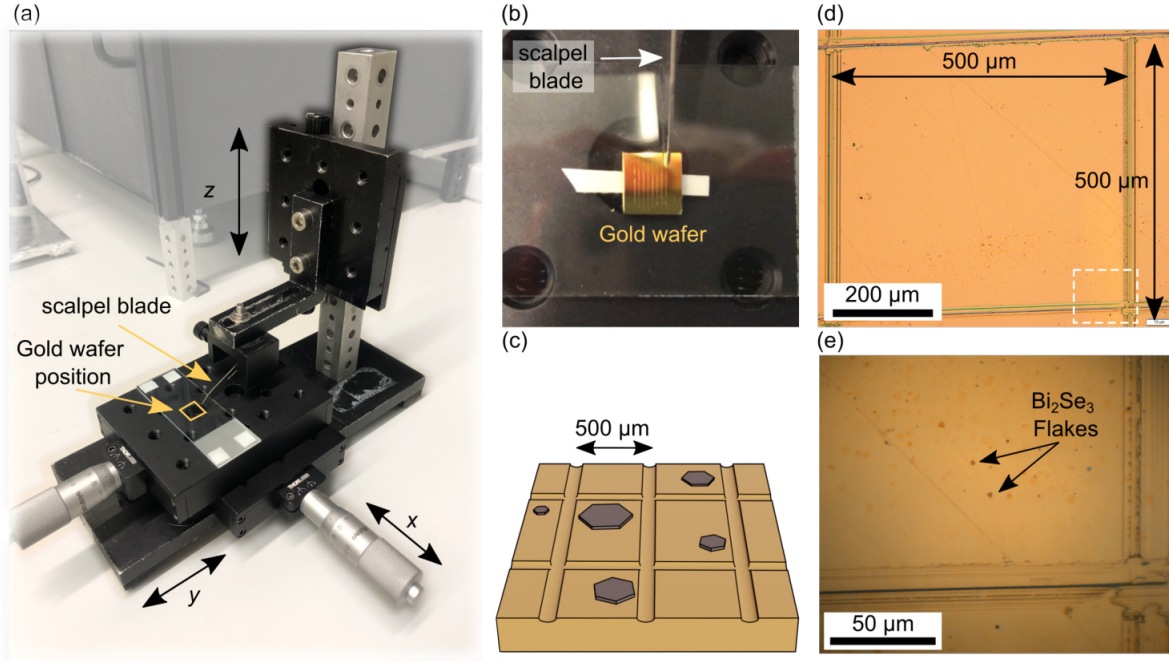


**Figure C.3:** (a) Photograph of the setup used to scratch regular grooves into the sputtered Au substrate. Grooves were created by lowering a scalpel blade onto the wafer via a  $z$ -stage and scratching vertical lines by moving the fixed sample via a  $y$ -stage. (b) Top view of the fixed Au substrate and scalpel blade with vertical grooves visible. (c) Schematic illustration of the created grooves with pitch  $500\ \mu\text{m}$ . (d) Microscope image of the Au substrate with a low resolution to see one pitch. The white dotted rectangle marks the magnified area shown in (e) with visible single  $\text{Bi}_2\text{Se}_3$  nanoflakes.

### C.2.2 Correlation of NF thickness to optical contrast on gold

The thickness  $d$  of the  $\text{Bi}_2\text{Se}_3$  and  $\text{Bi}_2\text{Te}_3$  NFs on gold can be directly correlated to their optical contrast  $OC$  to the underlying gold substrate. For quantification of the  $OC$  microscopy images of all NFs were obtained with identical acquisition software settings. The  $OC$  was calculated by determining the ratio of the average grayscale value of the NFs'  $GV^{\text{Flake}}$  to the surrounding gold substrate  $GV^{\text{Au}}$ :

$$OC = \frac{GV^{\text{Au}} - GV^{\text{Flake}}}{GV^{\text{Au}}} \quad (\text{C.1})$$

To ensure comparability, the area to determine the average gray value of each NF was  $20 \times 20$  pixel for  $\text{Bi}_2\text{Se}_3$  ( $10 \times 10$  pixel for  $\text{Bi}_2\text{Te}_3$ ) and the area on the gold substrate was  $100 \times 100$  pixel as illustrated in Figure C.4(b).

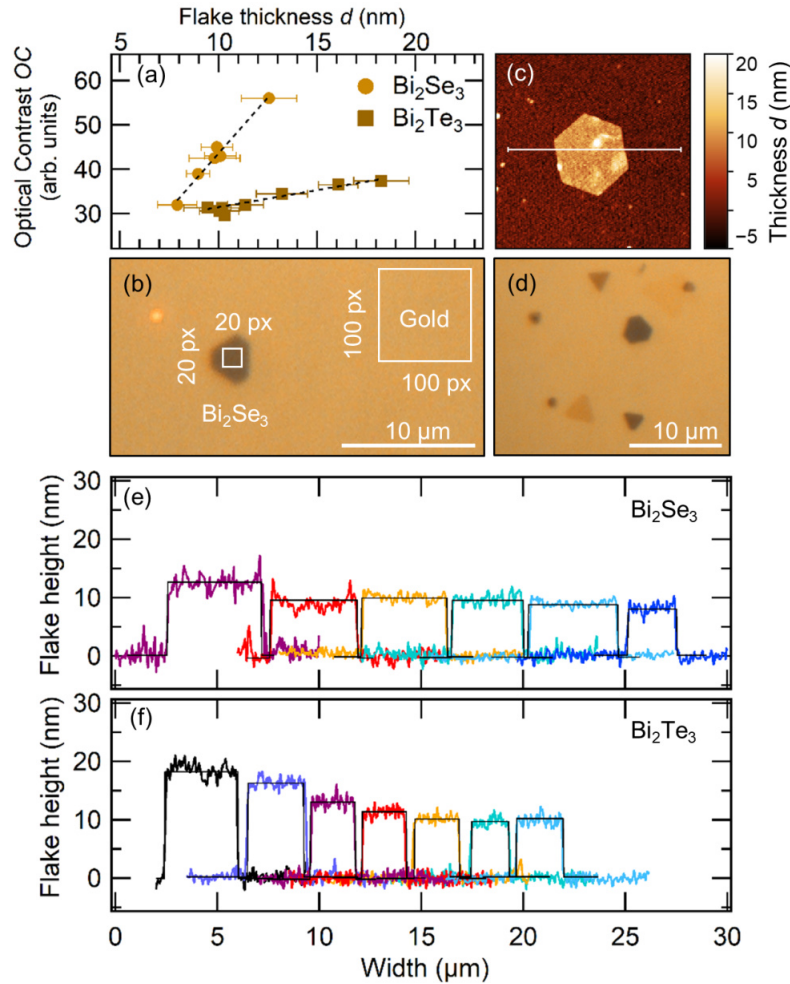
The strong difference in optical contrast for NFs differing in only a few numbers of quintuple layers (8 nm to 13 nm) makes the  $OC$  a reliable tool to estimate the NF thicknesses. Different color regimes can be assigned according to the NF heights with very bright, yellowish NFs ( $< 9$  nm), brown-orange NFs (9–12 nm) and dark brown to almost black appearing NFs ( $> 12$  nm). A representative area of the gold sample with  $\text{Bi}_2\text{Se}_3$  NFs of varying  $OC$  is shown in Figure C.4(d) to give an impression of the strongly varying contrast for NFs on gold differing by only a few nm in thickness. The  $OC$  was assigned to

certain NF thicknesses by evaluating Atomic Force Microscopy (AFM) measurements of the NFs. AFM measurements were taken on a commercial AFM setup (Q-Scope TM250 Nomad, Ambios Technology Corporation, California) with a  $40 \times 40 \mu\text{m}$  scan head in tapping mode. For each  $\text{Bi}_2\text{Se}_3$  ( $\text{Bi}_2\text{Te}_3$ ) NF an area of  $12 \mu\text{m}^2$  ( $10 \mu\text{m}^2$ ) was scanned with a scanning resolution of 300 rows, leading to a lateral resolution of  $0.04 \mu\text{m}$  ( $0.033 \mu\text{m}$ ). A topography measurement of a representative  $\text{Bi}_2\text{Te}_3$  NF is shown in Figure C.4(c). Horizontal line profiles (parallel to the AFM scanning direction) of the NFs were fit by a step height function to determine the thickness of the NFs. Profiles of all NFs investigated by Raman spectroscopy are shown in Figure C.4(e,f). The colors of the profiles correspond to the Raman spectrum of each NF shown in the main text in Figure 5.4 and Figure 5.5. The correlation between the  $OC$  and NF thickness is readily fit by a linear function in the investigated thickness regime between 8 nm and 20 nm, as shown in Figure C.4(a). A six times stronger dependency of the  $OC$  on the NF thickness for  $\text{Bi}_2\text{Se}_3$  than for  $\text{Bi}_2\text{Te}_3$  is found:

$$\begin{aligned} OC^{\text{Bi}_2\text{Se}_3} &\propto -6.822 + (5.04 \pm 0.357) \cdot d^{\text{Bi}_2\text{Se}_3} \\ OC^{\text{Bi}_2\text{Te}_3} &\propto 23.842 + (0.76 \pm 0.068) \cdot d^{\text{Bi}_2\text{Te}_3} \end{aligned}$$

Since the uncertainty in  $d$  determined from AFM measurements is about  $\pm 1 \text{ nm}$  the  $OC$  gives a precise value for the NF thickness and a direct control in the micro-Raman measurements. This is important as the NFs show a strong change in Raman response for thicknesses between only 8 nm and 13 nm. Hence, the linear dependence of  $OC$  with  $d$  allows its correlation to a certain NF height. The correlated NF thicknesses  $d^{\text{corr}}$  according to the relations given in the previous equations (see Table S5) were used to plot the Raman spectra fit parameters as a function of NF thickness in Figure 5.4(b-d), Figure 5.5(b-d) and Figure 5.7(c,d) in the main text. From Table S5 it is apparent that the correlated thicknesses  $d^{\text{corr}}$  vary by  $< 5 \%$  from the actually measured thicknesses  $d^{\text{AFM}}$ .

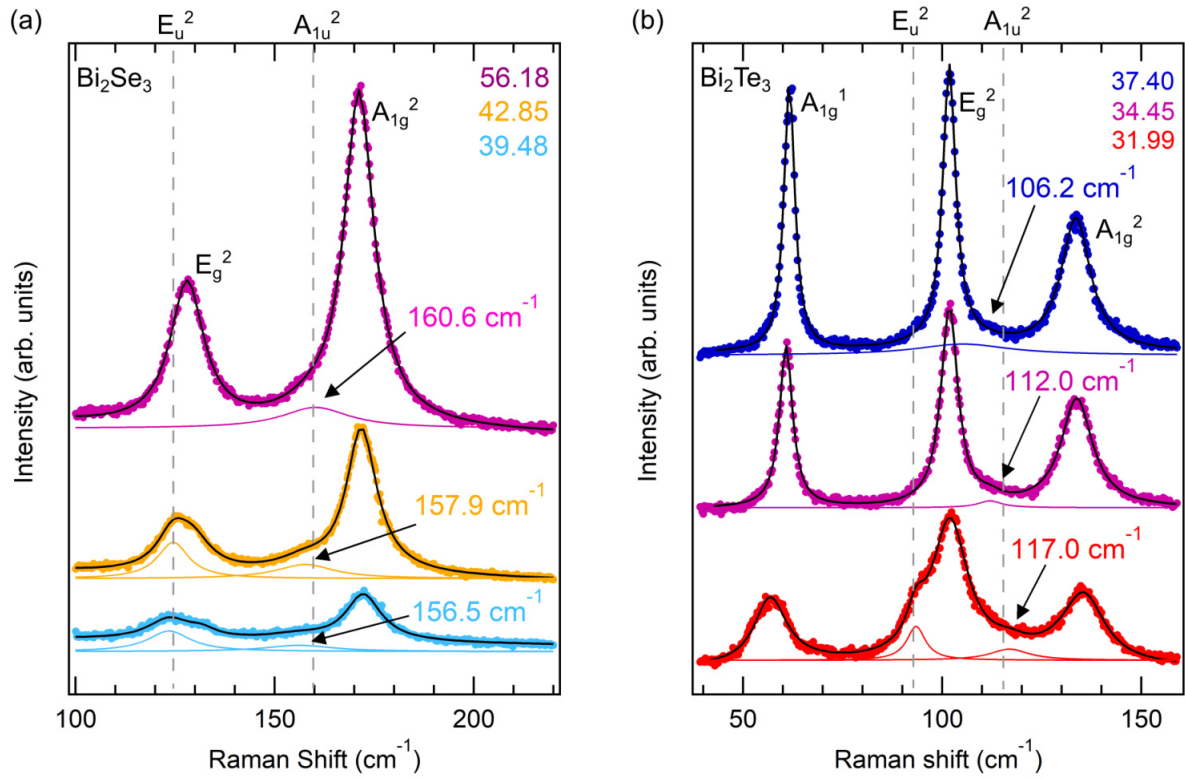




**Figure C.4:** Correlation between NF thickness and optical contrast to gold. (a)  $\text{Bi}_2\text{Se}_3$  and  $\text{Bi}_2\text{Te}_3$  optical contrasts as a function of NF thickness determined from AFM measurements with a linear correlation fit (dashed lines). (b) Microscope image of  $\text{Bi}_2\text{Se}_3$  NFs on gold substrate with indicated area sizes for gray value measurements. (c) AFM topography image of a  $\text{Bi}_2\text{Te}_3$  NF on gold with indicated horizontal cut (white line) corresponding to the red height profile shown in (f). (d) Microscope image of a representative area on the  $\text{Bi}_2\text{Se}_3$ -Au sample. (e,f) Height (thickness) profiles of the selected NFs measured by Raman spectroscopy. All profiles are calculated by an average of 5 rows from the evaluated AFM micrographs. The colors of the profiles are in agreement with the corresponding Raman spectra of the measured NFs given in the main text in Figure 5.4 and Figure 5.5.

**Table C.3:** Measured optical contrasts and NF thicknesses for NFs measured in the thickness dependent Raman study.

OC	$d^{\text{AFM}}$ from height profiles (nm)	$d^{\text{corr}}$ correlated to OC (nm)
<b>Bi<sub>2</sub>Se<sub>3</sub></b>		
56.18	$12.56 \pm 1.4$	$12.47 \pm 0.9$
44.83	$9.92 \pm 0.8$	$10.23 \pm 0.7$
42.85	$10.10 \pm 0.8$	$9.89 \pm 0.7$
42.38	$9.80 \pm 1.3$	$9.79 \pm 0.7$
39.48	$8.97 \pm 0.6$	$9.10 \pm 0.6$
31.51	$7.90 \pm 1.0$	$7.71 \pm 0.5$
<b>Bi<sub>2</sub>Te<sub>3</sub></b>		
37.40	$18.26 \pm 1.4$	$17.74 \pm 1.5$
36.56	$16.07 \pm 1.0$	$16.69 \pm 1.5$
34.45	$13.22 \pm 1.3$	$13.88 \pm 1.2$
31.99	$11.37 \pm 0.9$	$10.66 \pm 0.9$
31.30	$10.18 \pm 0.9$	$9.76 \pm 0.9$
31.38	$9.44 \pm 1.2$	$9.86 \pm 0.9$
30.62	$10.04 \pm 1.0$	$8.87 \pm 0.8$

C.2.3 Symmetry properties of  $\text{Bi}_2\text{Se}_3$  and  $\text{Bi}_2\text{Te}_3$  modes

**Figure C.5:** Raman spectra of selected (a)  $\text{Bi}_2\text{Se}_3$  and (b)  $\text{Bi}_2\text{Te}_3$  nanoflakes with varying thicknesses or equivalently optical contrast. The OC values are given in the right hand corners. Black graphs correspond to Lorentzian fits for all phonon modes and colored graphs show the deconvoluted fit profiles for the corresponding bulk IR modes. The peak position of the IR modes is indicated by gray vertical lines and the values for the  $A_{1u}^2$  IR modes are shown. When the  $E_u^2$  profile is not displayed it was not included in the fit.

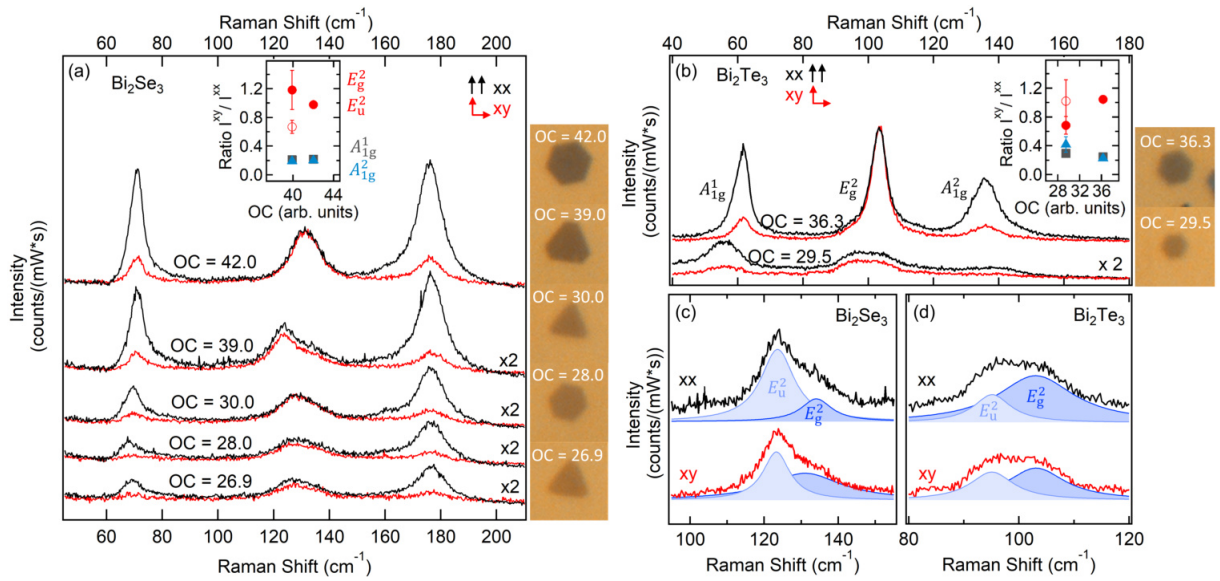


**Figure C.6:** Polarization dependence of phonon modes in (a)  $\text{Bi}_2\text{Se}_3$  and (b)  $\text{Bi}_2\text{Te}_3$  single NFs with varying optical contrasts given next to the spectra. Spectra were recorded in xx, and xy-configuration corresponding to the black and red graphs, respectively. Spectra were corrected for the spectrometer sensitivity of the respective incoming photon polarization. Insets show the intensity ratio of the four phonon modes extracted from Lorentzian fits in both polarization configurations. For  $\text{Bi}_2\text{Se}_3$  the results of the two thicker NFs with OCs of 39 and 42 are shown. (c,d) Deconvolution of the phonon mode contributions to the modes around  $125\text{ cm}^{-1}$  and  $100\text{ cm}^{-1}$  for  $\text{Bi}_2\text{Se}_3$  and  $\text{Bi}_2\text{Te}_3$ , respectively. Reprinted with permission from<sup>[129]</sup>. Copyright 2022 American Chemical Society.

# List of publications

- I **Temperature and magnetic field dependent Raman study of electron-phonon interactions in thin films of Bi<sub>2</sub>Se<sub>3</sub> and Bi<sub>2</sub>Te<sub>3</sub> nanoflakes**  
S. Buchenau, S. Scheitz, A. Sethi, J. E. Slimak, T. E. Glier, P. K. Das, T. Dankwort, L. Akinsinde, L. Kienle, A. Rusydi, C. Ulrich, S. L. Cooper, M. Rübhausen. *Phys. Rev. B* **101**, 245431 (2020).
  
- II **Carrier injection observed by interface-enhanced Raman scattering from topological insulators on gold substrates**  
S. Scheitz, T. E. Glier, C. Nweze, M. van Heek, I. Moch, R. Zierold, R. Blick, N. Huse, M. Rübhausen. *ACS Appl. Mater. Interfaces* **14**, 32625–32633. (2022).
  
- III **Conductance-strain behavior in silver-nanowire composites: network properties of a tunable strain sensor**  
T. E. Glier, M. Betker, B. Grimm-Lebsanft, S. Scheitz, T. Matsuyama, L. O. Akinsinde, M. Rübhausen. *Nanotechnology* **32**, 365701, (2021).
  
- IV **Surface characterization and resistance changes of silver-nanowire networks upon atmospheric plasma treatment**  
L. O. Akinsinde, T. E. Glier, M. Schwartzkopf, M. Betker, M. Nissen, M. Witte, S. Scheitz, C. Nweze, B. Grimm-Lebsanft, M. Gensch, A. Chumakov, I. Baev, U. Schürmann, T. Dankwort, F. Fischer, M. Martins, S. V. Roth, L. Kienle, M. Rübhausen. *Applied Surface Science* **550**, 1493262, (2021).
  
- V **Resistivity response to stress and strain of a flexible Bi<sub>2</sub>Te<sub>3</sub> based thermoelectric material**  
L. O. Akinsinde, S. Scheitz, L. Zimoch, J. K. Sierck, L. Siebert, R. Adelung, U. Schürmann, M. Rübhausen, T. Dankwort, L. Kienle. In: *4th International Conference on Nanotechnologies and Biomedical Engineering. ICNBME 2019. IFMBE Proceedings vol 77.*, Springer, Cham, 57-60, (2020).

*List of publications*

# Further publications

## Paper III








### Conductance-strain behaviour in silver-nanowire composites: network properties of a tunable strain sensor

Tomke E. Glier\*, Marie Betker\*, Benjamin Grimm-Lebsanft, **Sarah Scheitz**, Toro  
Matsuyama, Lewis Olaniyi Akinsinde, and Michael Rübhausen\*

Published in: Nanotechnology - 14 June 2021  
<https://doi.org/10.1088/1361-6528/ac04a4>

Reprinted with permission from T. E. Glier, M. Betker, B. Grimm-Lebsanft *et al.*, Nanotechnology **2021**, 32, 365701. Copyright 2021 IOP Publishing. All rights reserved.

# Conductance-strain behavior in silver-nanowire composites: network properties of a tunable strain sensor

Tomke E Glier<sup>1,3,\*</sup> , Marie Betker<sup>1,3,\*</sup> , Benjamin Grimm-Lebsanft<sup>1</sup> , Sarah Scheitz<sup>1</sup> , Toru Matsuyama<sup>2</sup> , Lewis O Akinsinde<sup>1</sup>  and Michael Rübhausen<sup>1,\*</sup> 

<sup>1</sup>Institut für Nanostruktur- und Festkörperphysik, Center for Free Electron Laser Science (CFEL), Universität Hamburg, Luruper Chaussee 149, D-22761, Hamburg, Germany

<sup>2</sup>Max-Planck-Institut für Struktur und Dynamik der Materie, Luruper Chaussee 149, D-22761 Hamburg, Germany

E-mail: [tglier@physnet.uni-hamburg.de](mailto:tglier@physnet.uni-hamburg.de), [marie.betker@desy.de](mailto:marie.betker@desy.de) and [mruebhou@physnet.uni-hamburg.de](mailto:mruebhou@physnet.uni-hamburg.de)

Received 2 March 2021, revised 16 April 2021

Accepted for publication 23 May 2021

Published 14 June 2021



CrossMark

## Abstract

Highly flexible and conductive nano-composite materials are promising candidates for stretchable and flexible electronics. We report on the strain–resistance relation of a silver-nanowire photopolymer composite during repetitive stretching. Resistance measurements reveal a gradual change of the hysteretic resistance curves towards a linear and non-hysteretic behavior. Furthermore, a decrease in resistance and an increase in electrical sensitivity to strain over the first five stretching cycles can be observed. Sensitivity gauge factors between 10 and 500 at 23% strain were found depending on the nanowire concentration and stretching cycle. We model the electrical behavior of the investigated silver nanowire composites upon repetitive stretching considering the strain induced changes in the local force distribution within the polymer matrix and the tunnel resistance between the nanowires by using a Monte Carlo method.

Supplementary material for this article is available [online](#)

Keywords: silver-nanowire composite, strain sensor, strain–resistance behavior, flexible electronics, functional printing, Monte Carlo simulation

(Some figures may appear in colour only in the online journal)

## 1. Introduction

Flexible electronic devices are subject of recent research as they can be used in a wide spectrum of applications such as displays [1–3], piezoelectric generators [4], energy storage devices [5], in various fields like health care [6], and renewable energy [7]. The combination of flexible substrates like PDMS or PET with conducting/semiconducting nano-materials such as silicon, graphene, or metallic nanotubes, -dots, and-wires is a promising way to manufacture flexible and conductive composites [8, 9]. Silver-nanowire (Ag-NW)

networks have proven to be a suitable conductive filler due to their excellent conductivity, high transparency, and potential to develop flexibility [10, 11]. High aspect ratios are advantageous for a high network connectivity and a low percolation threshold and, therefore, enable 2D network properties even with a small amount of material [12, 13]. A 3D printable polymer matrix enables functional additive manufacturing of these materials [14]. However, the resilience of elastomeric nanowire polymer composites is still crucial for the later performance. The embedding of 2D nanowire networks in a polymer matrix leads to highly conductive and thin composite layers. For this purpose, the nanowires are usually applied from a suspension to an auxiliary substrate, then covered with a liquid polymer resin, and peeled off after curing [15–17]. In

<sup>3</sup> M.B. and T.E.G. contributed equally.

\* Authors to whom any correspondence should be addressed.



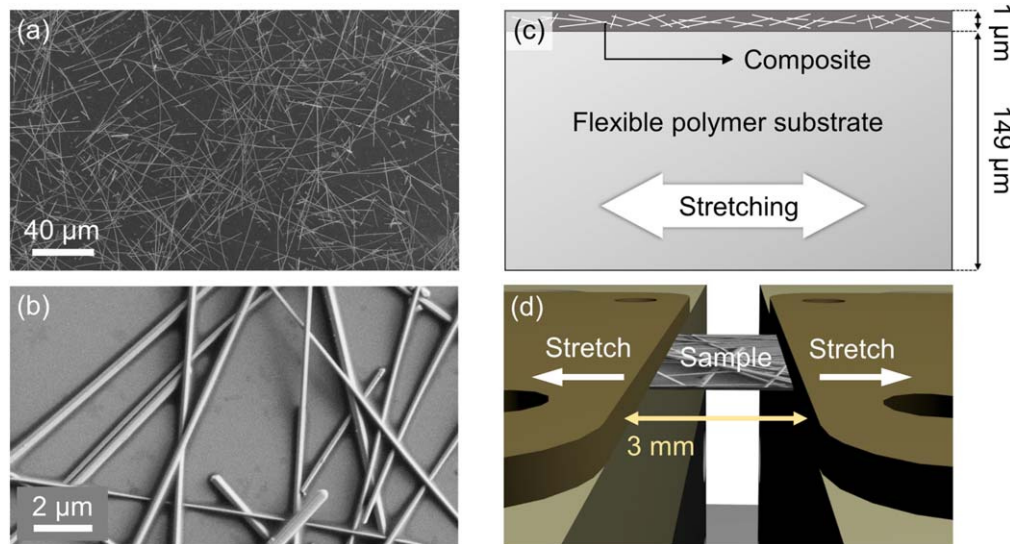


**Figure 1.** Stretching of Ag-NW composite samples. (a) Scanning electron micrograph of Ag-NWs deposited on a silicon wafer (before coating with polymer,  $c_{\text{NW}} \approx 50 \mu\text{g cm}^{-2}$ ). (b) High magnification scanning electron micrograph of Ag-NWs deposited on a silicon wafer. (c) Cross-sectional schematic view on the composite samples. The samples exhibit a total thickness of around  $150 \mu\text{m}$  with a  $1 \mu\text{m}$  composite top layer. (d) Sketch of the stretching experiment. The sample is clamped by two electrodes for conductivity measurements. Uniaxial strain is applied by two stepper-motor driven translation stages.

nanowire networks without post-treatment, the nanowire junctions remain flexible when stretched and the network conductivity recovers after the material has been relaxed [18]. During the wet-chemical and scalable Ag-NW synthesis, a stabilizing polymer ligand shell around the nanowires is created [19]. Thus, no direct contact between nanowires within the network can be achieved and the tunneling resistances between the nanowires dominate the network conductivity [20]. Great efforts have been made to produce modern strain sensors based on carbon nanotubes or metal nanowire composites with high sensitivity, biocompatibility, ease of manufacture, and high stability [17, 21–27]. The gauge factor (GF), which is defined as the slope of the change in electrical resistance or capacitance divided by the applied strain, is an often-used measure for the sensitivity of a strain sensor. Nano-composite based strain sensors exhibit GFs in a wide range. Typical Ag-NW PDMS composites have been reported to have tunable GFs in the range of 2–14 [17]. In general, the GFs are controlled by the density of the used nanowire networks [21]. Crack-induced Ag-NW strain sensors with GFs of 30 at 100% strain have been reported [22]. For zinc oxide (ZnO) nanowire polystyrene composites with nanobrush ZnO-NWs a GF of 116 has been found [28]. Ultra-sensitive strain sensors with GFs > 1000 have been fabricated based on graphene thin film polymer composites [29].

In this article, we report on the strain–resistance performance of highly conductive, flexible and printable Ag-NW photopolymer composites with different nanowire concentrations (40, 80, and  $120 \mu\text{g cm}^{-2}$ ) under repetitive strain by using a customized stretching-setup. The composites consist of drop-casted Ag-NW networks, which are embedded in a flexible and printable polymer matrix [14, 20]. Our composites show a gradual change of the hysteretic resistance curves to a linear dependence and an improved conductivity

after five stretching cycles. GFs between 10 and 500 at 23.33% strain were found depending on the nanowire concentration. We model the strain–resistance behavior of the Ag-NW composites based on the local force distribution within the polymer matrix and the tunneling resistance between the nanowires by a Monte Carlo method.

## 2. Materials and methods

Figure 1(a) shows a thin layer of Ag-NWs drop-casted on a silicon wafer forming a nanowire network with a concentration of around  $50 \mu\text{g cm}^{-2}$ . The Ag-NWs were synthesized via a polyol route and stored in isopropanol with a concentration of  $2 \text{ g l}^{-1}$  [14, 19, 20, 30]. By stepwise washing with acetone and isopropanol remaining educts, mainly polyvinylpyrrolidone (PVP), were removed from the nanowire reaction solution [14, 20]. Initial sheet resistances of the drop-casted nanowire networks in the range of 10–15  $\Omega/\text{sq}$  at an optical transmission of 90% have been obtained without further post-treatment [14]. Figure 1(b) shows nanowires of the same synthesis batch shown in (a) at a higher magnification. Networks are formed by nanowires laying above and below each other without welding or bonding between nanowires. This allows flexible sliding of the nanowires during stretching and a full recovering of the network resistance after relaxation [18].

The overall sample structure used in our experiments is shown in figure 1(c). The nanowire suspension was first drop-casted on an auxiliary substrate like silicon or glass to create two-dimensional nanowire networks. In a next step, these networks were coated with a liquid urethane-acrylate based photopolymer resin (Formlabs Flexible). A constant layer thickness was obtained by using a doctor blade, which was moved over the sample in a defined distance to the substrate.

The polymer layer was cured by illumination with UV light (laser driven light source EQ-99X Energetic) for 100 s and the sample was peeled off from the substrate resulting in a conductive composite top layer and a flexible polymer film underneath. For a medium concentration of  $60 \mu\text{g cm}^{-2}$  the mean thickness of the nanowire network is around 700 nm as determined by atomic force microscopy [14] resulting in conductive composite layers after polymer coating with a thickness of the order of  $1 \mu\text{m}$ . The total sample size was  $(12 \times 12) \text{ mm}^2$ . More details are given in the supporting information (SI 1 and SI 2 (available online at [stacks.iop.org/NANO/32/365701/mmedia](https://stacks.iop.org/NANO/32/365701/mmedia))). The use of the flexible and 3D printable polymer matrix (Formlabs Flexible) enables functional printing of the investigated material as already demonstrated in [14] by printing a flexible Ag-NW capacitor.

A sketch of the used stretching setup is illustrated in figure 1(d). The samples were clamped between the gold contacts of polyimide plates for conductivity measurements. The free-standing sample area between the two clamps had a size of  $(3 \times 12) \text{ mm}^2$ . Uniaxial strain was applied to the sample by two encoder-controlled stepper-motors (0.9-NEMA 17, Nanotec) driving micrometer translation stages (PT1/M, Thorlabs). The composites were stretched uniformly from both sides in  $100 \mu\text{m}$  steps up to a maximum elongation of 23.33%. Subsequently, the composites were relaxed in  $100 \mu\text{m}$  steps back to the starting position (see SI 3). After each step the electrical resistance was measured (see SI 4 for details) by using a DC voltage/current source (GS200, Yokogawa Japan) and a digital multimeter (34401A 6 12, Keysight USA). A constant current of 0.6 mA was applied to the nanowire composite samples and the voltage drop across the sample in stretching direction was measured.

For scanning electron microscopy measurements, a commercial field emission scanning electron microscope (SEM Zeiss, Germany) was used.

### 3. Results

#### 3.1. Experimental results

Figure 2(a) shows the line resistances in stretching direction for five stretching cycles as a function of elongation for three samples with a nanowire concentration of  $40 \mu\text{g cm}^{-2}$ ,  $80 \mu\text{g cm}^{-2}$ , and  $120 \mu\text{g cm}^{-2}$ , respectively. The initial resistances of the investigated samples before stretching are  $0.9 \Omega \text{ mm}^{-1}$  ( $R_{\text{Sheet}} = 31.9 \Omega/\text{sq}$ ) for a concentration of  $40 \mu\text{g cm}^{-2}$ ,  $2.9 \Omega \text{ mm}^{-1}$  ( $R_{\text{Sheet}} = 67.4 \Omega/\text{sq}$ ) at  $80 \mu\text{g cm}^{-2}$ , and  $0.7 \Omega \text{ mm}^{-1}$  ( $R_{\text{Sheet}} = 21.7 \Omega/\text{sq}$ ) at  $120 \mu\text{g cm}^{-2}$ . The deposition of the nanowires and, thus, the network formation is a stochastic process and the initial network resistances are distributed for different samples of the same concentration [14]. However, the qualitative behavior of the samples during stretching and relaxation was reproducible for more than 30 individual samples. By using light microscopy, flat and even composite surfaces were reproducibly found for repeated stretching cycles between 6.66% and 23.3% elongation [20]. We, therefore, normalize

the data to the resistance values of the pre-stretched samples at 6.66% elongation of the first stretching cycle. The detailed shape of a single stretching curve of the same material has been analyzed and modeled in [20].

The inset in figure 2(a) shows the first stretching cycle of the  $80 \mu\text{g cm}^{-2}$  sample, which exhibits a hysteresis between the resistance curve upon stretching (dark blue) and relaxation (light blue), respectively. The solid lines depict sigmoidal fits to the data. In figure 2(a), the hysteresis can also clearly be seen in the non-symmetrical shape of the resistance curves for all three concentrations in the first two stretching cycles. We observe a decrease in hysteresis for all samples as a function of stretching cycle up to the fifth cycle (see SI table S1 and figures S4–S6), resulting in a symmetric stretching and relaxation after four cycles. Beside the decrease of the hysteresis width, the resistance values itself are decreasing systematically as a function of stretching. Figure 2(b) shows the resistances at 23.33% strain depending on concentration normalized to the respective resistance of the pre-stretched samples at 6.66% of the first cycle. Samples with a lower concentration show a higher sensitivity of the network and correspondingly a higher change in resistance upon stretching due to the lower network connectivity. The resistance recovers after a full relaxation for all three concentrations as shown in figure 2(a).

In figure 2(c) the normalized line resistances as a function of elongation during the fifth stretching cycles of the three samples are shown. The data are normalized to the initial pre-stretched line resistance at 6.66% elongation of the first stretching cycle. During further stretching and relaxation a transition is observed, where the resistance changes are concentration dependent. In this so-called sensor region, the line resistance of each sample increases and decreases linearly. Their slopes increase with decreasing Ag-NW concentration. A measure for the sensitivity of a strain sensor is the GF, which is defined as

$$\text{GF} = \frac{(R - R_0)/R_0}{(L - L_0)/L_0}, \quad (1)$$

where  $R$  and  $L$  denote the resistance and length of the strained sample and  $R_0$  and  $L_0$  are the resistance and length of the unstrained sample, respectively. Figure 2(d) shows the GF for the resistance and length at 23% elongation in respect of the resistance and length at 6.66% strain. The GF is increasing for all three samples as a function of stretching cycle resulting in an increased sensitivity to strain of the sensors. Since the resistance at maximum elongation (23.3%) is decreasing as a function of stretching cycle (figure 2(b)), the increase in GF is due to a decrease in resistance even for small elongations (6.66%). During the first stretching cycle, the GF scales with the silver nanowire concentration linearly with an increased GF for lower network density. For additional stretching cycles, a clear cross-over between the high-concentration sample ( $120 \mu\text{g cm}^{-2}$ ) and samples with lower concentration ( $40$  and  $80 \mu\text{g cm}^{-2}$ ) can be observed. The high concentration sample has a GF of 7.8 for the sample in the first stretching cycle and 31 in the fifth cycle. However, the low-concentration samples ( $40$  and  $80 \mu\text{g cm}^{-2}$ ) converge at cycle 4 with a

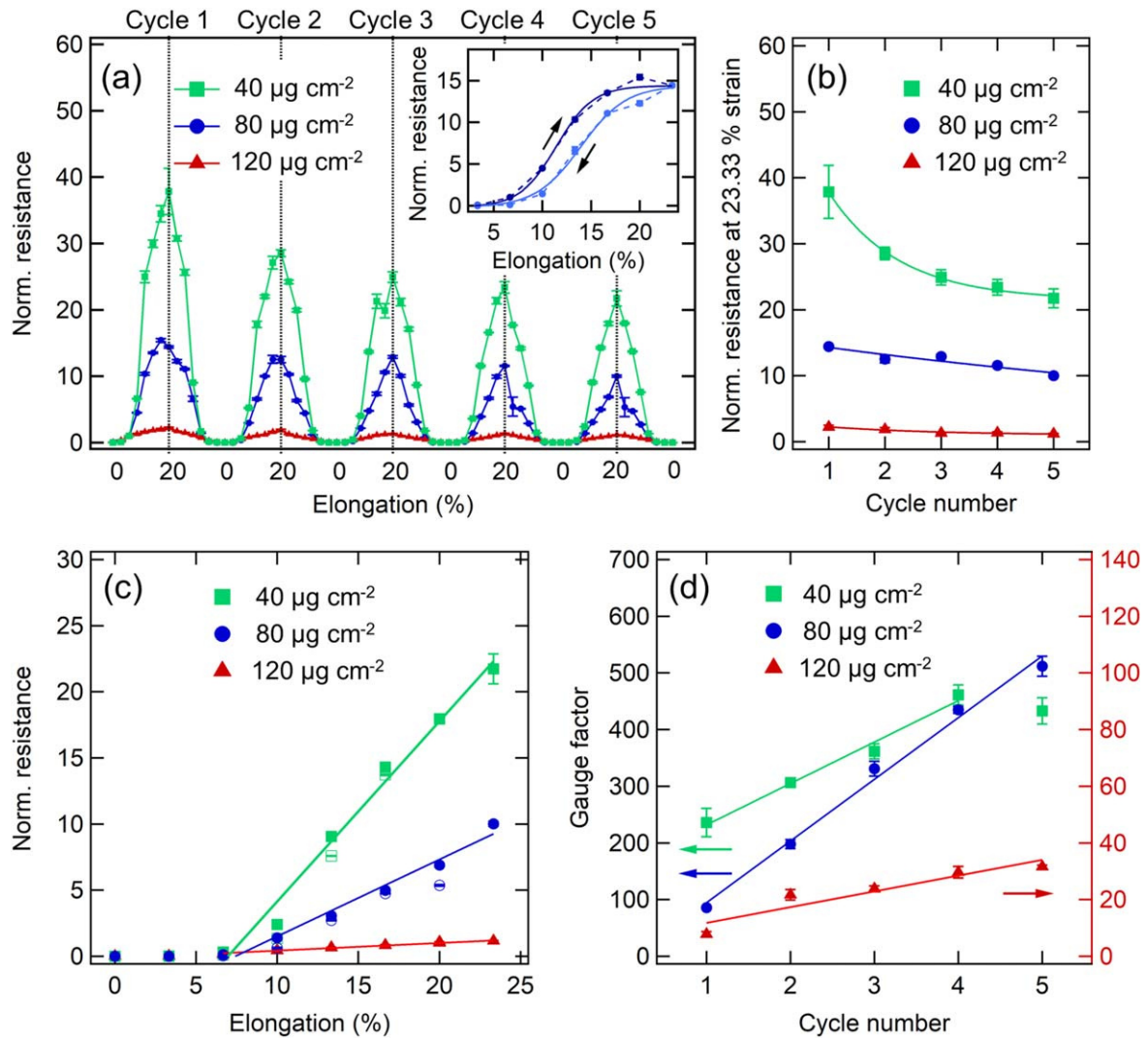


**Figure 2.** (a) Normalized line resistance in stretching direction as a function of elongation for five stretching cycles. Three samples with Ag-NW concentrations of 40  $\mu\text{g cm}^{-2}$  (green), 80  $\mu\text{g cm}^{-2}$  (blue), and 120  $\mu\text{g cm}^{-2}$  (red) are shown. The inset shows the line resistance during the first stretching (dark blue) and relaxation (light blue) of the sample with a nanowire concentration of 80  $\mu\text{g cm}^{-2}$ . (b) Amplitude (max. resistance) as a function of stretching cycle for the same samples shown in (a). (c) Normalized line resistance for the three samples during the fifth stretching cycle. Filled markers depict the data during stretching and blank markers represent the data during relaxation. Linear fits (solid lines) between 6.66% strain and 23.33% strain are used as guide to the eye. (d) Gauge factor as a function of stretching cycle for the three investigated nanowire concentrations. The gauge factor is defined as  $[(R_{23\%} - R_{6\%})/R_{6\%}]/[(L_{23\%} - L_{6\%})/L_{6\%}]$ . The solid lines represent linear fits to the data.

mean GF of around 450. Thus, we can conclude that the composite resistance is decreasing over multiple stretching cycles. Their hysteretic behavior is reduced over the first five stretching cycles and the sensitivity is increased.

### 3.2. Numerical modeling

In the following, the electrical properties of Ag-NW composites upon stretching are simulated by a Monte Carlo method. For this purpose, networks of randomly oriented nanowires ( $-90^\circ \leq \theta \leq 90^\circ$ ) with a random position ( $x_i, y_i$ ) within a certain sample size and a length  $L$  according to the length distribution determined by SEM analysis (see [20]) are created as illustrated in figure 3(a). In a next step, these networks are translated into resistor networks, where each nanowire is a node and each nanowire junction is a tunnel

resistor with a normalized tunneling resistance of  $r_{ij} = 1$ , resulting in a conductance of  $c_{ij} = r_{ij}^{-1} = 1$  (see figure 3(a)). The tunneling resistance between all wires, which are not intersecting, is infinity resulting in a conductance of zero.

Since silver is an excellent conductor, the resistance of the nanowire itself can be neglected and accordingly the tunnel resistance between the nanowires dominate the network resistance. The network resistance of the random resistor network is calculated as demonstrated by Wu *et al* [31] More detailed information on the simulation principle is given in [20].

In order to model the change in network resistance upon stretching, the corresponding changes in network connectivity have to be considered. First, each individual nanowire junction of the initial Monte Carlo simulated network is identified.



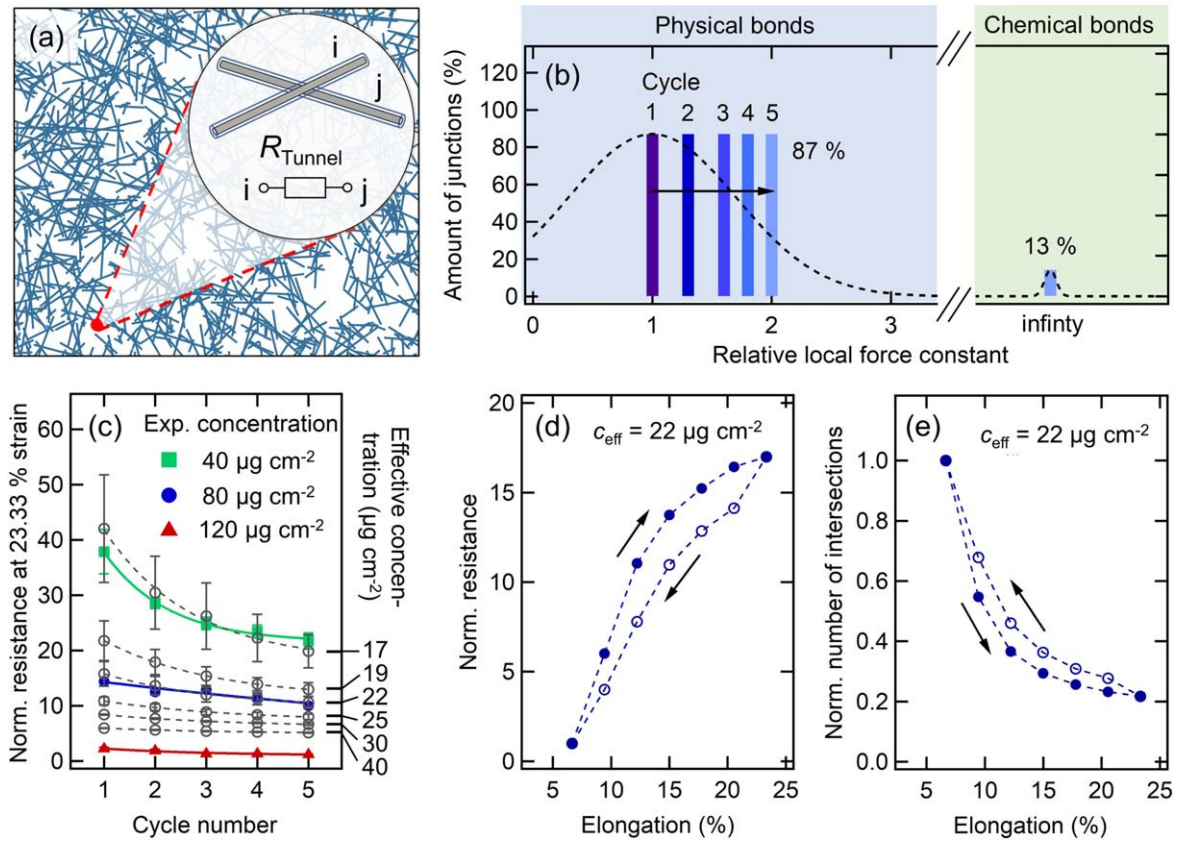


**Figure 3.** (a) Illustration of Monte Carlo simulated Ag-NW networks. Nanowires with random positions, random orientations, and lengths randomly drawn from a given length distribution are forming a 2D network. Each nanowire junction  $ij$  represents a tunnel resistor as shown in the inset. (b) Local force constant histogram. Class I (87%) represents the class of weak bonds within the polymer matrix (hydrogen bonds). Class II (13%) is taken to be infinity representing chemical bonds. The mean force constant of class I is shifting to higher values as a function of stretching cycle (black arrow). (c) Resistance at 23.33% strain normalized to the resistance value of the first stretching cycle at 6.66% as a function of stretching cycle for different nanowire concentrations. The filled markers (red, blue, and green) depict the experimental data (see figure 2(b)). Simulated results ( $n = 8$ ) are presented in gray for effective concentrations between 17 and  $40 \mu\text{g cm}^{-2}$  (see right axis). (d) Simulated normalized resistance as a function of elongation during stretching and relaxation, demonstrating the hysteric behavior (see figure 2(a) inset). (e) Normalized number of intersections within the simulated sample shown in (d).

We consider a distribution of local force constants within the polymer matrix, determining the local elongation and, thus, the local shifting of the nanowires upon stretching. For two intersecting wires  $i$  and  $j$  with the positions  $x_i$  and  $x_j$ , the local elongation  $\Delta x_{\text{local}}$  at the nanowire junction is defined as the relative movement of the nanowires  $\Delta x_{ij} = |x_i^1 - x_j^1| - |x_i^0 - x_j^0|$ . Here,  $x_{ij}^0$  is the initial  $x$ -position of the wires  $i$  and  $j$ , respectively, and  $x_{ij}^1$  is the respective  $x$ -position after stretching. In agreement with other publications, the cut-off distance for the tunnel current was taken to be 1 nm [21, 32, 33]. We assume two classes of local force constants: class I is characterized by elastomeric polymer chains bonded physically by hydrogen and Van-der-Waals bonds. Class II represents short chain elements with less elasticity dominated mainly by chemical bonds between the chain elements and, therefore, exhibits a much higher local force constant. In order to simulate the network properties within the polymer matrix, the nanowire junctions are randomly assigned to the two force constant classes. The higher the local force constant at a nanowire junction, the lower the local elongation following Hooke's law  $F_{\text{global}} = k_{\text{local}} \cdot \Delta x_{\text{local}}$  [34]. As a consequence,

nanowire junctions of class II remain intact over the complete stretching. This is the reason why the mean force constant of class II is set to infinity. Nanowire junctions of class I easily exceed the cut-off distance ( $F_{\text{global}}/k_{\text{local}} = \Delta x_{\text{crit}} = 1 \text{ nm}$ ) at a certain elongation making the network less connected and conductive. This approach allows a local mapping of the matrix force distribution on the scale of the nanowire network junctions. The lack of welded intersections leads to the elasticity of the network allowing us to assume a full recovery of nanowire junctions after relaxation, which agrees with the experimental data. In contrast to this, it is assumed that the polymer matrix ages upon stretching. Mechanical stress can lead to a rearrangement of physically bound polymer chains and, thus, to changes in the local force distribution [35–37].

The force constant distribution is illustrated in figure 3(b). The mean force constants of the two classes, which were used for the simulation, are depicted as blue bars. The dashed line represents a possible force distribution in class I for the first stretching. A shift in the mean force constant with stretching cycle can be attributed to a

rearrangement of polymer chains, in which strong bonds remain and weak bonds are energetically unfavorable and are changed during stretching. As can be seen in figure 3(c), we can successfully model the concentration dependent resistance change as a function of cycle number and, therefore, the aging of the polymer matrix. The relative distribution of classes I–II was 87%–13%. The mean force constants of class I normalized to the first cycle are 1.3 for the second cycle, 1.6 for the third cycle, 1.8 for the 4th, and 2.0 for the 5th cycle. On the right axis, the effective nanowire concentrations used for the simulations are given. As shown in [20], the effective concentrations are by a factor of about 4 lower than the experimental concentrations. The different concentrations for experiment and simulation can be attributed to a small amount of side products like silver particles in the reaction solution, the effective distribution of the nanowires in the composites as well as a coffee ring at the edge of the auxiliary substrate after drop-casting of the Ag-NW suspension. In figure 3(d), we model the hysteretic resistance curve for a sample with an effective concentration of  $22 \mu\text{g cm}^{-2}$ , corresponding to the experimental concentration of  $80 \mu\text{g cm}^{-2}$ . We can model the hysteretic behavior after stretching by shifting the mean force constant of class I by a factor of 1.5 (see figure 2(a)). This leads to the corresponding hysteretic number of intersections in the simulated network normalized to the number of intersections of the pre-stretched sample at 6.66% strain as shown in figure 3(e). These results indicate an aging in the polymer matrix due to the weak physical bonds. This behavior explains the changes in both, the network properties upon repetitive stretching cycles and the hysteretic behavior.

#### 4. Discussion

Stretching and relaxation of Ag-NW polymer composites affect their electrical properties depending on the Ag-NW concentration. This can mainly be attributed to the connectivity of the networks, since the nanowire junctions are the dominant resistors. The inter-connectivity, which we define as the mean number of junctions per nanowire, is therefore an important measure for the network resistance [20]. In order to understand the percolative properties of networks of 1D nanostructures, Monte Carlo methods have been used in many studies [38–41]. It is also known that the tunnel resistance at the nanowire junctions dominate the network resistance in most cases [32, 42].

The comparison of our experimental data with other studies shows that both, the nanowire network and the polymer matrix have a major influence on the electrical behavior under mechanical stress [15, 16, 21, 43–47]. The matrix material strongly interacts with the network during stretching, since it is the force-acting component. Many different mostly macroscopic models exist on the stress-strain behavior of polymers and the influence of nanofillers [48, 49]. The model used in this work offers a combination of matrix and filler network properties, explaining the influence of the local force distribution within the polymer

matrix upon stretching, which has a direct impact on the network inter-connectivity. The respective change in the force constant distribution as a function of the stretching cycle, therefore, depends on the properties of the matrix material. The 3D printable photo-resin used in this study enables the unique property that upon repetitive stretching the network resistance decreases and the electrical sensitivity to strain increases. Our results demonstrate prototypes for a tunable 3D printable strain sensor with tailored sensitivity. Furthermore, we are able to understand this behavior due to the combined properties of the Ag-NW composite under mechanical strain.

#### Acknowledgments

The authors thank Birger Höhling and Boris Fiedler for making the circuits boards. We thank Florian Biebl, Matthias Schwartzkopf, and Stephan Roth for their support and helpful discussions, and Robert Frömter and Nils Huse for using the scanning electron microscope. This research was funded by Bundesministerium für Bildung und Forschung (BMBF), grant number 05K19GU5 and the Helmholtz-Gemeinschaft Deutscher Forschungszentren through DESY.

Current address of MB: Deutsches Elektronen-Synchrotron, Notkestrasse 85, 22607 Hamburg, Germany; KTH, Royal Institute of Technology, 10044 Stockholm, Sweden.

#### Data availability statement


The data that support the findings of this study are available upon reasonable request from the authors.

#### Author contributions

Conceptualization, TEG and MR; software, MB, BGL, and TEG; validation, TEG, MB and MR; formal analysis, TEG and MR; investigation, MB, TEG, LOA, TM; writing—original draft preparation, MB and TEG; visualization, MB and TEG; supervision, TEG and MR; project administration, MR; funding acquisition, MR. All authors have read and agreed to the published version of the manuscript.

#### ORCID iDs


Tomke E Glier  <https://orcid.org/0000-0001-8943-1509>

Marie Betker  <https://orcid.org/0000-0001-6465-2188>

Benjamin Grimm-Lebsanft  <https://orcid.org/0000-0002-4070-3531>

Sarah Scheitz  <https://orcid.org/0000-0002-0305-5512>

Toru Matsuyama  <https://orcid.org/0000-0001-7878-7374>

Lewis O Akinsinde  <https://orcid.org/0000-0002-2147-4542>

Michael Rübhausen  <https://orcid.org/0000-0003-3868-392X>

## References

- [1] Ju S, Facchetti A, Xuan Y, Liu J, Ishikawa F, Ye P, Zhou C, Marks T J and Janes D B 2007 Fabrication of fully transparent nanowire transistors for transparent and flexible electronics *Nat. Nanotechnol.* **2** 378–84
- [2] Liang J, Li L, Chen D, Hajagos T, Ren Z, Chou S-Y, Hu W and Pei Q 2015 Intrinsically stretchable and transparent thin-film transistors based on printable silver nanowires, carbon nanotubes and an elastomeric dielectric *Nat. Commun.* **6** 7647
- [3] Gelinck G H *et al* 2004 Flexible active-matrix displays and shift registers based on solution-processed organic transistors *Nat. Mater.* **3** 106–10
- [4] Park K-I *et al* 2012 Flexible nanocomposite generator made of BaTiO<sub>3</sub> nanoparticles and graphitic carbons *Adv. Mater.* **24** 2999–3004
- [5] Pushparaj V L, Shajumon M M, Kumar A, Murugesan S, Ci L, Vajtai R, Linhardt R J, Nalamasu O and Ajayan P M 2007 Flexible energy storage devices based on nanocomposite paper *Proc. Natl Acad. Sci.* **104** 13574–7
- [6] Liu Y, Pharr M and Salvatore G A 2017 Lab-on-skin: a review of flexible and stretchable electronics for wearable health monitoring *ACS Nano* **11** 9614–35
- [7] Pagliaro M, Ciriminna R and Palmisano G 2008 Flexible solar cells *ChemSusChem* **1** 880–91
- [8] Rogers J A, Someya T and Huang Y 2010 Materials and mechanics for stretchable electronics *Science* **327** 1603–7
- [9] Nathan A *et al* 2012 Flexible electronics: the next ubiquitous platform *Proc. IEEE* **100** 1486–517
- [10] Hu L, Kim H S, Lee J-Y, Peumans P and Cui Y 2010 Scalable coating and properties of transparent, flexible, silver nanowire electrodes *ACS Nano* **4** 2955–63
- [11] De S, Higgins T M, Lyons P E, Doherty E M, Nirmalraj P N, Blau W J, Boland J J and Coleman J N 2009 Silver nanowire networks as flexible, transparent, conducting films: extremely high dc to optical conductivity ratios *ACS Nano* **3** 1767–74
- [12] Pike G E and Seager C H 1974 Percolation and conductivity: a computer study: I *Phys. Rev. B* **10** 1421–34
- [13] Munson-McGee S H 1991 Estimation of the critical concentration in an anisotropic percolation network *Phys. Rev.* **43** 3331–6
- [14] Glier T E *et al* 2019 Functional printing of conductive silver-nanowire photopolymer composites *Sci. Rep.* **9** 6465
- [15] Yun S, Niu X, Yu Z, Hu W, Brochu P and Pei Q 2012 Compliant silver nanowire-polymer composite electrodes for bistable large strain actuation *Adv. Mater.* **24** 1321–7
- [16] Xu F and Zhu Y 2012 Highly conductive and stretchable silver nanowire conductors *Adv. Mater.* **24** 5117–22
- [17] Amjadi M, Pichitpajongkit A, Lee S, Ryu S and Park I 2014 Highly stretchable and sensitive strain sensor based on silver nanowire-elastomer nanocomposite *ACS Nano* **8** 5154–63
- [18] Wu J, Zang J, Rathmell A R, Zhao X and Wiley B J 2013 Reversible sliding in networks of nanowires *Nano Lett.* **13** 2381–6
- [19] Sun Y, Yin Y, Mayers B T, Herricks T and Xia Y 2002 Uniform silver nanowires synthesis by reducing AgNO<sub>3</sub> with ethylene glycol in the presence of seeds and poly(vinyl pyrrolidone) *Chem. Mater.* **14** 4736–45
- [20] Glier T E, Betker M, Witte M, Matsuyama T, Westphal L, Grimm-Lebsanft B, Biebl F, Akinsinde L O, Fischer F and Rübhausen M 2020 Electrical and network properties of flexible silver-nanowire composite electrodes under mechanical strain *Nanoscale* **12** 23831–7
- [21] Amjadi M, Kyung K-U, Park I and Sitti M 2016 Stretchable, skin-mountable, and wearable strain sensors and their potential applications: a review *Adv. Funct. Mater.* **26** 1678–98
- [22] Lee C-J, Park K H, Han C J, Oh M S, You B, Kim Y-S and Kim J-W 2017 Crack-induced Ag nanowire networks for transparent, stretchable, and highly sensitive strain sensors *Sci. Rep.* **7** 7959
- [23] Hu N, Li J H, Shi D J, Liu X Y and Chen M Q 2013 Synthesis and self-assembly behaviors of four-armed amphiphilic polystyrene-b-poly(N-isopropylacrylamide) copolymers *Polym. Sci. Ser.* **55** 69–76
- [24] Alamusi H, N, Fukunaga H, Atobe S, Liu Y and Li J 2011 Piezoresistive strain sensors made from carbon nanotubes based polymer nanocomposites *Sensors* **11** 10691–723
- [25] Yao S and Zhu Y 2014 Wearable multifunctional sensors using printed stretchable conductors made of silver nanowires *Nanoscale* **6** 2345
- [26] Choi S *et al* 2018 Highly conductive, stretchable and biocompatible Ag–Au core-sheath nanowire composite for wearable and implantable bioelectronics *Nat. Nanotechnol.* **13** 1048–56
- [27] Xu H, Lv Y, Qiu D, Zhou Y, Zeng H and Chu Y 2019 An ultra-stretchable, highly sensitive and biocompatible capacitive strain sensor from an ionic nanocomposite for on-skin monitoring *Nanoscale* **11** 1570–8
- [28] Xiao X, Yuan L, Zhong J, Ding T, Liu Y, Cai Z, Rong Y, Han H, Zhou J and Wang Z L 2011 High-strain sensors based on ZnO nanowire/polystyrene hybridized flexible films *Adv. Mater.* **23** 5440–4
- [29] Li X *et al* 2012 Stretchable and highly sensitive graphene-on-polymer strain sensors *Sci. Rep.* **2** 870
- [30] Sun Y, Mayers B, Herricks T and Xia Y 2003 Polyol synthesis of uniform silver nanowires: a plausible growth mechanism and the supporting evidence *Nano Lett.* **3** 955–60
- [31] Wu F Y 2004 Theory of resistor networks: the two-point resistance *J. Phys. A: Math. Gen.* **37** 6653
- [32] Li C, Thostenson E T and Chou T-W 2007 Dominant role of tunneling resistance in the electrical conductivity of carbon nanotube-based composites *Appl. Phys. Lett.* **91** 223114
- [33] Balberg I 1987 Tunneling and nonuniversal conductivity in composite materials *Phys. Rev. Lett.* **59** 1305–8
- [34] Hooke R 1678 *Lectures de Potentia Reflituitiva or of Spring: Explaining the Power of Springing Bodies* (London: John Martyn)
- [35] Qi H J and Boyce M C 2005 Stress-strain behavior of thermoplastic polyurethanes *Mech. Mater.* **37** 817–39
- [36] Harwood J A C, Payne A R and Whittaker R E 1971 Stress-softening and reinforcement of rubber *J. Macromol. Sci. B* **5** 473–86
- [37] Lorenz H, Klüppel M and Heinrich G 2012 Microstructure-based modelling and FE implementation of filler-induced stress softening and hysteresis of reinforced rubbers *ZAMM —J. Appl. Math. Mech./Z. Angew. Math. Mech.* **92** 608–31
- [38] Yook S-H, Choi W and Kim Y 2012 Conductivity of stick percolation clusters with anisotropic alignments *J. Korean Phys. Soc.* **61** 1257–62
- [39] Ni X, Hui C, Su N, Jiang W and Liu F 2018 Monte Carlo simulations of electrical percolation in multicomponent thin films with nanofillers *Nanotechnology* **29** 075401
- [40] Balberg I, Binenbaum N and Anderson C H 1983 Critical behavior of the two-dimensional sticks system *Phys. Rev. Lett.* **51** 1605–8
- [41] Kumar A 2019 Electrical percolation in metal wire network-based strain sensors *IEEE Sens. J.* **19** 10373–8
- [42] Bao W S, Meguid S A, Zhu Z H and Weng G J 2012 Tunneling resistance and its effect on the electrical conductivity of carbon nanotube nanocomposites *J. Appl. Phys.* **111** 093726
- [43] Chen Y, Carmichael R S and Carmichael T B 2019 Patterned, flexible, and stretchable silver nanowire/polymer composite films as transparent conductive electrodes *ACS Appl. Mater. Interfaces* **11** 31210–9

- [44] Hu W, Niu X, Li L, Yun S, Yu Z and Pei Q 2012 Intrinsically stretchable transparent electrodes based on silver-nanowire-crosslinked-polyacrylate composites *Nanotechnology* **23** 344002
- [45] Kim J, Park J, Jeong U and Park J-W 2016 Silver nanowire network embedded in polydimethylsiloxane as stretchable, transparent, and conductive substrates *J. Appl. Polym. Sci.* **133** 1–7
- [46] Lee C, Oh Y, Yoon I S, Kim S H, Ju B-K and Hong J-M 2018 Flash-induced nanowelding of silver nanowire networks for transparent stretchable electrochromic devices *Sci. Rep.* **8** 2763
- [47] Lee P, Lee J, Lee H, Yeo J, Hong S, Nam K H, Lee D, Lee S S and Ko S H 2012 Highly stretchable and highly conductive metal electrode by very long metal nanowire percolation network *Adv. Mater.* **24** 3326–32
- [48] Michler G H and Baltá-Calleja F J 2016 *Mechanical Properties of Polymers based on Nanostructure and Morphology* ed G H Michler and F J Balta-Calleja (Boca Raton, FL: CRC Press)
- [49] Frankland S J V, Harik V M, Odegard G M, Brenner D W and Gates T S 2003 The stress-strain behavior of polymer-nanotube composites from molecular dynamics simulation *Compos. Sci. Technol.* **63** 1655–61

## **Paper IV**

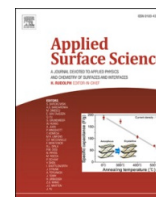
# **Surface characterization and resistance changes of silver-nanowire networks upon atmospheric plasma treatment**

Lewis Olaniyi Akinsinde\*, Tomke Eva Glier\*, Matthias Schwartzkopf, Marie Betker, Matz Nissen, Max Witte, **Sarah Scheitz**, Christian Nweze, Benjamin Grimm-Lebsanft, Marc Gensch, Andrei Chumakov, Ivan Baev, Ulrich Schürmann, Torben Dankwort, Frank Fischer, Michael Martins, Stephan V. Roth, Lorenz Kienle, and Michael Rübhausen\*

Published in: Applied Surface Science - 25 February 2021  
<https://doi.org/10.1016/j.apsusc.2021.149362>

Reprinted with permission from L. O. Akinsinde, T. E. Glier, M. Schwartzopf *et al.*, Applied Surface Science, **2021**, 550, 1493262. Copyright 2021 Elsevier.





## Full Length Article



# Surface characterization and resistance changes of silver-nanowire networks upon atmospheric plasma treatment

Lewis O. Akinsinde<sup>a,e,\*</sup>, Tomke E. Glier<sup>a,\*</sup>, Matthias Schwartzkopf<sup>c,\*</sup>, Marie Betker<sup>a,c</sup>, Matz Nissen<sup>b</sup>, Maximilian Witte<sup>d</sup>, Sarah Scheitz<sup>a</sup>, Christian Nweze<sup>a</sup>, Benjamin Grimm-Lebsanft<sup>a</sup>, Marc Gensch<sup>c</sup>, Andrei Chumakov<sup>c</sup>, Ivan Baev<sup>b</sup>, Ulrich Schürmann<sup>e</sup>, Torben Dankwort<sup>e</sup>, Frank Fischer<sup>d</sup>, Michael Martins<sup>b</sup>, Stephan V. Roth<sup>c,f</sup>, Lorenz Kienle<sup>e</sup>, Michael Rübhausen<sup>a,\*</sup>

<sup>a</sup> Institute for Nanostructures and Solid-State Physics, Center for Free-Electron Laser Science (CFEL), Universität Hamburg, Luruper Chaussee 149, D-22761 Hamburg, Germany

<sup>b</sup> Institute for Experimental Physics, Center for Free-Electron Laser Science (CFEL), Universität Hamburg, Luruper Chaussee 149, D-22761 Hamburg, Germany

<sup>c</sup> Deutsches Elektronen-Synchrotron (DESY), Notkestr. 85, D-22607 Hamburg, Germany

<sup>d</sup> Beiersdorf AG, Unnastraße 48, 20245 Hamburg, Germany

<sup>e</sup> Institute for Materials Science, Kiel University, Kaiserstr.2, D-24143 Kiel, Germany

<sup>f</sup> KTH Royal Institute of Technology, Teknikringen 56-58, SE-100 44 Stockholm, Germany

## ARTICLE INFO

## Keywords:

Silver nanowire networks  
Atmospheric plasma treatment  
Crystallinity  
In situ X-ray scattering  
Monte Carlo simulation  
Resistance

## ABSTRACT

Highly conductive silver-nanowire (Ag-NW) networks are used in composite materials as conductive channels. Their resistance tuning can be accomplished by changing the Ag-NW concentration, and, therefore, changing the network structure. In this study, an alternative pathway to resistance engineering of conductive Ag-NW networks by local atmospheric plasma treatment is employed. The corresponding changes in nanowire network morphology and crystallinity as a function of plasma etching time are investigated by time-resolved grazing-incidence X-ray scattering, field-effect scanning electron microscopy, and X-ray photoelectron spectroscopy. Three characteristic etching phases are identified. The first two phases enable the controlled engineering of the electrical properties with different rates of resistance change, which results from changes in nanowire shape, network morphology, and different oxidation rates. Phase III is characterized by pronounced fragmentation and destruction of the Ag-NW networks. These results show the feasibility of atmospheric plasma treatments to tune the local electrical properties of conductive Ag-NW networks. Furthermore, we present a physical Monte Carlo model explaining the electrical network properties as a function of plasma etching time based on the network connectivity and a constant plasma etching rate of  $570 \text{ ng s}^{-1} \text{ cm}^{-2}$ .

## 1. Introduction

Nanoparticles and nanowires in metal-polymer composite films have interesting and fascinating physical properties [1–4]. Their outstanding material elasticity, high durability, controllable size, and shapes contribute to their uniqueness [2,5]. The optimization of their synthesis as well as their characterization are highly important to tailor their electrical properties in a controlled fashion. Conductive electrodes consisting of nanowire network composites are used in enhancing the performance of organic light-emitting diodes (OLEDs), solar cells,

memory devices, sensors, touch screen devices and opto-electronics [6–14]. In addition, nanowire composites with a printable polymer matrix enable additive manufacturing and, therefore, high design flexibility and rapid prototyping [15]. By using a flexible polymer, flexible and bendable electrodes can be fabricated [15,16]. They represent a competitive counterpart to the existing materials of choice comprising mainly of indium tin oxide (ITO) or doped compounds of tin oxide [6,7], due to their attractive material properties including mechanical flexibility, low sheet resistance, and high optical transparency.

Networks made of silver-nanowires (Ag-NWs) with a well-defined

\* Corresponding authors.

E-mail addresses: [lakinsin@physnet.uni-hamburg.de](mailto:lakinsin@physnet.uni-hamburg.de) (L.O. Akinsinde), [tglier@physnet.uni-hamburg.de](mailto:tglier@physnet.uni-hamburg.de) (T.E. Glier), [matthias.schwartzkopf@desy.de](mailto:matthias.schwartzkopf@desy.de) (M. Schwartzkopf), [ruebhausen@physnet.uni-hamburg.de](mailto:ruebhausen@physnet.uni-hamburg.de) (M. Rübhausen).

<https://doi.org/10.1016/j.apsusc.2021.149362>

Received 21 December 2020; Received in revised form 18 February 2021; Accepted 18 February 2021

Available online 25 February 2021

0169-4332/© 2021 Elsevier B.V. All rights reserved.

shape, morphology, good crystallinity, and high aspect ratios (length to diameter ratio) of up to 1000 are excellent candidates for modern composite materials with tailored electrical properties [17–19]. Bulk silver exhibits a high electrical and thermal conductivity at room temperature [5,18]. Several publications have highlighted the fabrication of large scale Ag-NW networks by adopting simple and cost-effective chemical methods [17,19–24]. Recent publications show continuous improvements in the optimization of Ag-NW networks and transparent electrodes [13–15,25]. Also, current research focuses on the modification and tailoring of the electrical properties of Ag-NW networks using various techniques such as high-temperature thermal annealing [26], induced current flow [13], washing with solvents [15], mechanical pressing [13,14], and plasma treatment methods [13,25]. A common route to fabricate silver nanowires is the polyol method, which is associated with the formation of a polymer ligand shell (polyvinylpyrrolidone – PVP) around the nanowires [5,17]. The PVP layer has a detrimental effect on the electrical properties of the Ag-NW networks, as it forms an isolating layer at the wire-wire junctions. We, therefore, use a washing procedure with acetone and isopropanol, which causes an improvement in conductivity by a factor of around 100 and, therefore, reduces the PVP layer significantly [15] (see experimental section). In this way, highly conductive nanowire networks with initial sheet resistance in the range of 10–15  $\Omega/\text{sq.}$  at an optical transmittance of 90% are produced [15].

Traditionally, plasma treatment has been adopted to optimize the conductivity of Ag-NW networks due to the removal of PVP insulating layer as well as to study the degradation mechanism of Ag-NW electrodes [13,25]. Furthermore, several groups have reported on the deterioration phenomena in Ag-NW based electronic devices due to corrosive environment, elevated annealing temperature [14,26], long UV light irradiation exposure [26], induced electrical current [27,28] and humidity [12,29,30]. Here, an atmospheric plasma pen [31–35] is utilized as a versatile, simple, and direct tool to control the electrical properties of polyol grown and washed Ag-NW networks with high conductivities. The local manipulation of Ag-NW networks can enable future complex resistor designs within a premanufactured composite structure. The crystalline nanowires are monitored through a combination of time-resolved grazing-incidence small-and-wide-angle X-ray (GISAXS) and GIWAXS) scattering methods during the atmospheric plasma treatment. Moreover, the effects of the applied plasma on the sample morphology are investigated using field-effect scanning electron microscopy (FESEM). The chemical surface composition upon plasma treatment is measured by X-ray photoelectron spectroscopy (XPS). A physical model that explains the electrical network properties as a function of plasma etching time based on the network connectivity is presented. The model is based on a Monte Carlo simulation considering the experimental thickness and length distribution of the nanowires at a constant plasma etching rate and the tunneling resistances at the nanowire junctions.

## 2. Experimental section

### 2.1. Materials

(100) monocrystalline boron-doped silicon wafers (Si-Mat) with the dimension of  $15 \times 15 \text{ mm}^2$  were used as substrates, which were acidly cleaned in 1:2 mixture of sulfuric acid ( $\text{H}_2\text{SO}_4$ , 96%, Carl Roth) and hydrogen peroxide ( $\text{H}_2\text{O}_2$ , 30%, Carl Roth) according to the RCA-1 cleaning procedure [36]. More detailed information is given in the supplementary information (SI) S1.1.

The Ag-NWs were synthesized via a polyol wet chemical method at a temperature of 155 °C and a reaction time of 3 h. The precursors used were commercially purchased and comprise the following: silver nitrate ( $\text{AgNO}_3$ , 99.9%, Sigma Aldrich), polyvinylpyrrolidone (PVP, molecular weight,  $M_w = 55 \text{ kg mol}^{-1}$ , Sigma Aldrich, and PVP  $M_w = 360 \text{ kg mol}^{-1}$ , Carl Roth), anhydrous ethylene glycol (EG 99.8%, Sigma Aldrich) and

copper chloride ( $\text{CuCl}_2$  99.999% purity, Sigma Aldrich). A detailed description of the synthesis is given in Ref. [15].

After synthesis, the Ag-NW suspension was consecutively washed twice with isopropanol (99.5%, Sigma Aldrich), twice with acetone (99.8%, VWR), and finally again twice with isopropanol to eliminate remaining precursors and PVP from the synthesis. After each washing step, the suspension was centrifuged at 2000 rpm at 20 °C for 10 min. The final product was stored in isopropanol (99.5%, Sigma Aldrich). The synthesis yields silver nanowires with pentagonal cross-sections and were analyzed via TEM verifying the pentagonal shape [17] as well as the crystallinity as displayed in Figure S2 in the SI.

### 2.2. Ag-NW network preparation

20  $\mu\text{l}$  of the Ag-NW suspension were drop casted on a  $15 \times 15 \text{ mm}^2$  clean (100) monocrystalline silicon substrate at room temperature leading to a network of silver nanowires with a density of around  $26 \mu\text{g cm}^{-2}$ . After 5 min the solvent was evaporated. The film thickness of each sample is estimated to be approximately 1  $\mu\text{m}$  and typically averaged initial line resistances of  $(1.3 \pm 0.5) \Omega \text{ mm}^{-1}$  are found. A commercial hand-held atmospheric plasma pen device (Plasma Wand, Plasma Etch, Inc.) was adopted to treat the samples with varying treatment times from 0 s to 26 s (see SI S1.2). The plasma pen uses a piezo crystal to create very high voltages and is driven by a 30 W plasma generator with an integrated power supply ionizing surrounding gas. We use air from the surrounding atmosphere. Since the plasma temperature is smaller than 50 °C, ozone ( $\text{O}_3$ ) predominantly contributes to the plasma etching [private communication Plasma Etch Inc.] [37]. The setup enables various types of materials to be locally modified in the sub-micrometer to millimeter range. The treatment area is determined by the nozzle diameter, which was 10 mm for the presented experiments. For enabling the electrical discharge from the atmospheric plasma to attain the sample surface, a nozzle-to-sample height (NSH) of  $(10.5 \pm 0.5) \text{ mm}$  was used.

### 2.3. Grazing-incidence small-and-wide-angle X-ray scattering

For the structural investigation and the verification of the Ag-NW oxidation, *in situ* GISAXS/GIWAXS experiments were conducted at the Micro-and-Nanofocus X-ray scattering (MiNaXS) beamline P03 of the high-brilliance light source PETRA III at DESY, Hamburg [38]. We used an X-ray beam with a wavelength  $\lambda = (0.965 \pm 0.002) \text{ \AA}$  and a focus size of around  $20 \times 30 \mu\text{m}^2$ . The sample-to-detector distance (SDD) for GISAXS was  $(4380 \pm 2) \text{ mm}$  and for GIWAXS  $(116.5 \pm 0.5) \text{ mm}$ . The incident angle was  $\alpha_i = 0.425^\circ$ . A Pilatus 300 k detector (Dectris Ltd.) with an image dimension of  $487 \times 619$  pixels and a pixel size of  $172 \times 172 \mu\text{m}^2$  was used. GIWAXS data were acquired with a LAMBDA 750k detector (X-Spectrum GmbH) yielding an image dimension of  $512 \times 1536$  pixels and a pixel size of  $55 \times 55 \mu\text{m}^2$ . Lateral y-scans with a scan rate of 100 ms, step-width of 100  $\mu\text{m}$  and an overall length of 7 mm were carried out. In situ GISAXS and GIWAXS scans were carried out simultaneously on the sample before and after each atmospheric plasma treatment step.

### 2.4. Field emission scanning electron microscopy

The morphology of the Ag-NW networks (treated and untreated sample) and the shape of the nanowires were investigated by a field emission scanning electron microscope setup (Zeiss company) at an accelerating voltage of 3 kV and a focus distance of 7 mm.

### 2.5. X-ray photoelectron spectroscopy

The chemical surface composition was measured by using an X-ray photoelectron spectroscopy (XPS) with a hemispherical electron analyzer SES2002 (Scienta) measuring system.

## 2.6. Resistance measurements

After each atmospheric plasma treatment step, *in situ* GISAXS/GIWAXS scans and electrical resistance measurements using a Keithley 2000 multimeter (Tektronix) in a two-point resistance configuration were carried out [39]. The effects of the contact resistances of the electrical cables on the measured line resistances were considered. For the measurements, two coaxial cables with an insulating shield were connected to a lithographically patterned pad structure with gold contacts with a distance of 10 mm. Pieces of indium foil (max  $1 \times 1 \text{ mm}^2$ ) were utilized to obtain a gapless contact between the Ag-NWs and the gold contacts. At least 10 data points were recorded for each atmospheric plasma treatment time and averaged.

## 3. Results and discussion

In order to obtain a direct overview of the Ag-NW network changes upon atmospheric plasma etching, SEM images were recorded for different plasma treatment times. In Fig. 1 exemplary FESEM images of Ag-NW networks with a concentration of  $26 \mu\text{g cm}^{-2}$  after different atmospheric plasma treatment times are shown. An untreated (pristine) Ag-NW network (0 s) consisting of pentagonal nanowires with aspect ratios of up to 1000 can be observed in Fig. 1a. Small treatment times lead to marginal changes in the nanowire morphology like rounding of the nanowire facets as shown in Fig. 1b and 1f. Here, the robustness of the Ag-NW networks can be attributed to a strong wire-wire interconnectivity within the percolation network of the Ag-NWs [16,40–42]. However, for longer treatment times, enhanced destruction and fragmentation of the Ag-NW networks is observable [26,28] as shown in Fig. 1c–1f, which finally leads to the failure of the conductive Ag-NW networks. The degradation observed with longer treatment times is caused by mechanical ablation induced by the atmospheric plasma pen (see Fig. 1f (26 s)). In comparison, Li et al. [25] reported a low energy (45 W) plasma treatment in argon inert gas resulting in a decrease in Ag-NW network resistance due to the removal of PVP and welding of

nanowires in the first 20 min. A degradation of the Ag-NW electrode occurred after a prolonged treatment time of more than 20 min. Kim et al. [13] also used argon inert gas to treat Ag-NW networks at a power of 200 W, resulting in a rapid decrease in resistance after 2 min, which can be attributed to welding of the nanowires. Atmospheric plasma, however, is known to generate reactive oxygen species (ROS) [31–35] after air ionization and is also very versatile in applications for composite 3D printing. Here, the plasma treatment of the network can be used to manipulate the electrical properties locally. ROS enable ultra-fast morphological changes as well as surface oxidation that can be observed already after 10 sec treatment time.

In order to obtain a measure of the morphological network changes during plasma treatment, the Fiber Image Network Evaluation (FINE) algorithm [16,43,44] was used. Based on the SEM images for different plasma treatment times, the FINE algorithm determines the number of fiber families, their amplitudes, mean orientation, and dispersion, based on the cumulative angular orientation distribution (see SI S2.5 for details). Nanowires contribute to an anisotropic class of fiber families, whereas particle-like structures are detected as an isotropic contribution. Therefore, the FINE algorithm is a relevant tool for the quantitative analysis of the destruction, fragmentation, and melting of nanowires. The results are shown in Fig. 1g, where the amplitude of the isotropic fiber family is displayed in red. Blue denotes the amplitudes of the anisotropic class. Sigmoidal curves are used as guides to the eye. After 6 s plasma treatment, a clear increase in the isotropic family and a corresponding decrease in the anisotropic fiber family can be observed. This indicates a transition from slight changes on the nanowire surface to stronger morphological changes including an onset of fragmentation and melting of the nanowires. These morphological changes have a strong influence on the interconnectivity of the network and, thus, on the electrical network resistance.

Fig. 2a and b show exemplary XPS spectra of oxygen (O 1 s) and silver (Ag 3d) for plasma-treated Ag-NW networks. For a treatment time of 0 s and 6 s, the Ag 3d spectra display two characteristic peaks at  $(368.4 \pm 0.2) \text{ eV}$  and  $(374.4 \pm 0.2) \text{ eV}$ , which correspond to the Ag  $3d_{5/2}$

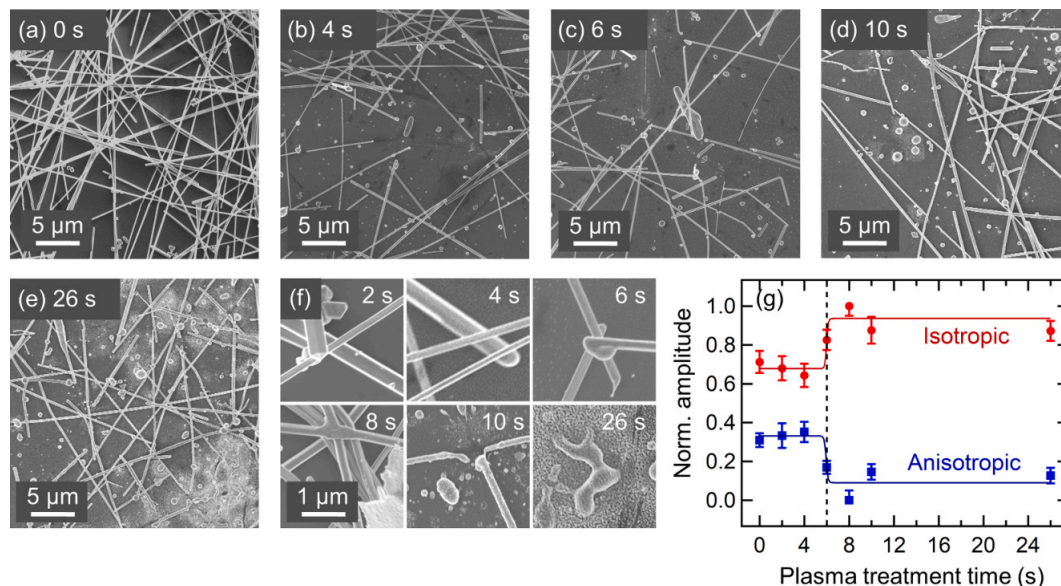


**Fig. 1.** (a)–(e) Exemplary scanning electron microscopy images of the investigated Ag-NW sample with a nanowire concentration of  $26 \mu\text{g cm}^{-2}$  after different atmospheric plasma treatment times (0 s to 26 s). Please note that different areas of the same sample are shown. Longer treatment times ( $>8 \text{ s}$ ) lead to enhanced fragmentation, melting, and destruction of the Ag-NWs. (f) Collage of six SEM images at high magnification for a plasma treatment time of 2 s, 4 s, 6 s, 8 s, 10 s, and 26 s, respectively. After 2 s, the pentagonal shape of the wires can still be observed. After 4 s, rounding is visible on individual wires. Further changes in the nanowire shape are observable after 6 s. After 8 s, welding of the nanowire junctions occurs and local destruction is already visible after 10 s. After 26 s, parts of the network are completely destroyed. (g) Amplitudes for the isotropic (red) and the anisotropic fiber family (blue) determined by the FINE algorithm based on the SEM images. Sigmoidal curves are guides to the eye. A clear increase in the isotropic particle class (particle-like structures, fragmented and melted nanowires) after 6 s plasma treatment (phase I) and a corresponding decrease in the anisotropic class can be observed.



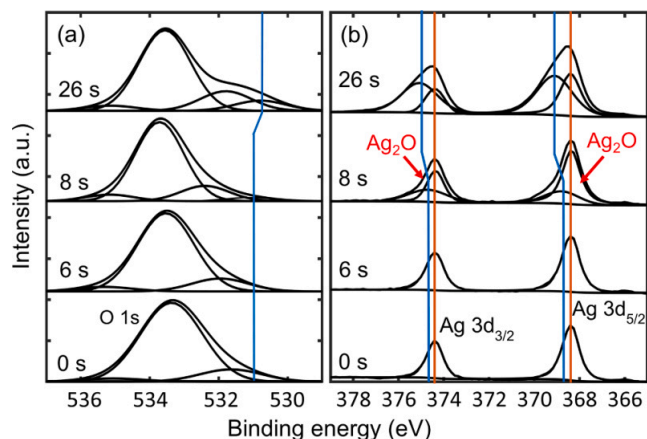


Fig. 2. Exemplary XPS spectra of the Ag-NW sample highlighting the characteristic oxygen (O 1s) (a) and silver (Ag  $3d_{3/2}$  and Ag  $3d_{5/2}$ ) (b) peak positions for a plasma treatment time of 0 s, 6 s, 8 s, and 12 s, respectively.

and  $3d_{3/2}$  binding energy of metallic Ag<sup>0</sup> (orange line) [45]. After 8 s treatment, peaks at  $(368.8 \pm 0.2)$  eV and  $(374.7 \pm 0.2)$  eV are observed and are attributed to oxidized species Ag<sub>2</sub>O (see red arrows in Fig. 2b) [45–47]. This oxidation process indicates the crossover between two characteristic phases induced by the atmospheric plasma treatment. Phase I lasts up to 6 s, where phase II begins. This also correlates strongly with the observation from the SEM analysis (see Fig. 1g).

Similarly, the O 1s spectra displayed in Fig. 2a exhibit three different oxygen species with peaks at  $(532.0 \pm 0.2)$  eV,  $(533.6 \pm 0.2)$  eV, and  $(535.0 \pm 0.2)$  eV, which we attribute to C=O, C-O, and H<sub>2</sub>O [48–53],

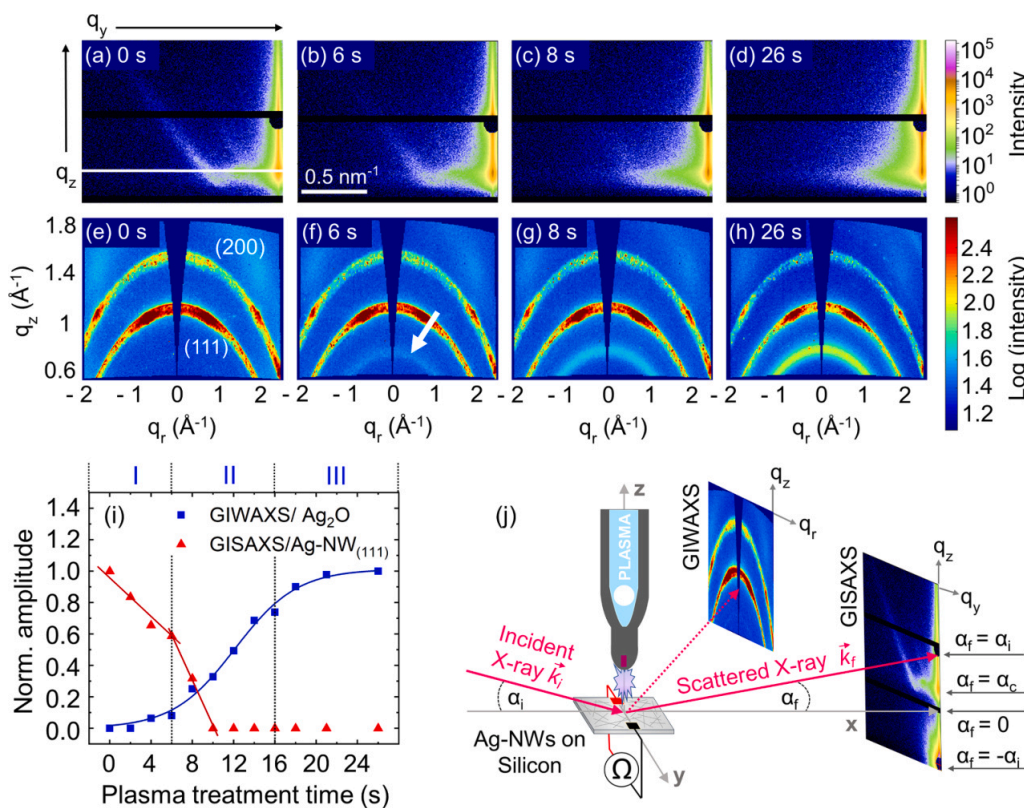


Fig. 3. (a)–(d) 2D GISAXS pattern for ( $26 \mu\text{g cm}^{-2}$  Ag-NW concentration) exemplary atmospheric plasma treatment times of 0 s, 6 s, 8 s, and 26 s. The position of the line cuts is shown in (a) as a white line for the horizontal line cut  $I(q_y)$  at  $q_z = 0.885 \text{ nm}^{-1}$ . (e)–(h) GIWAXS data showing the reciprocal space maps (RSM) [61] for a ( $26 \mu\text{g cm}^{-2}$  Ag-NW concentration) plasma treatment time of 0 s, 6 s, 8 s and 26 s, respectively. The characteristic face-centred-cubic (fcc) silver (111), (200) Miller's indices and oxidized Ag-NWs (Ag<sub>2</sub>O) reflections are indicated. The white arrow in (f) indicates the Bragg peak corresponding to the Ag<sub>2</sub>O diffractions [62–64]. (i) Normalized comparison of the Ag-NW flare intensity obtained by GISAXS (red), and the Ag<sub>2</sub>O Bragg intensity obtained by GIWAXS (blue) as a function of atmospheric plasma treatment time. Three characteristic phases can be observed as marked in blue in the upper part of the figure. (j) Schematic view on the experiment showing the operando atmospheric plasma pen above the Ag-NW/SiO<sub>x</sub> sample. The incident X-ray beam with an incident angle  $\alpha_i$ , the scattered X-ray beams in GIWAXS geometry (dashed line) and GISAXS mode (solid line) with a scattering angle  $\alpha_s$ , as well as two exemplary detector images for GIWAXS and GISAXS are shown. The digital multimeter represents the *in situ*

two-point resistance measurements.

respectively. These peaks are not unambiguous and presumably contain overlapping hydroxides or carboxyl groups from the PVP precursor [46,52,54]. Above 8 s treatment time, a peak at  $(531.0 \pm 0.2)$  eV is observed and is attributed to Ag<sub>2</sub>O [46,49,55]. The further shift in the O 1s spectra to lower binding energies at 26 s prolonged treatment time confirms the formation of AgO, which is characteristic for phase III of the treatment [48,49,55,56]. This view is also supported by an enhanced shoulder seen in Fig. 2b after 26 s treatment [46,47]. A detailed information on the XPS experimental information is given in the SI and also, an overview of all the identified elements as well as the Carbon 1s spectra are shown in Figure S6.

Surface-sensitive X-ray scattering using high flux X-ray beams enables time-resolved measurements and, thus, allows in-depth observation of morphological and nanostructural changes in a variety of processes [57–60]. In order to observe morphological and crystallinity changes, as well as changes in electrical properties of the Ag-NW networks during plasma treatment, operando GISAXS, GIWAXS and resistance measurements were carried out. The used measurement setup is illustrated in Fig. 3j. Further detailed experimental information is given in the experimental part and in the SI in Fig. S1.

GISAXS pattern of Ag-NW networks during atmospheric plasma treatment for exemplary treatment times are shown in Fig. 3a–d. The GISAXS pattern of the untreated Ag-NW network (Fig. 3a) is dominated by intensity streaks at around  $(36 \pm 2)^\circ$  starting from the direct beam as a consequence of the pentagonal shape of the Ag-NWs [15]. Upon plasma treatment the intensity of these streaks decreases monotonically. The streaks vanish completely after 8 s treatment time as shown in Fig. 3c and d. This indicates the rounding of the pentagonal Ag-NWs in the initial phase of the plasma treatment (phase I). Long treatment times (16 s – 26 s, Phase III) lead to melting, fragmentation, and degradation of the Ag-NWs as observed in Fig. 1, which is contributing to increased

diffuse scattering based on pronounced surface roughness as shown in Fig. 3d.

The reciprocal space maps (RSM) shown in Fig. 3e–h for different atmospheric plasma treatment times were obtained from the GIWAXS measurements. The original GIWAXS scattering patterns were transformed using the GIXSGUI [61] software. The pristine Ag-NW sample shown in Fig. 3e exhibit two anisotropic Bragg diffraction peaks stemming from X-ray diffraction at the characteristic face-centered-cubic (fcc) crystalline lattices of silver (111) and (200), respectively. After 6 s of atmospheric plasma treatment, the intensity of those two key features reduces gradually and the evolution of a crescent-like isotropic Bragg peak corresponding to the  $\text{Ag}_2\text{O}$  diffraction (see white arrow in Fig. 3f) can be observed. This observation indicates the more significant oxidation of Ag to  $\text{Ag}_2\text{O}$  in phase II in line with the XPS data (see Fig. 2 [62–64]).

In Fig. 3i, the extracted amplitudes (see Fig. S3 in the SI for details) representing the streak intensity and corresponding pentagonal shape of the Ag-NW from GISAXS (red), and the Bragg intensity corresponding to the  $\text{Ag}_2\text{O}$  signal obtained by GIWAXS (blue) of the Ag-NW sample upon atmospheric plasma treatment are shown. The extracted amplitudes are normalized to the maximum values, for GISAXS (0 s Fig. 3a) and GIWAXS (26 sec, Fig. 3h). In phase I rounding of the nanowires occurs resulting in a decrease of the GISAXS flare intensity with treatment time. These small changes in nanowire morphology as well as a weak oxidation (GIWAXS  $\text{Ag}_2\text{O}$ ) hardly affect the interconnectivity of the network and, thus, the electrical resistance (see Fig. 4f). The Bragg intensities for  $\text{Ag}_2\text{O}$  determined by GIWAXS (blue curve) follow a sigmoidal shape with only small changes in phase I, drastic changes in phase II, and attaining a saturation in phase III. Phase III represents the destructive melting and pronounced fragmentation of the Ag-NW network upon atmospheric plasma treatment (see Fig. 1). The XPS and GIWAXS data show that this phase is characterized by the enhanced oxidation of Ag to  $\text{Ag}_2\text{O}$ . The analyzed data show that the most relevant effect of the

atmospheric plasma treatment is the etching of the silver nanowires from the surface to the core and selective oxidation of the nanowires [65]. Since the nanowires are thoroughly washed and highly conductive (see experimental section), no notable influence of a ligand layer (PVP) can be observed. Thus, we do not observe any increase in conductivity for short plasma treatment times, which is typically observed to the removal of a PVP ligand shell [13,25].

#### 4. Electrical resistance & Monte Carlo simulation

The electrical behavior of Ag-NW networks can be simulated using a Monte Carlo method, in which the network resistance is calculated considering the tunnel resistances between the nanowires [16]. Fig. 4(a) shows the experimental radii of the Ag-NWs measured by SEM. The data are fitted using two Gaussian functions. In Fig. 4(b) the length distribution, also measured by SEM, is shown. Due to the high aspect ratio of the used nanowires, the lengths of the nanowires strongly dominate the network connectivity and the percolation threshold, while the exact thickness distribution of nanowires is not significant for the network. Atmospheric plasma etching, however, has a direct impact on the nanowires as shown earlier in the previous section. It can be assumed that the durability of a single nanowire during plasma treatment correlates strongly with its thickness. We, therefore, adopt a simplified model for simulating the electrical resistance of Ag-NW networks that is based on the lifetime of the nanowires during plasma treatment as a function of their thickness. For this, a constant plasma etching rate  $R_{\text{Etch}}$  is given, which indicates the etched mass of silver per unit of time  $t$  and sample area  $A_{\text{Sample}}$ . In order to calculate the life time of a wire upon plasma etching, a critical wire radius is required, from which the wire is counted as no longer functional. For the following simulation, the critical radii of all wires are assumed to be  $r_{i,\text{crit}} = 0.5r_{0,i}$  according to a critical mass of  $m_{i,\text{crit}} = 0.25m_{0,i} = 0.25\rho\pi r_{0,i}^2 \cdot L_i$ , where  $L_i$  is the length of wire  $i$  and  $r_{0,i}$  and  $m_{0,i}$  are the radius and mass of wire  $i$  at the time  $t =$

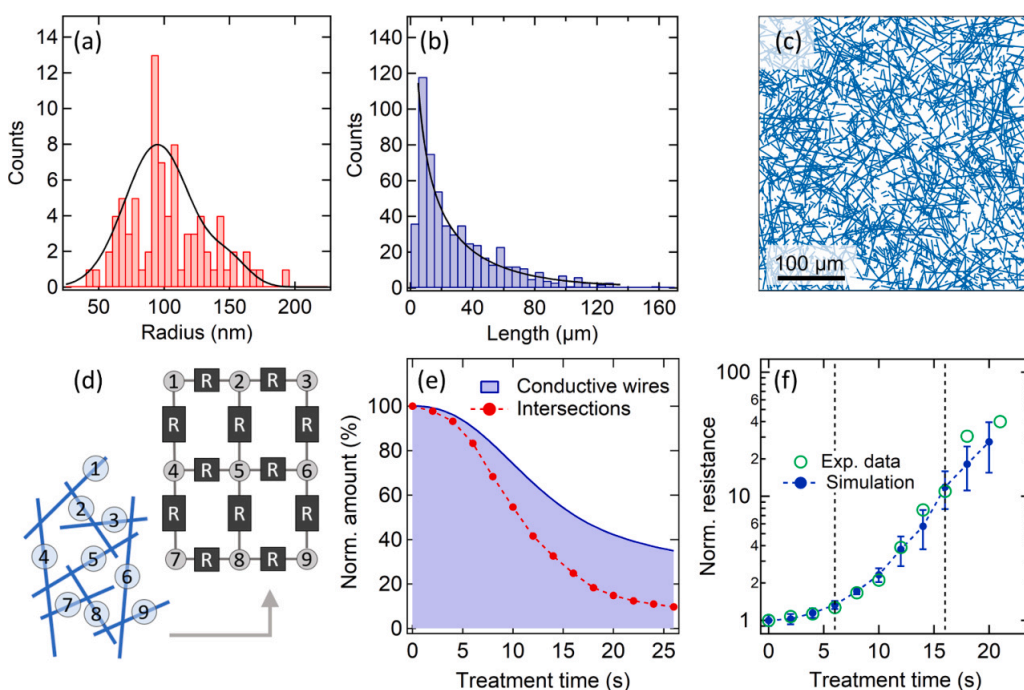


**Fig. 4.** (a) Radii of 83 Ag-NWs measured by SEM and represented as a histogram. The black solid line shows the sum of two Gaussian functions that were fitted to the data. (b) Length distribution of 564 Ag-NWs measured by SEM. The data was fitted by  $y_0 + A \exp(-(\ln(x/x_0) \cdot 1/\text{width})^2)$  (solid line). (c) Exemplary Monte Carlo simulated nanowire network with an effective concentration of  $11 \mu\text{g cm}^{-2}$  and a sample size of  $(400 \times 400) \mu\text{m}^2$ . The nanowire lengths correspond to the length distribution shown in (b). (d) Translation of a nanowire network (blue) into a resistor network (gray). Every wire is a node (circles), and every nanowire junction is a tunnel resistor (black squares). (e) Normalized number of intact wires (blue) and nanowire junctions (red) during plasma treatment obtained from Monte Carlo simulations for an etching rate of  $570 \text{ ng s}^{-1} \text{ cm}^{-2}$  and Ag-NW concentration of  $11 \mu\text{g cm}^{-2}$ . It is assumed that 28% of all wires are not affected by plasma etching. The number of intact wires as a function of plasma treatment time results directly from the radius distribution shown in (a). (f) Normalized resistance as a function of plasma treatment time. The

experimental data is shown in green and the simulated results are given in blue ( $n = 5$ ). The dashed lines denote the three characteristic plasma treatment phases. An etching rate of  $570 \text{ ng s}^{-1} \text{ cm}^{-2}$  was used with an effective Ag-NW concentration of  $11 \mu\text{g cm}^{-2}$ .

0, respectively. We also assume that each unit length element of the wires in the network is etched at the same rate. The rate for etching an individual wire can therefore be expressed as  $R_{Etch} \cdot A_{Sample} \cdot L_i L_{ges}^{-1}$ , where  $L_{ges}$  is the sum of the lengths of all wires. This leads to Eq. (1), which determines the critical live time of wire  $i$ .

$$t_{i,crit} = \frac{(m_{i,0} - m_{i,crit}) \cdot L_{ges}}{R_{Etch} \cdot L_i \cdot A_{Sample}} = \frac{0.75 \rho \pi r_{0,i}^2 \cdot L_{ges}}{R_{Etch} \cdot A_{Sample}} \quad (1)$$

Fig. 4(c) shows an exemplary Monte Carlo nanowire sample with an effective nanowire concentration of  $11 \mu\text{g cm}^{-2}$  and a sample size of  $(400 \times 400) \mu\text{m}^2$ . The effective concentration of nanowires, which contribute to the final network, is lower than the experimentally used concentration due to side products and the effective distribution of the nanowires [16]. In the case of drop-cast nanowires on a silicon surface, the effective concentration was found to be by a factor of around 2.4 lower than the experimental concentration. In addition to the nanowire lengths and concentration, the position and orientation of the nanowires are important parameters for defining a sample, as shown in Fig. 4(c). The positions are determined randomly within the size of the sample and the orientations are randomly distributed between  $-90^\circ$  and  $90^\circ$  in order to create an isotropic network. To determine the electrical network resistance, the nanowire networks have to be translated into resistor networks as illustrated in Fig. 4(d). For this, every wire is considered as a node and every wire junction presents a tunneling resistor with a unit resistance of  $r_{ij} = 1$  [16]. The resistance of a resistor network between two nodes can now be calculated as shown by F.Y. Wu [16,66].

Fig. 4(e) shows the normalized number of wires that were stable to the atmospheric plasma and the number of tunnel junctions within the network as a function of the plasma etch time. The number of intact wires as function of time results directly from the thickness distribution shown in Fig. 4(a). The presented simulation was carried out with an effective Ag-NW concentration of  $11 \mu\text{g cm}^{-2}$ , which corresponds to the used experimental concentration of  $26 \mu\text{g cm}^{-2}$ . In order to model the residual conductance in phase III, we assume that 28% of all wires remain conductive. The corresponding change in network resistances of the Ag-NW sample upon atmospheric plasma treatment together with the experimental data are shown in Fig. 4(f). By fitting the simulation results to the experimental data, an etching rate of  $570 \text{ ng s}^{-1} \text{ cm}^{-2}$  was found. For an exemplary nanowire with a mean radius of 100 nm and a mean length of  $25 \mu\text{m}$ , this etching rate corresponds to  $2.4 \cdot 10^9 \text{ atoms s}^{-1}$ . The simulated resistances and its error bars result from five Monte Carlo simulations ( $n = 5$ ).

Overall, we can identify three characteristic phases as indicated by nearly linear slopes on a logarithmic scale outlining exponential growths of the resistance as a function of plasma treatment time as highlighted in Fig. 4f. The initial phase I with relatively small resistance changes lasting until 6 s and exhibits a typical slope of the order of  $\Omega \text{ s}^{-1}$ . In phase II the resistance change upon plasma pen treatment time is approximately one order of magnitude larger than in phase I. Thus, in phase I and phase II it is possible to build a voltage divider with an exemplary voltage ratio of  $U_{in}:U_{out} = 3:2$  after 10 s treatment. After 16 s of atmospheric plasma treatment (phase III), an extreme increase in resistance can be observed, leading to a nearly infinite resistance and subsequent breakdown and failure of the Ag-NW network for treatment times beyond 26 s. The theoretical data show a strong match with the experiment for the analyzed resistance of the Ag-NW networks. The ultra-fast fragmentation and degradation observed in the giant resistance with the longer treatment at time scale above 16 s is attributed to aggressive etching mechanism induced by the reactive oxygen species (ROS) generated by the plasma during the treatment.

## 5. Conclusions

The effect of atmospheric plasma treatment on the electrical and

structural properties of highly conductive silver-nanowire (Ag-NW) networks as a function of treatment time was investigated. The results obtained provide a strong correlation between the changes in electrical resistance of the Ag-NW networks during plasma treatment and the selective oxidation of the Ag-NWs as well as the morphological network changes. Phase I (0 s to 6 s atmospheric plasma treatment) is characterized by the rounding of the pentagonal nanowires and by small and controlled changes in resistance. XPS and GIWAXS data confirm a pronounced evolution of silver oxide ( $\text{Ag}_2\text{O}$ ) in phase II (6 s to 16 s atmospheric plasma treatment), which is correlated with drastic but controllable resistance changes. Thus, phase I and II allow a controlled manipulation of the network resistance with an exponential dependence between resistance and atmospheric plasma treatment time with different rates of resistance change upon etching. After 16 s, phase III leads to an enhanced oxidation, fragmentation, and destruction of the Ag-NW network as validated by FESEM, XPS, GIWAXS and GISAXS. For the presented study, Ag-NWs were thoroughly washed before use leading to a nearly ligand free suspension and correspondingly low resistances of the untreated samples. We, therefore, observe no decrease in resistance upon plasma treatment according to a removal of an isolating ligand shell. In contrast, we initiate a controlled oxidation of our wires and offer an alternative approach to manipulate the local resistance of Ag-NW networks at a controllable rate for technological applications such as sensors, transparent electrodes, and integrated circuits. We simulate the electrical properties of the investigated nanowire networks upon plasma etching by a Monte Carlo method resulting in a physical model explaining the dependence between network resistance, connectivity, and etching rate.

## Author contributions

MS, LOA, TEG, SVR and MR designed the study and supervised the project. MB, LOA, and TEG fabricated the samples. MB, TEG, MS, MG, BG-L, LOA, SVR and MR conceived the experiment and facilitated the *in situ* conductivity setup. MB, LOA, MS, MG, and AC conducted the GIWAXS and GISAXS measurements. XPS measurements and data analysis were done by MN, IB and MM. SS, CN and LOA carried out FESEM studies on the samples. TEM studies and analysis were done by US, TD, and LK. MW and FF conducted FINE analysis. TEG conducted the Monte Carlo simulations. TEG, LOA and MR analyzed the data and wrote the manuscript. All authors contributed to the preparation of the manuscript. All authors have approved the final version of the manuscript.

## Funding

This work was supported by the Deutsche Forschungsgemeinschaft (DFG, German Research Foundation; grant number MA2561/6-1) and the Helmholtz society through DESY. This work was funded by the BMBF via 05K19GU5.

## Declaration of Competing Interest

The authors declare no competing financial or conflict of interest.

## Acknowledgements

The authors would like to thank Jan Rubeck, Anca Ciobanu, Milena Lippmann and André Rothkirch (DESY, Hamburg) and Stephan Martens (Universität Hamburg) for the technical support and helpful discussions. We are further thankful to Nils Huse and Robert Frömter for the usage of their scanning electron microscopes. We thank Christin Szillus for the ultramicrotome preparation of the TEM cross-sections of the pentagonal silver nanowires.



## Appendix A. Supplementary material

Supplementary data to this article can be found online at <https://doi.org/10.1016/j.apsusc.2021.149362>.

## References

- [1] M.C. Daniel, D. Astruc, Gold nanoparticles: assembly, supramolecular chemistry, quantum-size-related properties, and applications toward biology, catalysis, and nanotechnology, *Chem. Rev.* 104 (2004) 293–346, <https://doi.org/10.1021/cr030698t>.
- [2] Y. Xia, Y. Xiong, B. Lim, S. Skrabalak, Shape-controlled synthesis of metal nanocrystals: Simple chemistry meets complex physics? *Angew. Chemie - Int. Ed.* 48 (1) (2009) 60–103, <https://doi.org/10.1002/anie.200802248>.
- [3] F. Faupel, V. Zaporozhchenko, T. Strunskus, M. Elbahri, Metal-polymer nanocomposites for functional applications, *Adv. Eng. Mater.* 12 (12) (2010) 1177–1190, <https://doi.org/10.1002/adem.201000231>.
- [4] H. Yang, Y. Wang, X. Chen, X. Zhao, L. Gu, H. Huang, J. Yan, C. Xu, G. Li, J. Wu, A. J. Edwards, B. Dittrich, Z. Tang, D. Wang, L. Lehtovaara, H. Häkkinen, N. Zheng, Plasmonic twinned silver nanoparticles with molecular precision, *Nat. Commun.* 7 (2016) 1–8, <https://doi.org/10.1038/ncomms12809>.
- [5] Y. Sun, Y. Yin, B.T. Mayers, T. Herricks, Y. Xia, Uniform silver nanowires synthesis by reducing AgNO<sub>3</sub> with ethylene glycol in the presence of seeds and poly(vinyl pyrrolidone), *Chem. Mater.* 14 (11) (2002) 4736–4745, <https://doi.org/10.1021/cm020587b>.
- [6] D.S. Hecht, L. Hu, G. Irvin, Emerging transparent electrodes based on thin films of carbon nanotubes, graphene, and metallic nanostructures, *Adv. Mater.* 23 (13) (2011) 1482–1513, <https://doi.org/10.1002/adma.201003188>.
- [7] A. Kim, Y. Won, K. Woo, S. Jeong, J. Moon, All-solution-processed indium-free transparent composite electrodes based on Ag nanowire and metal oxide for thin-film solar cells, *Adv. Funct. Mater.* 24 (17) (2014) 2462–2471, <https://doi.org/10.1002/adfm.201303518>.
- [8] S. De, T.M. Higgins, P.E. Lyons, E.M. Doherty, P.N. Nirmalraj, W.J. Blau, J. Boland, J.N. Coleman, Silver nanowire networks as flexible, transparent, conducting films: extremely high DC to optical conductivity ratios, *ACS Nano* 3 (7) (2009) 1767–1774, <https://doi.org/10.1021/nn900348c>.
- [9] E. Braun, Y. Eichen, U. Sivan, G. Ben-Yoseph, DNA-templated assembly and electrode attachment of a conducting silver wire, *Nature* 391 (6669) (1998) 775–778, <https://doi.org/10.1038/35826>.
- [10] Y. Kim, J.W. Kim, Silver nanowire networks embedded in urethane acrylate for flexible capacitive touch sensor, *Appl. Surf. Sci.* 363 (2016) 1–6, <https://doi.org/10.1016/j.apsusc.2015.11.052>.
- [11] B. Yoo, Y. Kim, C.J. Han, M.S. Oh, J.W. Kim, Recyclable patterning of silver nanowire percolated network for fabrication of flexible transparent electrode, *Appl. Surf. Sci.* 429 (2018) 151–157, <https://doi.org/10.1016/j.apsusc.2017.07.285>.
- [12] C. Mayousse, C. Celle, A. Fraczkiewicz, J.-P. Simonato, Stability of silver nanowire based electrodes under environmental and electrical stresses, *Nanoscale*. 7 (5) (2015) 2107–2115, <https://doi.org/10.1039/C4NR06783E>.
- [13] D.G. Kim, J. Kim, S.B. Jung, Y.S. Kim, J.W. Kim, Electrically and mechanically enhanced Ag nanowires-colorless polyimide composite electrode for flexible capacitive sensor, *Appl. Surf. Sci.* 380 (2016) 223–228, <https://doi.org/10.1016/j.apsusc.2016.01.130>.
- [14] G. Deignan, I.A. Goldthorpe, The dependence of silver nanowire stability on network composition and processing parameters, *RSC Adv.* 7 (57) (2017) 35590–35597, <https://doi.org/10.1039/C7RA06524H>.
- [15] T.E. Glier, L. Akinsinde, M. Paufler, F. Otto, M. Hashemi, L. Grote, L. Daams, G. Neuber, B. Grimm-Lebsanft, F. Biebl, D. Rukser, M. Lippmann, W. Ohm, M. Schwartzkopf, C.J. Brett, T. Matsuyama, S.V. Roth, M. Rübhausen, Functional printing of conductive silver-nanowire photopolymer composites, *Sci. Rep.* 9 (2019) 6465, <https://doi.org/10.1038/s41598-019-42841-3>.
- [16] T.E. Glier, M. Betker, M. Witte, T. Matsuyama, L. Westphal, B. Grimm-Lebsanft, F. Biebl, L.O. Akinsinde, F. Fischer, M. Rübhausen, Electrical and network properties of flexible silver-nanowire composite electrodes under mechanical strain, *Nanoscale*. 12 (46) (2020) 23831–23837, <https://doi.org/10.1039/D0NR05734G>.
- [17] Y. Sun, B. Mayers, T. Herricks, Y. Xia, Polyol synthesis of uniform silver nanowires: a plausible growth mechanism and the supporting evidence, *Nano Lett.* 3 (2003) 955–960, <https://doi.org/10.1021/nl034312m>.
- [18] S.H. Park, M.W. Prior, T.H. LaBean, G. Finkelstein, Optimized fabrication and electrical analysis of silver nanowires templated on DNA molecules, *Appl. Phys. Lett.* 89 (2006) 2004–2007, <https://doi.org/10.1063/1.2234282>.
- [19] J. Chen, B.J. Wiley, Y. Xia, One-dimensional nanostructures of metals: Large-scale synthesis and some potential applications, *Langmuir* 23 (2007) 4120–4129, <https://doi.org/10.1021/la063193y>.
- [20] F. Fievet, J.P. Lagier, M. Figlarz, Preparing monodisperse metal powders in micrometer and submicrometer sizes by the polyol process, *MRS Bull.* 14 (12) (1989) 29–34, <https://doi.org/10.1557/S0883769400060930>.
- [21] K.E. Korte, S.E. Skrabalak, Y. Xia, Rapid synthesis of silver nanowires through a CuCl- or CuCl<sub>2</sub>-mediated polyol process, *J. Mater. Chem.* 18 (4) (2008) 437–441, <https://doi.org/10.1039/B714072J>.
- [22] L.D. Marks, Experimental studies of small particle structures, *Reports Prog. Phys.* 57 (6) (1994) 603–649, <https://doi.org/10.1088/0034-4885/57/6/002>.
- [23] X. Tang, M. Tsuji, Syntheses of Silver Nanowires in Liquid Phase, in: *Nanowires Sci. Technol.*, InTech, 2010. <https://doi.org/10.5772/39491>.
- [24] S. Coskun, B. Aksoy, H.E. Unalan, Polyol synthesis of silver nanowires: An extensive parametric study, *Cryst. Growth Des.* 11 (11) (2011) 4963–4969, <https://doi.org/10.1021/cg200874g>.
- [25] J. Li, Y. Tao, S. Chen, H. Li, P. Chen, M.Z. Wei, H. Wang, K. Li, M. Mazzeo, Y. Duan, A flexible plasma-treated silver-nanowire electrode for organic light-emitting devices, *Sci. Rep.* 7 (2017) 1–9, <https://doi.org/10.1038/s41598-017-16721-7>.
- [26] D.C. Choo, T.W. Kim, Degradation mechanisms of silver nanowire electrodes under ultraviolet irradiation and heat treatment, *Sci. Rep.* 7 (2017) 1–12, <https://doi.org/10.1038/s41598-017-01843-9>.
- [27] H.H. Khaligh, I.A. Goldthorpe, Failure of silver nanowire transparent electrodes under current flow, *Nanoscale Res. Lett.* 8 (2013) 2–7, <https://doi.org/10.1186/1556-276x-8-235>.
- [28] T. Sannicolo, N. Charvin, L. Flandin, S. Kraus, D.T. Papanastasiou, C. Celle, J.P. Simonato, D. Muñoz-Rojas, C. Jiménez, D. Bellet, Electrical Mapping of Silver Nanowire Networks: A Versatile Tool for Imaging Network Homogeneity and Degradation Dynamics during Failure, *ACS Nano*. 12 (2018) 4648–4659, <https://doi.org/10.1021/acsnano.8b01242>.
- [29] J. Jiu, J. Wang, T. Sugahara, S. Nagao, M. Nogi, H. Koga, K. Sugauma, M. Hara, E. Nakazawa, H. Uchida, The effect of light and humidity on the stability of silver nanowire transparent electrodes, *RSC Adv.* 5 (35) (2015) 27657–27664, <https://doi.org/10.1039/C5RA02722E>.
- [30] J.L. Elechiguerra, L. Larios-Lopez, C. Liu, D. Garcia-Gutierrez, A. Camacho-Bragado, M.J. Yacamán, Corrosion at the nanoscale: The case of silver nanowires and nanoparticles, *Chem. Mater.* 17 (2005) 6042–6052, <https://doi.org/10.1021/cm051532n>.
- [31] A. Kuzminova, T. Kretková, O. Klyán, J. Hanuš, I. Khalakhan, V. Prukner, E. Doležalová, M. Šimek, H. Biederman, Etching of polymers, proteins and bacterial spores by atmospheric pressure DBD plasma in air, *J. Phys. D. Appl. Phys.* 50 (13) (2017) 135201, <https://doi.org/10.1088/1361-6463/aa5c21>.
- [32] G. Bauer, D. Sersenová, D.B. Graves, Z. Machala, Cold atmospheric plasma and plasma-activated medium trigger RONS-based tumor cell apoptosis, *Sci. Rep.* 9 (2019) 1–28, <https://doi.org/10.1038/s41598-019-50291-0>.
- [33] A. Sonawane, M.A. Mujawar, S. Bhansali, Effects of cold atmospheric plasma treatment on the morphological and optical properties of plasmonic silver nanoparticles, *Nanotechnology*. 31 (36) (2020) 365706, <https://doi.org/10.1088/1361-6528/ab9788>.
- [34] I.-M. Chan, W.-C. Cheng, F.C. Hong, Enhanced performance of organic light-emitting devices by atmospheric plasma treatment of indium tin oxide surfaces, *Appl. Phys. Lett.* 80 (1) (2002) 13–15, <https://doi.org/10.1063/1.1428624>.
- [35] C. Tendero, C. Tixier, P. Tristant, J. Desmaison, P. Leprince, Atmospheric pressure plasmas: a review, *Spectrochim. Acta Part B*. 61 (2006) 2–30, <https://doi.org/10.1016/j.sab.2005.10.003>.
- [36] W. Kern, Evolution of silicon wafer cleaning technology, *Proc. - Electrochem. Soc.* 90 (1990) 3–19.
- [37] Plasma Etch, Inc., (n.d.). <https://www.plasmaetch.com/atmospheric-plasma-wafer-cleaner.php>.
- [38] A. Buffet, A. Rothkirch, R. Döhrmann, V. Körstgens, M.M. Abul Kashem, J. Perlich, G. Herzog, M. Schwartzkopf, R. Gehrke, P. Müller-Buschbaum, S.V. Roth, P03, the microfocus and nanofocus X-ray scattering (MiNaXS) beamline of the PETRA III storage ring: the microfocus endstation, *J. Synchrotron Radiat.* 19 (4) (2012) 647–653, <https://doi.org/10.1107/S0909049512016895>.
- [39] M. Gensch, M. Schwartzkopf, W. Ohm, C.J. Brett, P. Pandit, S.K. Vayalil, L. Bießmann, L.P. Kreuzer, J. Drewes, O. Polonskyi, T. Strunskus, F. Faupel, A. Stierle, P. Müller-Buschbaum, S.V. Roth, Correlating nanostructure, optical and electronic properties of nanogranular silver layers during polymer-templated-assisted sputter deposition, *ACS Appl. Mater. Interfaces*. 11 (32) (2019) 29416–29426, <https://doi.org/10.1021/acsami.9b08594>.
- [40] J. Li, S.L. Zhang, Finite-size scaling in stick percolation, *Phys. Rev. E - Stat. Nonlinear, Soft Matter Phys.* 80 (2009) 1–4, <https://doi.org/10.1103/PhysRevE.80.040104>.
- [41] S.M. Bergin, Y.H. Chen, A.R. Rathmell, P. Charbonneau, Z.Y. Li, B.J. Wiley, The effect of nanowire length and diameter on the properties of transparent, conducting nanowire films, *Nanoscale*. 4 (2012) 1996–2004, <https://doi.org/10.1039/c2nr30126a>.
- [42] M. Marus, A. Hubarevich, R.J.W. Lim, H. Huang, A. Smirnov, H. Wang, W. Fan, X. W. Sun, Effect of silver nanowire length in a broad range on optical and electrical properties as a transparent conductive film, *Opt. Mater. Express*. 7 (3) (2017) 1105, <https://doi.org/10.1364/OME.7.001105>.
- [43] M. Witte, S. Jaspers, H. Wenck, M. Rübhausen, F. Fischer, Noise reduction and quantification of fiber orientations in greyscale images, *PLoS One*. 15 (2020) 1–21, <https://doi.org/10.1371/journal.pone.0227534>.
- [44] M. Witte, S. Jaspers, H. Wenck, M. Rübhausen, F. Fischer, General method for classification of fiber families in fiber-reinforced materials: application to in-vivo human skin images, *Sci. Rep.* 10 (2020) 1–11, <https://doi.org/10.1038/s41598-020-67632-z>.
- [45] A.M. Ferraria, A.P. Carapeto, A.M. Botelho do Rego, X-ray photoelectron spectroscopy: silver salts revisited, *Vacuum* 86 (12) (2012) 1988–1991, <https://doi.org/10.1016/j.vacuum.2012.05.031>.
- [46] Z. Hui, Y. Liu, W. Guo, L. Li, N. Mu, C. Jin, Y. Zhu, P. Peng, Chemical sintering of direct-written silver nanowire flexible electrodes under room temperature, *Nanotechnology*. 28 (28) (2017) 285703, <https://doi.org/10.1088/1361-6528/aa76ce>.
- [47] J. Zhang, Y. Li, B.o. Wang, H. Hu, B. Wei, L. Yang, High brightness organic light-emitting diodes with capillary-welded hybrid diameter silver nanowire/graphene

- layers as electrodes, *Micromachines*. 10 (8) (2019) 517, <https://doi.org/10.3390/mi10080517>.
- [48] Thermo Scientific, XPS Database, (n.d.). <https://xpsimplified.com/elements/oxygen.php>.
- [49] L.Q. Zhou, C. Ling, M. Jones, H. Jia, Selective CO<sub>2</sub> reduction on a polycrystalline Ag electrode enhanced by anodization treatment, *Chem. Commun.* 51 (100) (2015) 17704–17707, <https://doi.org/10.1039/C5CC06752A>.
- [50] N.J. Firet, M.A. Blommaert, T. Burdyny, A. Venugopal, D. Bohra, A. Longo, W. A. Smith, Operando EXAFS study reveals presence of oxygen in oxide-derived silver catalysts for electrochemical CO<sub>2</sub> reduction, *J. Mater. Chem. A*. 7 (6) (2019) 2597–2607, <https://doi.org/10.1039/C8TA10412C>.
- [51] G. Beamson, D. Briggs, High-Resolution XPS of Organic Polymers: The Scienta ESCA300 Database, WILEY, Chichester (England); New York, 1993. <https://doi.org/10.1021/ed070pA25.5>.
- [52] X. Kong, D. Castarède, A. Boucly, L. Artiglia, M. Ammann, T. Bartels-Rausch, E. S. Thomson, J.B.C. Pettersson, Reversibly physisorbed and chemisorbed water on carboxylic salt surfaces under atmospheric conditions, *J. Phys. Chem. C*. 124 (9) (2020) 5263–5269, <https://doi.org/10.1021/acs.jpcc.0c00319>.
- [53] X-ray Photoelectron Spectroscopy (XPS) Reference Pages, (n.d.). <http://www.xpsfitting.com/2013/08/oxygen-1s-for-organic-compounds.html>.
- [54] Y. Wu, P. Jiang, M. Jiang, T.-W. Wang, C.-F. Guo, S.-S. Xie, Z.-L. Wang, The shape evolution of gold seeds and gold@silver core-shell nanostructures, *Nanotechnology*. 20 (30) (2009) 305602, <https://doi.org/10.1088/0957-4484/20/30/305602>.
- [55] W. Wei, X. Mao, L.A. Ortiz, D.R. Sadoway, Oriented silver oxide nanostructures synthesized through a template-free electrochemical route, *J. Mater. Chem.* 21 (2) (2011) 432–438, <https://doi.org/10.1039/C0JM02214D>.
- [56] J.A. McMillan, Magnetic properties and crystalline structure of AgO, *J. Inorg. Nucl. Chem.* 13 (1-2) (1960) 28–31, [https://doi.org/10.1016/0022-1902\(60\)80231-X](https://doi.org/10.1016/0022-1902(60)80231-X).
- [57] G. Santoro, S. Yu, M. Schwartzkopf, P. Zhang, S. Koyiloth Vayalil, J.F.H. Risch, M. A. Rübhausen, M. Hernández, C. Domingo, S.V. Roth, Silver substrates for surface-enhanced Raman scattering: correlation between nanostructure and Raman scattering enhancement, *Appl. Phys. Lett.* 104 (24) (2014) 243107, <https://doi.org/10.1063/1.4884423>.
- [58] S.V. Roth, G. Herzog, V. Körstgens, A. Buffet, M. Schwartzkopf, J. Perlich, M. M. Abul Kashem, R. Döhrmann, R. Gehrke, A. Rothkirch, K. Stassig, W. Wurth, G. Benecke, C. Li, P. Fratzl, M. Rawolle, P. Müller-Buschbaum, In situ observation of cluster formation during nanoparticle solution casting on a colloidal film, *J. Phys. Condens. Matter*. 23 (25) (2011) 254208, <https://doi.org/10.1088/0953-8984/23/25/254208>.
- [59] C.J. Brett, S. Montani, M. Schwartzkopf, R.A.T.M. van Benthem, J.F.G.A. Jansen, G. Griffini, S.V. Roth, M.K.G. Johansson, Revealing structural evolution occurring from photo-initiated polymer network formation, *Commun. Chem.* 3 (2020) 1–7, <https://doi.org/10.1038/s42004-020-0335-9>.
- [60] M. Witte, S. Jaspers, H. Wenck, M. Rübhausen, F. Fischer, Noise reduction and quantification of fiber orientations in greyscale images, *PLoS One*. 15 (2020) 1–21. <https://doi.org/10.1371/journal.pone.0227534>.
- [61] Z. Jiang, GIXSGUI: A MATLAB toolbox for grazing-incidence X-ray scattering data visualization and reduction, and indexing of buried three-dimensional periodic nanostructured films, *J. Appl. Crystallogr.* 48 (2015) 917–926, <https://doi.org/10.1107/S1600576715004434>.
- [62] P. Norby, R. Dinnebier, A.N. Fitch, Decomposition of silver carbonate; the crystal structure of two high-temperature modifications of Ag<sub>2</sub>CO<sub>3</sub>, *Inorg. Chem.* 41 (14) (2002) 3628–3637, <https://doi.org/10.1021/ic0111177>.
- [63] A. Werner, H.D. Hochheimer, High-pressure X-ray study of Cu<sub>2</sub>O and Ag<sub>2</sub>O, *Phys. Rev. B - Condens. Matter Mater. Phys.* 2 (1982) 2–7.
- [64] T. Wada, T. Sakuma, R. Sakai, H. Uehara, Xianglian, H. Takahashi, O. Kamishima, N. Igawa, S.A. Danilkin, Inter-atomic force constants of Ag<sub>2</sub>O from diffuse neutron scattering measurement, *Solid State Ionics* 225 (2012) 18–21, <https://doi.org/10.1016/j.ssi.2012.02.007>.
- [65] H. Seidel, L. Csepregi, A. Heuberger, H. Baumgärtel, Anisotropic etching of crystalline silicon in alkaline solutions: I. Orientation dependence and behavior of passivation layers, *J. Electrochem. Soc.* 137 (11) (1990) 3612–3626, <https://doi.org/10.1149/1.2086277>.
- [66] F.Y. Wu, Theory of resistor networks: The two-point resistance, Exactly Solved Model. *A Journey Stat. Mech. Sel. Pap. with Comment.* (2009) 489–509. <https://doi.org/10.1088/0305-4470/37/26/004>.



## Paper V

# Resistivity response to stress and strain of a flexible $\text{Bi}_2\text{Te}_3$ based thermoelectric material

Lewis Olaniyi Akinsinde\*, **Sarah Scheitz**, L. Zimoch, J. K. Sierck, Leonard Siebert, R. Adelong, Ulrich Schürmann, Michael Rübhausen, Torben Dankwort, and Lorenz Kienle

Published in: I. Tiginyanu et al. (eds.), 4th International Conference on Nanotechnologies and Biomedical Engineering - 18 September 2019  
[https://doi.org/10.1007/978-3-030-31866-6\\_12](https://doi.org/10.1007/978-3-030-31866-6_12)

Reprinted with permission from L. O. Akinsinde, S. Scheitz, L.Zimoch et al., *4th International Conference on Nanotechnologies and Biomedical Engineering*, **2020**, Springer International Publishing, IFMBE Proceedings Vol.77, 57-60. Copyright 2020 Springer Nature Switzerland AG.



# Resistivity Response to Stress and Strain of a Flexible Bi<sub>2</sub>Te<sub>3</sub> Based Thermoelectric Material

L. O. Akinsinde, S. Scheitz, L. Zimoch, J. K. Sierck, L. Siebert, R. Adelung, U. Schürmann, M. A. Rübhausen, T. Dankwort, and L. Kienle

## Abstract

Here we report about the synthesis of Bi<sub>2</sub>Te<sub>3</sub> based flexible thermoelectric materials and the response of the electrical resistivity to tensile and compressive stress. As a template fiber spun polymers have been used onto which a thin composite film of graphene and Bi<sub>2</sub>Te<sub>3</sub> nanoplates was deposited. The Bi<sub>2</sub>Te<sub>3</sub> nanoplates were synthesized using the polyol method. Upon straining the material, the resistivity dropped which is attributed to the increased contact between the individual wires.

## Keywords

Bi<sub>2</sub>Te<sub>3</sub> • Flexible thermoelectric materials • Composite materials • Polyol process • Wet chemical method • Polymer fibers

## 1 Introduction

Bismuth Telluride (Bi<sub>2</sub>Te<sub>3</sub>), belonging to the chalcogenide-based thermoelectrics is well known for its high efficiency with respect to room temperature applications [1–3]. To obtain thermoelectric devices, conventional high temperature synthesis routes are used. Afterwards the material is ball milled to obtain powders, which in a consecutive step are sintered and compacted to obtain thermoelectric legs [4, 5]. Thus, the processing is technically costly and time consuming. An alternative synthesis route was found using wet chemical approaches. With the polyol method [6], it was

possible to grow nanoplates (nanoflakes) of various relevant thermoelectric materials [7, 8] including Bi<sub>2</sub>Te<sub>3</sub> [9] at moderate temperatures. The obtained materials can be dried and sintered [10]. However, thermoelectric generators (TEGs) using sintered Bi<sub>2</sub>Te<sub>3</sub> thermoelectric legs are brittle which limits the applicability of these generators. In recent years, flexible TEGs have been designed using e.g. Bi<sub>2</sub>Te<sub>3</sub> suspensions, which were deposited on various types of flexible substrate materials [11, 12]. These types of thermoelectric materials have also attracted attention as self-powered pressure and temperature sensors [13].

In this contribution, we report about the synthesis of Bi<sub>2</sub>Te<sub>3</sub> nanoplates and an infiltration method using these nanoplates to obtain flexible thermoelectric materials. As a template fiber spun polymers have been used. To enhance the conductivity and facilitate sticking of the Bi<sub>2</sub>Te<sub>3</sub> nanoplates, graphene has been introduced. Furthermore, the response of the electrical resistivity to external stress and strain was investigated.

## 2 Experimental

The synthesis of stoichiometric single crystalline Bi<sub>2</sub>Te<sub>3</sub> nanoplates was carried out via a simple wet chemical polyol method. The high-quality grade precursors used were purchased from Sigma Aldrich. To achieve an ideal stoichiometric Bi:Te ratio of 2:3 chemicals are weighted to 485 mg of Bi(NO<sub>3</sub>) \* 5H<sub>2</sub>O (98%, Sigma Aldrich), 0.5 g of polyvinylpyrrolidone (PVP) (30 K, Roth), 415 mg K<sub>2</sub>TeO<sub>3</sub> \* H<sub>2</sub>O (97%, Alfa Aesar), 0.4 g NaOH (98%, Merck) and 50 ml of Ethylene glycol (EG) (>99.5%, Roth). The salts as well as the surfactants are dissolved in EG in a glass beaker on a hot plate set at a temperature of 65 °C while slightly stirring the mixture. The dissolved solution was then transferred via a long funnel into a three-neck round bottom flask connected to a water-cooled reflux. The flask remained closed during the entire synthesis with septum. The solution was stirred at 450 rpm with a Teflon bar and slowly heated

L. O. Akinsinde · S. Scheitz · M. A. Rübhausen  
Center for Free Electron Laser Science (CFEL), Institute for Nanostructures and Solid State Physics (INF), University of Hamburg, Luruper Chaussee 149, 22761 Hamburg, Germany

L. Zimoch · J. K. Sierck · L. Siebert · R. Adelung · U. Schürmann · T. Dankwort (✉) · L. Kienle  
Institute for Materials Science, Kiel University, Kaiserstrasse 2, Kiel, Germany  
e-mail: [td@tf.uni-kiel.de](mailto:td@tf.uni-kiel.de)

© Springer Nature Switzerland AG 2020

I. Tiginyanu et al. (eds.), *4th International Conference on Nanotechnologies and Biomedical Engineering*, IFMBE Proceedings 77, [https://doi.org/10.1007/978-3-030-31866-6\\_12](https://doi.org/10.1007/978-3-030-31866-6_12)

57

to allow the substance to mix homogeneously. This procedure further ensures proper nucleation of the seeds that later grow to form the nanoplates. After a duration of roughly 10 min, the solution reached the preset temperature of 180 °C and turned to a black color. The nanoplates were allowed to grow at 180 °C for 22 h. The solution was left to cool down to room temperature. Apparently, small black precipitates have formed. The isolation of the  $\text{Bi}_2\text{Te}_3$  precipitates was achieved through centrifugation in acetone and isopropanol to remove the core-shell-like structures of the residual PVP as well as EG from the synthesis and then stored inside a vial. The  $\text{Bi}_2\text{Te}_3$  nanoplates are dispersed in high purity isopropanol to avoid the agglomeration of the nanoplates.

In order to obtain a macroscopic flexible thermoelectric device, graphene-coated polymer composite fiber mesh was adopted and infiltrated with the  $\text{Bi}_2\text{Te}_3$  nanoplates. The infiltration of the fiber mesh consisting of Polycaprolactone (PCL) template with  $\text{Bi}_2\text{Te}_3$  nanoplates was achieved by dip-coating (soaking) simultaneously different fiber-meshes in 5 ml solution of  $\text{Bi}_2\text{Te}_3$  and Isopropanol for 24 h as well as 48 h under ambient conditions.

The morphology, shape and degree of infiltration of the samples were investigated using a commercial field emission scanning electron microscopy (FE-SEM), Sigma from Zeiss Company, Germany.

Nanostructural investigation were performed using a transmission electron microscope (TEM), FEI Tecnai F30 G<sup>2</sup> STwin equipped with an 300 kV field emission gun.

A custom-build setup was used to validate the electrical response of each sample, which allows to apply stress and strain to the sample while simultaneously measure the resistivity changes. Therefore, a constant DC-voltage was applied, and the electrical conductivity measured. According to ohm's law the resistivity was calculated. Further, the applied stress was measured with a load cell.

### 3 Results and Discussion

Nanoplates of  $\text{Bi}_2\text{Te}_3$  were synthesized by a reduction of a stoichiometric mixture in EG in the presence of PVP. PVP is very important due to its function as a capping agent as well as a trigger for crystal growth, i.e., it facilitates a uniform uniaxial growth [14–16]. More to this, PVP bonds to the polar basal planes of the crystal structure of  $\text{Bi}_2\text{Te}_3$  and suppresses the growth dynamic of the crystals in the *c*-axis direction [16]. The thin PVP core-shell layer is determined to be in the range of 2–5 nm and is mostly not completely removed through centrifugation. A complete PVP removal is detrimental and might be achieved at the expense of the  $\text{Bi}_2\text{Te}_3$  nanoplate being partly etched during the process. The transition between PVP- $\text{Bi}_2\text{Te}_3$  nanoplate is not readily determined.

To investigate the nanostructure of the  $\text{Bi}_2\text{Te}_3$  nanoplates TEM was used. Figure 1 depicts representative nanoplates of  $\text{Bi}_2\text{Te}_3$ . The different nanoplates extend over 3–5 micrometers, while their thickness is in the range of a few nanometers. Further, large particles are often decorated with smaller particles as also depicted in Fig. 1. The nanoplates were crystalline and exhibit rotational disordering [14, 15], thus the zone axis varies within a few nanometers and produces characteristic diffraction contrast (not shown here). This observation might be the result of a screw dislocation promoted growth [16].

Electron diffraction (ED) patterns in zone axis [001] exhibited additional reflections (not shown here), which indicates a lowering of the symmetry. Thus, it was concluded that due to slight variation in the stoichiometry a transition from *R*-3*m* to *P*-3*m*1 crystal structure is observed.

The HRTEM micrograph and corresponding Fourier Transform (FFT) in Fig. 1 highlight rotational disorder resulting in weak satellite reflections (marked in yellow) in the FFT and pronounced Moiré contrast.

The chemical composition of the nanoplates was characterized using energy dispersive X-ray spectroscopy (EDX) in scanning TEM mode. It was observed, that the stoichiometry slightly deviates from the ideal ratio of Bi:Te = 2:3. In our system the ratio was found to be 1.8:3.2, thus this deviation presumably might be attributed to impurities in the system.

The obtained nanoplates were deposited on a graphene-coated PCL fiber mesh. FESEM images (Fig. 2), revealed a strong adhesion of the  $\text{Bi}_2\text{Te}_3$  nanoplates on the coated fiber-meshes as seen in the long percolation network

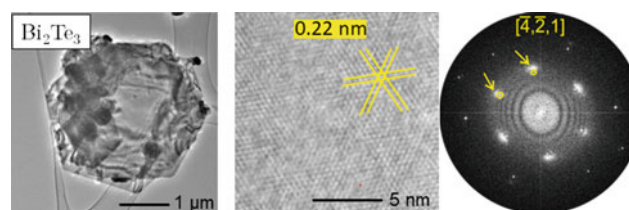


**Fig. 1** Bright field image, HRTEM micrograph and corresponding FFT of a  $\text{Bi}_2\text{Te}_3$  flake in zone axis  $[-4-21]$ . In the FFT satellite reflections are observed which can be attributed to rotational disorder

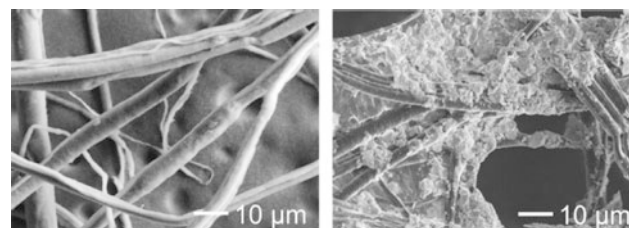


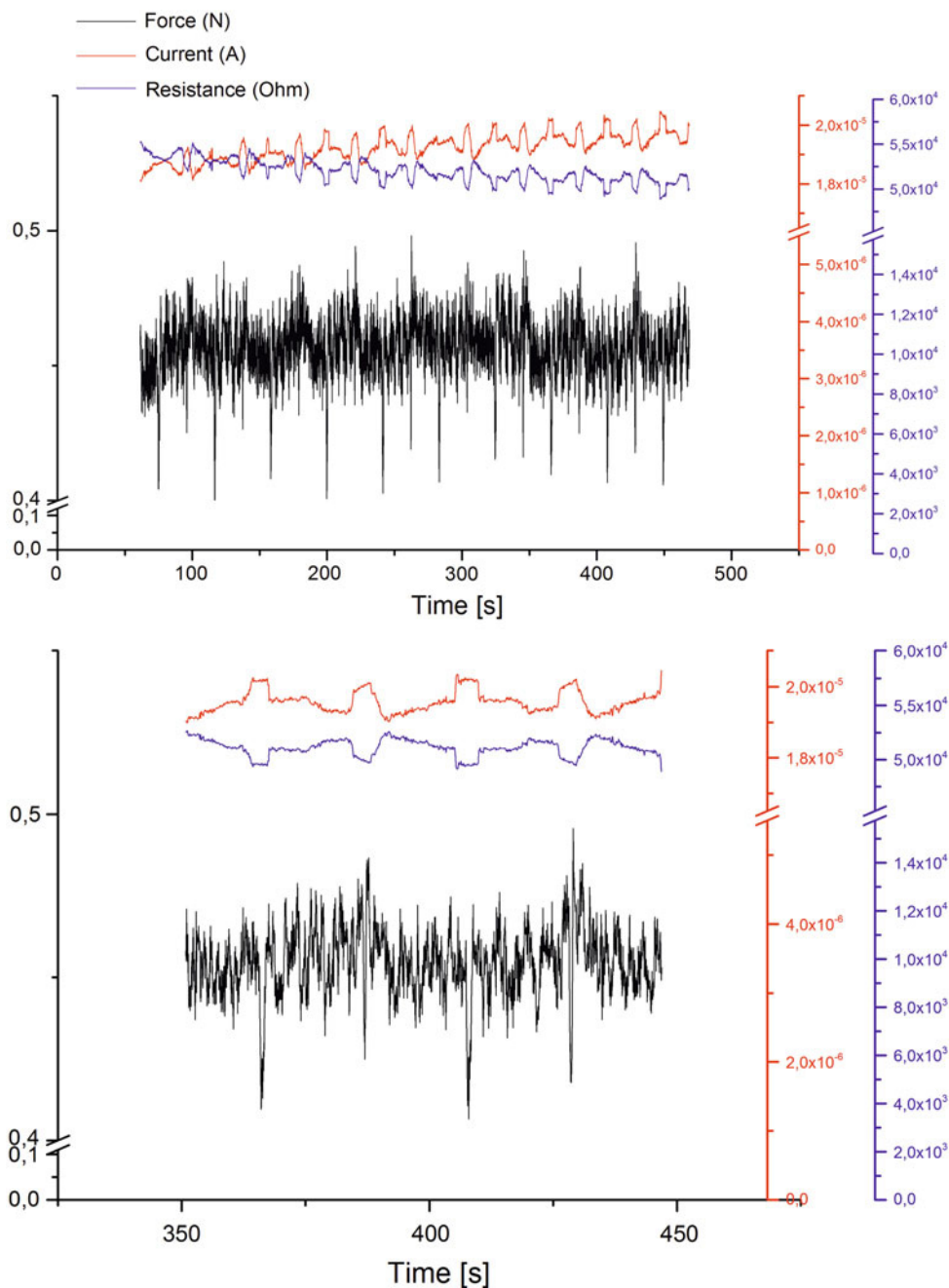
**Fig. 2** FESEM micrographs of polymer fibers before and after coating with  $\text{Bi}_2\text{Te}_3$  nanoplates

formed. Thus, strongly bonded Bi<sub>2</sub>Te<sub>3</sub> nanoplates are part of a closed composite film. Also, smaller ‘plate-like’ structures are randomly dispersed on the surface of the fiber matrix. Overall, we assume that the weak van-der-Waals forces existing at different junctions and interfaces between Bi<sub>2</sub>Te<sub>3</sub> nanoplates and the polymer fiber-mesh matrix is strongly responsible for the good adhesion. However, when no additional graphene was used the adhesion of Bi<sub>2</sub>Te<sub>3</sub> nanoplates was significantly reduced, thus leading to only low coverage of the fiber-mesh (not shown here).

The mass weight as well as the dimensions of the graphene coated fiber-mesh was measured before and after dipping in Bi<sub>2</sub>Te<sub>3</sub> suspension. The density of nanoplates deposited on the fiber-mesh matrix increases with the dwelling time. Lowest electrical resistivity was found for the samples with longest dwelling time.

The samples were folded, and tensile and compressive stress applied. Simultaneously, the resistivity was measured. A representative result of such measurement is depicted in Fig. 3.

**Fig. 3** Change of current and resistance in dependence of mechanical loading. The upper graph represents several loading cycles while the lower graph represents an enlarged section highlighting the effect of resistivity changes upon applying tensile and compressive stress



Repeatedly compressive and tensile stress were applied to the sample applying. It is observed that a decrease in resistivity and, accordingly, an increase in electrical conductivity is observed for both cases (as seen in Fig. 3). This effect can be attributed to the re-orientation and increased overlapping of different wires/nanoplates due to the stress which is applied. With the tensile stress, it allows the coated nanoplatelets to create a junction through bonding of numerous nanoplatelets contacting each other thereby, increasing locally the conductivity whereas this effect is not strong or perhaps predominates during compressive stress. The overlapping of the nanoplatelets is predominant and we assume, the bonding of the nanoplatelets might not be too strong and responsible for the light drop in the resistivity. Supposedly, the tunneling barrier of the electron mobility is thus not completely overwhelmed. Furthermore, a memory effect is observed. With increasing number of load cycles, the resistivity further decreases leading to a remnant change in the resistivity in the unloaded state. The origin for this behavior might be again the result of different wires/nanoplates getting in contact irreversibly and forming new junctions. Thus, with an increased number of loading cycles an accumulation takes place, consequently leading to a remnant change in resistivity.

#### 4 Conclusions

In this paper, we have highlighted the polyol wet chemical process as an effective simple chemical method to synthesize high quality and good grade nanoplates of  $\text{Bi}_2\text{Te}_3$  that are single crystalline. The obtained nanoplates exhibit areal dimensions in the range of 3–5  $\mu\text{m}$  and have a thickness of a few nanometers.

Furthermore, it was found that graphene coated PCL fiber spun polymers act as an ideal substrate for the deposition of  $\text{Bi}_2\text{Te}_3$  nanoplates forming a long-range percolation network.

In the mechano-electrical transport measurement, tensile and compressive stress lead to a decrease in resistivity while after several cycles the material exhibited a remnant change in electrical conductivity.

These results highlight the potential of flexible thermoelectric materials to be used as pressure sensors while simultaneously being able to implement a power source or a temperature sensor.

**Acknowledgements** The authors like to thank the Land Schleswig-Holstein and Hamburg for financial support. Further, the authors like to thank the group of Prof. Oepen for the use of the SEM.

**Conflict of Interest** The authors declare that they have no conflict of interest.

#### References

1. Rowe, D.M.: *Thermoelectrics Handbook: Macro to Nano*. CRC Press (2005)
2. Eibl, O., Nielsch, K., Peranio, N., Völklein, F.: *Thermoelectric  $\text{Bi}_2\text{Te}_3$  Nanomaterials*. John Wiley & Sons (2015)
3. Champness, C.H., Chiang, P.T., Parekh, P.: Influence of growth conditions and tellurium phase on the thermoelectric properties of bismuth telluride-type materials. *Can. J. Phys.* **43**, 653 (1965)
4. Böttner, H., Ebling, D.G., Jacquot, A., König, J., Kirste, L., Schmidt, J.: Phys. Structural and mechanical properties of spark plasma sintered n- and p-type bismuth telluride alloys. *Status Solidi RRL—Rapid Res. Lett.* **1**, 235 (2007)
5. Koenig, J., Winkler, M., Dankwort, T., Hansen, A.-L., Pernau, H.-F., Duppel, V., Jaegle, M., Bartholomé, K., Kienle, L., Bensch, W.: Thermoelectric efficiency of  $(1-x)(\text{GeTe})x(\text{Bi}_2\text{Se}_{0.2}\text{Te}_{2.8})$  and implementation into highly performing thermoelectric power generators. *Dalton Trans.* **44**, 2835 (2015)
6. Dong, H., Chen, Y.-C., Feldmann, C.: Polyol synthesis of nanoparticles: status and options regarding metals, oxides, chalcogenides, and non-metal elements. *Green Chem.* **17**, 4107 (2015)
7. Weller, D.P., Stevens, D.L., Kunkel, G.E., Ochs, A.M., Holder, C. F., Morelli, D.T., Anderson, M.E.: Thermoelectric performance of tetrahedrite synthesized by a modified polyol process. *Chem. Mater.* **29**, 1656 (2017)
8. Yang, L., Hng, H.H., Cheng, H., Sun, T., Ma, J.: Thermoelectric properties of p-type  $\text{CoSb}_3$  nanocomposites with dispersed  $\text{CoSb}_3$  nanoparticles. *Mater. Lett.* **62**, 2483 (2008)
9. Anderson, M.E., Bharadwaja, S.S.N., Schaak, R.E.: Modified polyol synthesis of bulk-scale nanostructured bismuth antimony telluride. *J. Mater. Chem.* **20**, 8362 (2010)
10. Soni, A., Yanyuan, Z., Ligen, Y., Aik, M.K.K., Dresselhaus, M.S., Xiong, Q.: Enhanced thermoelectric properties of solution grown  $\text{Bi}_2\text{Te}_{(3-x)}\text{Se}_{(x)}$  nanoplatelet composites. *Nano Lett.* **12**, 1203 (2012)
11. Yadav, A., Pipe, K.P., Shtein, M.: Fiber-based flexible thermoelectric power generator. *J. Power Sources* **175**, 909 (2008)
12. Du, Y., Xu, J., Paul, B., Eklund, P.: Flexible thermoelectric materials and devices. *Appl. Mater. Today* **12**, 366 (2018)
13. Zhang, F., Zang, Y., Huang, D., Di, C., Zhu, D.: Flexible and self-powered temperature–pressure dual-parameter sensors using microstructure-frame-supported organic thermoelectric materials. *Nat. Commun.* **6**, 8356 (2015)
14. Eising, G., Niebuur, B.-J., Pauza, A., Kooi, B.J.: Competing crystal growth in Ge–Sb phase-change films. *Adv. Funct. Mater.* **24**, 1687 (2014)
15. Kolosov, V.Y., Thölen, A.R.: Transmission electron microscopy studies of the specific structure of crystals formed by phase transition in iron oxide amorphous films. *Acta Mater.* **48**, 1829 (2000)
16. Zhuang, A., Li, J.-J., Wang, Y.-C., Wen, X., Lin, Y., Xiang, B., Wang, X., Zeng, J.: Transmission electron microscopy studies of the specific structure of crystals formed by phase transition in iron oxide amorphous films. *Angew. Chem. Int. Ed.* **53**, 6425 (2014)

*Further publications*

# Acknowledgments

During my time working on this thesis I gained a lot of experiences, not only in technical skills in the laboratory and knowledge about the underlying physics of my system. But also regarding the work in a scientific environment that relies on strong collaborations and mutual support and criticism. I would like to thank all people mentioned below for their individual input and am looking forward to explore the different aspects of scientific research in the future.

First of all, I am grateful to **Prof. Michael Rübhausen** for providing a research environment for me that allowed for individual freedom and ideas while also pushing for conclusive scientific output. Dear Michael, I want to thank you for all the support, in-depth discussions on theoretical aspects of Raman spectroscopy, and introduction in the scientific community.

I also want to express my gratitude to **Prof. Nils Huse** and **Prof. Dorota Koziej** who taught me plenty during my undergraduate courses about solid state physics and methods for manufacturing nanostructured devices. I am grateful for Prof. Huse to review this thesis and am thankful for every point of criticisms regarding the underlying physics. Furthermore, I am most thankful for him to reveal to me that lasers with wavelengths of 490 nm are indeed the most beautiful. I further would like to thank Prof. Koziej for participating in my defense and for advice and guidance regarding a career in academic research.

I further want to thank my additional defense committee members **Prof. Daniela Pfannkuche** and **Prof. Kai Rossnagel** for their scientific input.

Now comes the part where I want to show great gratitude to all group members, current and alumni, of the applied physics optics group that have created a supportive, learning and fun environment to work in.

First of all, my thanks goes to **Benjamin Grimm-Lebsanft** for always being the first contact for all issues, ranging from tackling software issues on the AFM computer, all technical and physics related questions in the optics lab, as well as locating the right person in CFEL for various administrative problems. Thank you for always having an open door and ear, and creating a wonderful warm and welcome atmosphere where no question is being judged.

I thank **Sören Buchenau** for introducing me into the field of topological insulators, where his enthusiastic and pictorial explanations of this topic has sparked the great interest in me to investigate this material. I am grateful for all comments and advice on manuscripts, theses and presentations. Our scientific exchange in Urbana-Illinois was very fruitful, which I relate to our mutual motivation and excitement for science that made the many late night hours in the lab a piece of cake.

My gratitude goes to **Tomke Glier** for her great enthusiasm and energy in the lab. Thank you for the very productive partnership during our measurements, where our quick consensus on scientific discussion has led to an immense motivation.



## *Further publications*

I am thankful to **Christian Nweze** for being my pleasant companion in our shared office. Thank you for the collaborative work we had in the lab with many interesting discussions about physics and Nigerian culture.

Furthermore, I want to thank **Lewis Akinsinde** for a great contact in the lab and office and many enjoyable conversations we shared. Also thank you for networking me with many scientific contacts at DESY that greatly helped in the characterization of the topological nanoflakes. My thanks goes to **Melissa Teubner** for her calm and reasonable approach on physics and many pleasant conversations. I want to thank **Florian Biebl** for great explanations regarding the network connections in the optics lab and laser setups. I am thankful for his support in setting up the AFM and beam path alignments for the micro-Raman setup. My thank goes to **Marie Betker** for entertaining late night shifts during beam times and her most positive attitude towards science. I want to thank **Lea Westphal** for her pleasant and fun nature that brings great joy into the lab. Furthermore, I am thankful for **Stephanie Baer** for her support in administrative questions and general open and kind nature.

My thanks goes to all the undergraduate students who I got to supervise and work with. Thanks for the great help in the investigation and optimization of the wet-chemical synthesis of the topological insulator nanoflakes. Their critical questions and different backgrounds in physics has challenged me to continuously search for better explanations of topological physics and lead to an in-depth understanding of the topic. **Mirko Pollok** thank you for encountering the first attempts in synthesizing flakes of mixed composition even though we faced many challenges. **Jakob Dilling** thank you for the collaborative research on implementing a synthesis of  $\text{Sb}_2\text{Te}_3$  nanoflakes and many fun hours in the chemistry lab. Dear **Marie-Charlot Dalchow** thank you for doing great work on the synthesis optimization for  $\text{Bi}_2\text{Te}_3$  and the friendship we have developed. Dear **Isa Moch** thank you for your laborious work on the AFM and your cheerful and positive energy that leads to great motivation in the lab. And last but not least thanks to **Malte van Heek** for his great interest in science and many profound questions that also helped me gaining a deeper understanding of physics.

I want to thank the many scientific collaborators who helped in the understanding of my material system and the successful creation of our manuscripts. Thank you **Robert Frömter** for teaching me your in-depth knowledge on scanning electron microscopy that I have strongly benefited from. I want to thank **Andrea Köppen** for her excellent transmission electron microscopy measurements on my nanoflakes and the creation of beautiful atomic resolution images. I further want to thank **Robert Zierold** for introducing me to scientific writing during practical courses for my undergraduate modules and his very helpful points of criticism on our current manuscript. I am further thankful for the manufacturing of the gold substrates that were used in the micro-Raman study. I sincerely thank **Stephan Martens** for endless in detail explanations of all my questions. I have greatly benefited from his extensive knowledge and supportive measurements on e.g. ellipsometry on the gold substrate.

I want to thank the group at the university of Illinois at Urbana-Champaign for our fruitful collaborations. Thanks to **Prof. Lance Cooper** for the great scientific input and warm welcome that we received during our stay. Further thanks goes to **Eddie Slimak** and



**Astha Sethi** for their very helpful support in the macro-Raman measurements and many fun hours in the optics lab.

I also want to thank my friends at CFEL that have given me many pleasant moments over coffee breaks supplying a great motivation to hop back into the lab. In particular, I thank **Felix Ritzkowksy** for scientific exchange on conferences, laser physics and general career in research. Our bonding moment was the collaborative rescue mission of a magnetic stirring bar that had fallen into the container for used solvents. I am grateful for this moment that has led to our friendship and has given me insight into different approaches on tackling physics. Secondly, I want to thank my lab neighbor **Hendrik Schikora** for many pleasant conversations and his creative mindset that has led to a high motivation in my experimental research career.

I want to thank the administrative team of CFEL especially **Gisbert Mantei** and **Sakir Sagir** for their support in various things and their delightful attitudes that created a cheerful mind set each morning.

I am indebted to my family for giving me all the love and support in finishing this degree. Thanks to my parents **Beate** and **Thomas Scheitz** who raised me and my sister to pursue any profession that we wanted and providing us with a mind set that we could achieve anything with hard work and kind treatment of the people around us. With this I express my deep gratitude to my sister **Laura Scheitz** for all the encouraging moments, great motivation, and pushing me to achieve any goal.

And finally I want to thank **Christoph Paus** for being my powerful backbone, for managing the house hold and cooking dinner when I spend late night hours in the lab or office. Without you and your support this thesis would have taken another year. Thank you for putting up with me for the last three years, for the countless moments where you lift me up, and for your endless support and love.